공학박사학위논문

# Studies on Nanostructured Transition and Post-transition Metal Compound Electrodes for Photoelectrochemical Cells

# 광전기화학전지를 위한 나노구조 전이금속 및 전이후금속 화합물 전극 연구

2015 년 8 월

서울대학교 대학원

화학생물공학부

강 진 수

# Studies on Nanostructured Transition and Post-transition Metal Compound Electrodes for Photoelectrochemical Cells

## 광전기화학전지를 위한 나노구조 전이금속 및 전이후금속 화합물 전극 연구

지도교수 성 영 은

이 논문을 공학박사학위논문으로 제출함

2015년 8월

서울대학교 대학원

화학생물공학부

강 진 수

강진수의 박사학위논문을 인준함

2015년 8월

위 원 장 최태환 (인)

부 위 원 장 성영은 (인)

위 원 김대형 (인)

위 원 최희만 (인)

위 원 고민재 (인)

# Abstract

# Studies on Nanostructured Transition and Post-transition Metal Compound Electrodes for Photoelectrochemical Cells

Jin Soo Kang

School of Chemical and Biological Engineering

The Graduate School

Seoul National University

Photoelectrochemical cells are electrochemical cells that generally comprise semiconductor photoelectrode, electrocatalytic counter electrode, and electrolyte. There are two types of photoelectrochemical cells according to the function of the electrolyte; (i) photovoltaic cell with regenerative redox electrolyte and (ii) photosynthetic cell with sacrificial electrolye. Mesoscopic sensitized solar cells and photoelectrochemical water splitting cells are the typical examples of each kind, respectively. In this thesis, nanostructured electrodes composed of transition and post-transition metal compound for those cells were investigated.

The main issues in the development of photoelectrodes, which are mainly metal oxide films, are improvements of light harvesting and charge collection. In contrast, replacement of high-cost and rare noble metal, typically platinum, with an economic and earth-abundant material has been the main objective of the research works on counter electrodes. Therefore, in this study, nanostructured metal oxides

with intrinsically fast charge transport property and state-of-the-art nanomaterials with enlarged surface area were utilized as photoelectrodes. Also, nanostructured low-cost carbide and nitride materials with facile preparation methods were employed as electrocatalytic counter electrodes. Besides the discussions on quatitative improvements, in-depth physicochemical analyses for characterization of materials and photoelectrochemical cells were performed.

After brief explanations of history, backgrounds, and previous research works on photoelectrochemical cells in chapter 1, in chapter 2 and 3, nanostructured metal oxide photoelectrodes with high carrier mobility are discussed. Mesoporous ZnO nanowire arrays with large surface area were synthesized by electrochemical anodization in a mild condition, and highly uniform $SnO_2$ nanochannels were prepared by ultrasonic-assisted anodic oxidation. These nanostructured electrodes were employed as photoanode in quasi-solid dye-sensitized solar cells (DSCs), and fair energy conversion efficiencies were obtained, with further improvements by atomic layer deposition of $TiO_2$ shells.

In the next two chapters, strategies for efficient light harvesting by increased surface area were discussed. In chpater 4, $TiO_2$ coated wrinkled silica nanoparticles were utilized as scattering centers in photoanode of DSCs. Superior performances to the DSCs with conventional sphere-shaped $TiO_2$ scatterers were achieved due to the enlarged surface area, and futher observations on the relationship between spectral scattering properties and interwrinkle distances were made. In chapter 5, electrochemically anodized titanium and iron foams prepared by freeze-casting were used as photoanodes of DSCs and photoelectrochemical water splitting cells, respectively. By the anodic oxidation processes, one-dimensional $TiO_2$ nanoatube arrays were formed on the titanium foam surface, and vertically aligned two-dimensional iron oxide nanoflakse were generated on the surface of the iron foam. These multidimensional

structures had following three advantages; (i) large surface area for light harvesting, (ii) low-dimensionally confined semiconductor structure for enhanced charge transport, and (iii) three-dimensionally extended current collector with very low resistnace. Based on these properties, large photocurrent densities were obtained in both DSCs and iron oxide based photoelectrochemical water splitting cells.

In chapter 6, nanostructured tungsten carbide synthesized by electrochemical anodization followed by heat treatment in carbon monoxide atmosphere was used as a counter electrode for DSCs employing cobalt bipyridyl redox electrolyte. The transformation of oxide into carbide was successfully and completely done due to the amorphous nature of anodic oxide materials. Moreover, superior electrocatalytic activity and photovoltaic performances were oberseved, which were attributed to the well known platinum-like electronic structure and nanoporous morphology.

In chapter 7 and 8, nanostructured nickel nitride and cobalt nitride were fabricated by reactive sputtering of nickel and cobalt in nitrogen atmosphere, respectively. By physicochemical charaterizations based on electron microscopy and X-ray analyses, the films were addressed to $Ni_2N$ and CoN with cauliflower-like morphologies. When these electrodes were used as counter electrodes of quantum dot-sensitized solar cells (QDSCs), both electrodes displayed superior performances to Pt. In addition, the energy conversion efficiency of DSC employing cobalt nitride counter electrode was comparable to that with platinum. Furthermore, in QDSCs, CoN exhibited higher stability than the state-of-the-art $Cu_2S$ counter. Photocurrent densities of QDSC with CoN counter electrode exceeded that with $Cu_2S$ within 20 min, though the initial performance was higher in QDSC employing $Cu_2S$.

***Keywords:*** photoelectrochemical cells, mesoscopic sensitized solar cells, photoelectrochemical water splitting cells, electrochemical anodization, reactive sputtering

***Student number:*** 2012-22577

# Contents

# List of Tables

# List of Figures

# Chapter 1. Introduction

## 1.1. General introduction to photoelectrochemical cells

### 1.1.1. Photoelectrochemical cells

On account of the rapid growing world population and industry, energy consumption has increased exponentially to this date, and much steeper rise is expected in the future. Since the main energy source at this moment is fossil fuels of which quantity in the earth's surface is limited in addition to the pollution problems, intensive attempts to produce electrical energy using a 'clean method' has been done for a few last decades. Among various energy sources, solar energy from sun is considered as the most promising candidate to replace conventional energy production systems.

Global energy consumption in 2000 was around 13 TW, and in 2013, it has increased to 17 TW. Within next 30 years, annual consumption is expected to be doubled [1,2]. The amount of solar energy is that hits the earth's surface is $1.7 \times 10^5$ TW per year, which is a large enough energy to satisfy the demand of the mankinds [3]. However, the energy density (i.e. the number of photons per unit area) of 1,000 W $m^{-2}$ is a significantly lower than that from the combusition of fossil fuels, and thus efficient utilization of solar energy is the most critical issue for the practical use of solar energy.

Among various methods to convert the photon energy into a useful form, solar cells are the most efficient way to convert sunlight into a useful form of energy, namely electricity. In general, solar cells are based on a semiconductor in which charge separation (formation of electron/hole pair) occurs as a consequence of light absorption, which sets a potential over the opposite sides of the electrical

circuit [4]. Though a solar cell is often composed of a junction between the semiconductors, the phase in contact with the semiconductor can be replaced with an electrolyte, constituting a photoelectrochemical cell.

A photoelectrochemical cell comprises a semiconductor photoelectrode, an electrocatalytic counter electrode, and an electrolyte. Introduction of the electrolyte enables a unique constitution of the cells, and according to the type of electrolytes, there are two kinds of photoelectrochemical cells. As shown in Figure 1.1a, photoelectrochemical cells with regenerative electrolyte operates as a conventional photovoltaic device, converting the solar energy into electrical energy without leaving any net chemical changes behind. In contrast, a photosynthetic cell (Figure 1.1b) employs sacrificial electrolyte which leads to a production of chemical fuels by the decomposition of electrolyte. In this research, preparation of various nanostructured electrodes for mesoscopic sensitized solar cells and photoelectrochemical water splitting cells, which are the most typical types of regenerative and photosynthetic cells, respectively, will be discussed.

### 1.1.2. Semiconductor photoelectrochemistry

Semiconductor photoelectrode is the heart of photoelectrochemical cells, in that the charge separation at the photoelectrode (which sets the potential) is the driving force for the operation. Figure 1.2 shows the schematic diagram of the operation of a semiconductor electrode for oxygen evolution reaction in water splitting, under assumptions that there are neither significant overpotentials nor any side reactions. Potentials were marked in accordace with the reversible hydrogen electrode (RHE) reference. Hydrogen evolution occurs at 0 V vs. RHE since the potential region for the $H_2$ generation is within the conduction band of the semiconductor electrode. However, because the oxygen evolution potential is located at the forbidden region of the semiconductor, $O_2$ evolution onset is located at the valence band edge position in dark condition (blue curve in Figure 1.2b). Under illumination of light

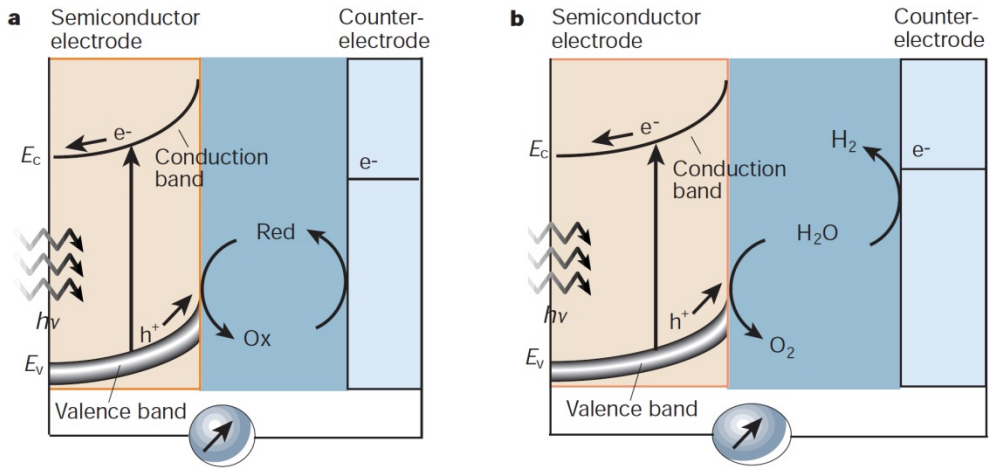


**Figure 1.1.** Schematic diagrams showing operation principles of (a) regenerative and (b) photosynthetic photoelectrochemical cells. (Adapted from Grätzel, M., *Nature* **2001**, *414*, 338)

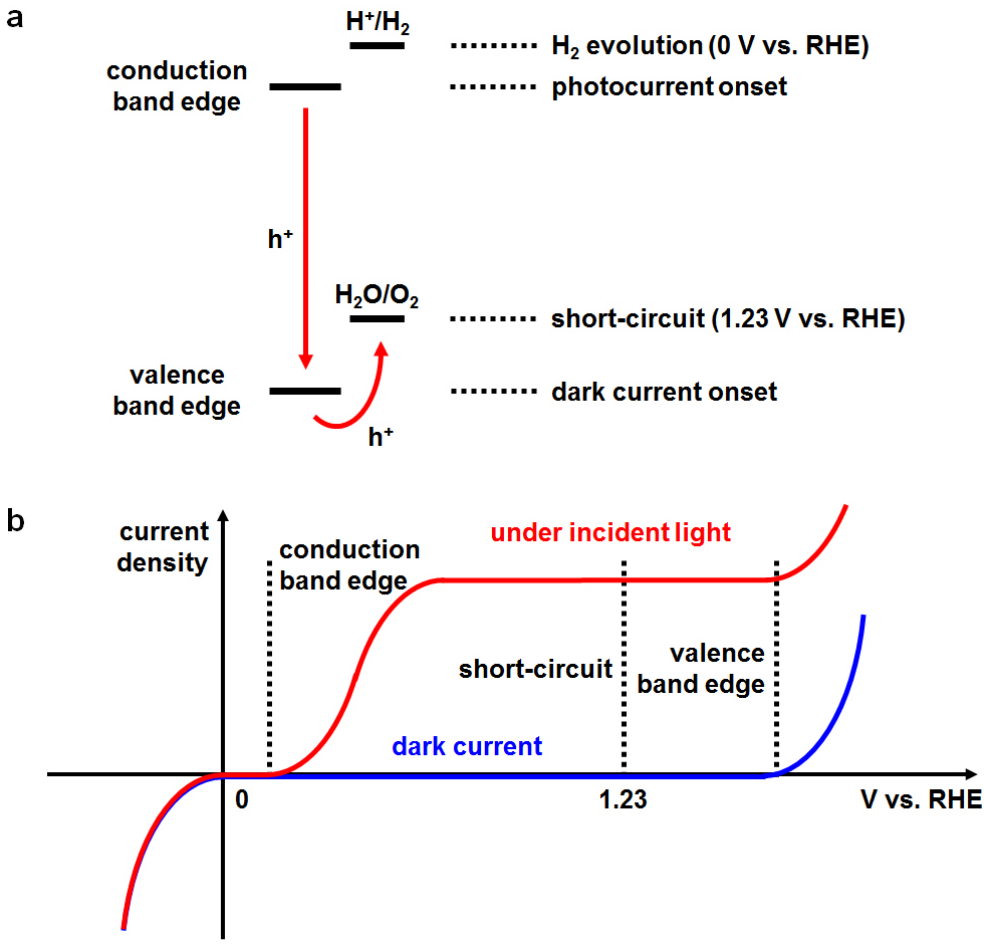


**Figure 1.2.** Schematic (a) energy diagram and (b) current density-voltage plot of oxygen evolution reaction at an n-type semiconductor electrode.

with photon energy larger than the bandgap of the semiconductor, charge separation occurs, leaving high energy electron in the conduction band and hole in the valence band. Therefore the oxygen evolution starts at the conduction band edge position of the semiconductor electrode, as displayed in Figure 1.2b (red line). In general, semiconductor electrode shifts the potential of a certain reaction up to its bandgap energy, by photon-assisted electron/hole separation.

### 1.1.3. Electrocatalysis

In a photoelectrochemical cell, beside the semiconductor photoelectrode, an electrocatalytic counter electrode is employed for the reciprocal reaction. Since photoelectrode governs the overall operation, materials with sufficiently high electrocatalytic activity, i.e. fast enough charge transfer kinetic that does not limit the overall reaction, have been favored for the use in counter electrodes. Generally, electrocatalysis comprises three steps; (i) adsorption of reactant, (ii) electron transfer, and (iii) desorption of product. Numerous experimental results and density functional theory (DFT) based calculations disclosed the dependence of reaction rate on the adsorption energy of reactant species on the surface of electrode [5-9].

In typical photoelectrochemical cells based on n-type semiconductors, the role of counter electrodes is reduction of electrolyte. Figure 1.3a shows the hydrogen evolution reactions that take place at the counter electrodes of photoelectrochemical water splitting cells. During this process, as shown in Figure 1.3b, the kinectics of electrocatalysts strongly depend on the electrode-hydrogen bond strength [7]. The situation is similar in the case of mesoscopic sensitized solar cells, wherein iodide redox electrolytes are most frequently employed. Figure 1.3c and 1.3d show adsorption structure and transition state position of iodine on platinum surface, respectively, and materials with electrode-iodidne bond strength within certain range (e.g. 0.3 – 1.2 eV) shows electrocatalytic activity high enough to generate photocurrent to some extent (Figure 1.3e) [9].

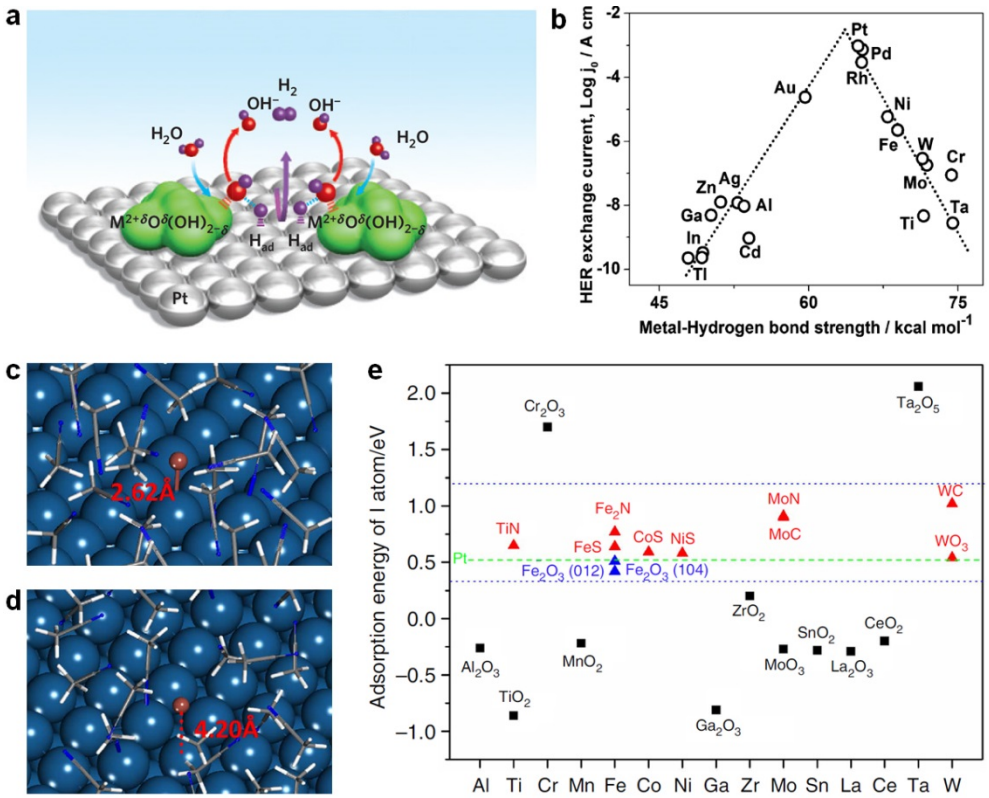


**Figure 1.3.** (a) Schematic image showing electrocatalytic hydrogen evolution reaction and (b) volcano plot showing the hydrogen evolution reaction rate at the surface of various elements according to the metal-hydrogen bond strength. (c) Schematic image of I atom adsorbed on a Pt (111) surface and (d) that at the transition-state. (e) Adsorption energy of I atom on various transition metal compounds. (Adapted from Subbaraman, R. et al., *Nat. Mater.* **2012**, *11*, 550, Calle-Vallejo, F. et al., *Chem. Soc. Rev.* **2013**, *42*, 5210, and Hou, Y. et al., *Nat. Commun.* **2013**, *4*, 1583)

## 1.2. Mesoscopic sensitized solar cells

### 1.2.1. Dye- and quantum dot-sensitized solar cells

From the middle of the twentieth century, efficient utilization of metal oxide semiconductors in photoelectrochemical cells has been the goal of many researchers over the world. $TiO_2$, ZnO, $SnO_2$, $Nb_2O_5$, and many other metal oxides have attractive properties such as abundancy in the earth's surface, facile and economic preparation methods, and environmental friendliness [4]. However, these metal oxides have wide bandgap energy close to or even larger than 3 eV. This limits the absorption of light to the ultraviolet (UV) region, which constitutes only ~5% of the photons in incident solar rays. Therefore, extending the absorption onset to visible light and further to near infrared (IR) region have been attempted, and significant improvements were achieved by dye-sensitization of nanostructured metal oxide films.

The first dye-sensitization concept was discovered by Vogel [10] in 1883, and was brought into the field of photoelectrochemical cells by Moser [11] in 1887. In these findings, dye-sensitization enhanced the photosensitivity of silver halide, especially in the long wavelength region. The mechanisms and phenomena of the sensitization have been addressed by the pioneering works of Nelson and Boudon reported in 1965 [12,13], and following works were mainly focused on the sensitization of ZnO. In 1970, Hauffe et al. obtained tens of nA $cm^{-2}$ scale photocurrent by using rhodamine B [14], and Tsubomura et al. [15-17] and Alonso et al. [18] reported significantly increased photocurrent by using rose bengal and related dyes.

In 1985, polycrystalline $TiO_2$ film was introduced as a smuconductor electrode for dye-sensitization by Grätzel group, and further advances were achieved by using a $TiO_2$ electrode with larger surface area [19-23]. Then in 1991, O'Regan and Grätzel reported mesoscopic solar cell based on a colloidal $TiO_2$

nanoparticle film with the roughness factor around 1,000 [24]. The performance of the cell exceeded 7%, being comparable to the conventional photovoltaic devices at that time. This paper gave birth to the research field of dye-sensitized solar cells, and propagated intensive investigations which are still ongoing these days. Figure 1.4 shows the transimission and scanning electron microscope images of typical nanocrystalline $TiO_2$ films used for the DSCs.

Over last 25 years, general composition and overall configuration of the DSCs haven't changed much [25-28], and a typical scheme of the DSC operation is shown in Figure 1.5. As dye molecules adsorbed on the $TiO_2$ surface absorbes photon with larger energy than the energy gap between the highest occupied molecular orbital (HOMO) and the lowest unoccupied molecular orbital (LUMO), charge separation (generation of electron/hole pair) takes place. Then the electron gets injected into the $TiO_2$ conduction band immediately and moves through the $TiO_2$ lattice by diffusion until it reaches the current collector, which is often fluorine-doped tin oxide (FTO) on a glass substrate. On the other hand, holes located at the HOMO level of dyes are scavenged by reduced species in the electrolyte. Then the oxidized components of the electrolyte move to the counter electrode where they get regerated by electrocatalytic reduction. The electrons that travel from the current collector in the photoanode to the counter electrolyte constitute the photocurrent, completing the electrochemical circuit with energy conversion from solar to electrical form.

Most of the research works that brough significant improvements in the performance of DSCs are based on the development of dyes with high extinction coefficient and redox electrolytes with low overpotentials. Ru dyes and $I_3^-/I^-$ redox electrolyte have been the best combination for two decades from 1991 [28]. N3 [29] and its deprotonated derivative (N719) [30] is the most frequently employed sensitizers even to this date. N749 dye with with absorption onset over 900 nm have shown the best performances until the outburst of efficient organic dyes

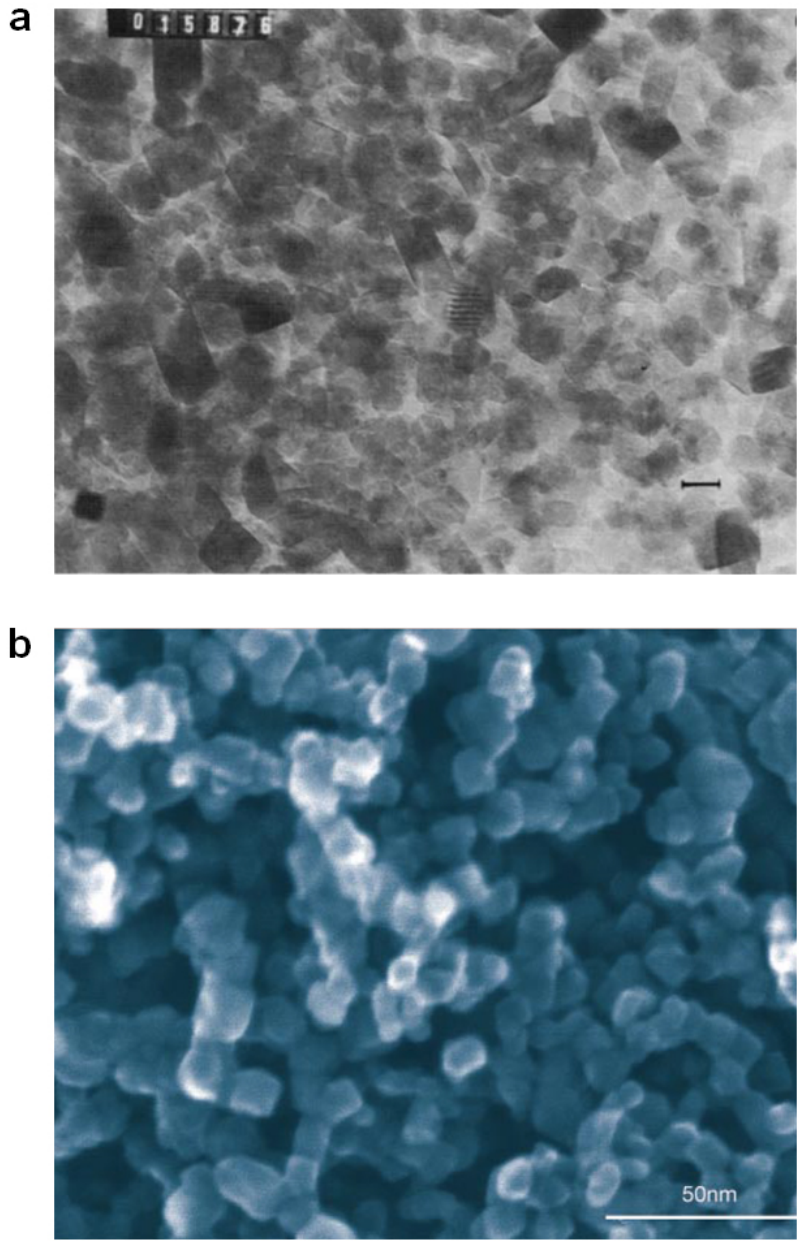


**Figure 1.4.** (a) Transition electron microscope and (b) scanning electron microscope images of typical $TiO_2$ nanoparticles employed in mesoscopic sensitized solar cells. (Adapted from O'Regan, B. et al. *Nature* **1991**, *353*, 737, and Grätzel, M., *Nature* **2001**, *414*, 338)

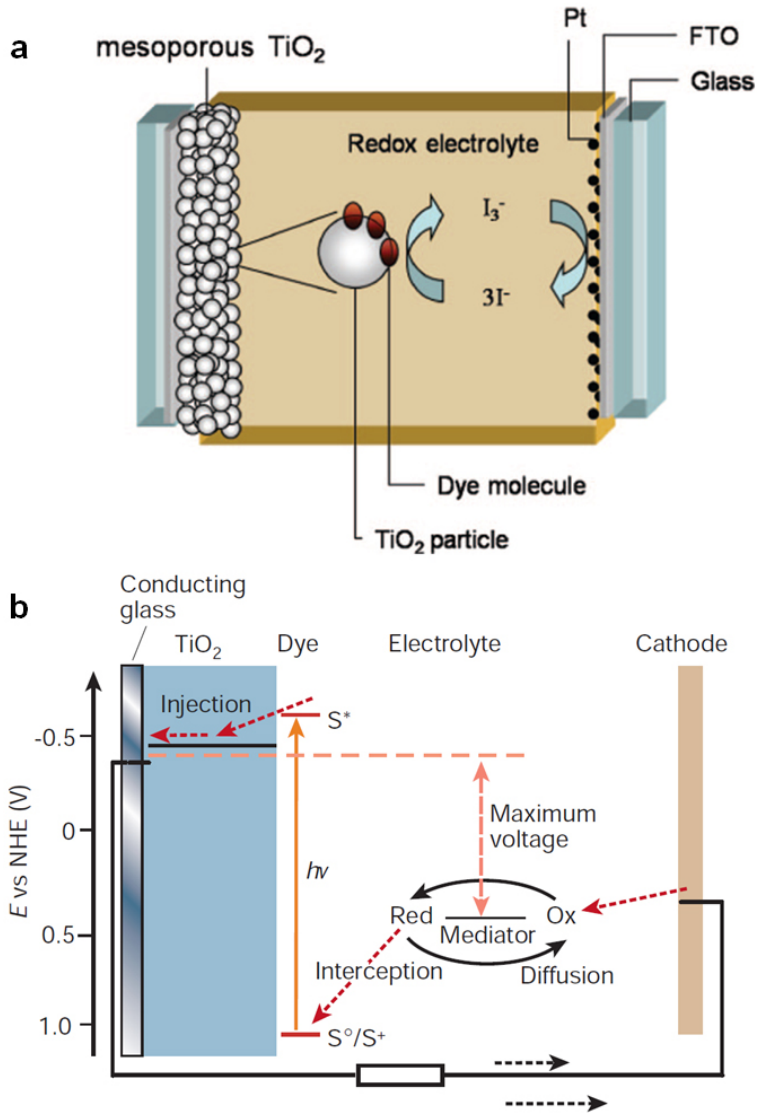


**Figure 1.5.** (a) Schematic image and (b) energy diagram showing typical configuration and operation principles of dye-sensitized solar cells, respectively. (Adapted from Hagfeldt, A.et al., *Chem. Rev.* **2010,** *110,* 6595, and Grätzel, M., *Nature* **2001**, *414*, 338)

[31,32]. Recently, Kinoshita et al. reported Ru based dye (DX1) which absorbs light up to 1,000 nm wavelength, and obtained short-circuit current density ($J_{sc}$) of 26.8 mA $cm^{-2}$ [33]. The structures of N3, N719, N749, and DX1 dyes are shown in Figure 1.6.

Beside iodide redox electrolyte, many other candidates were tested in DSCs in order to minimize the overpotential at the dye-regeneration process, and cobalt polypyridine electrolyte was anticipated to increase the photovoltage significantly due to its favorable redox potential [34,35]. However, severe charge recombination at the $TiO_2$/electrolyte interface dropped the overall performance of the solar cells. In 2010, Feldt et al. developed organic dye (D35) with alcoxy chains that sterically hinder the approach of redox species to the semiconductor surface, and the overall energy conversion efficiency went up to 6.7% [36]. Inspired by the concept of this work, further optimization of dye molecules was performed, and cconversion efficiency exceeding 10% with cobalt bipyridyl redox couples were achieved by Y123 dye [37,38]. Moreover, by development and modification of porphyrin dyes, DSCs with efficiency over 12% and of 13% were reported [39-42]. Figure 1.7 shows the molecular structures of the typical organic dye molecuels.

Quantum dot-sensitized solar cells (QDSCs) are pretty much similar to DSCs, in that only the sensitizing dye molecules are replaced with light absorbing quantum dots [43-46]. From the very beginning of its development, InP, CdSe, CdS, and PbS have been employed as the sensitizer [47-56], and further improvements were achieved by introducing dopants [57,58] or core/shell approaches [59,60]. Recently, $CuInSe_2$ and $CuInS_2$, which are well known materials with excellent light absorption properties, have been successfully employed in QDSCs, and efficiency over 7% has been reported [61,62]. For the electrolyte, polysulfide redox couples are often used due to their fast hole scavenging characteristics from the quantum dots.

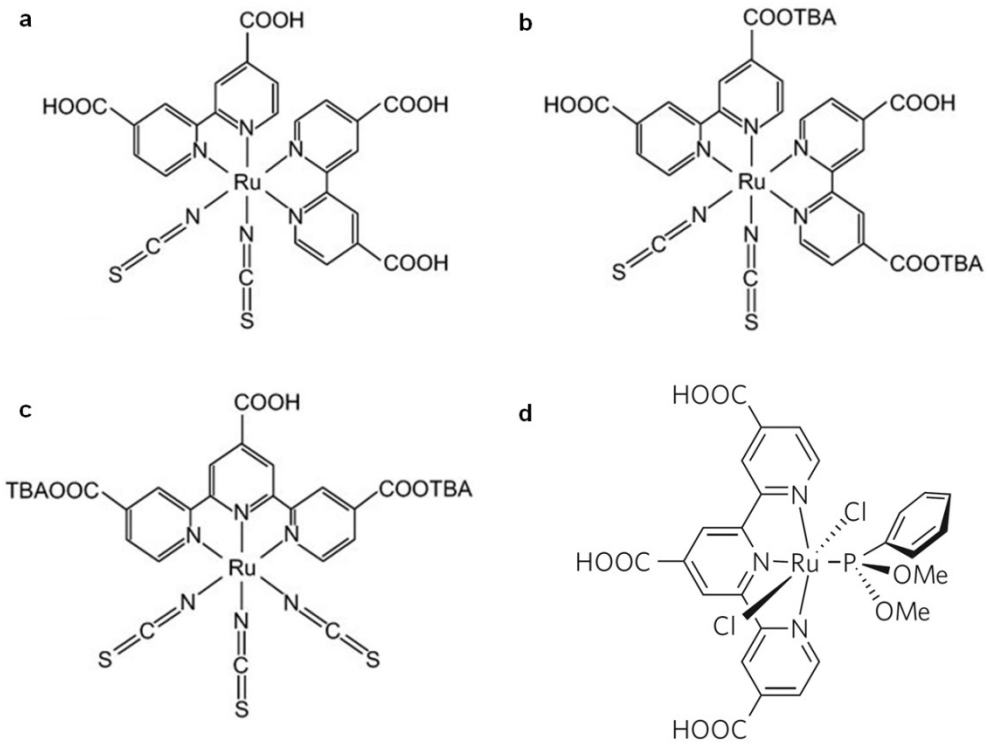


**Figure 1.6.** Molecular structures of (a) N3, (b) N719, (c) N749, and (d) DX1 dyes. (Adapted from Hagfeldt, A.et al., *Chem. Rev.* **2010,** *110,* 6595, and Kinoshita, T. et al. *Nat. Photon.* **2013**, *5*, 535)

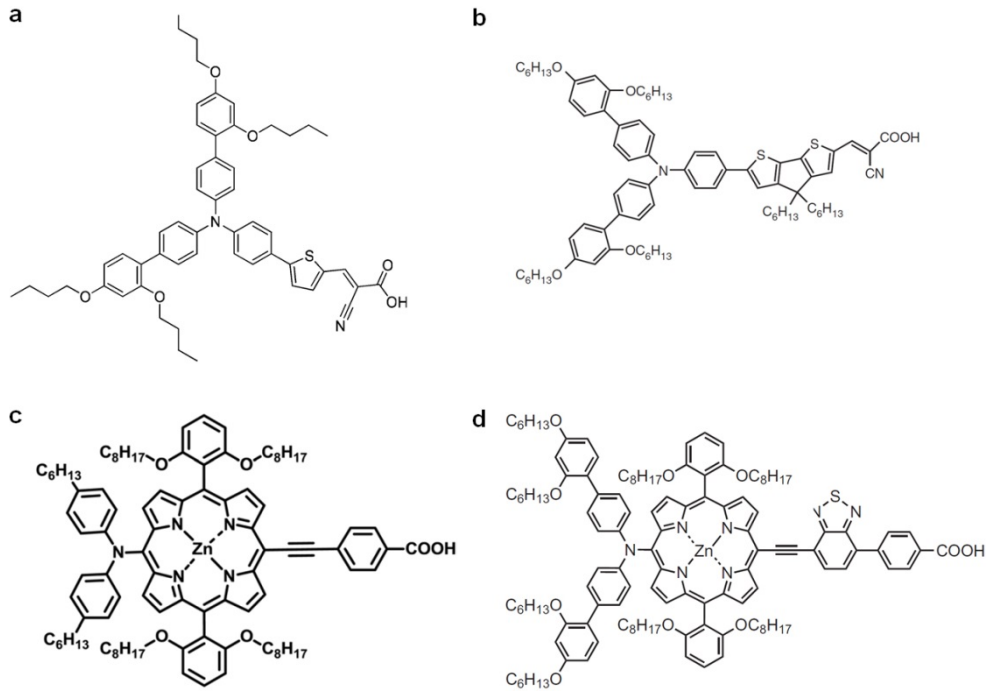


**Figure 1.7.** Molecular structures of (a) D35, (b) Y123, (c) YD2-o-C8, and (d) SM315 dyes. (Adapted from Feldt, S. M. et al., *J. Am. Chem. Soc.* **2010**, *132*, 16714, Yum, J.-H. et al., *Nat. Commun.* **2012**, *3*, 631, Yella, A. et al., *Science* **2011**, *334*, 629, and Mathew, S. et al., *Nat. Chem.* **2014**, *6*, 242)

### 1.2.2. Metal oxide materials for photoelectrodes

In general, efficient utilization of incident photons in mesoscopic sensitized solar cells is determined by four factors; light harvesting efficiency, quantum yield for electron injection and dye regeneration, and charge collection efficiency [28]. Among these, light harvesting and charge collection efficiency has largest potential for further advances, because mesoporous $TiO_2$ constituted of ~20 nm sized nanoparticles has low electron mobility and seldom scatters light, leaving significant portion of incident light to pass through the cell without contribution to the photocurrent generation [63]. Therefore, studies on efficient light harvesting and charge collection have been performed by compositional or structural modifications.

In general, for efficient light scattering, particles with dimension comparable to the wavelength of incident light are employed based on the theoretical calculation [63]. A few hundred of nanometer sized $TiO_2$ particles are most often used, either as scattering center in mesoporous film or as separate scattering layer located behind the ~20 nm $TiO_2$ nanoparticles [64-72]. For further enhancement in light harvesting, core/shell nanoparticles with improved scattering properties [73,74] or particles with large surface area for increased dye loading [68-72] have been done by many research groups, and additional advances in solar cell performances were reported.

Charge collection efficiency is important for the preparation of a high performance in mesoscopic solar cells, because the timescales of charge transport and recombination are quite comparable (Figure 1.8). In ordr to collect charges more efficiently, there have been two main directions of approaches. First one was replacing the $TiO_2$ with nanostructured metal oxides with intrinsic property of fast charge transport, such as ZnO or $SnO_2$ (electron transport being 2 to 3 orders of magnitude faster than that of $TiO_2$) [75-86]. However, ZnO suffered from chemical instability during the dye positioning step, because the anchoring group of a dye

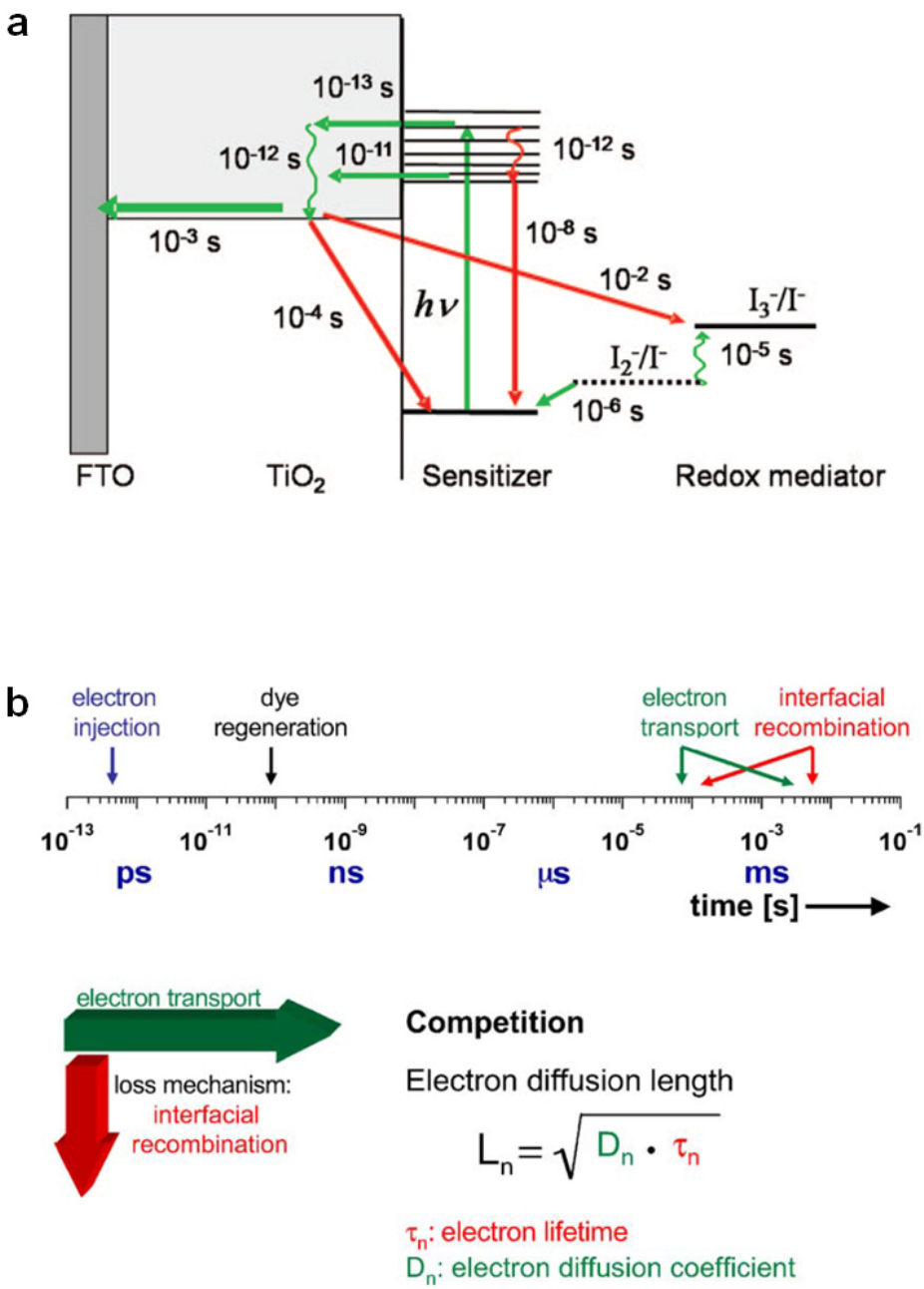


**Figure 1.8.** (a) Energy and (b) time diagram showing timescales of favorable (green colored) and unfavorable (red colored) reactions during the operation of dye-sensitized solar cells. (Adapted from Hagfeldt, A.et al., *Chem. Rev.* **2010,** *110*, 6595, and Grätzel, M., *J. Photochem. Photobiol. A* **2004**, *164*, 3)

molecules is carboxylic acid [87]. So the amount of dye-loading was significantly limited compared to the $TiO_2$, and the energy conversion efficiency is still tied up at 7% [88]. In contrast, $SnO_2$ showed excellent chemical stability, but its unfavorable conduction band position (-4.4 eV vs. vacuum level) and fast recombination kinetic result in a low energy conversion efficiency.

For a more efficient charge collection in $TiO_2$, after the pioneering work by Law et al. based on ZnO nanowires [89], structural engineering of $TiO_2$ to confine the conduction band electron pathways have been performed. Electron transport in $TiO_2$ lattice is best described by a random walk model [90], and thus vertically aligned structures are expected to reduce the distance of the electrons. Macák et al. and Mor et al. reported succeful dye-sensitization and photoanode application of anodic $TiO_2$ nanotube arrays in DSCs, respectively, and Zhu et al. quantitatively verified the enhanced electron transport in this nanotubular structure [91-93]. However, since the opague Ti metal substrate under $TiO_2$ nanotube arrays imposed unfavorable back-side illumination [94], $TiO_2$ nanowires and nanorods grown on FTO glass were also developed for mesoscopic sensitized solar cells [95,96], and by keen optimizations, long vertically aligned $TiO_2$ nanotubes were synthesized on FTO glass [97], resulting in an enhanced performance of mesoscopic solar cells.

### 1.2.3. Materials for electrocatalytic counter electrodes

In DSCs, platinum has shown the best performance from the very beginning in 1991 [24,28,42]. However, since the high-cost and rarity of Pt stands in the way for the practical usage and large scale commercialization of DSCs, various Pt-free counter electrode materials were developed. Carbonaceous materials [98-103] and conducting polymers [104-111] have shown results comparable to that of Pt, and the performances of metal alloys [112-114] and transition metal compounds [115-125] as counter electrodes were close to that of Pt counter.

On the contrary, there is no certain best material for the electrocatalytic

counter electrodes of QDSCs. Platinum, which is generally one of the best electrocatalysts in various reactions, suffers from the poisoning resulted from the chemisorption of $S^{2-}$ species on the electrode surface [46,126]. In QDSCs, sulfide materials have shown the best results, especially the $Cu_2S$ [59,62,127]. However, due to its poor stability under incident light [128], there are needs for the development of a new counter electrode that has both high electrocatalytic activity and chemical stability.

## 1.3. Photoelectrochemical water splitting cells

### 1.3.1. Operation principles and approaches

In most cases, photoelectrochemical water splitting cells are based on metal oxide semiconductors [129-131]. General operation principles of photoelectrochemical water splitting cells are displayed in Figure 1.1b and Figure 1.2. In case of photoelectrochecmialc cells based on n-type semiconductor electrodes, charge separation (formation of electron/hole pair) is followed by electron diffusion to the current collector. Then the electrons travel through the outer electric circuit and arrive at the counter electrode for the reduction of $H^+$ into $H_2$. On the other hand, holes move to the surface of the semiconductor electrode and oxidze $H_2O$ to $O_2$.

In 1972, Fujishima and Honda reported the first photoelectrochemical water splitting cells [132]. They used $TiO_2$ electrode as a photoanode, and achieved mA scale photocurrent. After this pioneering work, many researchers tried to extend the absorption spectrum of semiconductor photoelectrodes or to replace $TiO_2$ with other materials with superior light harvesting and charge transport properties. Also, minimization of overpotential for charge transfer reaction (electrocatalysis) at the surface of both photoelectrodes and counter electrodes have been performed intensively, and remarkable improvement was achieved by earth-abundant economical materials lately [133].

### 1.3.2. Materials for electrodes

In most of the photoelectrochemical cells based on metal oxide photoelectrodes, oxygen evolution reaction takes place at the photoelectrode, because oxide semiconductors with favorable band positions and photoelectrochemical properties for use in water splitting cells are often n-type [4]. Compared to p-type $Cu_2O$ and NiO, which suffer from low stability [134] and poor conductivity [135,136], respectively, n-type semiconductors such as $TiO_2$ [137-141], $WO_3$ [142], $BiVO_4$ [143,144], α-$Fe_2O_3$ [145-152] have been frequently employed in the water splitting cell and displayed superior performances.

Among these n-type oxide materials, $TiO_2$ alone has band edge positions capable of both hydrogen and oxygen evolution, but its large bandgap energy (3.2 eV for anatase) limits the utilization of sunlight to less than 5% [130]. In order to increase the solar energy utilization, donor such as C, N, and oxygen vacancies were doped to $TiO_2$ [153-155], and significantly increased photocurrent densities were observed. Also, for enhanced charge collection and minimization of recombination, as in the case of mesoscopic sensitized solar cells, 1-diemsntional structure or branched structures were employed [138,154-156].

Semiconductors with smaller bandgap energies, especially $WO_3$ (2.6 eV) and $BiVO_4$ (2.4 eV), were investigated as photoanodes for water splitting due to their fine photocatalyric activities [142-144,157,158]. Moreover, α-$Fe_2O_3$ (with bandgap energy of 2.1 eV) gained great attention due to its abundancy and environmental compatibility [150]. However, hole diffusion lengths in α-$Fe_2O_3$ (2-4 nm) was significantly smaller than those in other other metal oxides (e.g. $TiO_2$ and $WO_3$; ~150 nm) [159-161], and this greatly limited the overall performance. Therefore, various dopants were introduced into the lattice of α-$Fe_2O_3$ for enhanced hole diffusion [145-148], and Si-doped α-$Fe_2O_3$ prepared by atmospheric pressure-chemical vapor deposition induced three-fold increase in overall performance as shown in Figure 1.9 [145,146]. The origin of this high performance was verified by

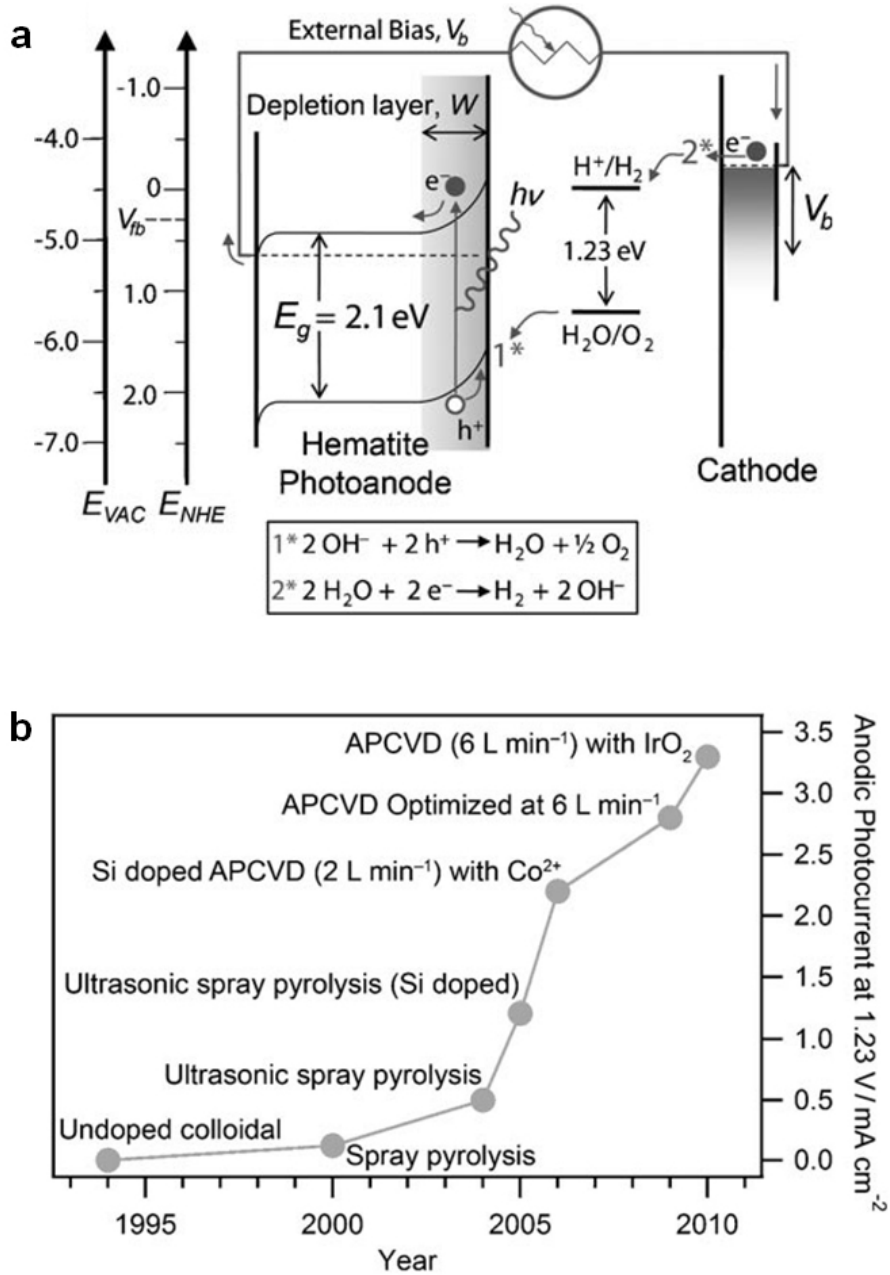


**Figure 1.9.** (a) Energy diagram and (b) performance chart of photoelectrochemical cells empoying α-$Fe_2O_3$ based material as photoanode. (Adapted from Sivula, K. et al., *ChemSusChem* **2011**, *4*, 432)

Warren et al. in 2013 [147].

Besides doping and structural engineering of metal oxide semiconductors, which tunes the intrinsic light absorption and charge transport properties, respectively, photoelectrodes employing heterojunction are also under intensive research [162]. These heterojunctions are constituted of a relatively narrow bandgap semiconductor for wide range light absorption at the outer part, and a semiconductor with relatively high conductivity at the inner part. This division of labor-like electrode design enables enhanced charge separation and carrior transport, $BiVO_4$ based heterojunctions have shown fair performances [163-165]. In addition, mesoscopic sensitized photoelectrodes have been introduced in photoelectrochemical cells, with the same purposes as heterojunctions [166,167].

In photoelectrochemical cells, poor water oxidation kinetic is one of the most critical factors that limit the overall cell performance. Therefore, decoration of cocatalysts on the surface of the electrode is often performed to minimize the charge transfer resistance at the electrode/electrolyte interface. Co or $IrO_2$ have been used most often due to their well known fast oxygen evolution kinetics [168-170], and they increased the water splitting rate to a large extent [146,171]. Recently, Kim et al. [133] and Luo et al. [172] reported hydroxide based high performance oxygen evolution catalysts. These nonrare and inexpensive materials showed superioir activity to conventional cocatalyst in photoelectrochemical water splitting cells.

For hydrogen evolving counter electordes, Pt is often employed due to its unrivaled high performance [7], as can be seen from the DFT calculation results in Figure 1.3b. However, because the oxygen evolution kinetic is by far slower than that of the hydrogen evolution, low cost materials with intermediate performances are also under intensive research and transition metal compounds with Pt like electronic structure such as WC [173,174] have shown fine performances [175]. Among them, $MoS_2$ displays the best performance among economical

electrocatalysts due to their feasible hydrogen adsorption energy at the edge sites [176].

## 1.4. References


[1] Service, R. F., *Science* **2005**, *309*, 548.

[2] Potocnik, J., *Science* **2007**, *315*, 810.

[3] Schiermeier, Q.; Tollefson, J.; Scully, T.; Witze, A.; Morton, O., *Nature* **2008**, *454*, 816.

[4] Grätzel, M., *Nature* **2001**, *414*, 338.

[5] Lopez, N.; Nørkov, J. K., *J. Am. Chem. Soc.* **2002**, *124*, 11262.

[6] Nørkov, J. K.; Rossemeisl, J.; Logadottir, A.; Lindqvist, L.; Kitchin, J. R.; Bligaard, T.; Jónsson, H., *J. Phys. Chem. B* **2004**, *108*, 17886.

[7] Nørkov, J. K.; Bligaard, T.; Logadottir, A.; Kitchin, J. R.; Chen, J. G.; Pandelov, S.; Stimming, U., *J. Electrochem. Soc.* **2005**, *152*, J23.

[8] Greely, J.; Stephens, I. E. L.; Bondarenko, A. S.; Johansson, T. P.; Hansen, H. A,; Jaramillo, T. F.; Rossmeisl, J.; Chorkendorff, I.; Nørkov, J. K., *Nat. Chem.* **2009**, *1*, 552.

[9] Hou, Y.; Wang, D.; Yang, X. H.; Fang, W. Q.; Zhang, B.; Wang, H. F.; Lu, G. Z.; Hu, P.; Zhao, H. J.; Yang, H. G., *Nat. Commun.* **2013**, *4*, 1583.

[10] West, W., *Photogr. Sci. eng.* **1974**, *18*, 35.

[11] Moser, J., *Monatsh. Chem.* **1887**, *8*, 373.

[12] Nelson, R. C., *J. Phys. Chem.* **1965**, *69*, 714.

[13] Boudon, J., *J. Phys. Chem.* **1965**, *69*, 705.

[14] Hauffe, K.; Danzmann, H. J.; Pusch, H.; Range, J.; Volz, H., *J. Electrochem. Soc.* **1970**, *117*, 993.

[15] Tsubomura, H.; Marsumura, M.; Nomura, Y.; Amamiya, T., *Nature* **1976**, *261*, 402.

[16] Matsumura, M.; Nomura, Y.; Tsubomura, H., *Bull. Chem. Soc. Jpn.* **1977**, *50*, 2533.

[17] Matsumura, M.; Matsudaira, S.; Tsubomura, H.; Takata, M.; Yanagida, H., *I&E Prod. Res. Devel.* **1980**, *19*, 415.

[18] Alonso, N.; Beley, V. M.; Chartier, P.; Ern, V., *Rev. Phys. Appl.* **1981**, *16*, 5.

[19] Desilvestro, J.; Grätzel, M.; Kavan, L.; Moser, J.; Augusynski, J., *J. Am. Chem. Soc.* **1985**, *107*, 2988.

[20] Kalayanasundaram, K.; Vlachopoulos, N.; Krishnan, V.; Monnier, A.; Grätzel, M., *J. Phys. Chem.* **1987**, *91*, 2342.

[21] Vlachopoulos, N.; Liska, P.; McEvoy, A. J.; Grätzel, M., *Surf. Sci.* **1987**, *189*, 823.

[22] Vrachnou, E.; Vlachopoulos, N.; Grätzel, M., *J. Chem. Soc. Chem. Commun.* **1987**, 868.

[23] Vlachopoulos, N.; Liska, P. Augustynski, J.; Grätzel, M., *J. Am. Chem. Soc.* **1988**, *110*, 1216.

[24] O'Regan, B.; Grätzel, M., *Nature* **1991**, *353*, 737.

[25] Hagfeldt, A.; Grätzel, M., *Chem. Rev.* **1995**, *95*, 49.

[26] Grätzel, M., *Inorg. Chem.* **2005**, *44*, 6841.

[27] Grätzel, M., *Accounts Chem. Res.* **2009**, *42*, 1788.

[28] Hagfeldt, A.; Boschloo, G.; Sun, L.; Kloo, L.; Pettersson, H., *Chem. Rev.* **2010,** *110*, 6595.

[29] Nazeeruddin, M. K.; Kay, A.; Rodicio, I.; Humphry-Baker, R.; Mueller, E.; Liska, P.; Vlachopoulos, N.; Grätzel, M., *J. Am. Chem. Soc.* **1993**, *115*, 6382.

[30] Nazeeruddin, M. K.; Zakeeruddin, S. M.; Humphry-Baker, R.; Jirousek, M.; Liska, P.; Vlachopoulos, N.; Shklover, V.; Fischer, C. H.; Grätzel, M., *Inorg. Chem.* **1999**, *38*, 6298.

[31] Nazeeruddin, M. K.; Pechy, P.; Grätzel, M. *Chem. Commun.* **1997**, 1705.

[32] Chiba, Y.; Islam, A.; Watanabe, Y.; Komiya, R.; Koide, N.; Han, L., *Jpn. J. Appl. Phys.* **2006**, *45*, L638.

[33] Kinoshita, T.; Dy, J. T.; Uchida, S.; Kubo, T.; Segawa, H., *Nat. Photonics* **2013**, *7*, 535.

[34] Sapp, S. A.; Elliott, C. M.; Contado, C.; Caramori, S.; Bignozzi, C. A., *J. Am. Chem. Soc.* **2002**, *124*, 11215.

[35] Klahr, B. M.; Hamann, T. W., *J. Phys. Chem. C* **2009**, *113*, 14040.

[36] Feldt, S. M.; Gibson. E. A.; Gabrielsson, E.; Sun, L.; Boschloo, G.; Hagfeldt, A., *J. Am. Chem. Soc.* **2010**, *132*, 16714.

[37] Tsao, H. N.; Yi, C.; Moehl, T.; Yum, J.-H.; Zakeeruddin, S. M.; Nazeeruddin, M. K.; Grätzel, M., *ChemSusChem* **2011**, *4*, 591.

[38] Tsao, H. N.; Burschka, J.; Yi, C.; Kessler, F.; Nazeeruddin, M. K.; Grätzel, M., *Energy Environ. Sci.* **2011**, *4*, 4921.

[39] Bessho, T.; Zakeeruddin, S. M.; Yeh, C.-Y.; Diau, E. W.-G.; Grätzel, M., *Angew. Chem. Int. Ed.* **2010**, *49*, 6646.

[40] Yella, A.; Lee, H.-W.; Taso, H. N.; Yi, C.; Chandiran, A. K.; Nazeeruddin, M. K.; Diau, E. W.-G.; Yeh, C.-Y.; Zakeeruddin, S. M.; Grätzel, M., *Science* **2011**, *334*, 629.

[41] Lan, C.-M.; Wu, H.-P.; Pan, T.-Y.; Chang, C.-W.; Chao, W.-S.; Chen, C.-T.; Wang, C.-L.; Lin, C.-Y.; Diau, E. W.-G., *Energy Environ. Sci.* **2012**, *5*, 6460.

[42] Matthew, S.; Yella, A.; Gao, P.; Humphry-Baker, R.; Curchod, B. F. E.; Ashari-Astani, N.; Tavernelli, I.; Rothlisberger, U.; Nazeeruddin, M. K.; Grätzel, M., *Nat. Chem.* **2014**, *6*, 242.

[43] Hodes, G., *J. Phys. Chem. C* **2008**, *112*, 17778.

[44] Kamat, P. V., *J. Phys. Chem. C* **2008**, *112*, 18737.

[45] Rühle, S.; Shalom, M.; Zaban, A., *ChemPhysChem* **2010**, *22*, 2290.

[46] Yang, Z.; Chen, C.-Y.; Roy, P.; Chang, H.-T., *Chem. Commun.* **2011**, *47*, 9561.

[47] Liu, D.; Kamat, P. V., *J. Phys. Chem.* **1993**, *97*, 10769.

[48] Zaban, A.; Mićić, O. I.; Gregg, B. A.; Nozik, A. J., *Langmuir* **1998**, *14*, 3153.

[49] Shalom, M.; Rühle, S.; Hod, I.; Yahav, S.; Zaban, A., *J. Am. Chem. Soc.* **2009**, *131*, 9876.

[50] Farrow, B.; Kamat, P. V., *J. Am. Chem. Soc.* **2009**, *131*, 11124.

[51] Bang, J. H.; Kamat, P. V., *ACS Nano* **2009**, *3*, 1467.

[52] Tvrdy, K.; Frantsuzov, P. A.; Kamat, P. V., *Proc. Natl. Acad. Sci. USA* **2011**, *108*, 29.

[53] Hossain, M. A.; Jennings, J. R.; Koh, Z. Y.; Wang, Q., *ACS Nano* **2011**, *5*, 3172.

[54] Kang, S. H.; Zhu, K.; Neale, N. R.; Frank, A. J., *Chem. Commun.* **2011**, *47*, 10419.

[55] Braga, A.; Giménez, S.; Corcina, I.; Vomiero, A.; Mora-Seró, I., *J. Phys. Chem. Lett.* **2011**, *2*, 454.

[56] Zhou, N.; Chen, G.; Zhang, X.; Cheng, L.; Luo, Y.; Li, D.; Meng, Q., *Electrochem. Commun.* **2012**, *20*, 97.

[57] Santra, P. K.; Kamat, P. V., *J. Am. Chem. Soc.* **2012**, *134*, 2508.

[58] Lee, J.-W.; Son, D.-Y.; Ahn, T. K.; Shin, H.-W.; Kim, I.-Y.; Hwang, S.-J.; Ko, M. J.; Sul, S.; Han, H.; Park, N.-G., *Sci. Rep.* **2013**, *3*, 1050.

[59] Wang, J.; Mora-Seró, I.; Pan, Z.; Zhao, K.; Zhang, H.; Feng, Y.; Yang, G.; Zhong, X.; Bisquert, J., *J. Am. Chem. Soc.* **2013**, *135*, 15913.

[60] Hossain, M. A.; Jennings, J. R.; Koh, Z. Y.; Wang, Q., *ACS Nano* **2011**, *5*, 3172.

[61] Yang, J.; Kim, J.-Y.; Yu, J. H.; Ahn, T.-Y.; Lee, H.; Choi, T.-S.; Kim, Y.-W.; Joo, J.; Ko, M. J.; Hyeon, T., *Phys. Chem. Chem. Phys.* **2013**, *15*, 20517.

[62] Pan. Z.; Mora-Seró, I.; Shen, Q.; Zhang, H.; Li, Y.; Zhao, K.; Wang, J.; Zhong, X.; Bisquert, J., *J. Am. Chem. Soc.* **2014**, *136*, 9203.

[63] Zhang, Q.; Myers, D.; Lan, J.; Jenekhe, S. A.; Cao, G., *Phys. Chem. Chem. Phys.* **2012**, *14*, 14982.

[64] Barbé, C. J.; Arendse, F.; Comte, P.; Jirousek, M.; Lenzmann, F.; Shklover, V.; Grätzel, M., *J. Am. Ceram. Soc.* **1997**, *80*, 3157.

[65] Son, S., Hwang, S. H.; Kim, C.; Yun, J. Y.; Jang, J., *ACS Appl. Mater. Interfaces* **2013**, *5*, 4815.

[66] Usami, A., *Chem. Phys. Lett.* **1997**, *277*, 105.

[67] Yu, I. G.; Kim, Y. J.; Kim, H. J.; Lee, C.; Lee, W. I., *J. Mater. Chem* **2011**, *21*, 532.

[68] Yang, L.; Lin, Y.; Jia, J.; Xiao, X.; Li, X.; Zhou, X., *J. Power Sources* **2008**, *182*, 370.

[69] Gao, X.-D.; Li, X.-M.; Gan, X.-Y.; Wu, Y.-Q.; Zheng, R.-K.; Wang, C.-L.; Gu, Z,-Y.; He, P., *J. Mater. Chem.* **2012**, *22*, 18930.

[70] Koo, H.-J.; Kim, Y. J.; Lee, Y. H.; Lee, W. I.; Kim, K.; Park, N.-G., *Adv. Mater.* **2008**, *20*, 195.

[71] Wu, W.-Q.; Xu, Y.-F.; Rao, H.-S.; Su, C.-Y.; Kuang, D.-B., *Nanoscale* **2013**, *5*, 4362.

[72] Lv,. F.; Xiao, S.; Zhu, J.; Li, H., *RSC Adv.* **2014**, *4*, 36206.

[73] Hsu, W. P.; Yu, R.; Matijević, E. J., *J. Colloid Interface Sci.* **1993**, *156*, 56.

[74] Small, A.; Hong, S.; Pine, D., *J. Polym. Sci., Part B: Polym. Phys.* **2005**, *43*, 3534.

[75] Rensmo, H.; Keis, K.; Lindström, H.; Södergren, S., Solbrand, A.; Hagfeldt, A.; Lindquist, S.-E.; Wang, L. N.; Muhammed, M., *J. Phys. Chem. B* **1997**, *101*, 2598.

[76] Tennakone, K.; Kumara, G. R. R. A.; Kottegoda, I. R. M.; Perera, V. P. S., *Chem. Commun.* **1999**, 15.

[77] Keis, K.; Magnusson, E.; Lindström, H.; Lindquist, S.-E.; Hagfeldt, A., *Sol. Energy Mater. Sol. Cells* **2002**, *73*, 51.

[78] Chappel, S.; Chen, S.-G.; Zaban, A., *Langmuir* **2002**, *18*, 3336.

[79] Saito, M.; Fujihara, S., *Energy Environ. Sci.* **2008**, *1*, 280.

[80] Zhang, Q.; Dandeneau, C. S.; Zhou, X.; Cao, G., *Adv. Mater.* **2009**, *21*, 4087.

[81] Qian, J.; Liu, P.; Xiao, Y.; Jiang, Y.; Cao, Y.; Zi, X.; Yang, H., *Adv. Mater.* **2009**, *21*, 3663.

[82] Park, K.; Zhang, Q.; Battalla, B.; Zhou, X.; Jeong, Y.-H.; Cao, G., *Adv. Mater.* **2010**, *22*, 2329.

[83] Snaith, H. J.; Ducanti, C., *Nano Lett.* **2010**, *10*, 1259.

[84] Noack, V.; Weller, H.; Eychmuller, A., *J. Phys. Chem. B* **2002**, *106*, 8514.

[85] Wu, J. J.; Chen, G. R.; Lu, C. C.; Wu, W. T.; Chen, J. S., *Nanotechnology* **2008**, *19*, 105702.

[86] Green, A. N. M.; Palomares, E.; Haque, S. A.; Kroon, J. M.; Durrant, J. R., *J. Phys. Chem. B* **2005**, *109*, 12525.

[87] Keis, K.; Lindgren, J.; Lindquist, S.-E.; Hagfeldt, A., *Langmuir* **2000**, *16*, 4688.

[88] Xu, C.; Wu, J.; Desai, U. V.; Gao, D., *J. Am. Chem. Soc.* **2011**, *133*, 8122.

[89] Law, M.; Greene, L. E.; Johnson, J. C.; Saykally, R.; Yang, P., *Nat. Mater.* **2005**, *4*, 455.

[90] Nelson, J., *Phys. Rev. B* **1999**, *59*, 15374.

[91] Macák, J. M.; Tsuchiya, H.; Ghicov, A.; Schmuki, P., *Electrochem. Commun.* **2005**, *7*, 1133.

[92] Mor, G. K.; Shankar, K.; Paulose, M.; Varghese, O. K.; Grimes, C. A., *Nano Lett.* **2006**, *6*, 215.

[93] Zhu, K.; Neale, N. R.; Miedaner, A.; Frank, A. J., *Nano Lett.* **2007**, *7*, 69.

[94] Mor, G. K.; Varghese, O. K.; Paulose, M.; Shankar, K.; Grimes, C. A., *Sol. Energy Mater. Sol. Cells* **2006**, *90*, 2011.

[95] Feng, X.; Shankar, K.; Varghese, O. K.; Paulose, M.; Latempa, T. J.; Grimes, C. A., *Nano Lett.* **2008**, *8*, 3781.

[96] Liu, B.; Aydil, E. S., *J. Am. Chem. Soc.* **2009**, *131*, 3985.

[97] Varghese, O. K.; Paulose, M.; Grimes, C. A., *Nat. Nanotechnol.* **2009**, *4*, 592.

[98] Kay, A.; Grätzel, M., *Sol. Energy Mater. Sol. Cells.* **1996**, *44*, 99.

[99] Suzuki, K.; Yamaguchi, M.; Kumagai, M; Yanagida, S., *Chem. Lett.* **2003**, *32*, 1.

[100] Murakami, T. N.; Ito, S.; Wang, Q.; Nazeeruddin, M. K.; Bessho, T.; Cesar, I.; Liska, P.; Humphry-Baker, R.; Comte, P.; Péchy, P.; Grätzel, M., *J. Electrochem. Soc.* **2006**, *153*, A2255.

[101] Ramasamy, E.; Lee, W. J.; Lee, D. Y.; Song, J. S., *Appl. Phys. Lett.* **2007**, *90*, 173103.

[102] Huang, Z.; Liu, X.; Li, K.; Li, D.; Luo, Y.; Li, H.; Song, W.; Chen, L. Q.; Meng, Q., *Electrochem. Commun.* **2007**, *9*, 596.

[103] Lee, W. J.; Ramasamy, E.; Lee, D. Y.; Song, J. S., *ACS Appl. Mater. Interfaces* **2009**, *1*, 1145.

[104] Saito, Y.; Kubo, W.; Kitamura, T.; Wada, Y.; Yanagida, S., *J. Photochem. Photobiol. A* **2004**, *164*, 153.

[105] Ahmad, S.; Yum, J.-H.; Xianxi, Z.; Grätzel, M.; Butt, H.-J.; Nazeeruddin, M. K., *J. Mater. Chem.* **2010**, *20*, 1654.

[106] Lee, K. S.; Lee, H. K.; Wang, D. H.; Park, N.-G.; Lee, J. Y.; Park, O. O.; Park, J. H., *Chem. Commun.* **2010**, *46*, 4505.

[107] Trevisan, R.; Döbbelin, M.; Boix, P. P.; Barea, E. M.; Tena-Zaera, R.; Mora-Seró, I.; Bisquert, J., *Adv. Energy Mater.* **2011**, *1*, 781.

[108] Tan, S.; Zhai, J.; Xue, B.; Wan, M.; Meng, Q.; Li, Y.; Jiang, L.; Zhu, D., *Langmuir* **2004**, *20*, 2934.

[109] Li, Q.; Wu, J.; Tang, Q.; Lan, Z.; Li, P.; Lin, J.; Fan, L., *Electrochem. Commun.* **2008**, *10*, 1299.

[110] Li, Z.; Ye, B.; Hu, X.; Ma, X.; Zhang, X.; Deng, Y., *Electrochem. Commun.* **2009**, *11*, 1768.

[111] Sun, H.; Luo, Y.; Zhang, Y.; Li, D.; Yu, Z.; Li, K.; Meng, Q., *J. Phys. Chem. C* **2010**, *114*, 11673.

[112] Chen, X.; Tang, Q.; He, B.; Lin, L.; Yu, L., *Angew. Chem. Int. Ed.* **2014**, *53*, 10799.

[113] Wan, J.; Fang, G.; Yin, H.; Liu, X.; Liu, D.; Zhao, M.; Ke, W.; Tao, H.; Tang, Z., *Adv. Mater.* **2014**, *26*, 8101.

[114] He, B.; Meng, X.; Tang, Q.; Li, P.; Yuan, S.; Yang, P., *J. Power Sources* **2014**, *260*, 180.

[115] Wang, M.; Anghel, A. M.; Marsan, B.; Ha, N.-L. C.; Pootrakulchote, N.; Zakeeruddin, S, M.; Grätzel, M., *J. Am. Chem. Soc.* **2009**, *131*, 15976.

[116] Li, G. R.; Song, J.; Pan, G. L.; Gao, X. P., *Energy Environ. Sci.* **2011**, *4*, 1680.

[117] Sun, H.; Qin, D.; Huang, S.; Guo, X.; Li, D.; Luo, Y.; Meng, Q., *Energy Environ. Sci.* **2011**, *4*, 2630.

[118] Wu, M.; Zhang, Q.; Xiao, J.; Ma, C.; Lin, X.; Miao, C.; He, Y.; Gao, Y.; Hagfeldt, A.; Ma, T., *J. Mater, Chem.* **2011**, *21*, 10761.

[119] Wang, Y.; Wu, M.; Lin, X.; Shi, Z.; Hagfeldt, A.; Ma, T., *J. Mater. Chem.* **2012**, *22*, 4009.

[120] Mulmudi, H. K.; Batabyal, S. K.; Rao, M.; Prabhakar, R. R.; Mathews, N.; Lam, Y. M.; Mhaisalkar, S. G., *Phys. Chem. Chem. Phys.* **2011**, *13*, 19307.

[121] Guai, G. H.; Leiw, M. Y.; Ng, C. M.; Li, C. M., *Adv. Energy Mater.* **2012**, *2*, 334.

[122] Chi, W. S.; Han, J. W.; Yang, S.; Roh, D. K.; Lee, H.; Kim, J. H., *Chem. Commun.* **2012**, *48*, 9501.

[123] Wu, M.; Lin, X.; Wang, Y.; Wang, L.; Guo, W.; Qi, D.; Peng, X.; Hagfeldt, A.; Grätzel, M.; Ma, T., *J. Am. Chem. Soc.* **2012**, *134*, 3419.

[124] Liao, Y.; Pan, K.; Wang, L.; Pan, Q.; Zhou, W.; Miao, X.; Jiang, B.; Tian, C.; Tian, G.; Wang, G.; Fu, H., *ACS Appl. Mater. Interfaces* **2013**, *5*, 3663.

[125] Hou, Y.; Wang, D.; Yang, X. H.; Fang, W. Q.; Zhang, B.; Wang, H. F.; Lu, G. Z.; Hu, P.; Zhao, H. J.; Yang, H. G., *Nat. Commun.* **2013**, *4*, 1583.

[126] Loucka, T., *J. Electroanal. Chem.* **1972**, *36*, 355–367.

[127] Radich, J. G.; Dwyer, R.; Kamat, P. V., *J. Phys. Chem. Lett.* **2011**, *2*, 2453.

[128] Hodes, G.; Manassen, J.; Cahen, D., *J. Electrochem. Soc.* **1980**, *127*, 544.

[129] Walter, M. G.; Warren, E. L.; McKone, J. R.; Boettcher, W.; Mi, Q.; Santori, E. A.; Lewis, N. S., *Chem. Rev.* **2010**, *110*, 6446.

[130] Abe, R., *J. Photochem. Photobiol. C* **2010**, *11*, 179.

[131] Osterloh, F. E., *Chem. Soc. Rev.* **2013**, *42*, 2294.

[132] Fujishima, A.; Honda, K., *Nature* **1972**, *238*, 37.

[133] Kim, T. W.; Choi, K.-S., *Science* **2014**, *343*, 990.

[134] Zhang, Z.; Wang, P., *J. Mater. Chem.* **2012**, *22*,2456.

[135] Mori, S.; Fukuda, S.; Sumikura, S.; Takeda, Y.; Tamaki, Y.; Suzuki, E.; Abe, T., *J. Phys. Chem. C* **2008**, *112*, 16134.

[136] Li, L.; Gibson, E. A.; Qin, P.; Boschloo, G.; Gorlov, M.; Hagfeldt, A.; Sun, L., *Adv. Mater.* **2010**, *22*, 1759.

[137] Kahn, S. U. M.; Al-Shahry, M.; Ingler Jr, N. B., *Science* **2002**, *297*, 2243.

[138] Roy, P.; Das, C.; Lee, K.; Hahn, R.; Ruff, T.; Moll, M.; Schmuki, P., *J. Am. Chem. Soc.*, **2011**, *133*, 5629.

[139] Hamedani, H. A,; Allam, N. K.; Garmestani, H.; El-Sayed, M. A., *J. Phys. Chem. C* **2011**, *115*, 12480.

[140] Banerjee, S.; Mohapatra, S. K.; Misra, M., *J. Phys. Chem. C* **2011**, *115*, 12643.

[141] Zhang, Z. H.; Hossain, M. F.; Takahashi, T., *Int. J. Hydrogen Energy* **2010**, *35*, 8528.

[142] Santato, C.; Odziemkowski, M.; Ulmann, M.; Augustynski, J., *J. Am. Chem. Soc.* **2001**, *123*, 10639.

[143] Iwase, A.; Kudo, A., *J. Mater. Chem.* **2010**, *20*, 7536.

[144] Berglund, S. P.; Flaherty, D. W.; Hahn, N. T.; Bard, A. J.; Mullins, C. B., *J. Phys. Chem. C* **2011**, *115*, 3794.

[145] Kay, A.; Cesar, I.; Grätzel, M., *J. Am. Chem. Soc.* **2006**, *128*, 15714.

[146] Tilley, S. D.; Cornuz, M.; Sivula, K.; Grätzel, M., *Angew. Chem. Int. Ed.* **2010**, *49*, 6405.

[147] Warren, S. C.; Voïtchovsky, K.; Dotan, H.; Leroy, C. M.; Cornuz, M.; Stellacci, F.; Hébert, C.; Rothschild, A.; Grätzel, M., *Nat. Mater.* **2013**, *12*, 842.

[148] Sivula, K.; Zboril, R.; Le Formal, F.; Robert, R.; Weidenkaff, A.; Tucek, J.; Frydrych, J.; Grätzel, M., *J. Am. Chem. Soc.* **2010**, *132*, 7436–7444.

[149] Mohapatra, S. K.; John, S. E.; Banerjee, S.; Misra, M., *Chem. Mater.* **2009**, *21*, 3048.

[150] Sivula, K.; Le Formal, F; Grätzel, M., *ChemSusChem* **2011**, 4, 432.

[151] Klahr, B.; Gimenez, S.; Fabregat-Santiago, F.; Hamann, T.; Bisquert, J., *J. Am. Chem. Soc.* **2012**, *134*, 4294.

[152] Barroso, M.; Mesa, C. A.; Pendlebury, S. R.; Cowan, A. J.; Jisatomi, T.; Sivula, K.; Grätzel, M.; Klug, D. R.; Durrant, J. R., *Proc. Natl. Acad. Sci. USA* **2012**, *109*, 15640.

[153] Chen, X.; Burda, C., *J. Am. Chem. Soc.* **2008**, *130*, 5018.

[154] Park, J. H.; Kim, S.; Bard, A. J., *Nano Lett.* **2006**, *6*, 24.

[155] Wang, G.; Wang, H.; Ling, Y.; Tang, Y.; Yang, X.; Fitzmorris, R. C.; Wang, C.; Zhang, J. Z.; Li, Y., *Nano Lett.* **2011**, *11*, 3026.

[156] Mor, G. K.; Shankar, K.; Paulose, M.; Varghese, O. K.; Grimes, C. A., *Nano Lett.* **2005**, *5*, 191.

[157] Kudo, A.; Ueda, K.; Kato, H., *Catal. Lett.* **1998**, *53*, 299.

[158] Kudo, A.; Omori, K.; Kato, H., *J. Am. Chem. Soc.* **1999**, *121*, 11459.

[159] Kennedy, J. H.; Frese, K. W., *J. Electrochem. Soc.* **1978**, *125*, 709.

[160] Maruska, H. P.; Ghosh, A. K., *Sol. Energy Mater.* **1979**, *1*, 237.

[161] Butler, M. A., *J. Appl. Phys.* **1977**, *48*, 1914.

[162] Moniz, S. J. A.; Shevlin, S. A.; Martin, D. J.; Guo, Z.-X.; Tang, J., *Energy Environ. Sci.* **2015**, *8*, 731.

[163] Jeong, H. W.; Jeon, T. H.; Jang, J. S.; Choi, W.; Park, H., *J. Phys. Chem. C* **2013**, *117*, 9104.

[164] Chi, X.; Choi, I. Y.; Zhang, K.; Kwon, J.; Kim, D. Y.; Lee, J. L.; Oh, S. H.; Kim, J. K.; Park, J. H., *Nat. Commun.* **2014**, *5*, 4775.

[165] Ma, M.; Kim, J. K.; Zhang, K.; Shi, X.; Kim, S. J.; Moon, J. H.; Park, J. H., *Chem. Mater.* **2014**, *26*, 5592.

[166] Youngblood, W. J.; Lee, S.-H. A.; Maeda, K.; Mallouk, T. E., *Accouts Chem. Res.* **2009**, *42*, 1966.

[167] Swierk, J. R.; Mallouk, T. E., *Chem. Soc. Rev.* **2013**, *42*, 2357.

[168] Steinmiller, E. M. P.; Choi, K. S., *Proc. Natl. Acad. Sci. USA* **2009**, *106*, 20633.

[169] Kiwi, J.; Grätzel, M., *Angew. Chem. Int. Ed.* **1978**, *17*, 860.

[170] Kiwi, J.; Grätzel, M., *Angew. Chem. Int. Ed.* **1979**, *18*, 624.

[171] Liu, Q.; He, J.; Yao, T.; Sun, Z.; Cheng, W.; He, S.; Xie, Y.; Peng, Y.; Cheng, H.; Sun, Y.; Jiang, Y.; Hu, F.; Xie, Z.; Yan, W.; Pan, Z.; Wu, Z.; Wei, S., *Nat. Commun.* **2014**, *5*, 5122.

[172] Luo, J.; Im, J.-H.; Mayer, M. T.; Schreier, M.; Nazeeruddin, M. K.; Park, N.-G.; Tilley, S. D.; Fan, H. J.; Grätzel, M., *Science* **2014**, *345*, 1593.

[173] Levy, R. B.; Boudadrt, M., *Science* **1973**, *181*, 547.

[174] Colton, R. J.; Huang, J.-T. J.; Rabalais, J. W., *Chem. Phys. Lett.* **1975**, *34*, 337.

[175] Fan, X.; Zhou, H.; Guo, X., *ACS Nano* **2015**, *9*, 5125.

[176] Jaramillo, T. F.; Jørgensen, K. P.; Bonde, J.; Nielsen, J. H.; Horch, S.; Chorkendorff, I., *Science*, **2007**, *317*, 100.

# Chapter 2. Vertically aligned mesoporous anodic zinc oxide nanowire arrays as photoelectrode

## 2.1. Introduction

Ever since Brian O'Regan and Michael Grätzel reported photoelectrochemical solar cells based on Ru complex-sensitized colloidal $TiO_2$ nanoparticles (NPs) [1], dye-sensitized solar cells (DSCs) have been of a great interest to both research community and industrial field because of their excellent performance and reliability in spite of facile and economic preparation methods [2-4]. Owing to various optimizations of the electrodes [5-8], rapid advances in organic dyes [9-15] and redox electrolytes [9,16-18], the energy conversion efficiency reached 13% lately [15].

Beside sensitzer and electrolyte, DSCs are composed of two electrodes; a photoanode based on nanostructured metal oxide semiconductor film and an electrocatalytic counter electrode. From the inception of DSCs two decades ago, mesoscopic colloidal $TiO_2$ and Pt have been the best performing photoanode and counter electrode, respectively. However, the overall photovoltaic performances of DSCs are significantly limited by the charge collection process through the electron diffusion within the semiconductor in photoanode [3,4]. Excited electrons generated in dye molecules immediately move to the semiconductor and diffuse toward the current collector until they arrive at the current collector, but some of them recombine with oxidized species in the electrolyte at the semiconductor/electrolyte interface. Therefore, the recombination which competes with the charge collection should be minimized in order to increase the photocurrent generation and energy conversion efficiency.

In order to suppress charge recombination, numerous research works were reported based on the following strategies; (i) confinement of the electron pathways within the semiconductor electrode by modifying the morphology of the semiconductor into one-dimensional structure, and (ii) replacing $TiO_2$ with other metal oxide semiconductor with intrinsic property of fast charge transport. In case of the strategy (i), $TiO_2$ nanotubes (NTs) [19-22] or nanowires (NWs) [23-26] were employed instead of the colloidal $TiO_2$ nanoparticle film, and charge recombination were reduced to some extent [26-28], though the overall energy conversion efficiencies inferior to that of the conventional NPs due to a less amount of loaded dye molecules, which resulted from relatively small surface area. In the reports based on strategy (ii), nanostructured ZnO or $SnO_2$ films were often utilized [29-38], because the electron conductivity within these materials are larger than that of in $TiO_2$ lattice by around 3 orders of magnitude [39-41]. However, due to the chemical instability of ZnO in acidic environment, dye molecules with carboxylic anchoring group cannot be sufficiently positioned on the ZnO surface, and dissolved $Zn^{2+}$ and dye molecules form insoluble aggregates [42]. Therefore, the photovoltaic performances were generally inferior to the case of $TiO_2$. Also, for $SnO_2$, unfavorable band position and low charge transfer resistance at the $SnO_2$/redox electrolyte interface resulted in lowering of energy conversion efficiency.

Nevertheless, there are numerous ongoing researches on the structural engineering of ZnO for use as high-performance photoanode for DSCs. Among the candidate materials, ZnO NWs, which are well known for easy fabrication method [43], meet both of the strategies described above. Since the pioneering works by Yang's and Aydil's groups [44-47], single crystalline ZnO NWs grown on the FTO glass were frequently employed as photoanode of DSCs [48-50]. In 2011, Di Gao and his colleagues reported multilayer-assembled ZnO NWs fabricated by selective masking of the ZnO NWs on the side and repeated growth of the NWs in vertical

direction, and this approach gave the energy conversion efficiency up to 7% (with $TiO_2$ shells) [51]. However, this result is still far from the best results from the conventional DSCs, because the surface area of ZnO NWs with typical diameter of 100 nm far short of that in the case of 20 nm sized nanoparticles.

Among the methods for the preparation of ZnO NWs, electrochemical anodization is facile and reliable to produce polycrystalline ZnO nanostructures. There were numerous reports on the anodic oxidation of Zn in aqueous electrolytes such as zincated saturated KOH [52] and ethanolic $H_2SO_4$ [53]. Meanwhile, in 2010, anodic ZnO NWs prepared with $KHCO_3$ electrolye were reported [54]. There were two notable characteristics in this method, that the fabrication of ZnO with a very high aspect ratio was rapidly done in a mild condition, and the produced ZnO NWs had mesoporous structure. Inspired by this work, in this study, anodic ZnO NWs were employed as photoanode of DSCs. Since the remaining Zn metal substrate after anodic oxidation is unstable when exposed to the corrosive $I_3^-/I^-$ redox electrolyte, quasi-solid electrolyte were used instead. Though the complete elimination of Zn dissolution was impossible, the superior properties of anodic ZnO NWs in DSCs were verified by various physicochemical characterizations. Moreover, by coating thin $TiO_2$ shell on the ZnO surface by atomic layer deposition (ALD), high energy conversion efficiency was obtained.

## 2.2. Experimental section

### 2.2.1. Fabrication of ZnO and ZnO/$TiO_2$ nanowires and preparation of dye-sensitized solar cells

Zinc foil (Sigma Aldrich, 99.999% purity, 0.25 mm thick) was cut into 2.0 cm × 1.5 cm and flattened as best as possible by pressing. Then the foils were cleaned with the assistance of ultrasonication in acetone, ethanol, and distilled water for 10 min each. Electrochemical anodization of Zn was performed in two electrode

system using Pt mesh as counter electrode and 10 mM $KHCO_3$ aqueous solution as electrolyte. The distance between the working electrode and the counter electrode was 3 cm. During the anodization, 10 V bias was applied continuously, and the temperature was fixed at 25 °C by cooling jacket and circulator. After the anodization, the electrode was washed with ethanol and went under thermal annealing in air at 400 °C for 1 h, in order to remove the organic remnants on the ZnO surface and improve the crystallinity for enhanced charge transport. For the preparation of ZnO/$TiO_2$ NWs, $TiO_2$ was deposited on the ZnO surface by ALD in laminar flow type reactor at 150 °C. One ALD cycle included $TiCl_4$ exposure for 1 s followd by 20 sec of purging step, $H_2O$ exposure for 1s, and 20 sec purging. $TiCl_4$ (UP Chemical) and $H_2O$ were exposed in vapor form, and the purging was done with $N_2$ gas (99.999% purity) with a flow rate of 400 sccm. More details of ALD processes are described in a previous publication [38]. For the $TiO_2$ shell formation, 5 ALD cycles were conducted, and the electrodes were heat treated at 400 °C for 1 h in air once again to enhance the adhesion of the $TiO_2$ shell on ZnO surface. Dye-sensitization of ZnO and ZnO/$TiO_2$ electrodes were performed by immersing the electrodes in ethanolic 0.5 mM N719 (Ru 535-bisTBA, Solaronix) dye solution for 48 h at 30 °C. Pt-FTO counter electrodes were fabricated by spin coating of isopropanol containing 10 mM $H_2PtCl_6$ on FTO glass followed by heat treatment at 400 °C for 20 min. A photoanode and a counter electrode were assembled by spring clamps with a surlyn film as spacer. For the enhanced stability of the cell, commercial iodide gel electrolyte based on 3-methoxypropionitrile solvent (EL-SGE, Dyesol) was used instead of the conventional liquid electrolyte.

### 2.2.2. Physical and electrochemical characterization of materials

The morphologies of the anodic ZnO and ZnO/$TiO_2$ NWs were characterized by using a scanning electron microscope (SEM; Carl Zeiss AURIGA). Also, detailed structure of the NWs and elemental analyses were performed with transmission

electron microscope (TEM; JEOL JEM-2100F) equipped electron energy loss spectroscopy (EELS) accessary. The crystal structures were analyzed by X-ray diffraction (XRD) using Rigaku D/MAX 2500 V with Cu Kα source, and elemental composition and chemical states of the ZnO and ZnO/$TiO_2$ NWs' surface were characterized by X-ray photoelectron spectroscopy (XPS; Thermo SIGMA PROBE) with Al Kα radiation source in an ultra-high vacuum (UHV) chamber of which base pressure was maintained at ~$10^{-10}$ Torr. Specific surface area and pore distribution was observed by Brunauer-Emmett-Teller (BET; Micrometrics ASAP 2010) measurement. Photoelectrochemical properties of the DSCs employing ZnO and ZnO/$TiO_2$ NWs as photoanode were characterized under standard AM 1.5G condition with 100 mW/$cm^2$ incident light intensity by using a solar simulator equipped with a 500 W Xe lamp (SERIC XIL 05A50KS) and a potentiostat (Solartron 1480 Multistat).

## 2.3. Results and discussion

### 2.3.1. Syntheses and characterization of anodic ZnO nanowires

For the fabrication of optimized ZnO nanostructures, the effect of the electrolyte concentration was first observed. Figure 2.1 shows the SEM images of the anodic ZnO NWs synthesized by 30 min of electrochemical anodization at 10 V using 10, 30, and 50 mM $KHCO_3$ aqueous electrolyte. From SEM images displayed in Figure 2.1a and 2.1b, which show the morphologies of the anodic ZnO synthesized by 10 mM electrolyte, formation of vertically aligned NWs at this electrolyte concentration is clearly observable. In contrast, as the electrolyte concentration increased to 30 mM, upper parts of the NWs were lumped with each other (Figure 2.1c and 2.1d), and the degree of agglomeration increased further when 50 mM $KHCO_3$ electrolyte was used (Figure 2.1e and 2.1f). Therefore, it was concluded

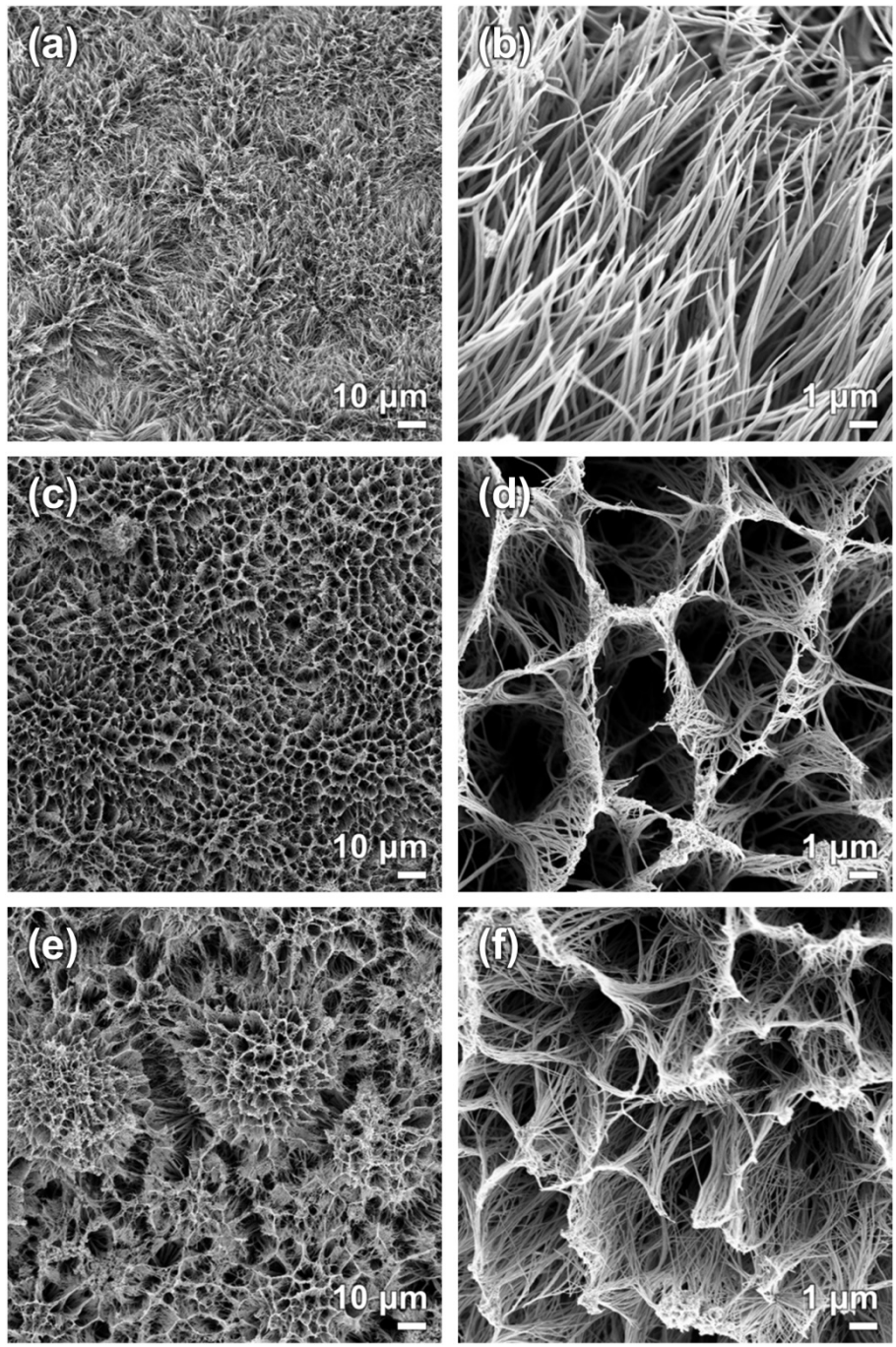


**Figure 2.1.** SEM images of anodic ZnO nanowires prepared by electrochemical anodization of Zn foil by using (a) 10 mM, (b) 30 mM, and (c) 50 mM $KHCO_3$ aqueous solution as electrolyte.

that 10 mM $KHCO_3$ solution is the optimum electrolyte concentration for the fabrication of vertically aligned ZnO NWs which are separated from each other.

Then the growth rate of the anodic ZnO NWs was verified by the time-dependent anodization of Zn foil followed by SEM analyses on their cross-sections. Figure 2.2a-2.2d show the side-view SEM images of the anodic ZnO NWs synthesized by 30, 60, 90, and 120 min of electrochemical anodization, respectively. The lengths of ZnO NWs increase by about 20 μm per 30 min of anodization, and this indicates that the growth rate of ZnO NWs is ~40 μm/h. Meanwhile, there is one noteworthy thing from the cross-sectional SEM images that the lateral crack between the bottom part of the NWs and the substrate emerges as the anodization period exceeds 90 min (Figure 2.2c). This phenomenon became more severe as the anodic oxidation time was elongated (Figure 2.2d).

Figure 2.3 shows the morphologies of the anodic ZnO NWs synthesized by 60 min of electrochemical anodization. From the low magnification SEM image (Figure 2.3a), highly uniform ZnO NW arrays are clearly observable. Figure 2.3b and 2.3c show that there is no significant agglomeration on tips of the NWs and the NWs are aligned in vertical direction to the substrate, respectively. Also, high magnification SEM image shown in Figure 2.3d clearly shows that the lateral structure of ZnO NW is hexagonal with its diameter around 100 nm. Moreover, Figure 2.3d displays that the ZnO NWs were consisted of ZnO nanoparticles with various sizes, typically of a few tens of nanometers. These observations implies that the anodic ZnO prepared in this research have both large surface area and structural 1-D confinement for enhanced charge transport rate. Further SEM analyses were performed to verify the structure of anodic ZnO NWs' tips, and the morphologies of pointed tips are shown in Figure 2.4.

Figure 2.5 shows the XRD patterns of the Zn foil before and after the 60 min anodization, and the peaks are assigned according to JCCPDS 04-0831 (Zn) and JCPDS 36-1451 (ZnO). The Zn peaks observed in the XRD pattern of the anodized

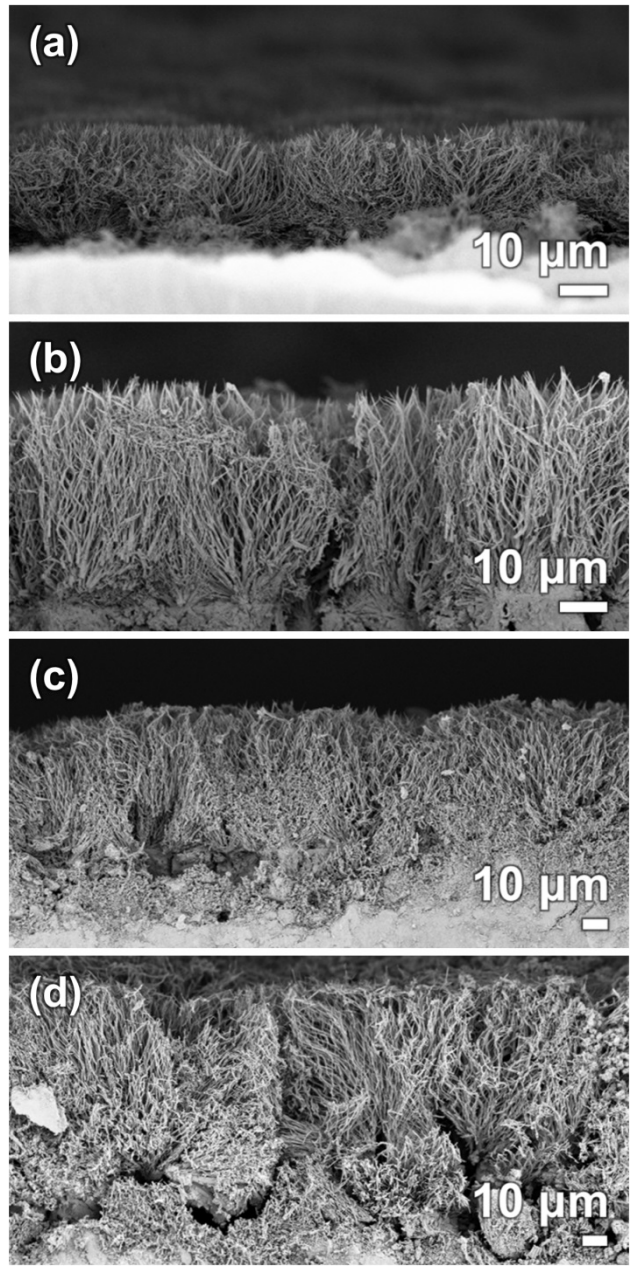


**Figure 2.2.** Side-view SEM images of anodic ZnO nanowires fabricated by (a) 30 min, (b) 60 min, (c) 90 min, and (d) 120 min of electrochemical anodic oxidation using 10 mM $KHCO_3$ aqueous electrolyte.

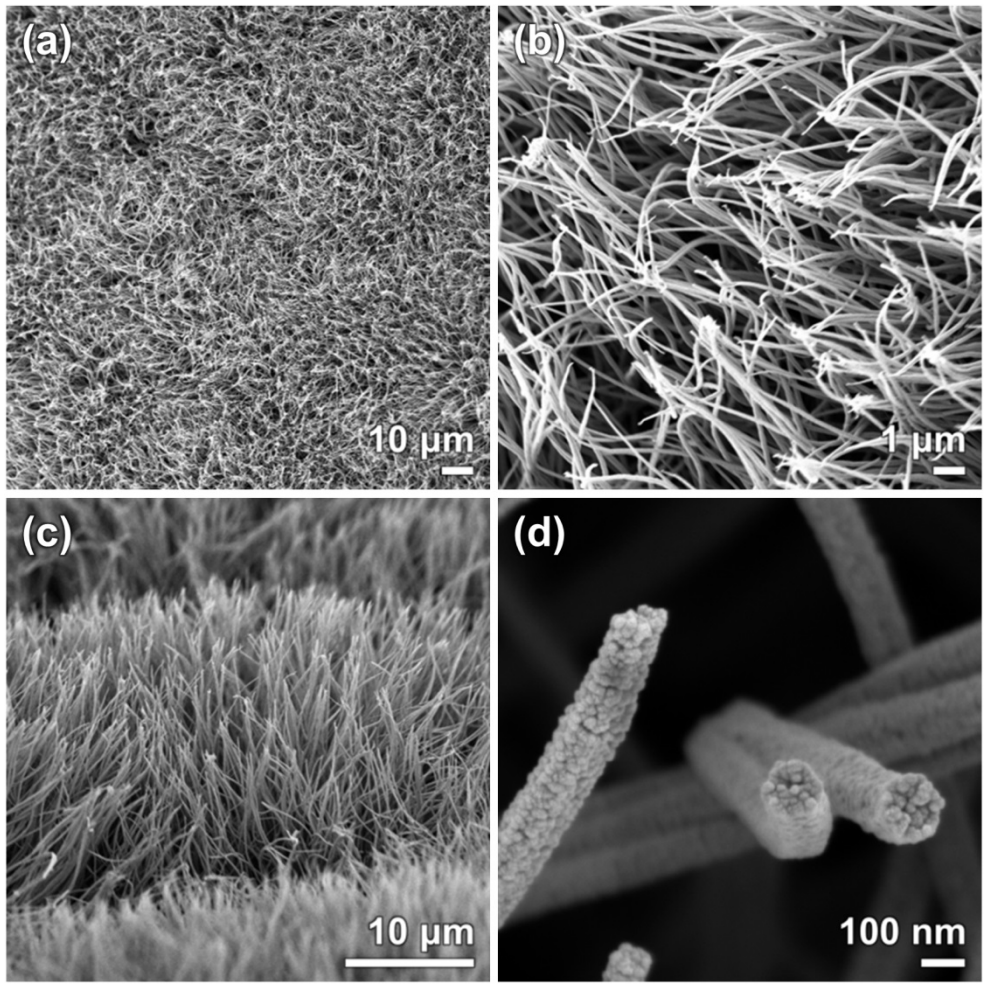


**Figure 2.3.** (a, b) Top-view, (c) side-view, and (d) cross-sectional-view SEM images of anodic ZnO nanowires.

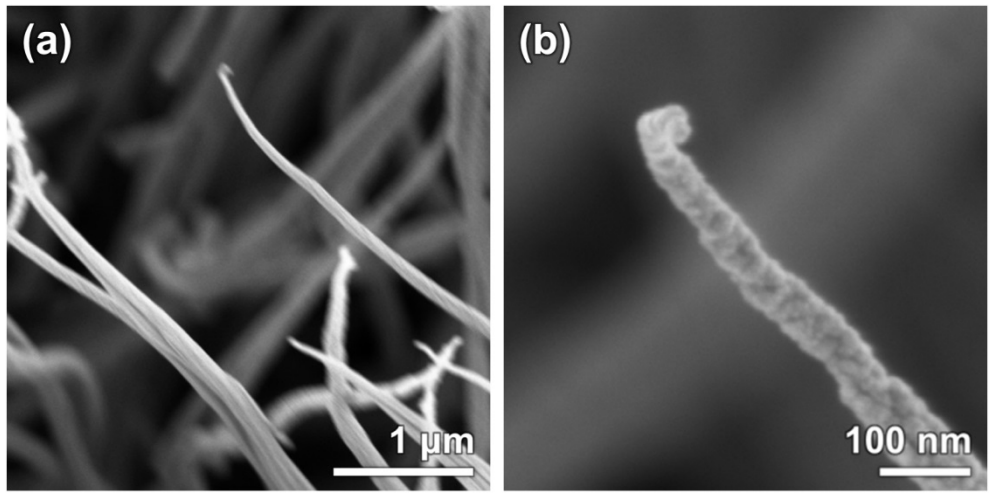


**Figure 2.4.** (a) SEM image of the ZnO nanowire tip and (b) its enlarged image.

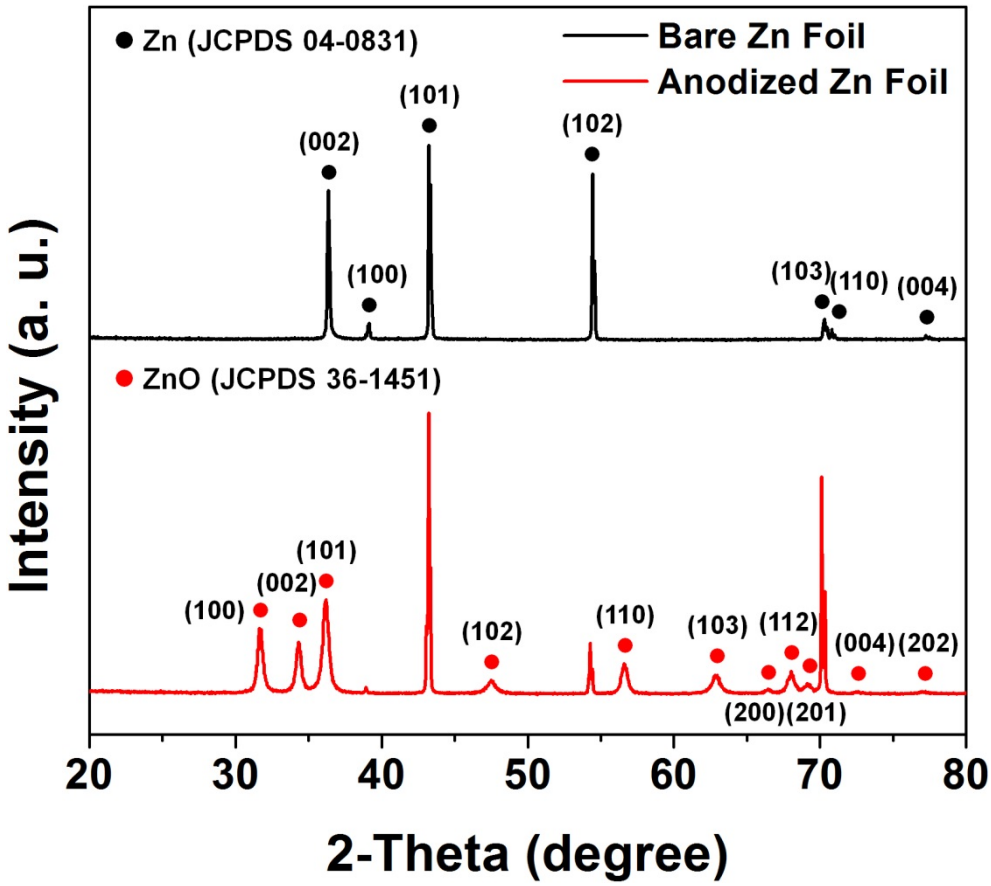


**Figure 2.5.** XRD patterns of bare Zn foil and anodized Zn foil after 400 °C heat treatment in air for 1 h.

Zn foil indicate the presence of metallic Zn foil, and variations of the relative intensity of Zn peaks after the anodization followed by the heat treatment seem to be mainly attributed to the sintering process at 400 °C. Also, from the XRD pattern of anodized Zn, presence of ZnO is clearly observable. The average crystallite size of ZnO was obtained by the (101) peak data and Scherrer's equation, and the result of calculation was 17 nm.

Further characterizations on morphologies and elemental analyses of the ZnO NWs were performed with TEM, and the results are shown in Figure 2.6. Figure 2.6a and 2.6b shows mesoporous structure of the ZnO NWs, and the lattice spacing of 0.28 nm displayed in the HR-TEM image (Figure 2,6c) matches with the d-spacing of ZnO (100) plane. Figure 2.6d shows the selected area diffraction pattern (SAED) of the ZnO NWs, and the ring patterns indicate that the ZnO NWs are polycrystalline. Figure 6e and 6f are elemental energy filtered (EF)-TEM maps of O and Zn, respectively, clearly displaying the presence of O and Zn all over the NWs.

In various electrochemical applications including photoelectrochemical cells, surface area of an electrode is correlated with the overall performance, because the surface is the spot where the electrochemical reaction takes place. Therefore, we performed BET analyses in order to measure the specific surface area and pore distributions of the fabricated ZnO NWs. Figure 2.7a shows the nitrogen adsorption-desorption curves of the anodic ZnO NWs. The specific surface area calculated by the BET isotherm was 14.45 $m^2/g$. and this value is higher than a typical value from single crystalline hexagonal ZnO NWs of ~40 nm diameter of which BET surface area is around 10 $m^2/g$ [43]. Figure 2.7b shows the pore distribution of the anodic ZnO NWs, and it was clearly observable that significant portion of pores was sized below 50 nm, indicating the mesoporous structure of anodic NWs.

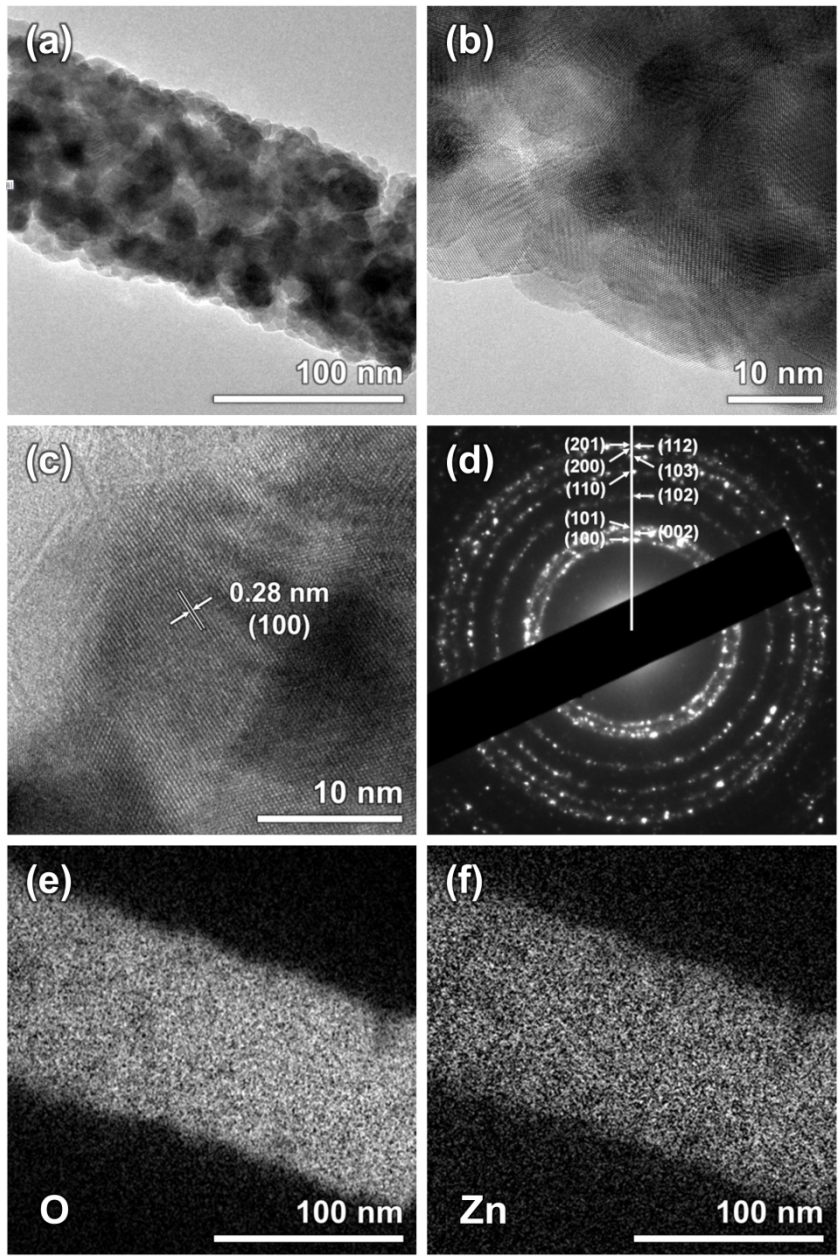


**Figure 2.6.** (a,b) TEM image of anodic ZnO nanowire and (c) HR-TEM image of ZnO nanowire showing the lattice spacing of 0.28 nm matching the (100) plane of ZnO. (d) SAED patterns of the anodic ZnO nanowires and (e, f) elemental EF-TEM maps showing the presence of (e) O and (f) Zn.

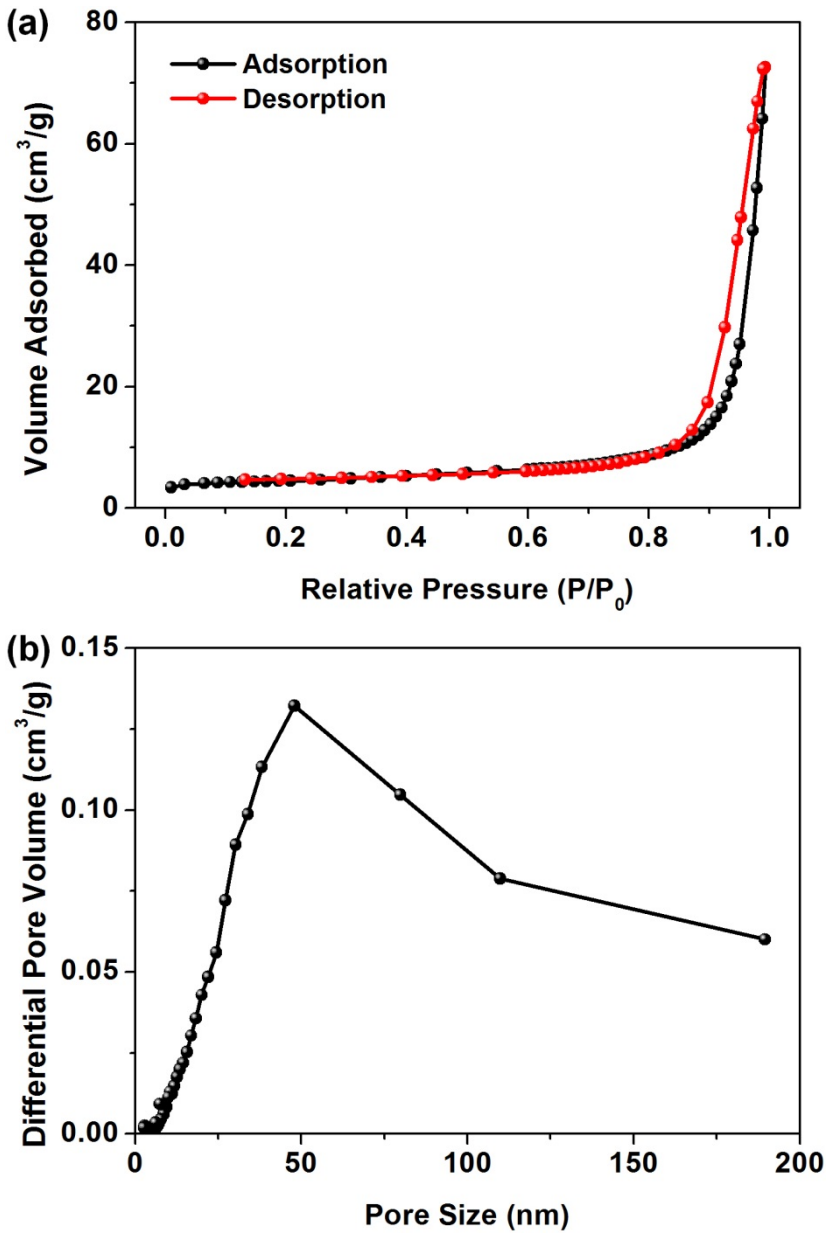


**Figure 2.7.** (a) $N_2$ adsorption and desorption isotherms and (b) pore-size distribution of the anodic ZnO nanowires.

### 2.3.2. Application of anodic ZnO nanowires in dye-sensitized solar cells

For the application of anodic ZnO NWs in DSCs, anodized Zn foils were sensitized in 0.5 mM ethanolic N719 dye solution for 1 h according to the reports by Law et al. [45]. ZnO is well known for poor chemical stability in even weak acid solutions, and therefore it is often sensitized in dye solution for a short time compared to the conventional $TiO_2$ films, because the anchoring carboxylic group of the dye is acidic. Platinized FTO glass was used as the counter electrode and two layers of 50 μm thick surlyn film was used as spacer. However, because $I_3^-/I^-$ redox electrolyte is extremely corrosive, gel-electrolyte based on iodide redox couple and 3-methoxypropionitrile solution was used instead of the conventional liquid electrolyte based on acetonitrile. Therefore, the electrolyte was pre-injected into the cell before the assembly using the laboratory spring clamps instead of melting surlyn films which have thermoplastic characteristic.

The performances of DSCs based on anodic ZnO NWs were characterized at standard 1 sun condition (100 mW/cm$^2$, AM 1.5G filtered), and the results are shown in Table 2.1 and Figure 2.8. For DSC applications, ZnO NWs prepared by 30, 60, 90, and 120 min of anodic oxidation were used. The energy conversion efficiency ($\eta$) was 2.36% at 30 min and increased to 3.57% at 60 min. However, due to the significant decrease in $V_{oc}$, $\eta$ decreases from the 90 min anodized case. This seems to be mainly attributed to the lateral cracks between the nanowire arrays and the substrate observed as the anodization time exceeds 90 min, as shown in Figure 2.2c and 2.2d. In this situation, the electrolyte may easily penetrate into the cracks and reach the metallic Zn substrate. Then a severe corrosion of Zn substrate may occur, forming Zn-I complexes as a result. This reduces the shunt resistance of the cell and gets rid of the pathways for the charge collection, leading to the significant drop in $V_{oc}$ and *FF*. For this reason, in spite of the larger photocurrent value, 90 min anodized ZnO gives lower performance in DSCs compared to the 60 min sample. Moreover, due to the more severe lateral cracks,

| anodic oxidation time (min) | $V_{oc}$ (V) | $J_{sc}$ (mA/cm$^2$) | *FF* (%) | $\eta$ (%) |
|---|---|---|---|---|
| 30 | 0.658 | 10.3 | 35.0 | 2.36 |
| 60 | 0.693 | 12.7 | 40.7 | 3.57 |
| 90 | 0.623 | 15.8 | 35.5 | 3.49 |
| 120 | 0.573 | 13.0 | 33.0 | 2.45 |

**Table 2.1.** Summary of *J-V* characteristics of DSCs based on anodic ZnO nanowires photoanodes prepared by various anodic oxidation times.

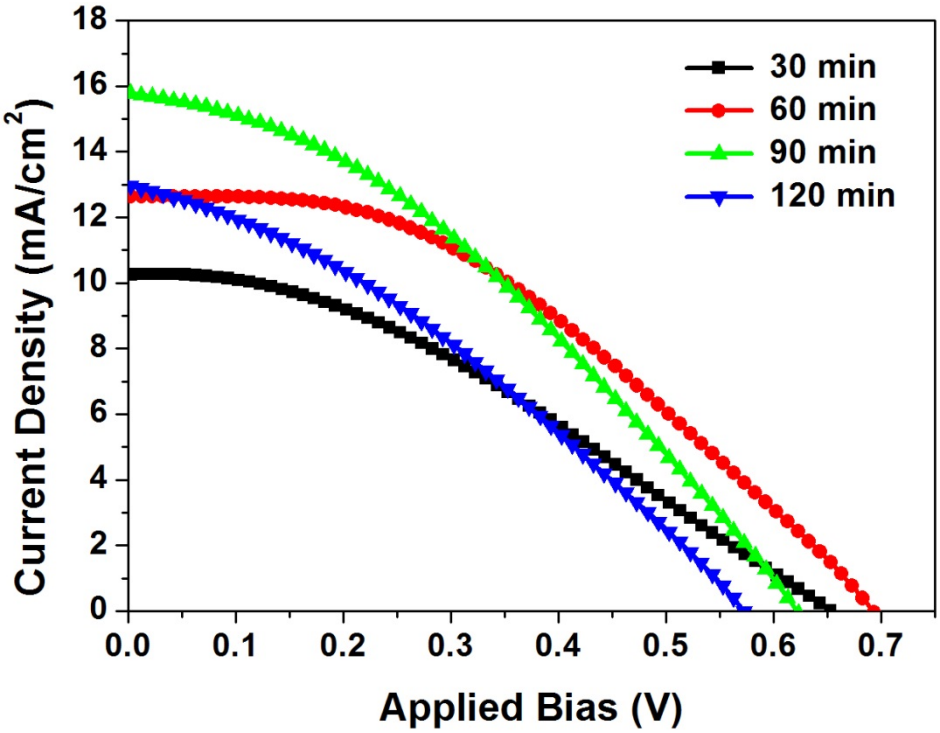


**Figure 2.8.** *J-V* characteristics of DSCs employing anodic ZnO nanowires prepared by 30, 60, 90, and 120 min of anodization as photoanode.

photovoltaic performance of the DSC employing 120 min anodized ZnO NWs are even lower than the 90 min case.

As a matter of fact, even though the gel electrolyte which provides higher stability in DSC applications, DSCs with anodic ZnO photoanode were very unstable and lost the photovoltaic performances within 1 min. The main reason for this is that the iodide redox couples in gel electrolyte consequently reaches at the Zn substrate, resulting in severe corrosion as a consequence. Therefore we could not characterize the DSCs further with measurements other than *J-V*, such as incident photon-to-current efficiency (IPCE) or electrochemical impedance spectroscopy (EIS). To solve the corrosion problem, there were attempts to utilize cobalt bipyridyl redox electrolyte which is non-corrosive. However, because the lengths of anodic ZnO NWs ranged from around 20 to 80 μm, the distance between the photoanode and counter electrode was far too large compared to an optimum distance (less than 25 μm for cobalt bipyidyl redox electrolyte). Therefore, limitation from the mass transfer was very severe, and thus it was impossible to obtain proper *J-V* results.

### 2.3.3. Synthesis and photovoltaic applications of ZnO/$TiO_2$ nanowires

In order to further increase the photovoltaic performance of the anodic ZnO NWs, ALD of $TiO_2$ was performed on the ZnO surface. Figure 2.9 shows the TEM images of ZnO/$TiO_2$ NWs prepared by 5 ALD cycles of $TiO_2$ followed by heat treatment at 400 °C in air for 1 h in order to remove remaining $TiO_2$ precursors and improve the adhesion between ZnO and $TiO_2$. From relatively low magnification images shown in Figure 2.9a and 2.9b, it is clearly observable that there is no significant change in the mesoporous structure of the NWs, indicating that the coated $TiO_2$ layer is very thin. This was confirmed by the HR-TEM image in Figure 2.9c, and the thickness of the $TiO_2$ layer was ~0.5 nm. Moreover, elemental EF-TEM maps of Figure 2.9a were obtained to check the presence of Ti, and the O,

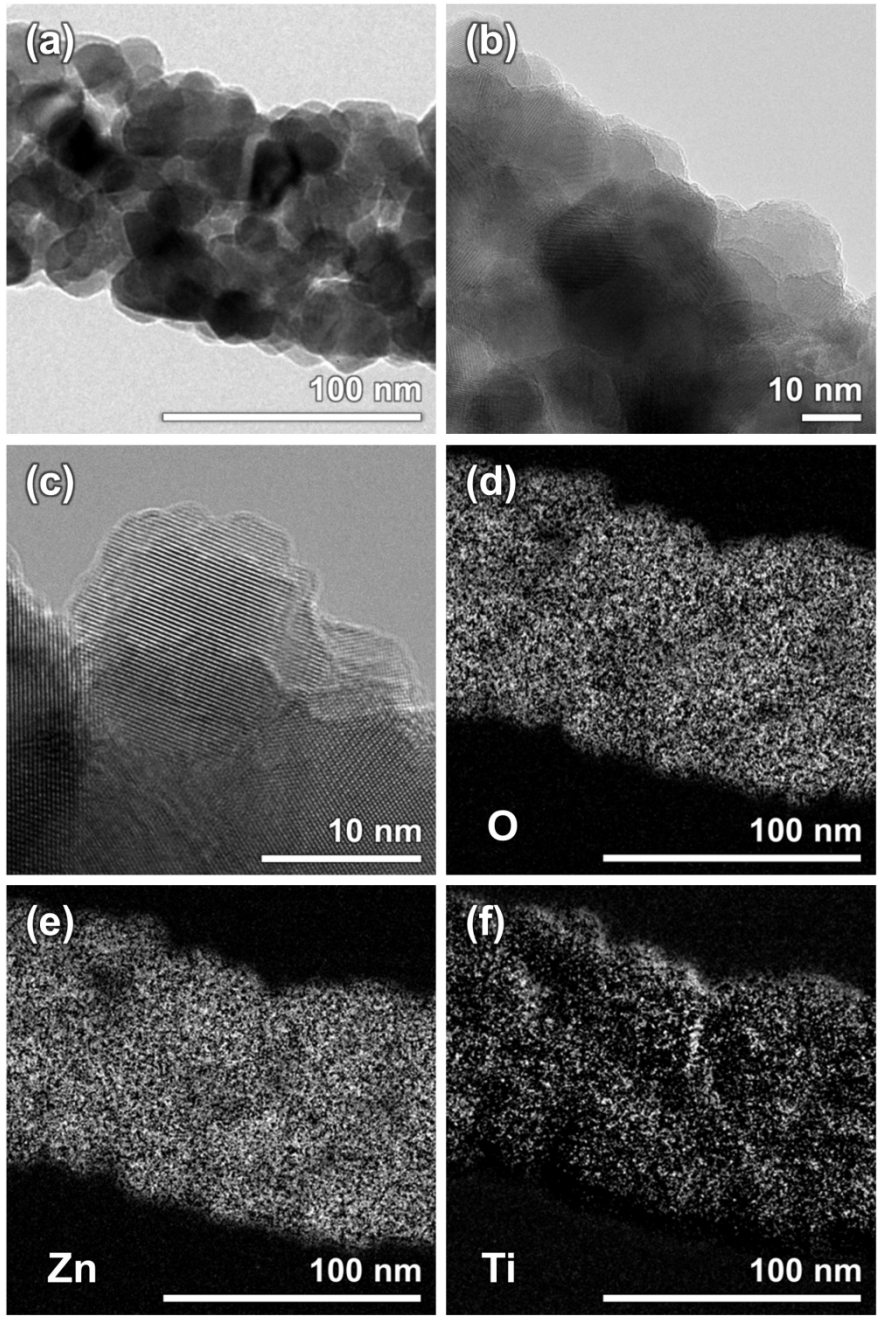


**Figure 2.9.** (a, b) TEM images and (c) HR-TEM image of $ZnO/TiO_2$ nanowires prepared by 5 cycles of ALD. (d-f) Elemental EF-TEM maps of (a) displaying the locations of (d) O, (e) Zn, and (f) Ti.

Zn, and Ti maps are presented in Figure 2.9d-2.9f, respectively. These 3 elements were located all over the ZnO NWs, and the uniformity of $TiO_2$ shell was verified.

Figure 2.10 shows the XPS spectra of the anodized Zn foil before and after the ALD of $TiO_2$. Survey spectra in Figure 2.10a shows that there are negligible change in the chemical composition and state during the ALD process and following heat treatment. Zn 2p XPS spectra in Figure 2.10b shows $2p_{1/2}$ and $2p_{3/2}$ peaks appearing at 1044.7 eV and 1021.7 eV, respectively, in both ZnO and $ZnO/TiO_2$ NWs, which correspond to the signals from ZnO [55]. Figure 2.10c shows O 1s spectra of which peaks are located at the identical positions. The largest peak observed at 530.5 eV is mainly attributed to the $O^{2-}$ ions on $Zn^{2+}$ ion array (530.15 eV) and $O^{2-}$ ions in the O deficient parts in ZnO matrix (531.25 eV) [56]. The peak around 532.4 eV is from the loosely bound O atoms in a specific chemical species such as adsorbed $O_2$ or $H_2O$. [56] From the exactly same peak positions in Zn and O XPS spectra, the effect of ALD process on anodic ZnO NWs could be neglected. Figure 2.10d shows the Ti 2p spectra, and the deposited $TiO_2$ is clearly detected from the peaks located at around 458.5 eV ($2p_{1/2}$) and 464.2 eV ($2p_{3/2}$) in ALD processed sample [55]. There was no signal related to Ti in the results of anodic ZnO NWs before ALD.

Finally, 5 ALD cycled $ZnO/TiO_2$ NWs were applied as photoanode of DSCs. The *J-V* characteristic shown in Figure 2.11 gives the results as follows; $V_{oc}$: 0.635 V; $J_{sc}$: 18.3 mA/cm$^{-2}$; *FF*: 56.1%; $\eta$: 6.52%. As mentioned in the introduction, ZnO based DSCs often give energy conversion efficiencies around 3-4% in most of the cases [34], and hardly reached 6.3 and 7.0 efficiencies [36,51]. Considering these, the results from this study is very promising, because (i) this result was obtained by back-side light illumination, and (ii) there were still indication of Zn metal substrate being corroded by the redox electrolyte. The cell also gave stable performance within around 1 min, and therefore further analyses could not be

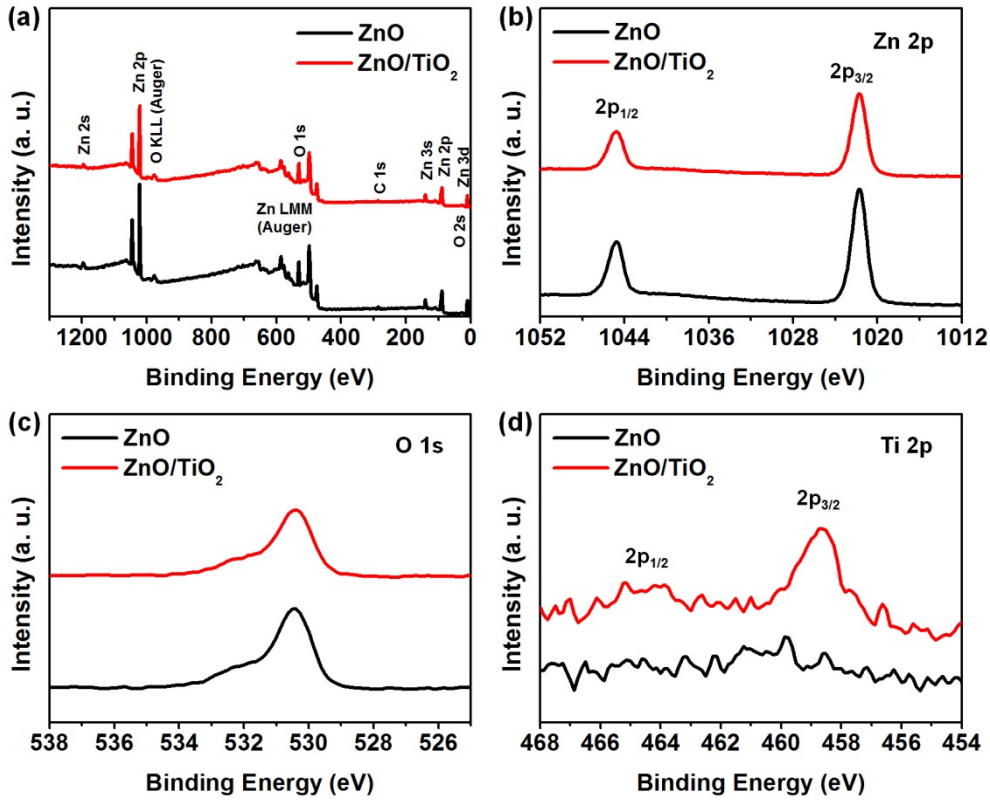


**Figure 2.10.** XPS (a) survey, (b) Zn 2p, (c) O 1s, and (d) Ti 2p spectra of anodic ZnO nanowires before and after $TiO_2$ shell deposition by using ALD method.

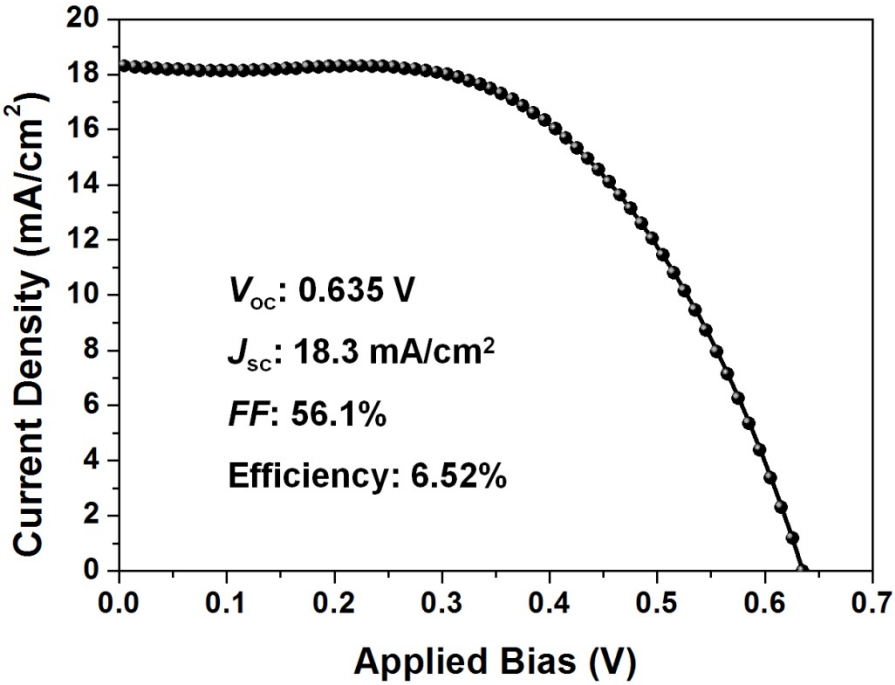


**Figure 2.11.** *J-V* characteristics of the DSCs employing ZnO/$TiO_2$ nanowires as photoanode and corresponding photovoltaic parameters calculated from *J-V*.

performed. However, this result strongly supports the superior characteristics of anodic ZnO NWs. To the best our our knowledge, the $J_{sc}$ value of 18.3 mA/cm$^{-2}$ is the highest ever reported, and the main reasons for the high photocurrent density are expected to be large surface area and fast charge transport due to the intrinsic property of ZnO and 1-D confinement of the electron pathways.

## 2.4. Conclusions

In this research, mesoporous ZnO NWs were synthesized via electrochemical anodization process. This anodic ZnO NWs had large specific surface area of 14.45 m$^2$/g, and when they were employed as photoelectrode in DSCs, fine photovoltaic performances were obtained. Moreover, for the further improvements in the energy conversion efficiency of the DSCs, the ZnO NWs were coated with $TiO_2$ by ALD method, and the coated layer and its thickness was confirmed by the TEM and XPS analyses. The resulting ZnO/$TiO_2$ NWs gave 6.52% efficiency with $J_{sc}$ value of 18.3 mA/cm$^{-2}$, which is the highest photocurrent density ever reported in ZnO based DSCs. Given that this result is obtained from the back-side light illumination, though the Zn substrate beneath the ZnO NWs caused stability problem, it was concluded that large surface area and 1-D structure, which enables efficient light harvesting and charge transport, suggest anodic ZnO NWs as a photoelectrode for DSCs. By further optimizations such as deposition of Zn on FTO glass followed by electrochemical anodization, the anodic ZnO NWs are anticipated to bring a significant increase in the photovoltaic performances.

## 2.5. References


[1] O'Regan, B; Grätzel, M., *Nature* **1991**, *353*, 737.

[2] Grätzel, M., *Nature* **2001**, *414*, 338.

[3] Grätzel, M., *Inorg. Chem.* **2005**, *44*, 6841.

[4] Hagfeldt, A.; Boschloo, G.; Sun, L.; Kloo, L.; Pettersson, H., *Chem. Rev.* **2010,** *110*, 6595.

[5] Ito, S.; Liska, P.; Comte, P.; Charvet, R. L.; Pechy, P.; Bach, U.; Schmidt-Mende, L.; Zakeeruddin, S. M.; Kay, A.; Nazeeruddin, M. K.; Grätzel, M., *Chem. Commun.* **2005**, 4351.

[6] Hore, S.; Nitz, P.; Vetter, C.; Prahl, C.; Niggemann, M.; Kern, R., *Chem. Commun.* **2005**, 2011.

[7] Zhang, Z. P.; Ito, S.; O'Regan, B.; Kuang, D. B.; Zakeeruddin, S. M.; Liska, P.; Charvet, R.; Comte, P.; Nazeeruddin, M. K.; Pechy, P.; Humphry-Baker, R.; Koyanagi, T.; Mizuno, T.; Grätzel, M., *Z. Phys. Chem.* **2007**, *221*, 319.

[8] Yum, J.-H.; Moehl, T.; Yoon, J.; Chandiran, A. K.; Kessler, F.; Gratia, P.; Grätzel, M., *J. Phys. Chem. C* **2014**, *118*, 16799.

[9] Feldt, S. M.; Gibson. E. A.; Gabrielsson, E.; Sun, L.; Boschloo, G.; Hagfeldt, A., *J. Am. Chem. Soc.* **2010**, *132*, 16714.

[10] Tsao, H. N.; Yi, C.; Moehl, T.; Yum, J.-H.; Zakeeruddine, S. M.; Nazeerudding, M. K.; Grätzel, M., *ChemSusChem* **2011**, *4*, 591.

[11] Bessho, T.; Zakeeruddin, S. M.; Yeh, C.-Y.; Diau, E. W.-G.; Grätzel, M., *Angew. Chem. Int. Ed.* **2010**, *49*, 6646.

[12] Yella, A.; Lee, H.-W.; Taso, H. N.; Yi, C.; Chandiran, A. K.; Nazeeruddin, M. K.; Diau, E. W.-G.; Yeh, C.-Y.; Zakeeruddin, S. M.; Grätzel, M., *Science* **2011**, *334*, 629.

[13] Lan, C.-M.; Wu, H.-P.; Pan, T.-Y.; Chang, C.-W.; Chao, W.-S.; Chen, C.-T.; Wang, C.-L.; Lin, C.-Y.; Diau, E. W.-G., *Energy Environ. Sci.* **2012**, *5*, 6460.

[14] Yum, J.-H.; Holcombe, T. W.; Kim, Y.; Rakstys, K.; Moehl, T.; Teuscher, J.; Delcamp, J. H.; Nazeeruddin, M. K.; Grätzel, M., *Sci. Rep.* **2013**, *3*, 2446.

[15] Matthew, S.; Yella, A.; Gao, P.; Humphry-Baker, R.; Curchod, B. F. E.; Ashari-Astani, N.; Tavernelli, I.; Rothlisberger, U.; Nazeeruddin, M. K.; Grätzel, M., *Nat. Chem.* **2014**, *6*, 242.

[16] Sapp, S. A.; Elliott, M.; Contado, C.; Caramori, S.; Bignozzi, C. A., *J. Am. Chem. Soc.* **2002**, *124*, 11215.

[17] Klahr, B. M.; Hamann, T. W., *J. Phys. Chem. C* **2009**, *113*, 14040.

[18] Yum, J.-H.; Baranoff, E.; Kessler, F.; Moehl, T.; Ahmad, S.; Bessho, T.; Marchioro, A.; Ghadiri, E.; Moser, J.-E.; Yi, C.; Nazeerudding, M. K.; Grätzel, M., *Nat. Commun.* **2011**, *3*, 631.

[19] Macák, J. M.; Tsuchiya, H.; Ghicov, A.; Schmuki, P., *Electrochem. Commun.* **2005**, *7*, 1133.

[20] Mor, G. K.; Shankar, K.; Paulose, M.; Varghese, O. K.; Grimes, C. A., *Nano Lett.* **2006**, *6*, 215.

[21] Jennings, J. R.; Ghicov, A.; Peter, L. M.; Schmuki, P.; Walker, A. B., *J. Am. Chem. Soc.* **2008**, *130*, 13364.

[22] Varghese, O. K.; Paulose, M.; Grimes, C. A., *Nat. Nanotechnol.* **2009**, *4*, 592.

[23] Feng, X.; Shankar, K.; Varghese, O. K.; Paulose, M.; Latempa, T.; Grimes, C. A., *Nano Lett.* **2008**, *8*, 3781.

[24] Liu, B.; Aydil, E. S., *J. Am. Chem. Soc.* **2009**, *131*, 3985.

[25] Liao, J.-Y.; Lei, B.-X.; Chen, H.-Y.; Kuang, D.-B., Su, C.-Y., *Energy Environ. Sci.* **2012**, *5*, 5750.

[26] Kang, S. H.; Choi, S.-H.; Kang, M.-S.; Kim, J.-Y.; Kim, H.-S.; Hyeon, T.; Sung, Y.-E., *Adv. Mater.* **2008**, *20*, 54.

[27] Zhu, K.; Neale, N. R.; Miedaner, A.; Frank, A. J., *Nano Lett.* **2007**, *7*, 69.

[28] Zhu, K.; Vinzant, T. B.; Neale, N. R.; Frank, A. J., *Nano Lett.* **2007**, *7*, 3739.

[29] Rensmo, H.; Keis, K.; Lindström, H.; Södergren, S., Solbrand, A.; Hagfeldt, A.; Lindquist, S.-E.; Wang, L. N.; Muhammed, M., *J. Phys. Chem. B* **1997**, *101*, 2598.

[30] Tennakone, K.; Kumara, G. R. R. A.; Kottegoda, I. R. M.; Perera, V. P. S., *Chem. Commun.* **1999**, 15.

[31] Keis, K.; Magnusson, E.; Lindström, H.; Lindquist, S.-E.; Hagfeldt, A., *Sol. Energy Mater. Sol. Cells* **2002**, *73*, 51.

[32] Chappel, S.; Chen, S.-G.; Zaban, A., *Langmuir* **2002**, *18*, 3336.

[33] Saito, M.; Fujihara, S., *Energy Environ. Sci.* **2008**, *1*, 280.

[34] Zhang, Q.; Dandeneau, C. S.; Zhou, X.; Cao, G., *Adv. Mater.* **2009**, *21*, 4087.

[35] Qian, J.; Liu, P.; Xiao, Y.; Jiang, Y.; Cao, Y.; Zi, X.; Yang, H., *Adv. Mater.* **2009**, *21*, 3663.

[36] Park, K.; Zhang, Q.; Battalla, B.; Zhou, X.; Jeong, Y.-H.; Cao, G., *Adv. Mater.* **2010**, *22*, 2329.

[37] Snaith, H. J.; Ducanti, C., *Nano Lett.* **2010**, *10*, 1259.

[38] Kim, J.-Y.; Kang, J. S.; Shin, J.; Kim, J.; Han, S.-J.; Park, J.; Min, Y.-S.; Ko, M. J.; Sung, Y.-E., *Nanoscale* **2015**, *7*, 8368.

[39] Noack, V.; Weller, H.; Eychmuller, A., *J. Phys. Chem. B* **2002**, *106*, 8514.

[40] Wu, J. J.; Chen, G. R.; Lu, C. C.; Wu, W. T.; Chen, J. S., *Nanotechnology* **2008**, *19*, 105702.

[41] Green, A. N. M.; Palomares, E.; Haque, S. A.; Kroon, J. M.; Durrant, J. R., *J. Phys. Chem. B* **2005**, *109*, 12525.

[42] Keis, K.; Lindgren, J.; Lindquist, S.-E.; Hagfeldt, A., *Langmuir* **2000**, *16*, 4688.

[43] Greene, L. E.; Law, M.; Goldberger, J.; Kim, F.; Johnson, J. C.; Zhang, Y. Saykally, R. J.; Yang, P., *Angew. Chem. Int. Ed.* **2003**, *42*, 3031.

[44] Law, M.; Greene, L. E.; Johnson, J. C.; Saykally, R.; Yang, P., *Nat. Mater.* **2005**, *4*, 455.

[45] Law, M.; Greene, L. E.; Radenovic, A.; Kuykendall, T.; Liphardt, J.; Yang, P., *J. Phys. Chem. B* **2006**, *110*, 22652.

[46] Baxter, J. B.; Aydil, E. S., *Appl. Phys. Lett.* **2005**, *86*, 053114.

[47] Baxter, J. B.; Walker, A. M.; van Ommering, K.; Aydil, E. S., *Nanotechnology* **2006**, *17*, S304.

[48] Galoppini, E.; Rochford, J.; Chen, H.; Saraf, G.; Lu, Y.; Hagfeldt, A.; Boscholoo, G., *J. Phys. Chem. B* **2006**, *110*, 16159.

[49] Martinson, A. B. F.; McGarrah, J. E.; Parpia, M.; O. K.; Hupp, J. T., *Phys. Chem. Chem. Phys.* **2006**, *8*, 4655.

[50] Xu, C.; Shin, P.; Cao, L.; Gao, D., *J. Phys. Chem. C* **2010**, *114*, 125.

[51] Xu, C.; Wu, J.; Desai, U. V.; Gao, D., *J. Am. Chem. Soc.* **2011**, *133*, 8122.

[52] Wu, X.; Lu, G.; Li, G.; Shi, G., *Nanotechnology* **2006**, *17*, 4936.

[53] Kim, S. J.; Choi, J., *Electrochem. Commun.* **2008**, *10*, 175.

[54] Hu, Z.; Chen, Q.; Li, Z.; Yu, Y. Peng, L.-M., *J. Phys. Chem. C* **2010**, *114*, 881.

[55] Wagner, C. D.; Riggs, W. M.; Davi, L. E.; Moulder, J. F.; Muilenberg, G. E., *Handbook of X-ray Photoelectron Spectroscopy*, Perkin-Elmer (Physical Electronics Division), Eden-Priarie: MN, **1979**.

[56] Chen, M.; Wang, X.; Yu, Y. H.; Pei, Z. L.; Bai, X. D.; Sun, C.; Huang, R. F.; Wen, L. S., *Appl. Surf. Sci.* **2000**, *158*, 134.

# Chapter 3. Highly uniform anodic tin oxide nanochannel arrays as photoelectrode

## 3.1. Introduction

Nanostructured transition metal oxides prepared by electrochemical anodic oxidation have received significant attention for diverse applications in nanomaterial synthesis [1-3], photonic crystals [4,5], biosensors [6,7], and photovoltaics [8-20], owing to their unique properties stemming from one-dimensional geometry and vertically aligned pore structure, as well as the advantages of the anodic oxidation process such as simplicity, reliability, and low cost for large-scale production. Firstly, anodic aluminum oxides (AAOs) prepared by anodic oxidation of Al have been studied over the past six decades, especially in the field of nanotechnology. In addition, since Macák et al. first used highly ordered $TiO_2$ nanotube arrays, prepared by anodic oxidation of Ti as photoanodes in dye-sensitized solar cells (DSCs) [8], the optimization and application of these $TiO_2$ nanotube or nanochannel arrays for photovoltaic devices have been intensively studied [9-17]. Vertically oriented nanotube or nanochannel electrodes have been considered as ideal structures for electron transport in photovoltaic devices; indeed, it was shown that these one-dimensional structures exhibit lower electron recombination rate and stronger light scattering effect compared with the conventional randomly oriented structures based on spherical nanoparticles [10]. Furthermore, vertically aligned pore structures are advantageous for the diffusion of redox couples and interfacial contacts with electrolytes or hole conductors in photovoltaic devices [12,14].

Although, besides Al and Ti, anodic oxidation of other transition metals such as Nb [18,21], Zr [22,23], W [24,25], Ta [26], Hf [27], and Sn [28-31] for the formation of vertically aligned nanotube or nanochannel metal oxide arrays has been reported, the studies and applications have been relatively insufficient for these various metals compared to the cases of Al and Ti. In particular, vertically aligned $SnO_2$ nanochannel arrays might be an attractive material for photovoltaic applications. Although the electron recombination rate in $SnO_2$ is faster by two to three orders of magnifitude [32] and conversion efficiency is poorer compared with those of the conventional $TiO_2$ as a photoanode material of mesoscopic sensitized solar cells (dye- or quantum dot-sensitized solar cells), it has received much attention due to its potential properties such as faster electron transport rate and tolerance to UV illumination resulting from the larger band gap (3.6 eV, cf. $TiO_2$ ~3.2 eV) [32-29]. In addition, because the conduction band potential of $SnO_2$ is 0.4 eV more positive than that of $TiO_2$, electron injection becomes possible from dyes or inorganic sensitizers (quantum dots) that are energetically unfavorable with respect to $TiO_2$ [36-38].

However, a direct application of anodic $SnO_2$ nanochannel arrays maintaining vertically aligned structures as photoelectrodes in photovoltaic devices has not been reported yet. This is due to the difficulty of fabricating anodic $SnO_2$ electrodes with uniform nanoporous structures over large areas without lateral cracks. Because the Sn anodic oxidation process is very fast in general [28], it is difficult to fabricate anodic $SnO_2$ electrodes with nanoporous surface structures over large areas. In addition, due to the vigorous oxygen evolution during the Sn anodic oxidation process, many lateral cracks are generated, resulting in the discontinuous nanochannel structure composed of stacked layers several hundreds of nanometers thick [28-31]. Although Hossain et al. [40] and Teh et al. [41] reported the mesoscopic sensitized solar cells employing anodic nanoporous $SnO_2$ as photoanode materials, they could not directly utilize anodic nanoporous $SnO_2$

maintaining vertically aligned structures. Instead, these researchers peeled off the anodic nanoporous $SnO_2$ from the Sn metal substrate, and then used the peeled material to prepare a paste for deposition onto the conductive substrate (FTO glass), resulting in a randomly oriented structure of photoanode material.

In this chapter, a modified process of Sn metal anodic oxidation for fabrication of large-scale $SnO_2$ nanochannel arrays with uniform structure but without lateral cracks was developed. The Sn anodic oxidation process was performed in an oxalic acid solution with the assistance of ultrasonication. Using ultrasonication, a uniform nanoporous structure was formed over large surface areas and lateral cracks were not generated, yielding vertically aligned continuous nanochannel arrays. These nanochannel arrays were directly used in quasi-solid state DSCs as photoanodes. To the best of our knowledge, it is the first photovoltaic application of vertically aligned anodic $SnO_2$ nanochannel arrays. The thickness of $SnO_2$ nanochannel arrays was controlled by varying the anodic oxidation time. Photovoltaic performances were examined for $SnO_2$ nanochannel arrays with different thicknesses. Owing to the significantly short anodic oxidation time (330 s) for achieving the optimal thickness (7.0 μm) for photovoltaic performance, and owing to the utilization of a gel-type electrolyte, the devices in this study were fabricated through a simple and rapid process. Furthermore, in order to enhance the photovoltaic performance, a $TiO_2$ shell layer was deposited onto the $SnO_2$ nanochannel by atomic layer deposition (ALD). The enhanced photovoltaic properties, in particular the prolonged electron lifetime resulting from the $TiO_2$ shell addition, were characterized.

## 3.2. Experimental section

### 3.2.1. Preparation of $SnO_2$ and $SnO_2/TiO_2$ nanochannel arrays

Vertically aligned $SnO_2$ nanochannel arrays were fabricated by using a modified anodic oxidation method. Tin foil (Alfa Aesar, 99.8% purity, 0.25 mm thick, 2.0 cm × 1.5 cm in size) was anodized in 0.5 M oxalic acid aqueous solution [28]. The anodic oxidation process was carried out with ultrasonication (60 W, 28 kHz, MUJIGAE SD-120H). A Pt mesh was used as a counter electrode, and the distance between the tin foil and Pt mesh was 5 cm. A dc potential of 10 V was applied and the anodic oxidation time was varied from 90 to 390 s. The as-anodized $SnO_2$ electrode was washed in distilled water under ultrasonication, followed by thermal annealing at 500 °C for 3 h in air. The $TiO_2$ shell layer was grown on the surface of $SnO_2$ nanochannel arrays at 150 $^oC$ by using a laminar flow type ALD reactor. One ALD cycle for $TiO_2$ consists of four steps: $TiCl_4$ exposure (1 s) – purging (5 s) – $H_2O$ exposure (1 s) – purging (20 s). The ALD cycle was repeated for growing the ultrathin $TiO_2$ with thicknesses of 1, 2, 5, and 10 Å. For each $TiO_2$ thickness, the ALD process was repeated for 3, 6, 15, and 30 cycles considering the growth-per-cycle of 0.34 Å/cycle measured on bare Si wafers. $TiCl_4$ (UP Chemical Co., Ltd.) and $H_2O$ were vaporized from external canisters at room temperature and led into the reactor through solenoid valves without any carrier gas. High-purity $N_2$ gas (99.999%) was used as a purging gas with a flow rate of 400 sccm. All delivery lines were maintained at 120 $^oC$. The base pressure of the reactor was below 10 mTorr and ALD was processed at a working pressure of 200–600 mTorr.

### 3.2.2. Characterization of materials

The morphology and the structure of the $SnO_2$ nanochannel arrays were examined using a scanning electron microscope (SEM; Carl Zeiss SUPRA 55VP), and transmission electron microscope (TEM; JEOL JEM-2010). The cross-sectional

images of the $SnO_2$ nanochannel arrays were obtained using SEM (Cal Zeiss AURIGA) after focused ion beam (FIB) milling. The chemical states were confirmed by elemental energy-filtered (EF)-TEM maps (JEOL JEM-2100F). The crystalline phase was confirmed using high power X-ray diffraction (XRD; Rigaku D/MAX 2500 V diffractometer) with Cu Kα radiation. The surface compositions were characterized by using X-ray photoelectron spectroscopy (XPS; Thermo SIGMA PROBE), using an Al *Kα* X-ray source in an UHV system with a chamber base pressure of ~$10^{-10}$ Torr.

### 3.2.3. Fabrication of solar cells

The prepared $SnO_2$ nanochannel electrodes were dipped into a $5\times10^{-4}$ M N719 dye (Ru 535-bisTBA, Solaronix) solution in ethanol for 24 h at room temperature. The Pt-counter electrodes were prepared by spin-casting a drop of 10 mM $H_2PtCl_6$ in 2-propanol onto F-doped $SnO_2$ (FTO) glass followed by heat treatment at 400 °C for 15 min in air. A thermal adhesive film (Surlyn, thickness: 30 μm) was attached on the dye-adsorbed $SnO_2$ electrodes. Commercial gel-type electrolyte containing $I^-/I_3^-$ redox couples (EL-SGE, Dyesol) was cast on the dye-adsorbed $SnO_2$ electrodes, followed by covering with Pt-counter electrodes in the aid of clamps.

### 3.2.4. Characterization of solar cells

Standard photocurrent density-voltage (*J-V*) measurements were performed using a 500 W xenon lamp (XIL model 05A50KS source measure units and an AM 1.5G filter) at a power of 100 mW/$cm^2$ and a potentiostat (Solartron 1480). The solar cells were covered by a black aperture mask before the measurements in order to avoid the additional illumination through the lateral space [42,43]. The electrochemical impedance spectra were obtained in the dark condition with the bias potential of -0.5 V by Zahner IM6. The magnitude of the sinusoidal perturbations was 10 mV, and the frequency ranged from 0.1 Hz to 100 kHz.

## 3.3. Results and discussion

### 3.3.1. Synthesis and characterization of $SnO_2$ nanochannel arrays

Figure 3.1 shows scanning electron microscope (SEM) images of annealed $SnO_2$ nanochannel arrays prepared by the conventional anodic oxidation process (under 10 V for 330 s, without ultrasonication) according to the previous report [28]. As shown in Figure 3.1a, the Sn substrate surface was not uniformly anodized over large areas. Porous layers and relatively compact layers coexisted, and this trend was consistent throughout the whole areas of the samples. Nanochannel structure with pore size of 50-80 nm and wall thickness of 20-30 nm was observed in the porous layers. However, the coexisting compact layers did not seem to be sufficiently porous to be utilized as photoanodes of mesoscopic sensitized solar cells.

On the other hand, the samples prepared by anodic oxidation with ultrasonication (under 10 V for 330 s) had uniform nanochannel structures over large areas, as shown in Figure 3.2a. Compact layers were not oberserved throughout the whole areas of these samples. As shown in Figure 3.2b, the pore size and wall thickness were identical to those of the samples prepared by using the conventional method. Figure 3.1c shows the cross-sectional image of $SnO_2$ nanochannel arrays, representing the vertically aligned pore structure and partially one-dimensional wall structure. Figure 3.2d shows the current transient during the Sn anodic oxidation, exhibiting a profile similar to that of other valve metals. However, compared to the well-known anodic oxidation processes (such as anodic oxidation of Ti and Al), the time-scale was significantly short, implying the rapid reaction process. For example, the step for initial formation of compact oxide layers (step (i) in Figure 3.2d) generally takes about 5-10 minutes in the anodic oxidation process of Ti [44]; however, in this work, the same step for Sn took only about only 2 s. This rapid anodic oxidation process accompanying vigorous oxygen

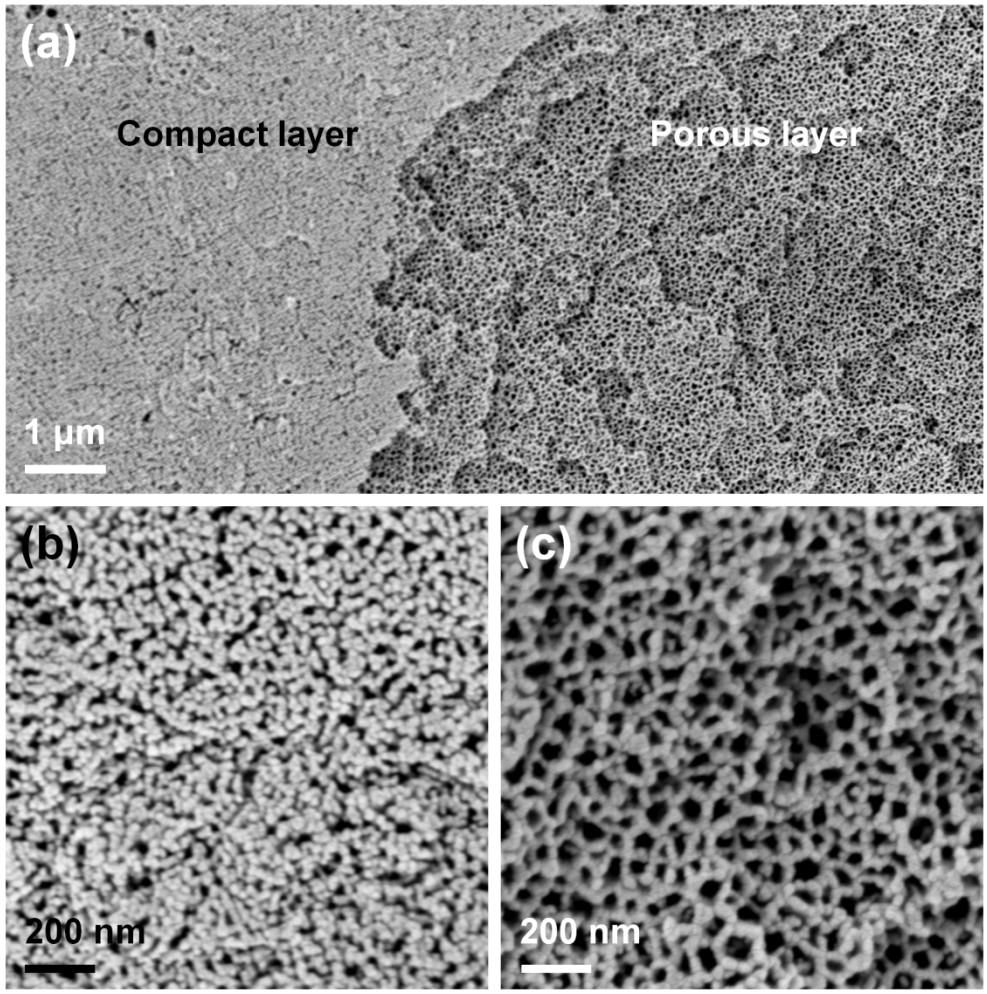


**Figure 3.1.** SEM images of annealed $SnO_2$ nanochannel arrays prepared by using the conventional anodic oxidation process. (a) Low-magnification surface image. (b) High-magnification image of a compact layer in (a). (c) High-magnification image of a porous layer in (a).

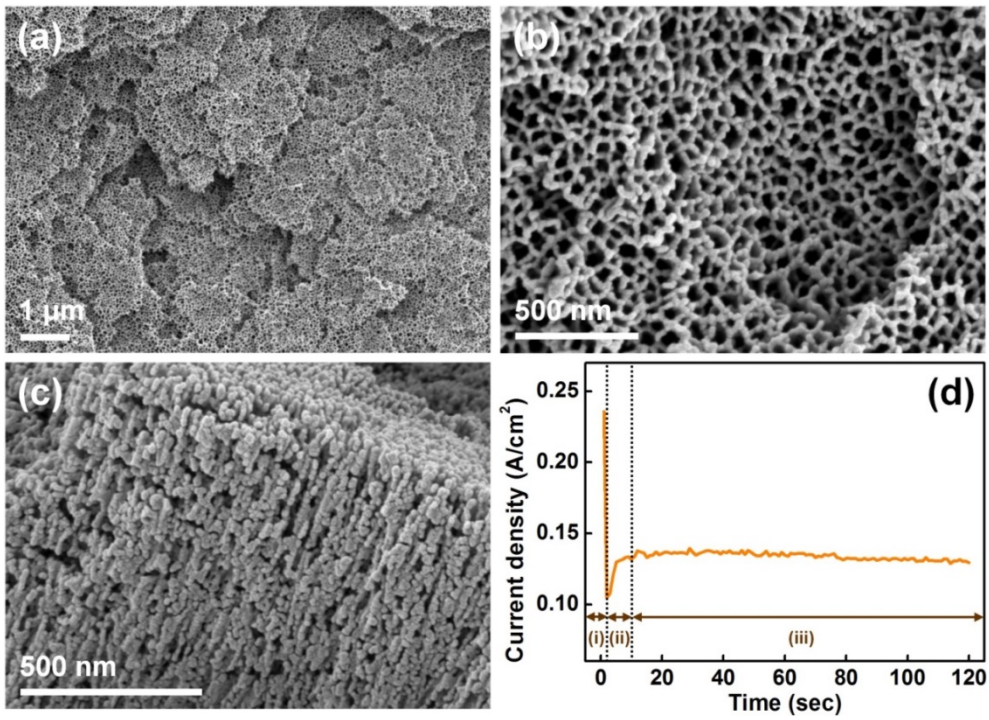


**Figure 3.2.** (a) Low-magnification surface SEM image of annealed $SnO_2$ nanochannel arrays prepared with ultrasonication. (b) High-magnification image of (a). (c) Cross-sectional image of annealed $SnO_2$ nanochannel arrays prepared with ultrasonication. (d) Current transient during anodic oxidation of Sn foil with ultrasonication. Step (i): Formation of compact $SnO_2$ layers; Step (ii): Chemical and field-assisted dissolution of the formed oxide layer resulting in nucleation of nanopores; Step (iii): Formation of porous nanochannel structures.

evolution [28] led to nonhomogeneous distribution of chemical and field-assisted dissolution throughout the surface, resulting in the formation of non-uniform pore structure when the conventional method was applied. However, with ultrasonication, ultrasonic waves assisted the oxygen gas to escape rapidly and smoothly, leading to homogeneous distribution of chemical and field-assisted dissolution of the formed $SnO_2$ layers throughout the whole surface [45]. As a result, uniform pore structure was formed with ultrasonication as shown in Figure 3.2a.

Figure 3.3a shows the X-ray diffraction (XRD) patterns for the prepared $SnO_2$ nanochannel arrays before and after annealing. The as-anodized sample exhibited nearly the same pattern as the Sn foil, indicating that the as-anodized sample has an amorphous phase. After annealing at 500 °C for 3 h in air, the sample was crystallized and exhibited the pattern corresponding to the cassiterite $SnO_2$ phase [46,47]. The (101) peak corresponding to the Sn metal still remained, because the Sn foil was located beneath the $SnO_2$ layer. The average crystallite size calculated by using the Scherrer equation [48] was about 22.7 nm. Figure 3.3b and 3.3c show the transmission electron microscopy (TEM) images of the annealed sample. The nanochannel structures were confirmed again as already observed in the SEM images. Figure 3.3b is the top view of the $SnO_2$ nanochannel with pore size of 50-80 nm and wall thickness of 20-30 nm, which accorded with the SEM images. Figure 3.3c is the lateral view of the $SnO_2$ nanochannel, exhibiting the one-dimensional wall structure. In addition, the crystal phase was cross-checked by using the selected area electron diffraction (SAED) pattern as shown in Figure 3.3d, which was consistent with the XRD pattern presented in Figure 3.3a.

Since the thickness of the photoanode can greatly affect photovoltaic performance of mesoscopic sensitized solar cells [49,50], the dependence of $SnO_2$ nanochannel array thickness on anodic oxidation time was precisely measured by

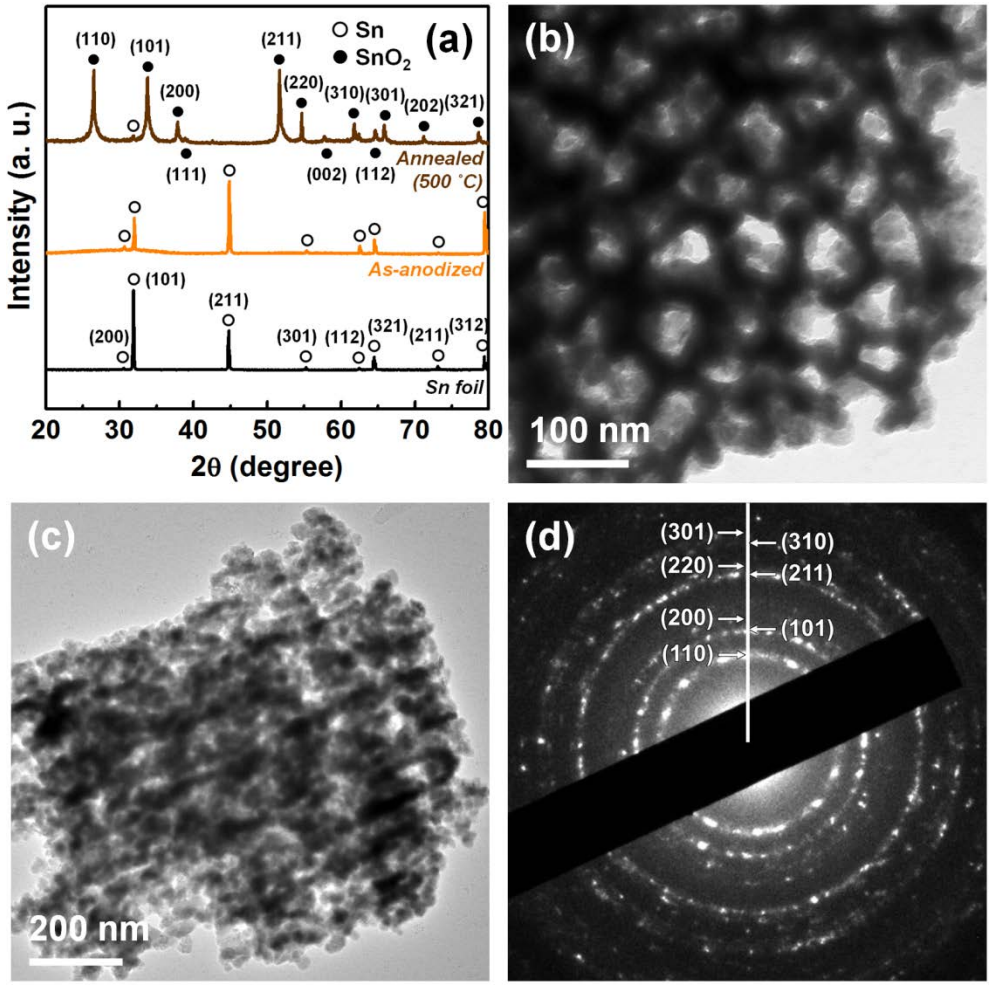


**Figure 3.3.** (a) XRD patterns of Sn foil, as-anodized and annealed $SnO_2$ nanochannel arrays. TEM images (b, c) and SAED pattern (d) of annealed $SnO_2$ nanochannel arrays.

using the SEM images obtained after focused ion beam (FIB) milling (Figure 3.4). The $SnO_2$ nanochannel arrays thicknesses were about 1.5, 2.3, 4.0, 6.0 and 7.0 μm for anodic oxidation times of 90, 150, 210, 270, 330 s, respectively. As shown in Figure 3.5, the thickness increased linearly at the growth rate of about 1.47 μm/min. However, anodic oxidation longer than 330 s resulted in the poor adhesion between the Sn metal substrate and the grown $SnO_2$ nanochannel arrays, leading to the partial peeling off. The thickness of remaining $SnO_2$ nanochannel arrays on the Sn metal is shown in Figure 3.4f. The thickness of $SnO_2$ nanochannel arrays was about 6.4 μm for anodic oxidation time of 390 s, yielding thinner arrays than those for anodic oxidation time of 330 s. As a result, the maximal thickness of $SnO_2$ nanochannel arrays was 7.0 μm, obtained for 330 s long anodic oxidation. It is noteworthy that the obtained vertically aligned pore structure was continuous without lateral cracks through this long range. Using the conventional anodic oxidation process, many lateral cracks were generated resulting in the discontinuous nanochannel structure, as shown in Figure 3.6, which is consistent with previous reports [28-31]. Crack creation was likely owing to the rapid anodic oxidation reaction and vigorous oxygen evolution, which created turbulence in the electrolyte and local stresses during the formation of $SnO_2$ nanochannels [28]. As already mentioned, ultrasonic waves assisted the oxygen gas to escape rapidly and smoothly, preventing the generation of lateral cracks as a consequence.

### 3.3.2. Photovoltaic application of $SnO_2$ nanochannel arrays

These $SnO_2$ nanochannel arrays with large-scale uniform structures were utilized as photoanodes in DSCs. The $SnO_2$ nanochannel arrays were utilized directly, maintaining the vertically-aligned structure as depicted in Figure 3.7a. The whole size of photoanode was 2.0 cm × 1.5 cm, and the active area was 0.25 $cm^2$. Polymer gel electrolytes containing iodide redox couples ($I^-/I_3^-$) and conventional Pt/FTO glass counter electrodes were utilized for the fabrication of the devices.

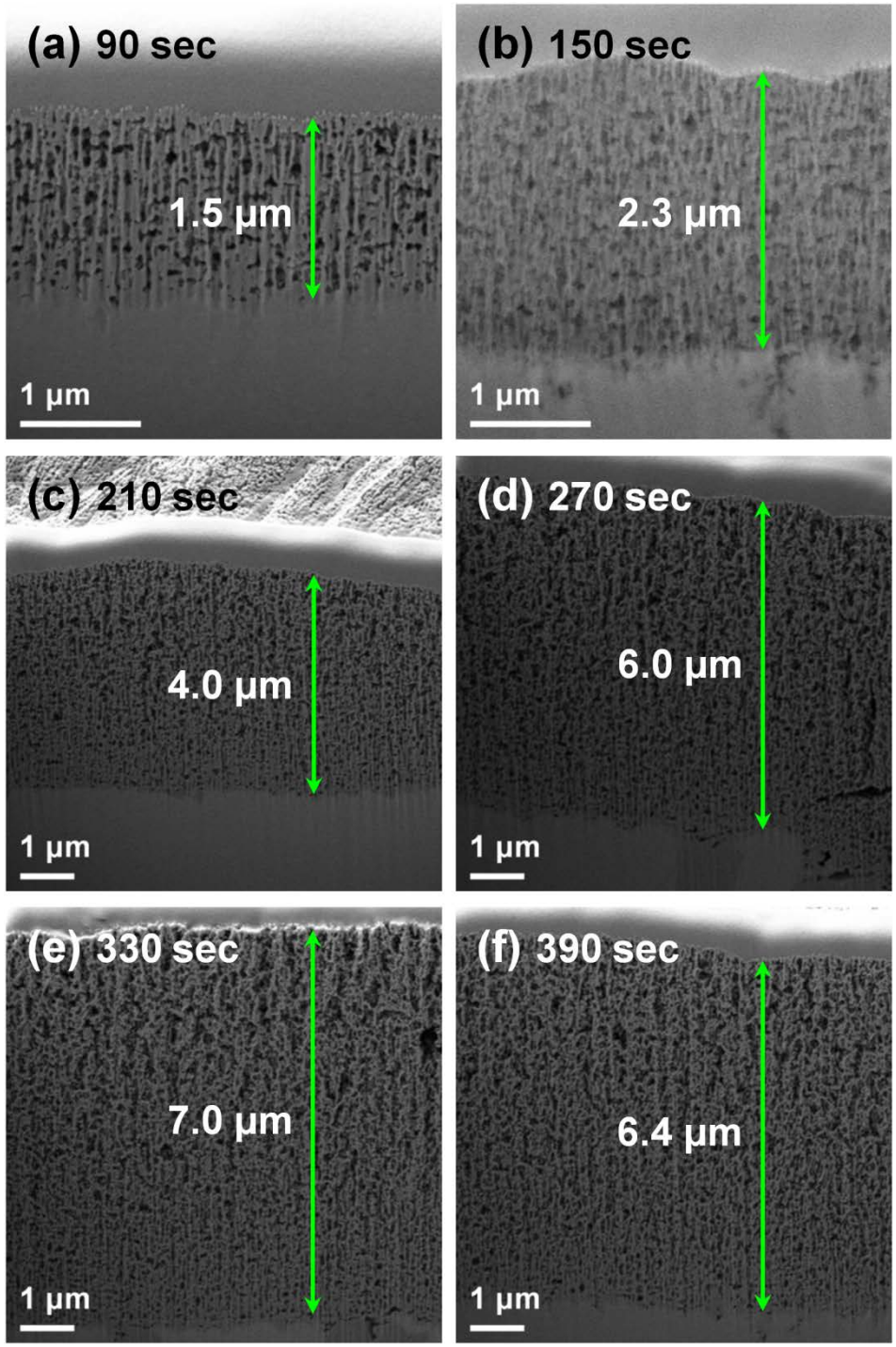


**Figure 3.4.** Cross-sectional SEM images (taken after FIB-milling) of $SnO_2$ nanochannel arrays grown by anodic oxidation for 90-390 s.

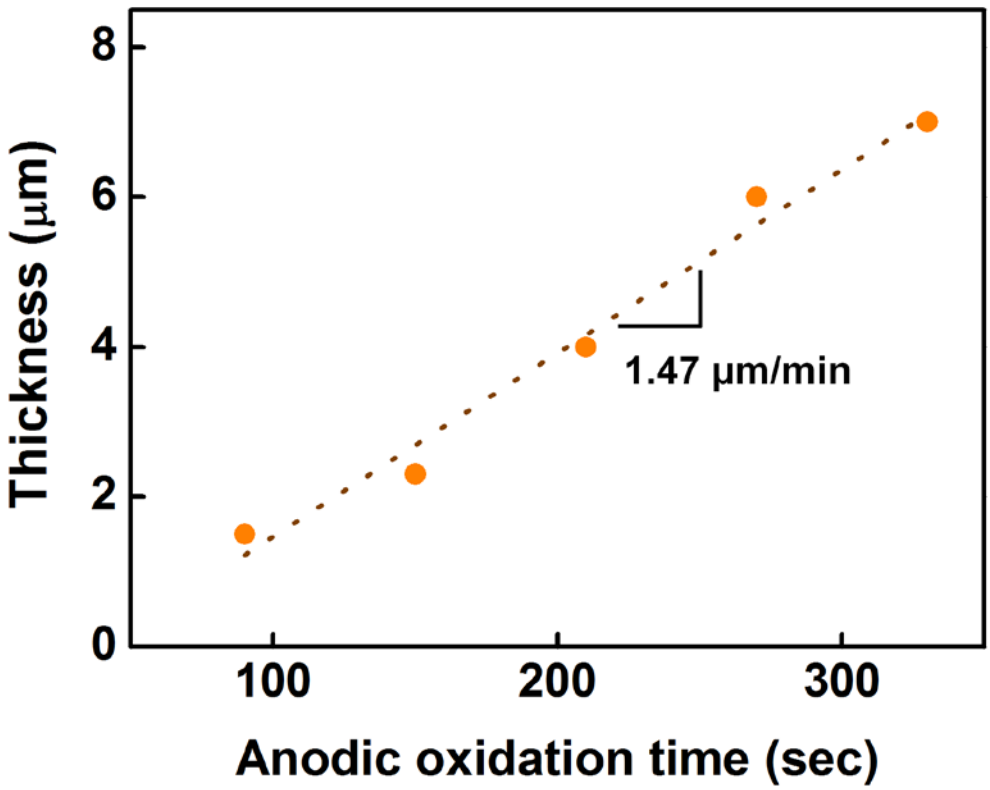


**Figure 3.5.** Thicknesses of annealed $SnO_2$ nanochannel arrays prepared with ultrasonication, for different anodic oxidation times.

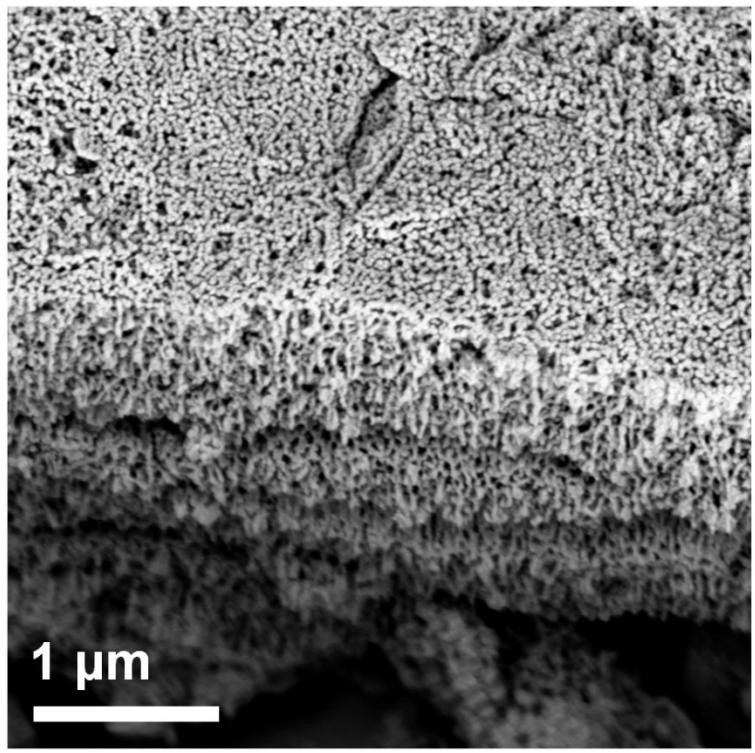


**Figure 3.6.** SEM image of annealed $SnO_2$ nanochannel arrays prepared by the conventional anodic oxidation process (This image was obtained after tilting the edge side of prepared sample during the SEM analysis).

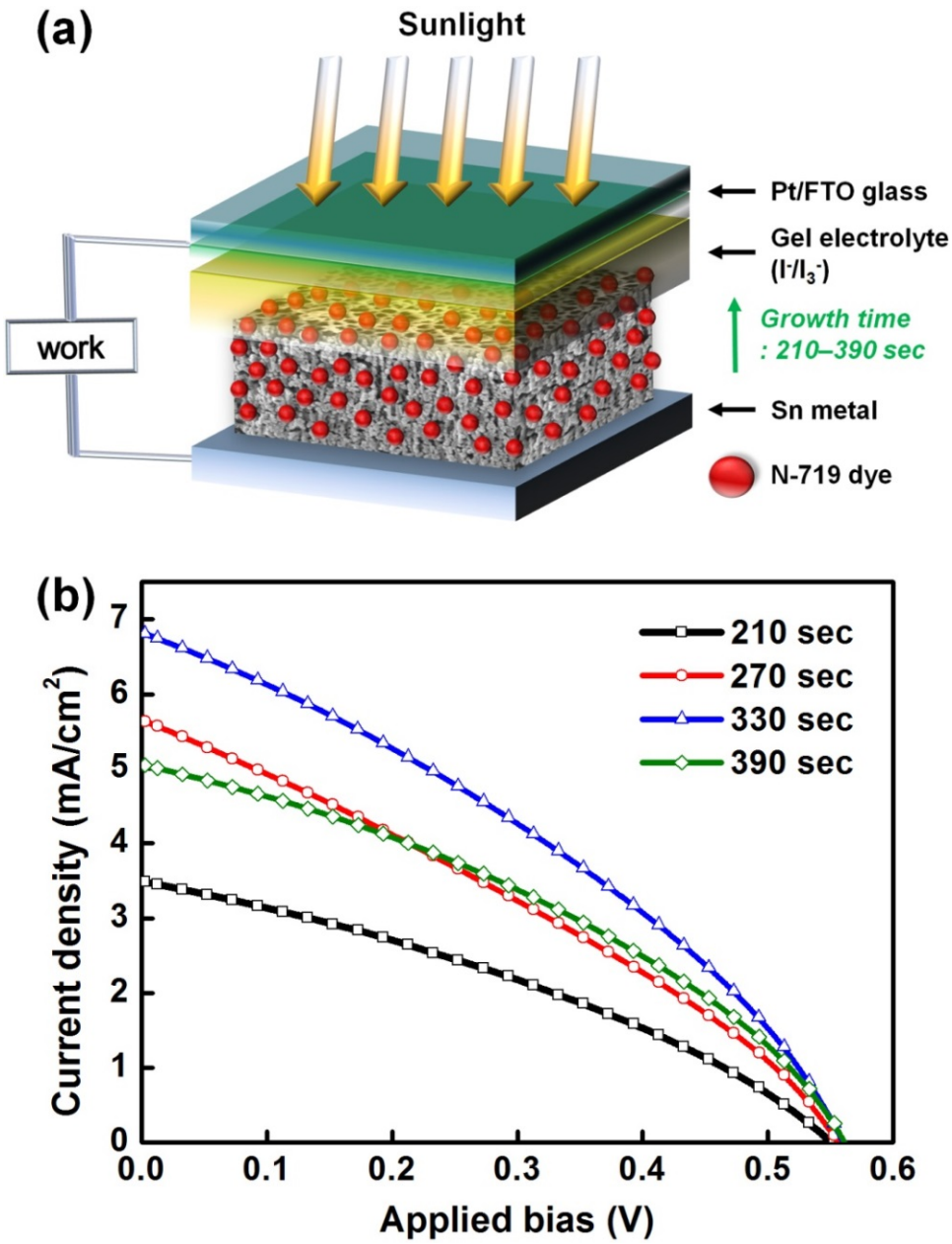


**Figure 3.7.** (a) Schematic for the device structure of the dye-sensitized solar cell employing the $SnO_2$ nanochannel electrode. (b) Photocurrent density-voltage (*J*-*V*) characteristics of the $SnO_2$ nanochannel electrodes for different anodic oxidation times under standard 1 sun illumination (light intensity: 100 mW/cm$^2$, AM 1.5G filterd).

The photocurrent density-voltage (*J-V*) characteristics for different anodic oxidation times are shown in Figure 3.7b., and photovoltaic parameters from the *J-V* curves are listed in Table 3.1 with the adsorbed amount of dye. The open-circuit voltage ($V_{oc}$) and fill factor (*FF*) did not significantly vary among the samples; however, the short-circuit photocurrent density ($J_{sc}$) strongly depended on the nanochannel thickness. This was attributed to the increased amount of adsorbed dye molecules with increasing thickness. As a result, the conversion efficiency was optimized to be 1.31% at the largest thickness. According to the literature, conversion efficiencies of DSCs with conventional $SnO_2$ nanoparticles were about 1.2-1.6% under one sun light intensity [34,35,51]. In this study, a polymer gel electrolyte was used instead of the conventional liquid-type electrolyte. Gel electrolyte is superior in stability; however, it is inferior to the liquid electrolyte considering the conversion efficiency of DSCs. In addition, owing to the opaque Sn metal substrate, the *J-V* data were obtained under back-side illumination. Compared with the results for under front-side illumination, the conversion efficiency of the DSC is generally decreased by about 40% under back-side illumination owing to the light absorption by Pt/FTO glass counter electrode and electrolyte [50]. Considering these unfavorable conditions, the obtained conversion efficiency of 1.31% in this work is a promising result. This was attributed to the vertically aligned one-dimensional structure and to the uniform nanoporous surface structure of the $SnO_2$ nanochannel electrode, which are favorable for light absorption, electron collection and interfacial contact with viscous gel electrolyte [10,14].

Furthermore, it is noteworthy that anodic oxidation time was significantly short (330 s) for achieving the optimal thickness for photovoltaics applications. Typically, for the preparation of $TiO_2$ or $SnO_2$ photoanodes in DSCs, a viscous paste should be prepared *via* many complex steps including a sol-gel reaction, hydrothermal growth, and homogenization (mixing) processes. This process takes a

| anodic oxidation time (sec) / Thickness (μm) | $J_{sc}$ (mA/cm$^2$) | $V_{oc}$ (mV) | $FF$ (%) | $\eta$ (%) | adsorbed amount of dye ($\times 10^{-8}$ mol/cm$^2$) |
|---|---|---|---|---|---|
| 210 / 4.0 | 3.92 | 535 | 33.4 | 0.70 | 6.51 |
| 270 / 6.0 | 4.99 | 575 | 36.6 | 1.05 | 9.18 |
| 330 / 7.0 | 6.51 | 570 | 35.3 | 1.31 | 9.51 |
| 390 / 6.4 | 5.65 | 550 | 35.4 | 1.10 | 9.23 |

**Table 3.1.** Summary of the *J-V* characteristics of the $SnO_2$ nanochannel electrodes for different anodic oxidation times.

long time, even up to several days. In this work, owing to the short anodic oxidation time and direct utilization of the anodized electrodes, the devices could be fabricated by simple and rapid process. Even compared with the conventional anodic oxidation of Ti, the growth rate of the $SnO_2$ nanochannel in this study was much faster. The growth rate of the conventional anodic oxidation of Ti for achieving similar pore structures was reported to be about 50-300 nm/min [10-14,52,53], which is 5 to 30 times slower compared with that of the $SnO_2$ nanochannel in this study (1.47 μm/min). In addition, by employing a gel-type electrolyte instead of the conventional liquid one, the additional step of drilling and sealing small holes in the substrate for electrolyte injection could be omitted, allowing the whole process to be simpler and faster.

### 3.3.3. Preparation and application of $SnO_2/TiO_2$ nanochannel arrays

To further enhance the photovoltaic performance of the $SnO_2$ nanochannel electrode, $TiO_2$ shell layer was deposited onto the surface of nanochannel arrays. In particular, poor dye-loading and short electron lifetime of the $SnO_2$ electrode could be enhanced by using the $TiO_2$ shell layer [34,35]. For the $TiO_2$ deposition, solution-based methods such as the well-known $TiCl_4$ treatment were not used [34,54]; rather, the ALD process was employed to avoid further annealing. Additional annealing could increase the thickness of a compact $SnO_2$ barrier at the $SnO_2$ nanochannel/Sn metal interface, resulting in the increased internal resistance [10,13]. The $TiO_2$ shell layer thickness was controlled by varying the number of ALD cycles (3, 6, 15, 30 cycles). Figure 3.8a-3.8c shows the TEM images of the $SnO_2/TiO_2$ nanochannel electrode prepared by using 15 ALD cycles. These images demonstrate that the prepared $SnO_2$ nanochannel is highly crystalline. In the high-resolution image (Figure 3.8b), the (110) and (101) lattice planes (fringe spacing ~0.34 and ~0.27 nm, respectively) corresponding to the cassiterite $SnO_2$ phase are discernible [55]. In addition, the $TiO_2$ shell layer deposited onto the surface of the

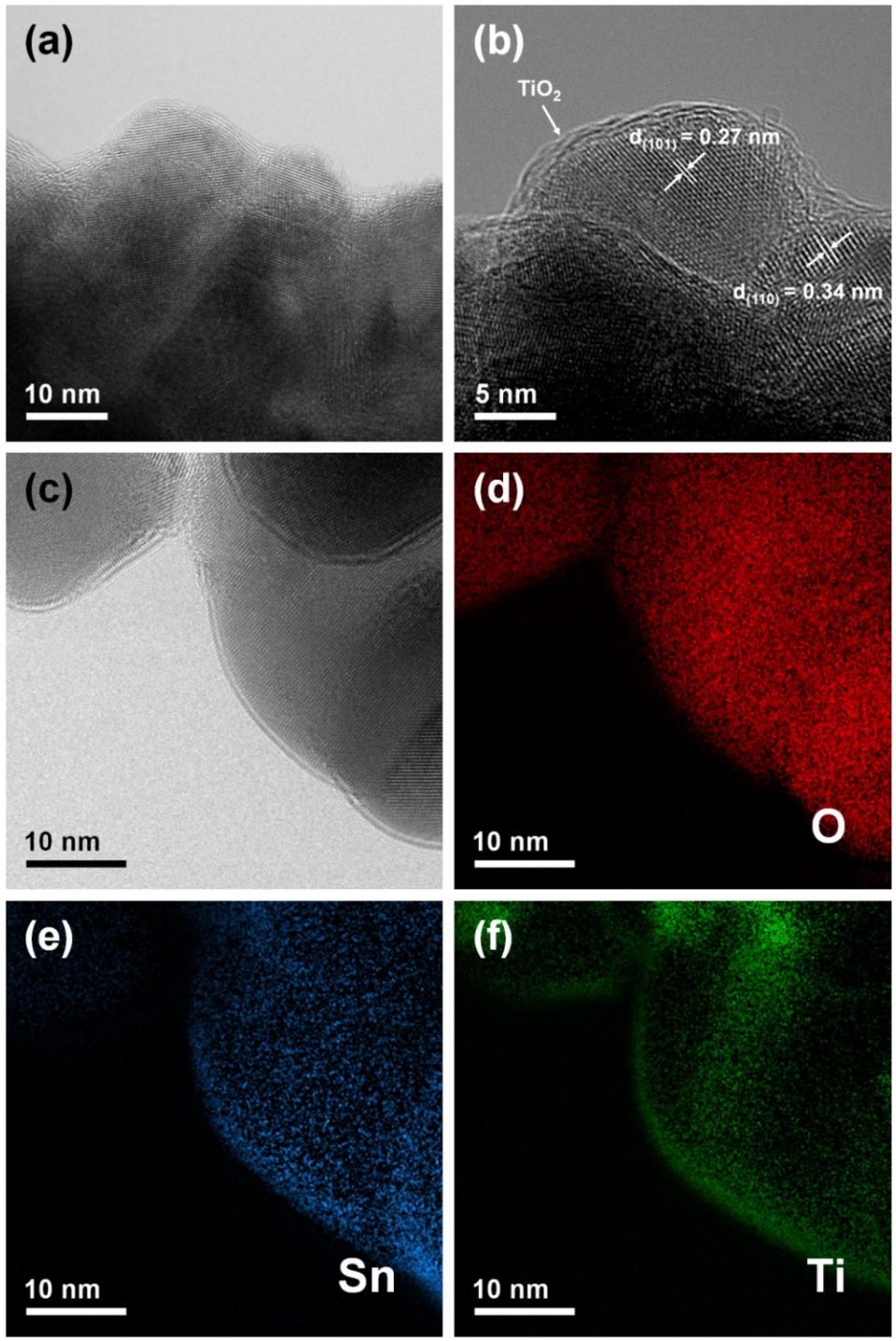


**Figure 3.8.** (a-c) TEM images of $SnO_2/TiO_2$ nanochannel arrays after 15 $TiO_2$ ALD cycles. (d-f) Elemental EF-TEM maps of O, Sn, Ti for the image in (c).

$SnO_2$ nanochannel is clearly seen. Furthermore, elemental energy-filtered (EF)-TEM maps (Figure 3.8d-3.8f) show that the $TiO_2$ shell layer is homogeneously distributed on $SnO_2$ nanochannel surface. Figure 3.9 shows the X-ray photoelectron spectroscopy (XPS) spectra of the bare $SnO_2$ and $SnO_2/TiO_2$ nanochannel electrodes. The binding energies (BE) of Sn $3d_{5/2}$ and O 1s were not noticeably different for both samples. The BEs of Sn $3d_{5/2}$ and O 1s were 486.7 eV and 530.6 eV, respectively, which corresponds to $SnO_2$ [56,57]. In addition, the measured BEs of Ti 2p (458.9 eV and 464.8 eV for $2p_{3/2}$ and $2p_{1/2}$, respectively) indicate the presence of the $TiO_2$ shell [58,59].

The dependence of *J-V* characteristics on the number of ALD cycles is shown in Figure 3.10a. The *J-V* parameters are listed in Table 3.2 with the adsorbed amount of dye. As anticipated, the adsorbed amount of dye was increased by the deposition of $TiO_2$ shell, owing to the higher isoelectric point for $TiO_2$, compared with $SnO_2$, in the dye solution [35]. However, the $SnO_2/TiO_2$ electrode prepared with 30 ALD cycles exhibited a lower adsorbed amount of dye compared with the bare sample. The reason for the reduction in the adsorbed amount of dye is that byproducts (i.e., HCl) of the reaction for $TiO_2$ ALD from $TiCl_4$ and $H_2O$ were adsorbed on the interior surface of the porous nanochannel, occupying the adsorption sites for the dye-loading. In a previous study [60], it was found that HCl molecules, produced as a byproduct during the $TiO_2$ ALD process, could chemically adsorb on vacant sites prior to the adsorption of $TiCl_4$. Furthermore, the occupancy of the adsorption sites by HCl molecules becomes much higher as the ALD cycle number increases. Therefore, it is believed that the reduction of the dye-loading in the 30 ALD-cycled electrodes can be attributed to the adsorption of byproducts, such as HCl, on the interior surface of the $SnO_2/TiO_2$ nanochannel, preventing the adsorption of the dye molecules.

As shown in Table 3.2, the $V_{oc}$ and *FF* did not significantly depend on the $TiO_2$ shell layer presence. The trend of conversion efficiency was mainly affected

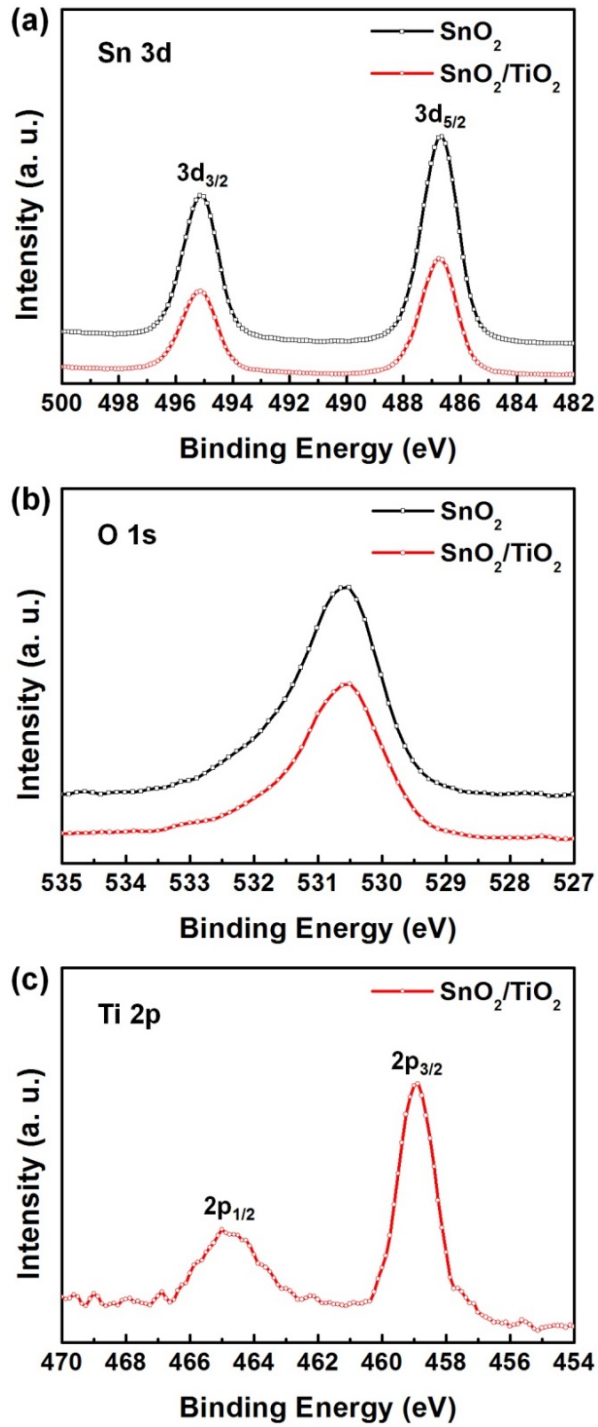


**Figure 3.9.** XPS spectra of the bare $SnO_2$ and $SnO_2/TiO_2$ nanochannel electrodes prepared with 15 ALD cycles.

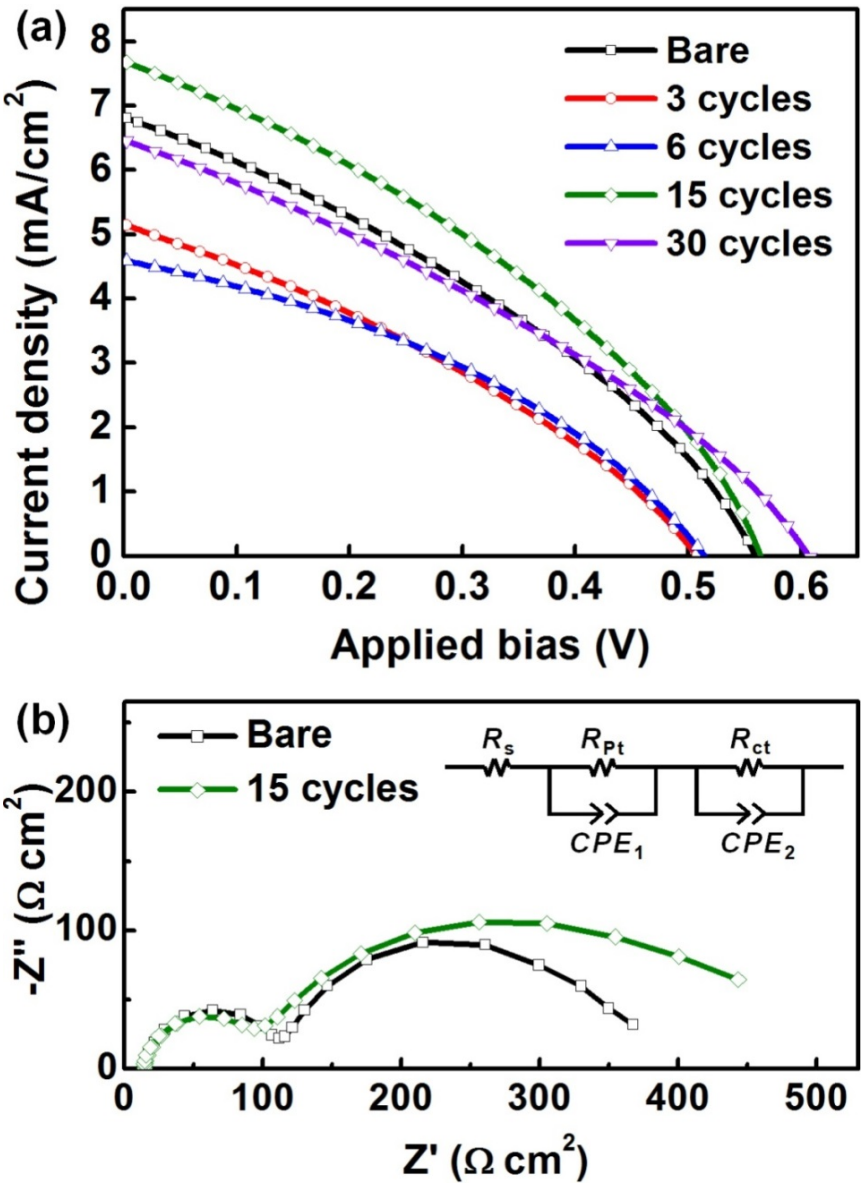


**Figure 3.10.** (a) Photocurrent density-voltage (*J-V*) characteristics of the $SnO_2/TiO_2$ nanochannel electrodes vs. the number of $TiO_2$ ALD cycles, under standard 1 sun illumination (light intensity: 100 mW/cm$^2$, AM 1.5G filterd). (b) Electrochemical impedance spectra of $SnO_2$ nanochannel electrodes under dark condition with the bias potential of -0.5 V. The inset shows the equivalent circuit model.

| ALD cycles | $J_{sc}$ (mA/cm$^2$) | $V_{oc}$ (mV) | *FF* (%) | $\eta$ (%) | adsorbed amount of dye ($\times 10^{-8}$ mol/cm$^2$) |
|---|---|---|---|---|---|
| Bare | 6.51 | 570 | 35.3 | 1.31 | 9.51 |
| 3 cycles | 5.84 | 485 | 35.3 | 1.00 | 11.78 |
| 6 cycles | 5.66 | 495 | 33.2 | 0.93 | 12.54 |
| 15 cycles | 8.55 | 570 | 32.8 | 1.60 | 11.44 |
| 30 cycles | 6.49 | 590 | 34.2 | 1.31 | 9.06 |

**Table 3.2.** Summary of the *J-V* characteristics of the $SnO_2/TiO_2$ nanochannel electrodes for different number of $TiO_2$ atomic layer deposition cycles.

by the $J_{sc}$. The electrodes prepared with 3 and 6 cycles exhibited lower $J_{sc}$ and lower conversion efficiency compared with the bare one. However, the $J_{sc}$ and conversion efficiency were enhanced and optimized in the electrode prepared with 15 cycles, where the $J_{sc}$ and conversion efficiency increased by 20% and 19%, respectively, compared with the bare electrode. Because only a sub-monolayer can be grown by one ALD cycle, several cycles are required for forming a full monolayer by ALD. Considering the density (3.5 ~ 3.9 g/cm$^3$) of amorphous $TiO_2$ and the growth-per-cycle (~0.34 Å/cycle) in our ALD process [61], about 8 to 10 cycles are required for forming the full monolayer of $TiO_2$. Therefore, 3 to 6 ALD cycles were not sufficient for forming the full monolayer of $TiO_2$. Such a sub-monolayer might unfavorably affect the photovoltaic performance, decreasing the electron injection and collection efficiency [62]. It is also believed that the thicker $TiO_2$ shell layer (15 cycles) can act as an energy barrier layer to prevent electron recombination between the $SnO_2$ electrode and the gel electrolyte [35], consequently leading to the enhanced $J_{sc}$ and conversion efficiency. The electrode with 30 cycles exhibited substantially enhanced $V_{oc}$ compared with the bare one, implying that the coated layer efficiently reduced the electron recombination [35,63]. However, the $J_{sc}$ decreased owing to the reduced adsorbed amount of dye, resulting in similar conversion efficiency compared to that of the bare electrode.

To confirm the contribution of the $TiO_2$ shell layer to the electron recombination reduction, the electrochemical impedance spectroscopy analysis was performed. Figure 3.10b shows Nyquist diagrams of DSCs in the dark condition with the bias potentials of –0.5 V. As shown in the inset, the equivalent circuit model comprises the series resistance ($R_s$), the impedance at the gel electrolyte/Pt counter electrode ($R_{Pt}$ and $CPE_1$), and the impedance at the gel electrolyte/$SnO_2$ electrode ($R_{ct}$ and $CPE_2$). The chemical capacitance ($C_\mu$) of the $SnO_2$ electrode can be obtained from $CPE_2$. The impedance spectra were fitted by using the ZView software, and the obtained parameters are listed in Table 3.3. The interfacial charge

| ALD cycles | $R_s$ ($\Omega$ cm$^2$) | $R_{ct}$ ($\Omega$ cm$^2$) | $C_\mu$ ($\mu$F/cm$^2$) | $\tau_n$ (ms) |
|---|---|---|---|---|
| Bare | 14.20 | 254.8 | 699.2 | 178 |
| 15 cycles | 13.73 | 390.9 | 612.6 | 239 |

**Table 3.3.** Parameters determined by fitting the impedance spectra of $SnO_2$ nanochannel electrodes obtained in the dark state at the bias potential of –0.5 V.

transfer resistance ($R_{ct}$) was greatly increased by adding the $TiO_2$ shell layer, implying significantly reduced electron recombination rate. The $C_{\mu}$ denotes the extent of electron accumulation in the photoanode, that is, the $SnO_2$ electrode [64]. Under identical conditions (same utilized electrolyte and same bias potential), this value decreases as the conduction band potential of the photoanode exhibits a negative shift, because the bias potential denotes the energy difference between the redox potential of the electrolyte and the Fermi level of the photoanode [65]. Because the isoelectric point of $TiO_2$ is higher compared with that of $SnO_2$, resulting in the establishment of a surface dipole directed toward the $SnO_2$ core, the conduction band potential of the $SnO_2$ electrode can exhibit a negative shift by the $TiO_2$ shell deposition [66]. Therefore, the decreased $C_{\mu}$ for the $SnO_2$ nanochannel electrode with $TiO_2$ shell indicates the negative shift of the conduction band potential. The electron lifetime, $\tau_n$, can be evaluated from the product of $R_{ct}$ and $C_{\mu}$ [67]. As shown in Table 3.3, the $\tau_n$ of the $SnO_2$ nanochannel electrode increased by 34% with the addition of the $TiO_2$ shell layer, implying that the $TiO_2$ shell layer contributed to more efficient electron collection in the photoanode.

It was reported that the conformal coating is not guaranteed only by using the typical ALD process, especially when the substrate has a nanoporous structure with high aspect ratio, such as nanotubular or nanochannel arrays [68]. The ALD process used in this work has not yet been optimized to be suitable for the $SnO_2$ nanochannel arrays. For the conformal coating of the shell layer onto the $SnO_2$ nanochannel arrays, the exposure times of precursors and purging times in the ALD process should be elaborately adjusted [68,69]. It can be expected that the conversion efficiency would be further enhanced by optimizing the ALD process for conformal coating of $TiO_2$ shells. In addition, in this work, the DSCs were illuminated from the back-side for the *J-V* characterization, due to the opaque Sn metal substrate. For higher conversion efficiency, it is desirable to prepare the $SnO_2$ nanochannel arrays onto the transparent conducting glass substrate by depositing

the Sn metal, followed by anodic oxidation process [13]. These approaches are promising for realizing highly efficient DSCs based on $SnO_2$ electrodes.

## 3.4. Conclusions

In summary, vertically aligned $SnO_2$ nanochannel arrays with large-scale uniform structure without lateral cracks were prepared by using a modified anodic oxidation process of Sn metal. These vertically aligned arrays were directly and successfully applied in quasi-solid state DSCs as photoanodes, yielding reasonable conversion efficiency under back-side illumination. Given that the anodic oxidation time was greatly short (330 s) for achieving the optimal thickness (7.0 μm) for the photovoltaic performance, the preparation process proposed in this study is a rapid and cost-effective one. In addition, the $TiO_2$ shell layer was coated by using the ALD process without further annealing. Owing to the enhanced dye-loading and increased electron lifetime with the $TiO_2$ shell, the $J_{sc}$ and conversion efficiency were increased by 20% and 19%, respectively. These results provide important insight into the development of efficient electrode structures based on the $SnO_2$ for photovoltaic applications in a simple, rapid, and low-cost fabrication process. Furthermore, the large-scale vertically aligned $SnO_2$ nanochannel arrays developed in this chapter would also be effectively applied in other electrochemical devices such as sensors, capacitors, and lithium ion batteries.

## 3.5. References


[1] Xia, Y; Yang, P.; Sun, Y.; Wu, Y.; Mayers, B.; Gates, B.; Yin, Y.; Kim, F.; Yan, H., *Adv. Mater.* **2003**, *15*, 353.

[2] Maqableh, M. M.; Huang, X.; Sung, S.-Y.; Reddy, K. S. M.; Norby, G.; Victora R. H.; Stadler, B. J. H.; *Nano Lett.* **2012**, *12*, 4102.

[3] Wu, S.; Wildhaber, F.; Vazquez-Mena, O.; Bertsch, A.; Brugger J.; Renaud, P., *Nanoscale* **2012**, *4*, 5718.

[4] Lin, J.; Liu K.; Chen, X., *Small* **2011**, *7*, 1784.

[5] Zhang, Z.; Zhang, L.; Hedhili, M. N.; Zhang, H.; Wang, P., *Nano Lett.* **2013**, *13*, 14.

[6] Alvares, S. D.; Li, C. P.; Chiang, C. E.; Schuller, I. K.; Sailor, M. J., *ACS Nano* **2009**, *3*, 3301.

[7] Mun, K.-S.; Alvarez, S. D.; Choi, W.-Y.; Sailor, M. J., *ACS Nano* **2010**, *4*, 2070.

[8] Macák, J. M.; Tsuchiya, H.; Ghicov, A.; Schmuki, P., *Electrochem. Commun.* **2005**, *7*, 1133.

[9] Mor, G. K.; Shankar, K.; Paulose, M.; Varghese, O. K.; Grimes, C. A., *Nano Lett.* **2006**, *6*, 215.

[10] Zhu, K.; Neale, N. R.; Miedaner, A.; Frank, A. J., *Nano Lett.* **2007**, *7*, 69.

[11] Zhu, K.; Vinzant, T. B.; Neale, N. R.; Frank, A. J., *Nano Lett.* **2007**, *7*, 3739.

[12] Mor, G. K.; Kim, S.; Paulose, M.; Varghese, O. K.; Shankar, K.; Basham, J.; Grimes, C. A., *Nano Lett.* **2009**, *9*, 4250.

[13] Varghese, O. K.; Paulose, M.; Grimes, C. A., *Nat. Nanotechnol.* **2009**, *4*, 592.

[14] Kim, J.-Y.; Lee, K. J.; Kang, S. H.; Shin, J.; Sung, Y.-E., *J. Phys. Chem. C* **2011**, *115*, 19979.

[15] Kongkanand, A.; Tvrdy, K.; Takechi, K.; Kuno, M.; Kamat, P. V., *J. Am. Chem. Soc.* **2008**, *130*, 4007.

[16] Guo, W.; Xue, X.; Wang, S.; Lin, C.; Wang, Z. L., *Nano Lett.*, **2012**, *12*, 2520.

[17] Tao, L.; Xiong, Y.; Liu, H.; Shen, W., *Nanoscale* **2014**, *6*, 931.

[18] Ou, J. Z.; Rani, R. A.; Ham, M.-H.; Field, M. R.; Zhang, Y.; Zheng, H.; Reece, P.; Zhuiykov, S.; Sriram, S.; Bhaskaran, M.; Kaner, R. B.; Kalantar-zadeh, K., *ACS Nano* **2012**, *6*, 4045.

[19] Wu, J.; Liu, L.; Liu, S.; Yu, P.; Zheng, Z.; Shara, M.; Zhou, Z.; Li, H.; Ji, H.; Wang, Z. M., *Nano Lett.* **2014**, *14*, 6002.

[20] Qi, H.; Wolfe, J.; Wang, D.; Fan, H. J.; Fichou, D.; Chen, Z., *Nanoscale* **2014**, *6*, 13457.

[21] Sieber, I. V.; Hildebrand, H.; Friedrich, A.; Schmuki, P., *Electrochem. Commun.* **2005**, *7*, 97.

[22] Tsuchiya, H.; Macak, J. M.; Taveira, L.; Schmuki, P., *Chem. Phys. Lett.*, **2005**, *410*, 188.

[23] Berger, S.; Jakubka, F.; Schmuki, P., *Electrochem. Commun.* **2008**, *10*, 1916.

[24] de Tacconi, N. R.; Chenthamarakshan, C. R.; Yogeeswaran, G.; Watcharenwong, A.; de Zoysa, R. S.; Basit, N. A.; Rajeshwar, K., *J. Phys. Chem. B* **2006**, *110*, 25347.

[25] Nah, Y.-C.; Ghicov, A.; Kim, D.; Berger, S.; Schmuki, P., *J. Am. Chem. Soc.* **2008**, *130*, 16154.

[26] Sieber, I. V.; Schmuki, P., *J. Electrochem. Soc.* **2005**, *152*, C639.

[27] Tsuchiya, H.; Schmuki, P., *Electrochem. Commun.* **2005**, *7*, 49.

[28] Shin, H.-C.; Dong, J.; Liu, M., *Adv. Mater.* **2004**, *16*, 237.

[29] Zaraska, L.; Czopik, N.; Bobruk, M.; Sulka, G. D.; Mech, J.; Jaskula, M., *Electrochim. Acta* **2013**, *104*, 549.

[30] Lee, J.-W.; Park, S.-J.; Choi, W.-S.; Shin, H.-C., *Electrochim. Acta* **2011**, *56*, 5919.

[31] Palacios-Padros, A.; Altomare, M.; Tighineanu, A.; Kirchgeorg, R.; Shrestha, N. K.; Diez-Perez, I.; Caballero-Briones, F.; Sanz, F.; Schmuki, P., *J. Mater. Chem. A* **2014**, *2*, 915.

[32] Green, A. N. M.; Palomares, E.; Haque, S. A.; Kroon, J. M.; Durrant, J. R., *J. Phys. Chem. B* **2005**, *109*, 12525.

[33] Ramasamy, E.; Lee, J., *J. Phys. Chem. C* **2010**, *114*, 22032.

[34] Kay, A.; Grätzel, M., *Chem. Mater.* **2002**, *14*, 2930.

[35] Kim, J.-Y.; Kim, J. Y.; Lee, D. K.; Kim, B. S.; Kim, H.; Ko, M. J., *J. Phys. Chem. C* **2012**, *116*, 22759.

[36] Tian, H.; Liu, P.-H.; Meng, F.-S.; Gao, E.; Cai, S., *Synth. Met.* **2011**, *121*, 1557.

[37] Subbaiyan, N. K.; Maligaspe, E.; D'Souza, F., *ACS Appl. Mater. Interfaces* **2011**, *3*, 2368.

[38] Pijpers, J. J. H.; Koole, R.; Evers, W. H.; Houtepen, A. J.; Boehme, S.; Donega, C. de M.; Vanmaekelbergh, D.; Bonn, M., *J. Phys. Chem. C* **2010**, *114*, 18866.

[39] Ramasamy, E.; Lee, J., *Energy Environ Sci.* **2011**, *4*, 2529.

[40] Hossain, M. A.; Yang, G.; Parameswaran, M; Jennings, J. R.; Wang, Q., *J. Phys. Chem. B* **2010**, *114*, 21878.

[41] Teh, J. J.; Guai, G. H.; Wang, X.; Leong, K. C.; Li, C. M.; Chen, P., *J. Renewable Sustainable Energy* **2013**, *5*, 023120.

[42] Ito, S.; Nazeeruddin, K.; Liska, P.; Comte, P.; Charvet, R.; Péchy, P.; Jirousek, M.; Kay, A.; Zakeeruddin, S. M.; Grätzel, M., *Prog. Photovolt: Res. Appl.* **2006**, *14*, 589.

[43] Park, J.; Koo, H.-J.; Yoo, B.; Yoo, K.; Kim, K.; Choi, W.; Park, N.-G., *Sol. Energy Mater. Sol. Cells* **2007**, *91*, 1749.

[44] Prakasam, H. E.; Shankar, K.; Paulose, M.; Varghese, O. K.; Grimes, C. A., *J. Phys. Chem. C* **2007**, *111*, 7235.

[45] Mohapatra, S. K.; John, S. E.; Banerjee, S.; Misra, M., *Chem. Mater.* **2009**, *21*, 3048.

[46] *Pattern* No. 41-1445, JCPDS **1996**.

[47] Russo, P. A.; Donato, N.; Leonardi, S. G.; Baek, S.; Conte, D. E.; Neri, G.; Pinna, N., *Angew. Chem. Int. Ed.* **2012**, *51*, 11053.

[48] Cullity, B. D. *Elements of X-Ray Diffraction, 2nd Ed.*; Addison-Wesley Pub. Co.: Reading, Mass. **1978**.

[49] Ghicov, A.; Albu, S. P.; Hahn, R.; Kim, D.; Stergiopoulos, T.; Kunze, J.; Schiller, C.-A.; Falaras, P.; Schmuki, P., *Chem. Asian J.*, **2009**, *4*, 520.

[50] Ito, S.; Ha, N.-L. C.; Rothenberger, G.; Liska, P.; Comte, P.; Zakeeruddin, S. M.; Péchy, P.; Nazeeruddin, M. K.; Grätzel, M., *Chem. Commun.* **2006**, 4004.

[51] Lee, C.; Lee, G.-W.; Kang, W.; Lee, D.-K.; Ko, M. J.; Kim, K.; Park, N.-G., *Bull. Korean Chem. Soc.* **2010**, *31*, 3093.

[52] Paulose, M.; Shankar, K.; Yoriya, S.; Prakasam, H. E.; Varghese, O. K.; Mor, G. K.; Latempa, T. A.; Fitzgerald, A.; Grimes, C. A., *J. Phys. Chem. B* **2006**, *110*, 16179.

[53] Sreekantan, S.; Saharudin, K. A.; Lockman, Z.; Tzu, T. W., *Nanotechnology* **2010**, *21*, 365603.

[54] Sommeling, P. M.; O'Regan, B. C.; Haswell, R. R.; Smit, H. J. P.; Bakker, N. J.; Smits, J. J. T.; Kroon, J. M.; van Roosmalen, J. A. M., *J. Phys. Chem. B* **2006**, *110*, 19191.

[55] Wang, C.; Zhou, Y.; Ge, M.; Xu, X.; Zhang, Z.; Jiang, J. Z., *J. Am. Chem. Soc.* **2010**, *132*, 46.

[56] Fujihara, S.; Maeda, T.; Ohgi, H.; Hosono, E.; Imai, H.; Kim, S.-H., *Langmuir* **2004**, *20*, 6476.

[57] Renard, L.; Brotz, J.; Fuess, H.; Gurlo, A.; Riedel, R.; Toupance, T., *ACS Appl. Mater. Interfaces* **2014**, *6*, 17093.

[58] Choudhury, T.; Saied, S. O.; Sullivan, J. L.; Abbott, A. M., *J. Phys. D* **1989**, *22*, 1185.

[59] Gonbeau, D.; Guimon, C.; Pfister-Guillouzo, G.; Levasseur, A.; Meunier, G.; Dormoy, R., *Surf. Sci.* **1991**, *254*, 81.

[60] Park, I.; Leem, J.; Lee, H.-Y.; Min, Y.-S., *Bull. Korean Chem. Soc.* **2013**, *34*, 519.

[61] Triani, G.; Evans, P. J.; Mitchell, D. R. G.; Attard, A. J.; Finnie, K. S.; James, M.; Hanley, T.; Latella, B.; Prince, K. E.; Bartlett, J. Atomic Layer Deposition of $TiO_2/Al_2O_3$ Films for Optical Applications. *Advances in Thin-Film Coatings for Optical Applications II (Proceedings of SPIE)*; Fulton, M. L., Kruschwitz, J. D., Eds.; SPIE: Bellingham, WA, **2005**; Vol. 5870, p 587009.

[62] Law, M.; Greene, L. E.; Radenovic, A.; Kuykendall, T.; Liphardt, J.; Yang, P., *J. Phys. Chem. B* **2006**, *110*, 22652.

[63] Diamant, Y.; Chappel, S.; Chen, S. G.; Melamed, O.; Zaban, A., *Coord. Chem. Rev.* **2004**, *248*, 1271.

[64] Fabregat-Santiago, F.; Bisquert, J.; Palomares, E.; Otero, L.; Kuang, D.; Zakeeruddin, S. M.; Grätzel, M., *J. Phys. Chem. C* **2007**, *111*, 6550.

[65] Koops, S. E.; O'Regan, B. C.; Barnes, P. R. F.; Durrant, J. R., *J. Am. Chem. Soc.* **2009**, *131*, 4808.

[66] Zhang, Q.; Cao, G., *Nano Today* **2011**, *6*, 91.

[67] Fabregat-Santiago, F.; Garcia-Belmonte, G.; Mora-Seró, I.; Bisquert, J., *Phys. Chem. Chem. Phys.* **2011**, *13*, 9083.

[68] Lee, H.-Y.; An, C. J.; Piao, S. J.; Ahn, D. Y.; Kim, M.-T.; Min, Y.-S., *J. Phys. Chem. C* **2010**, *114*, 18601.

[69] Marichy, C.; Bechelany, M.; Pinna, N., *Adv. Mater.* **2012**, *24*, 1017.

# Chapter 4. Wrinkled silica/titania nanoparticles for light scattering in mesorporous $TiO_2$ photoelectrode

## 4.1. Introduction

Solar to electric energy conversion has been considered as one of the most promising candidate to replace the conventional energy production based on fuels. Among various kinds of photovoltaic systems, Si and thin film solar cells stand out in the market these days due to their fine performance and long-term stability. However, their high fabrication costs hinder the commercial utilization in large scale, and therefore many other types of photovoltaic devices based on organic and low-cost inorganic materials are under intensive investigations. Among them, dye-sensitized solar cells (DSCs) have received great attention due to their excellent performance and reliability [1-4]. Generally, DSCs are based on dye-adsorbed nanostructured $TiO_2$ photoelectrode, which is composed of $TiO_2$ nanoparticles of around 20 nm size. The large surface area resulting from this nanostructure is the key for the high performance of DSCs, because this allows large amount of dye adsorption which enables enhanced light harvesting. However, the 20 nm dimension which cause negligible amount of light scattering in visible light region leaves considerable portion of incident photons to pass through the photoelectrode without contributing to the solar-to-electric energy conversion [5-8].

In order to maximize the incident light utilization, there have been many reports on light scattering particles designed for DSCs. Generally, structures with dimension comparable to the wavelength of incident light are known to efficiently scatter the photons [7]. Therefore, a few hundreds of nanometer sized scatterers such as cavities and photonic crystals were frequently employed [8-14], and $TiO_2$

nanoparticles with similar dimension have generally shown enhanced performances [15-25]. These light scattering $TiO_2$ particles were incorporated within the photoelectrode by embedding them into the mesoscopic $TiO_2$ layer [17-20] or forming an additional layer composed of light scatterers [21-25]. Moreover, various attempts to increase the surface area of the scattering particles were made [18,19,23-25]. On the other hand, there were approaches to tune the scattering properties of the $TiO_2$ scattering particles by compositional modifications, and silica/titania core/shell nanoparticles received great attention due to the enhanced light scattering property compared to bare $TiO_2$ due to the difference in refractive indices between silica and titania [26,27]. Based on this knowledge, aerogel based silica/titania photoanodes and size controlled silica/titania scatteres with enhanced light harvesting properties for DSCs also have been reported [19,20].

Among the various methods to control the morphologies of silica nanoparticles, wrinkled silica nanoparticles have drawn great interests due to the usefulness of their fibrous morphology and capability for application in various fields [28-33]. Moreover, Moon et al. reported that the formation of wrinkled silica nanoparticles is based on Winsor III system [34,35]. Based on the understanding on mechanism, they developed methods to control interwrinkle distance within the nanoparticle by adding alcohols with various alkyl groups as co-solvent. Inspired by the large surface area and ease of morphology control during the synthesis, we herein report wrinkled silica/titania nanoparticles as scattering materials in DSCs. In contrast to the former report, wrinkled silica nanoparticles with different interwrinkle distances were synthesized by varying the amount of co-solvent (1-pentanol), and this method resulted in a high and reliable control over morphologies of the particles. After coating the particles with $TiO_2$ shell, the fabricated wrinkled silica/titania nanoparticles were incorporated into the photoanode of DSCs for efficient light scattering. In addition to the enhancement in photocurrent density and energy conversion efficiency, further observations on the

dependence of spectral characteristics on the interwrinkle distances were made.

## 4.2. Experimental section

### 4.2.1. Synthesis of wrinkled silica/titania nanoparticles

Wrinkled silica nanoparticles were synthesized in a bicontinuous microemulsion phase containing water and oil by hydrolysis and condensation of tetraethylorthosilicate (TEOS) using hexadecyltrimethylammonium bromide (CTAB) as surfactant. 1 g of CTAB and 600 mg of urea were dissolved in 30 mL of distilled water, and then, various amounts of 1-pentanol in 30 mL cyclohaxane was added, which was followed by 30 min stirring of the mixture solution at room temperature. Under vigorous stirring, 1.25 g (6 mmol) of TEOS was added dropwise to the mixture solution, and the reaction temperature was raised to 70 °C immediately and maintained for 16 h. The white products were washed with ethanol by centrifugation, which was conducted three times at 13,000 rpm for 10 min each, and the products were re-dispersed in ethanol. In order to remove the remaining CTAB in the product, 10% HCl aqueous solution (1:10 vol. ratio to ethanol) was added and the mixture was stirred for overnight. Then the products were purified by centrifugation, and 200 mg of them were dispersed in 200 mL of mixed solution of acetonitrile and ethanol of which composition were 1:1 on volumetric ratio, and 2 mL of ammonia solution was added. Then 20 mL of mixture of acetonitrile and ethanol (1:1 vol.) containing various amounts of $Ti(OBu)_4$ was injected. The temperature of the solution was maintained at 25 ℃ for 2 h and the final product was obtained by three times of centrifugation (13,000 rpm for 10 min each).

### 4.2.2. Synthesis of spherical silica/titania and titania nanoparticles

Spherical silica/titania and titania particles were prepared based on seed growth

method. For the synthesis of silica/titania, silica cores were prepared by stober method. 1.2 mL of TEOS was dissolved in mixture of 1-propanol and 1-butanol (1:1 vol. ratio), and 6 mL of ammonia solution, and 2 mL of distilled water were added. After 6 h, white products were formed, and they were dispersed in ethanol after purification by centrifugation. Then the titania shell was coated on silica particle by the same method used for the synthesis of wrinkled silica/titania particles. For the preparation of the spherical titania nanoparticles, 1.5 mL of $Ti(OBu)_4$ dissolved in 60 mL of mixture solution (acetonitrile and ethanol by 1:1 vol. ratio) was added to the 200 mL mixture solution containing 2 mL of ammonia solution. After 2 h, ammonia solution (0.5 mL), $Ti(OBu)_4$ (1.0 mL) in the mixed acetonitrile and ethanol solution (1:1 vol.) were added to increase the size of titania particles. The products were purified by centrifugation after 2 more hours of reaction.

### 4.2.3. Preparation of dye-sensitized solar cells

For the fabrication of mesocopic $TiO_2$ photoanode with embedded scattering particles, commercial paste containing ~20 nm sized $TiO_2$ nanoparticles (DSL 18NR-T, Dyesol) was dispersed in ethanol. Based on the measurements of $TiO_2$ content in the paste (20.7 wt%) by Grätzel and his colleagues [10], wrinkled and spherical silica/titania nanoparticles and spherical titania nanoparticles were mixed with the ethanolic $TiO_2$ paste solution with the amount of scatterer to be 10 wt% after removing solvents and organic binders. After 5 min (2 sec on - 2 sec off for 10 min) of ultrasonication for uniform dispersion of scattering nanoparticles, ethanol in the mixture solution was removed by rotary evaporation, resulting in a viscous paste as a final product. For the exact evaluation of embedded scattering particles, paste without scatterers was prepared by dispersion of commercial $TiO_2$ paste in ethanol followed by evaporation of ethanol. Then the paste was cast on the FTO glass with $TiO_2$ blocking layer by doctor blading method followed by heat

treatment at 500 °C in air. The prepared electrodes were immersed into an ethanolic solution containing 0.5 mM N719 dye (Ru 535-bisTBA, Solaronix) solution for 48 h at 30 °C for the positioning of dye molecules on the semiconductor oxide surface. Counter electrodes were prepared by spin coating of 50 mM $H_2PtCl_6$ containing 2-propanol solution on FTO glass and following thermal treatment at 400 °C for 20 min in air. For the cell assembly, 50 μm thick thermoplastic sealants (Surlyn, DuPont) were used, and the electrolyte containing $I_3^-/I^-$ redox couple was injected through the pre-drilled holes. The exact composition of the electrolyte was 0.6 M 1-butyl-3-methylimidazolium iodide, 30 mM $I_2$, 0.1 M guanidinium thiocyanate, and 0.5 M 4-*tert*-butylpyridine in a mixture solution of acetonitrile and valeronitrile with vol. ratio of 85:15.

### 4.2.4. Physicochemical characterization of materials and photoelectrochemical analyses

The morphologies of synthesized particles were characterized by using a scanning electron microscope (SEM; Hitachi S-4300) and a transmission electron microscope (TEM; Hitachi-7400). More detailed TEM images and elemental analyses were performed by using analytical TEM (FEI Tecnai F20) equipped with an energy dispersive spectroscopy (EDS) system. UV-Vis absorbance spectra were obtained with Beckman DU 650 spectrophotometer and diffuse reflectance were measured by using Jasco V-670 spectrophotometer with an integrating sphere. X-ray diffraction (XRD) patterns were obtained by using Rigaku D/MAX 2500 V with Cu Kα radiation source, and Brunauer-Emmett-Teller (BET) analyses were performed with Micrometrics ASAP 2420. Photoelectrochemical evaluation of the DSCs were performed by obtaining photocurrent density-voltage curve under incident AM 1.5G light (intensity: 100 mW/cm$^2$) by using a solar simulator (XIL model 05A50KS source measure units equipped with an AM 1.5G filter) and a potentiostat (Solartron 1480). Incident photon-to-current efficiency (IPCE) spectra

were obtained by McScience K3100.

## 4.3. Results and discussion

### 4.3.1. Synthesis and morphology control of silica/titania nanoparticles

Figure 4.1 shows the SEM images of the wrinkled silica nanoparticles with various interwrinkle distances due to the different amounts of co-solvent (1-pentanol) added during the synthesis. For the preparation of nanoparticles shown in Figure 4.1a-4.1d, 0.16 mL, 0.33 mL, 0.65 mL, and 1.3 mL of 1-pentanol were added, respectively. The resulting morphologies of the wrinkled silica nanoparticles indicate that an increased amount of co-solvent widens the interwrinkle distances. During the synthesis of wrinkled silica nanoparticles, the reaction mixture forms a Winsor III system, in which 3 phases coexist; oil (nonpolar solvent) at the top, bicontinuous microemulsion (composed of mostly surfactant and about equal amount of water and oil) in the middle, and water (polar solvent) at the bottom. [34,35] When alcohols with long alkyl chain (which is not miscible with water) such as 1-pentanol are introduced into the reaction mixture, volume fraction of oil in the microemulsion phase increases. This results in the change in phase behavior toward Winsor II system, where water-in-oil microemulsion and oil layer exist together. Therefore, as the amount of added 1-pentanol increases, portion of oil phases in the reaction mixture gets higher. Since the oil to water ratio has positive correlation to interwrinkle distances according to a previous report [34], the observations on the morphologies of wrinkled silica nanoparticles seem to be reasonable. Among the 4 synthesis conditions, the 0.16 mL and 0.65 mL 1-pentanol added cases were selected for the investigations on the effects of interwrinkle distance on scattering properties in visible light region efficiently. That is, conditions resulting in a siginificant difference in wrinkled morphology but maintaining the spherical structure of the particles close to sphere were chosen.

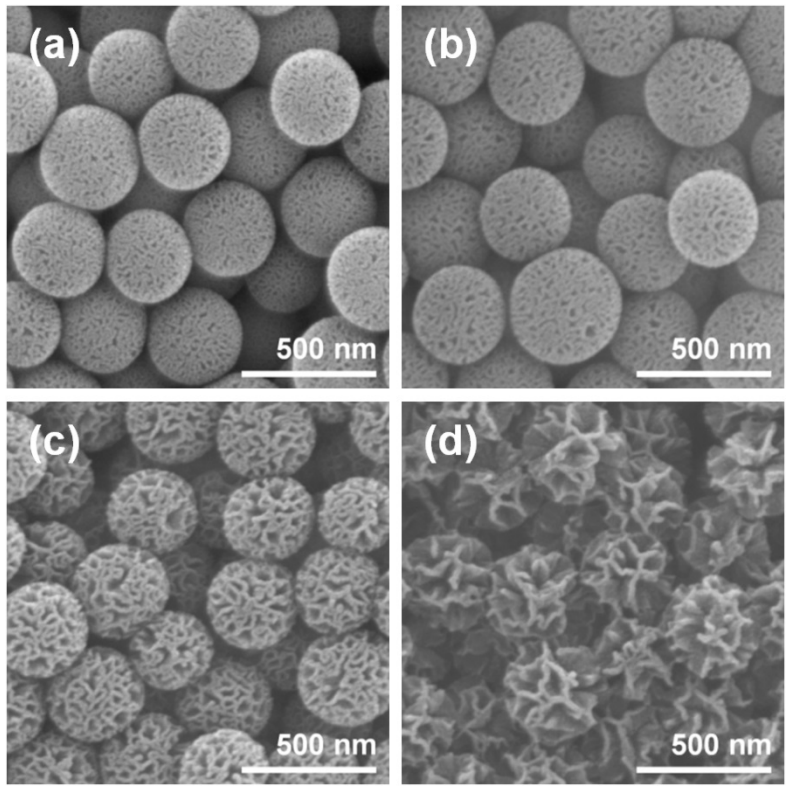


**Figure 4.1.** SEM images of wrinkled silica nanoparticles with different interwrinkle distances controlled by the amount of co-solvent (1-pentanol); (a) 0.16 mL, (b) 0.33 mL, (c) 0.65 mL, and (d) 1.30 mL.

Wrinkled silica nanoparticles synthesized by the former and latter experimental conditions were named as narrowly wrinkled silica nanoparticles (NWSNs) and widely wrinkled silica nanoparticles (WWSNs), respectively.

For the formation of $TiO_2$ shell on the silica nanoparticle surface, hydrolysis and condensation of $Ti(OBu)_4$ on silica surface was used. The concentration of $Ti(OBu)_4$ was varied for the formation of $TiO_2$ shell with different thicknesses. Figure 4.2 shows the SEM images of NWSNs (Figure 4.2a) and $TiO_2$ coated NWSNs prepared with different amount of added $Ti(OBu)_4$ to the reaction mixture; 0.5 mL (Figure 4.2b), 1.0 mL (Figure 4.2c), 2.0 mL (Figure 4.2d). As the amount of $Ti(OBu)_4$ increased, the $TiO_2$ shell got thicker and completely filled the wrinkles of NWSNs in the case of 2.0 mL $Ti(OBu)_4$ (Figure 4.2d). Considering that the main target application of this silica/titania scattering particles is DSCs, the thicker $TiO_2$ shell is preferred for the enhanced electron transport. Since the conduction band position of silica is close to the vacuum level, excitons in $TiO_2$ lattice cannot move into the silica but are only able move within $TiO_2$, and thus thicker shells provide wider electron pathways with lower resistance. Therefore, further $TiO_2$ formations were performed by adding 1.0 mL of $Ti(OBu)_4$, because this condition gives relatively thick $TiO_2$ shell without damaging the wrinkled structure significantly.

Then, the effects of thermal annealing on the nanoparticles were characterized, because high temperature heat treatment is inevitable for the preparation of photoelectrode for DSCs. SEM images in Figure 4.3 shows the morphologies of spherical silica/titania nanoparticles (SSTNs; Figure 4.3a and 4.3b), spherical titania nanoparticles (STNs; Figure 4.3c and 4.3d), narrowly wrinkled silica/titania nanoparticles (NWSTNs; Figure 4.3e and 4.3f), and widely wrinkled silica/titania nanoparticles (WWSTNs; Figure 4.3g and 4.3h) before (left side of Figure 4.3) and after (right side of Figure 4.3) heat treatment at 500 °C for 30 min in air. For all cases, there was no significant change in morphologies of the

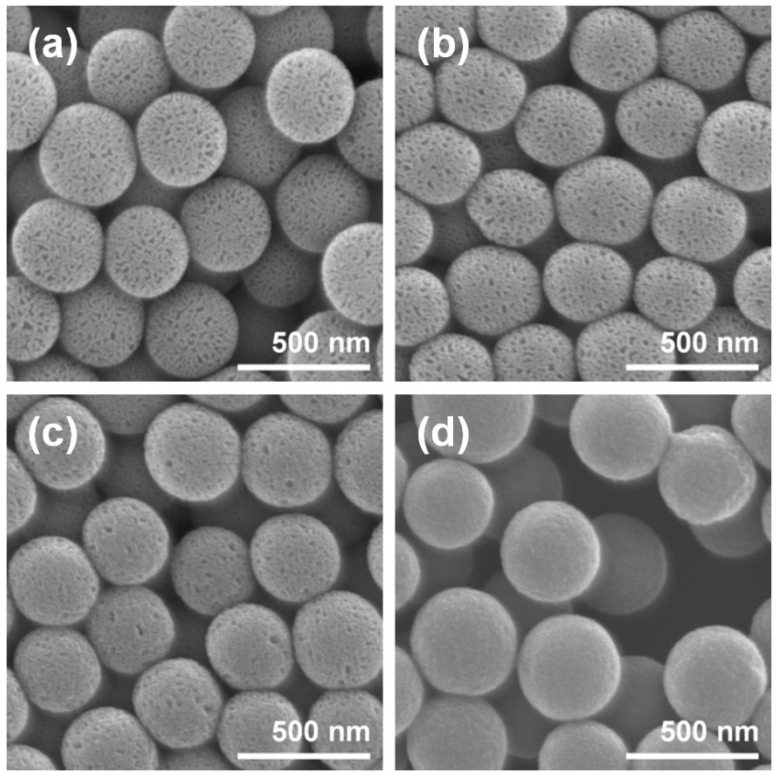


**Figure 4.2.** SEM images of narrowly wrinkled silica nanoparticles (a) and the same particles with $TiO_2$ shell on the surface (b-d), of which thickness varied by different amount of $TiO_2$ precursor ($Ti(OBu)_4$); (b) 0.5 mL, (c) 1.0 mL, and (d) 2.0 mL.

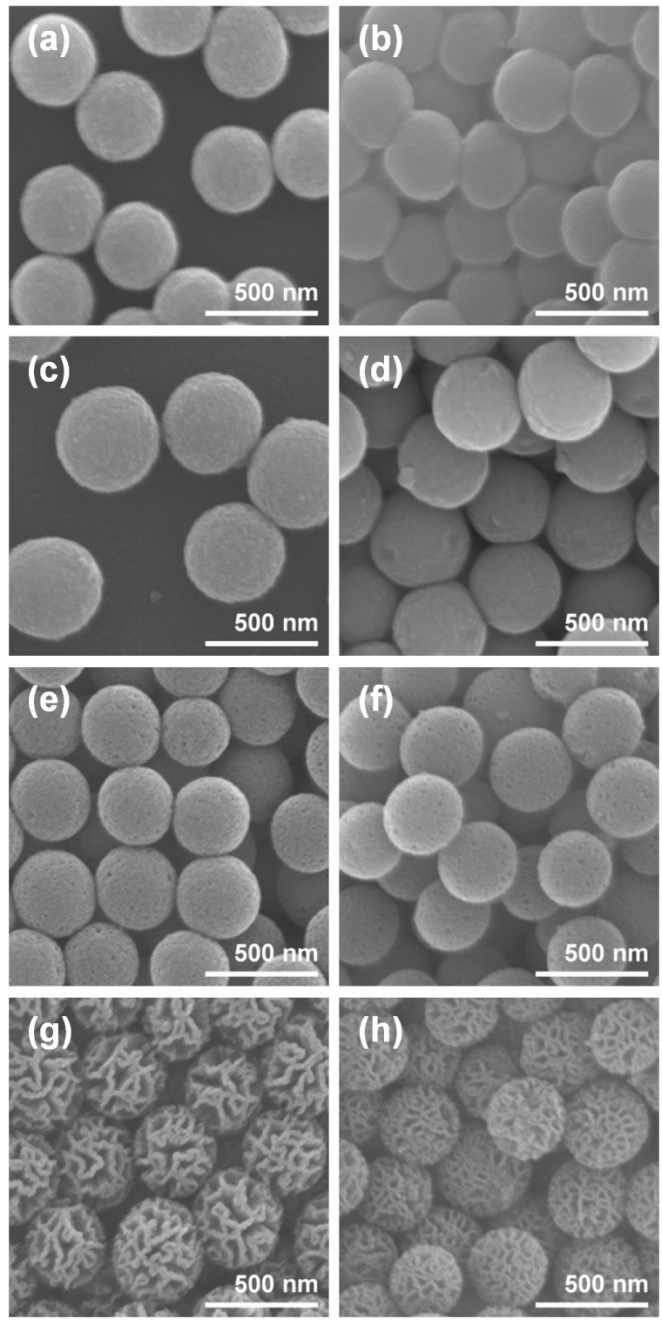


**Figure 4.3.** SEM images of scattering particles before (a,c,e,g) and after (b,d,f,h) heat treatment at 500 °C in air. (a,b) spherical silica/titania, (c,d) spherical titania, (e,f) narrowly wrinkled silica/titania, and (g,h) widely wrinkled silica/titania nanoparticles.

nanoparticles, indicating that the particles are sufficiently stable during the heat treatment.

Moreover, the effects of $TiO_2$ shell coating and heat treatment were confirmed by additional characterization based on TEM analyses. Figure 4.4a-4.4f show the morphologies of the NWSNs, WWSNs, NWSTNs, WWSTNs, thermally annealed NWSTNs, and WWSTNs after heat treatment, respectively. From these images, it is clear that the effect of $TiO_2$ coating on silica nanoparticles and heat treatment on the wrinkled structure is negligible. Figure 4.5 shows the scanning transmission electron microscope (STEM) images of SSTN (Figure 4.5a), NWSTN (Figure 4.5b), WWSTN (Figure 4.5c) and corresponding elemental EDS mapping results on O, Ti, and Si. The STEM images and EDS maps clearly present that the $TiO_2$ shells on silica surface are very uniform and do not affect the initial morphology of the silica nanoparticles.

### 4.3.2. Materials properties and spectral characteristics of silica/titania nanoparticles

Figure 4.6 shows the XRD patterns of the WWSTNs, NWSTNs, SSTNs, and STNs. In all particles, anatase $TiO_2$ peaks are apparent (JCPDS 21-1272) though the $TiO_2$ peaks in wrinkled nanoparticles are very broad. This indicates that the $TiO_2$ shells in WWSTNs and NWSTNs have very small crystallite sizes, which is unfavorable for charge transport due to the high density of trap sites in grain boundaries. In contrast, $TiO_2$ shells in SSTNs showed relatively sharper anatase $TiO_2$ peaks. The crystallite sizes of $TiO_2$ in of WWSTNs, NWSTNs, SSTNs, and STNs were calculated by (101) peak using Scherrer's equation, and the results were 3.90 nm, 4.05 nm, 16.42 nm, and 34.66 nm, respectively. The presence of amorphous silica in WWSTNs, NWSTNs, and SSTNs were observed by the very broad peak at 2-theta position of around 20 to 30 (JCPDS 42-0005).

In DSCs, surface area of the photoanode is a critical factor for a high

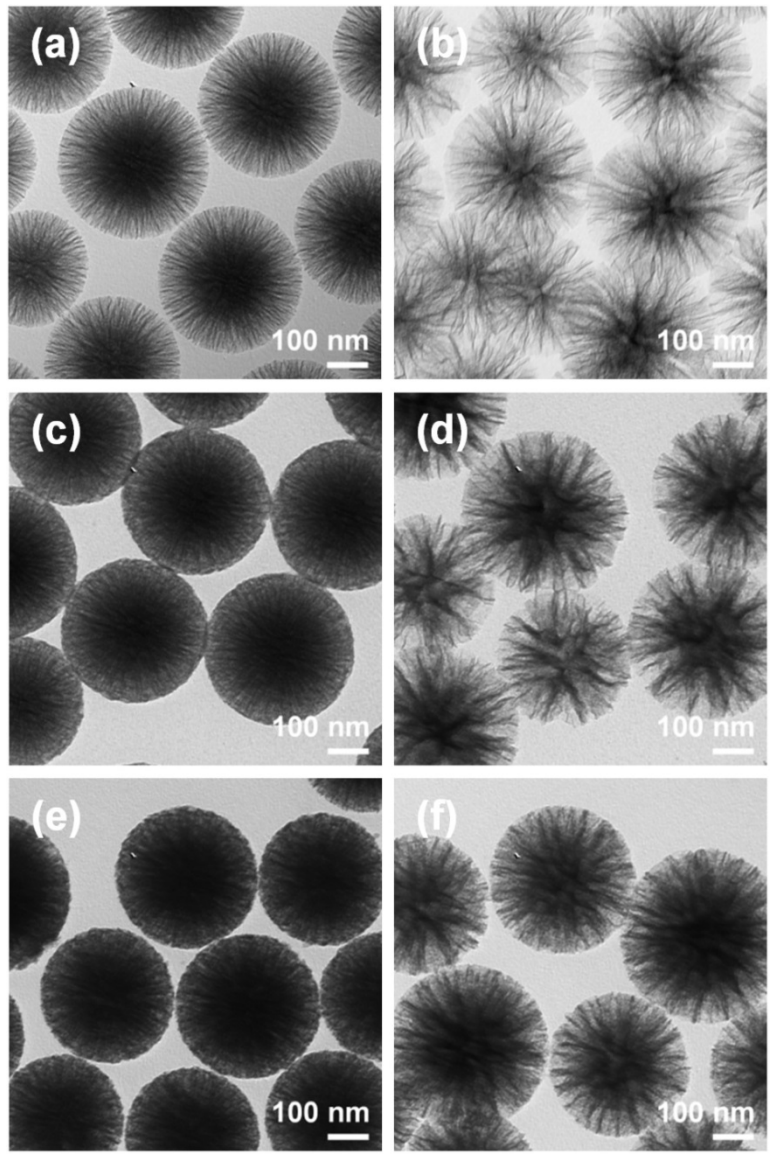


**Figure 4.4.** TEM image of (a) narrowly and (b) widely wrinkled silica nanoparticles, and (c,e) narrowly and (d,f) widely wrinkled silica/titania nanoparticles (c,d) before and (e,f) after heat treatment at 500 °C in air.

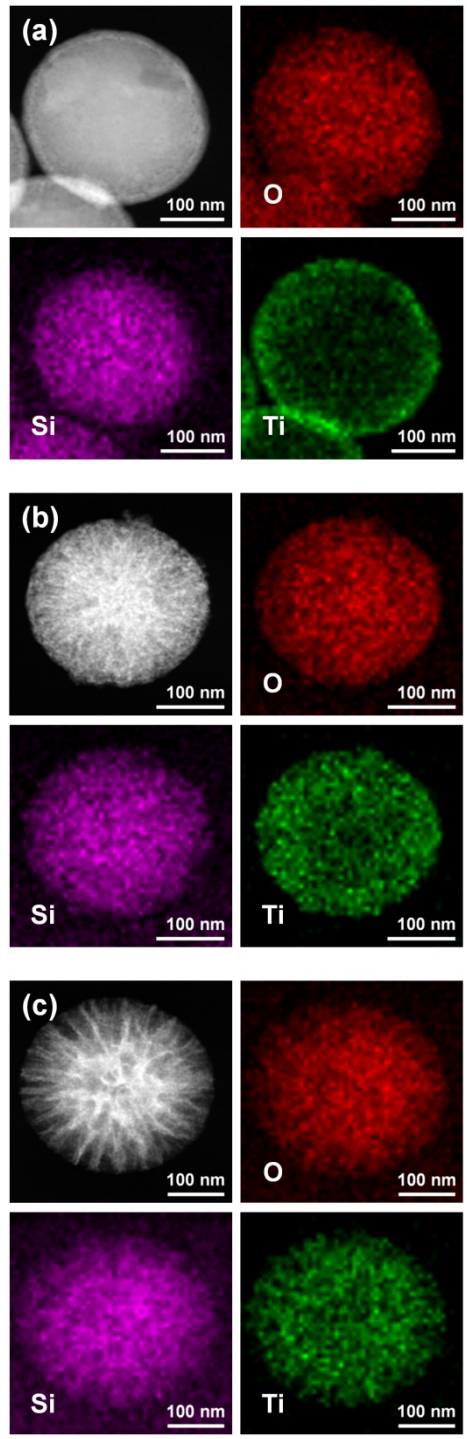


**Figure 4.5.** STEM images and corresponding elemental O, Si, and Ti EDS maps of (a) SSTNs, (b) NWSTNs, and (c) WWSTNs.

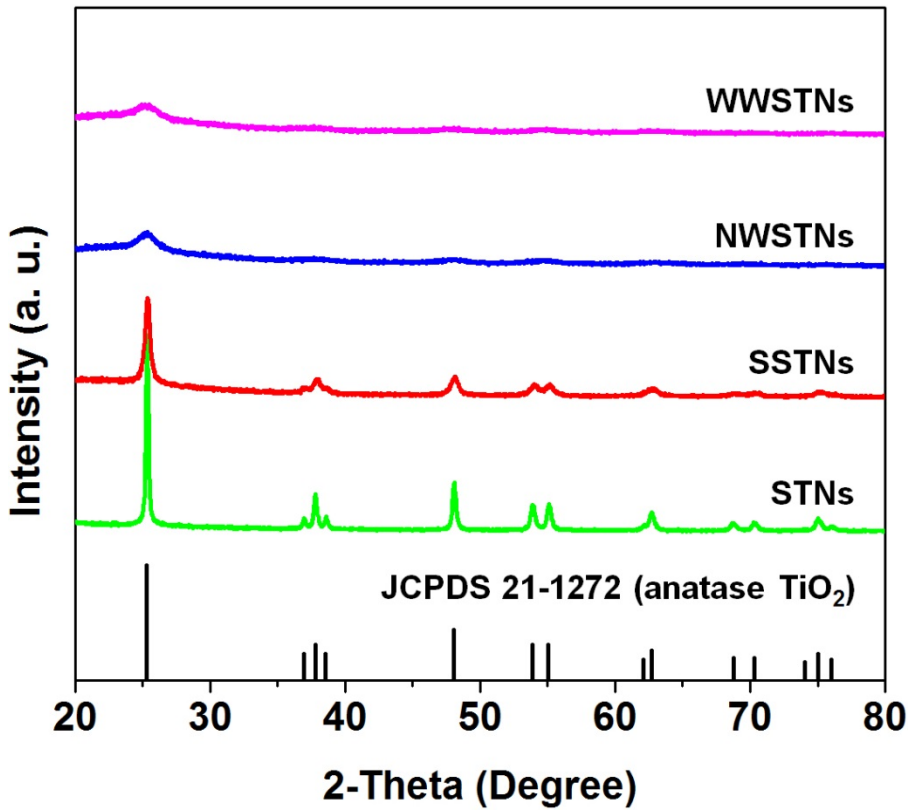


**Figure 4.6.** XRD patterns of WWSTNs, NWSTNs, SSTNs, and STNs after 500 °C heat treatment in air.

performance. Because light absorbing dye molecules adsorb on the oxide semiconductor surface, larger surface area is favored. Therefore, specific surface areas of the synthesized scattering particles were characterized and compared with that of 20 nm sized commercial $TiO_2$ nanoparticles (P25, Degussa). Figure 4.7 shows the $N_2$ adsorption and desorption isotherms of P25s, SSTNs, STNs, NWSTNs, WWSTNs, NWSNs, and WWSNs. The BET surface areas of these nanoparticles were calculated based on these results, and the values are displayed in Table 4.1 and 4.2. As expected from the analyses on their morphologies, wrinkled structure (> 400 $m^2/g$) provided more than 20 times larger surface area compared to the spherical structure (< 20 $m^2/g$). By comparing the specific surface areas of wrinkled silica nanoparticles before and after $TiO_2$ coating, it was verified that $TiO_2$ shell lowered the surface area to 2/3. Interestingly, interwrinkle distances had no significant effect on the surface area. The difference between the surface areas of NWSTNs and WWSTNs was 0.31%, and that of NWSNs and WWSNs was 0.56%. Meanwhile, there were significant gap between the surface area of SSTNs and STNs, which seems to be attributed to the different atomic weight of the Si and Ti. The atomic weight of Si is 28.086 g/mol, while that of Ti (47.867 g/mol) is significantly larger. This indicates that when the same weight of SSTNs and STNs are present, there are larger number SSTNs compared to STNs, resulting in a larger surface area per unit mass.

Moreover, effective surface of the nanoparticles were compared by measuring the amount of adsorbed dye molecules on the surface of the particles of equal mass. The particles were immersed in ethanolic solution containing 0.5 mM N719 dye for 48 h at 30 °C, and then the dye molecules were detach by using 1 M NaOH solution. Figure 4.8 shows the absorbance spectra of the detached N719 dye molecules in 1 M NaOH solutions, and Table 4.2 shows the loaded dye amounts on the oxide surface calculated by the extinction coefficient reported elsewhere. Since

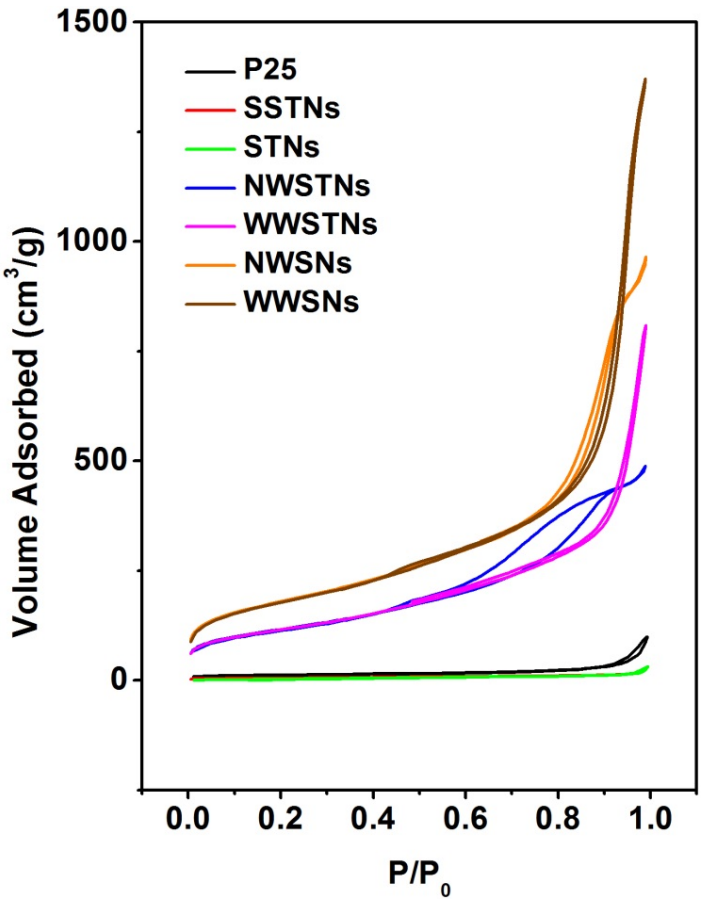


**Figure 4.7.** $N_2$ adsorption-desorption isotherms of P25 $TiO_2$ nanoparticles, spherical scattering nanoparticles, wrinkled silica/titania nanoparticles, and wrinkled silica nanoparticles.

| | BET surface area ($m^2/g$) | Loaded amount of dye ($\times 10^{-5}$ mol/g) |
|---|---|---|
| P25 | 40.12 | 6.01 |
| SSTNs | 17.29 | 1.33 |
| STNs | 13.52 | 0.77 |
| NWSTNs | 417.70 | 4.23 |
| WWSTNs | 416.39 | 5.23 |

**Table 4.1.** BET surface areas and specific dye loading amounts on P25 $TiO_2$ nanoparticles, spherical scattering particles, and wrinkled scatterers.

| | BET surface area ($m^2/g$) |
|---|---|
| NWSNs | 646.40 |
| WWSNs | 642.81 |

**Table 4.2.** BET surface areas of wrinkled silica nanoparticles with different interwrinkle distances.

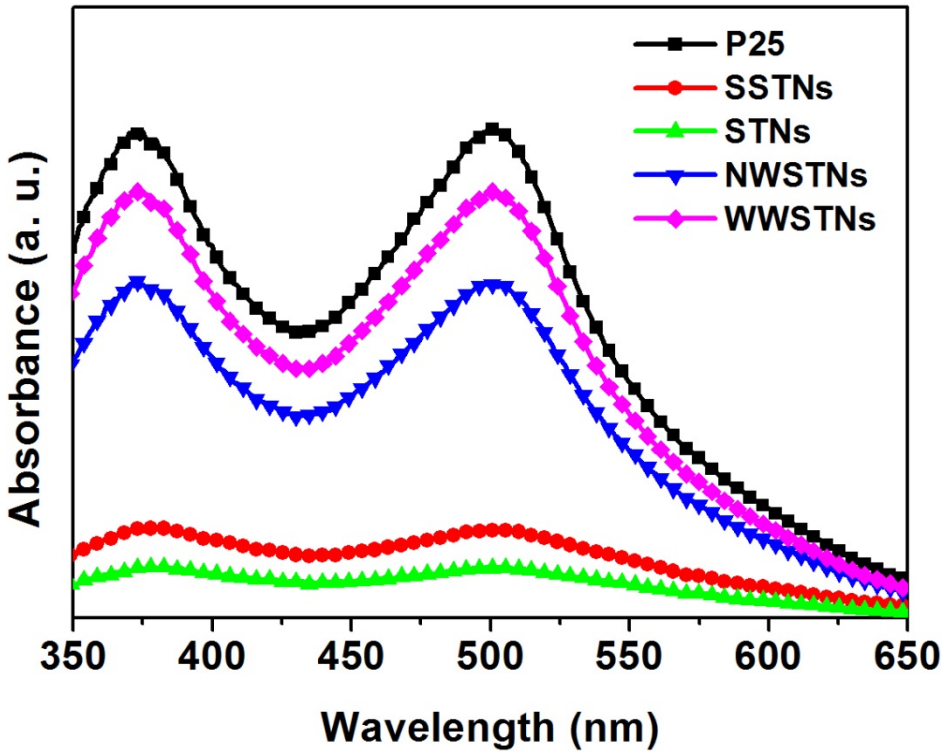


**Figure 4.8.** Absorbance spectra of detached dye molecules from 10 mg of P25, and spherical and wrinkled scattering particles in 1 M NaOH solution.

the size of N719 dye molecule is much larger than $N_2$, trend of dye loading amounts was different from that of BET surface areas. P25 had largest effective surface area ($6.01 \times 10^{-5}$ mol/g), and thaose of the wrinkled silica/titania nanoparticles were slightly lower; $4.26 \times 10^{-5}$ mol/g for NWSTNs and $5.23 \times 10^{-5}$ mol/g for WWSTNs. To our surprise, dye loadings on wrinkled silica/titania nanoparticles were less than 10 times larger than those of spherical nanoparticles ($1.33 \times 10^{-5}$ mol/g for SSTNs and $0.77 \times 10^{-5}$ mol/g for STNs). Unlike $N_2$ molecules, relatively large N719 dye molecules seem to have been unable to move into the narrow pores or crevasses formed by the wrinkles, and this is clearer as from the results of NWSTNs and WWSTNs. Though the difference in the specific surface area of NWSTNs and WWSTNs was only 0.31%, there was a significant difference (~20%) in dye-loadings on NWSTNs and WWSTNs. This implies that the dye molecules were unable to diffuse into the narrow nanostructures and that a larger interwrinkle distance reduces the steric hindrance by providing a wider pathway for dye molecules to move into deeper parts of the wrinkled pores.

Figure 4.9 shows the diffuse reflectance spectra of SSTNs, STNs, NWSTNs, and WWSTNs. Since $TiO_2$ has band gap around 3.2 eV, significant portion of photons with wavelengths below 380 nm were absorbed. However, all of the synthesized scattering nanoparticles were highly reflective in 400 – 800 nm wavelength range. SSTNs showed largest reflectance in broadest region, and the reflectivity NWSTNs and WWSTNs were slightly lower than that. In case of STNs, the reflectance was close to unity (> 95%) at wavelength of 700 nm or higher, but it was significantly lower at below 550 nm. One interesting observation was that the diffuse reflectance of WWSTNs seemed as if that of NWSTNs have shifted to a lower wavelength region. In order to confirm that trend is general or not, diffuse reflectance spectra of NWSNs and WWSNs were obtained, and they are displayed in Figure 4.10. Among these two wrinkled silica nanoparticles, reflectance of NWSNs is higher than that of WWSNs in relatively larger wavelength region

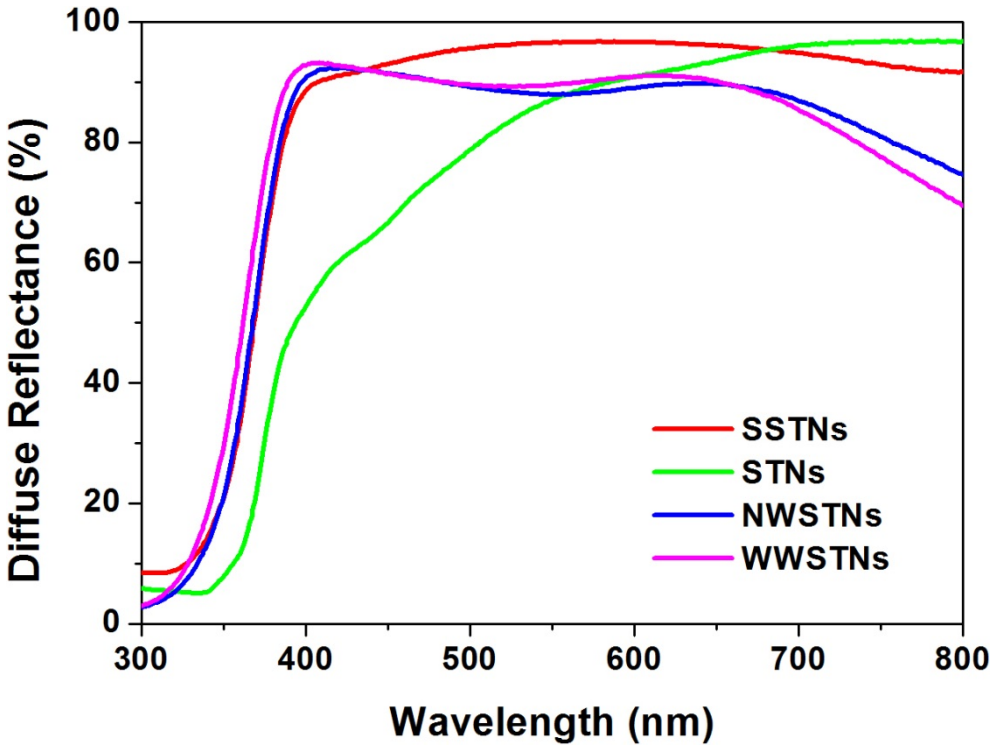


**Figure 4.9.** Diffuse reflectance spectra of SSTNs, STNs, NWSTNs, and WWSTNs measured by using an integrating sphere.

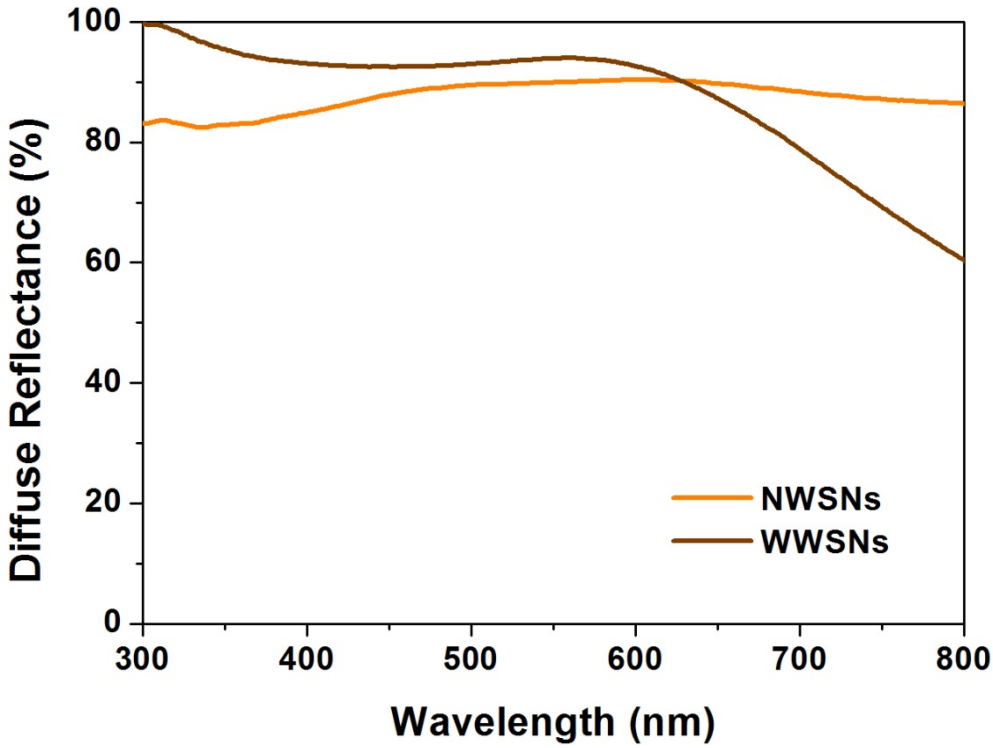


**Figure 4.10.** Diffuse reflectance spectra of NWSNs and WWSNs measured by using an integrating sphere.

(above 630 nm), but in lower wavelength region (below 630 nm), WWSNs have higher reflection properties than NWSNs. These results imply that there is a relationship between the interwrinkle distance and the wavelength region showing the highest reflectance, which is roughly a negative correlation. Though the $TiO_2$ shell significantly reduces this correlation, controlling the interwrinkle distance for spectral modifications in scattering properties may be useful in other applications where wrinkled silica nanoparticles without further surface modification are preferred.

### 4.3.3. Dye-sensitized solar cell applications

For the preparation of DSCs based on scatterer-embedded $TiO_2$ nanoparticle photoanodes, scattering particles were dispersed in ethanol with certain amount of paste containing ~20 nm sized $TiO_2$ nanoparticles. After harsh ultrasonication for uniform dispersion, ethanol in the mixture solution was evaporated, resulting in a viscous paste containing 10 wt% of scattering nanoparticles in regard to the amount of original $TiO_2$ content. The pastes containing SSTNs, STNs, NWSTNs, WWSTNs, or no scatterer were cast on FTO glass and sintered at 500 °C for 30 min in order to remove solvent and organic binders, and also to enhance the connectivity between the nanoparticles. Then these electrodes were sensitized with N719 dye by immersing them in the ethanolic dye solution for 48 h.

Figure 4.11 shows the photocurrent density ($J$)-voltage ($V$) characteristics of the DSCs employing the fabricated scattering nanoparticles, and the parameters obtained from the $J$-$V$ curve representing the photovoltaic performances and loaded dye amounts on the photoanodes are displayed in Table 4.3. By investigating the short-circuit photocurrent density ($J_{sc}$) values, magnitude of light scattering and surface area can be indirectly compared, because $J_{sc}$ has strong positive correlation with light harvesting efficiency, which is related to the loaded dye amounts and efficient light scattering [4]. DSCs employing wrinkled silica/titania nanoparticles

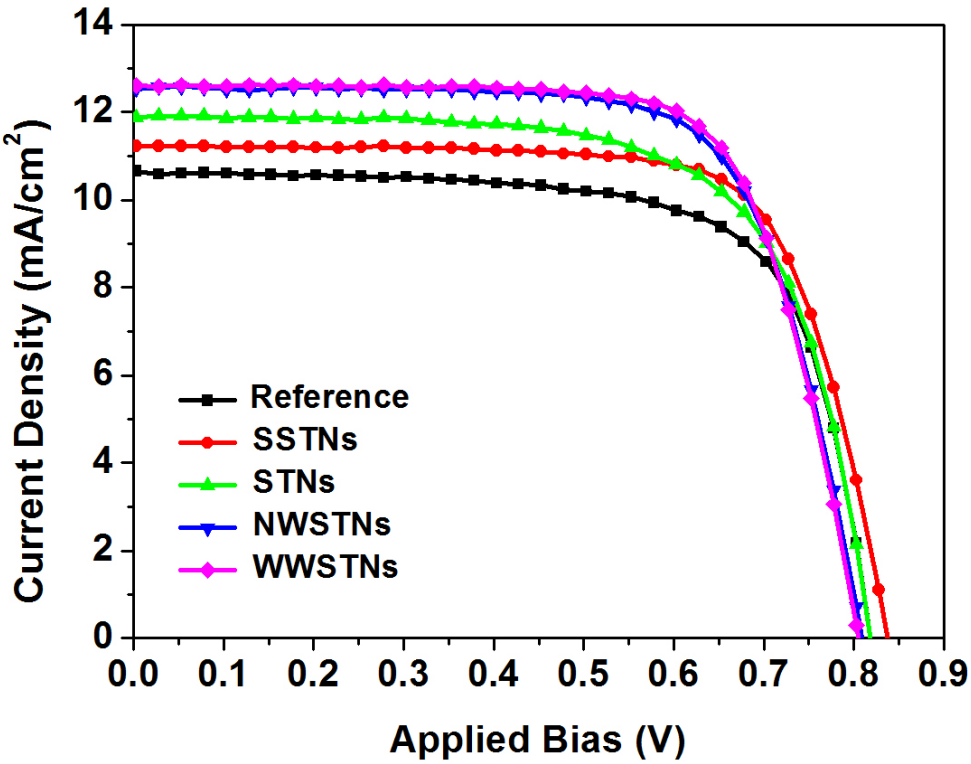


**Figure 4.11.** *J-V* characteristics of reference DSC and DSCs employing scattering nanoparticles.

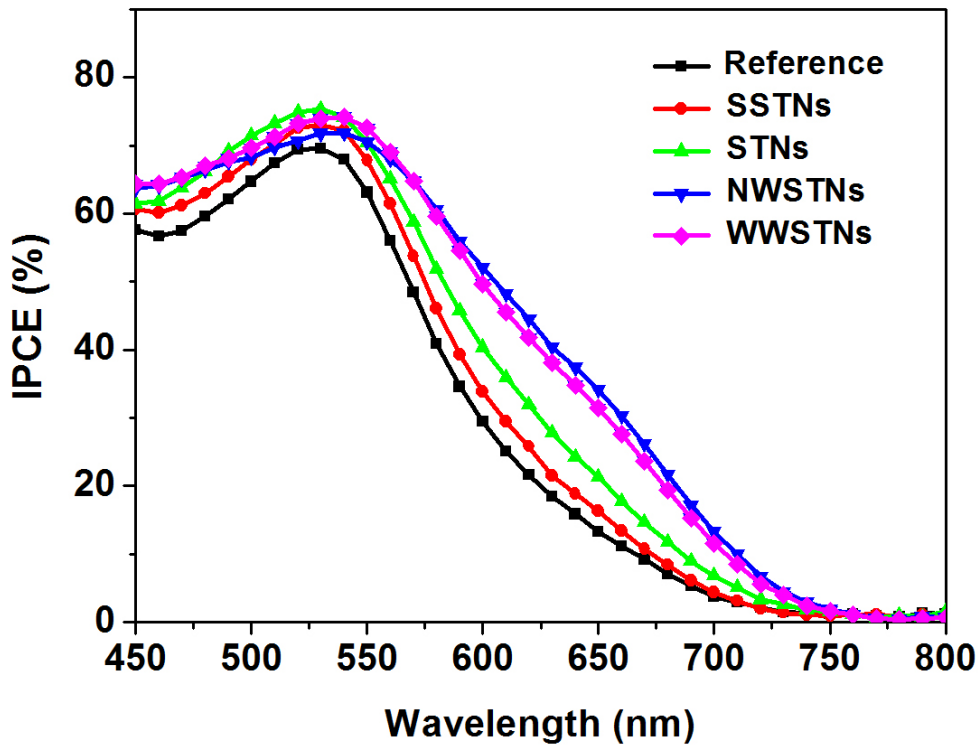


**Figure 4.12.** IPCE spectra of reference DSC and DSCs employing scattering nanoparticles.

| | $V_{oc}$ (V) | $J_{sc}$ (mA/cm$^2$) | $FF$ (%) | $\eta$ (%) | adsorbed amount of dye ($\times 10^{-7}$ mol/cm$^2$) |
|---|---|---|---|---|---|
| Reference | 0.819 | 10.7 | 70.4 | 6.17 | 1.423 |
| SSTNs | 0.838 | 11.2 | 73.1 | 6.86 | 1.212 |
| STNs | 0.819 | 11.9 | 68.4 | 6.67 | 1.179 |
| NWSTNs | 0.809 | 12.5 | 71.4 | 7.22 | 1.351 |
| WWSTNs | 0.806 | 12.6 | 72.4 | 7.35 | 1.364 |

**Table 4.3.** *J-V* characteristics of the reference DSC without scatterer and DSCs employing spherical and wrinkled scatterering particles.

as scatteres showed largest $J_{sc}$ values, and also the highest energy conversion efficiencies were observed in these cells. This is mainly attributed to the large surface for dye loading and efficient light scattering properties. As can be seen from the measured values in Table 4.3, the dye loading amounts on the photoanode incorporating NWSTNs and WWSTNs are about 95% of that on the reference photoanode containing only ~20 nm sized $TiO_2$ nanoparticles. Also, from the IPCE spectra in Figure 4.12, it was clear that the wrinkled silica/titania particles most effectively scattered light in the wavelength region beyond 550 nm, showing the excellent light scattering and harvesting properties. In addition, one noteworthy observation was made on IPCE results that the spectral trend in light scattering observed by reflectance spectra is still valid in photovoltaic application. This indicates the usefulness of spectral modification of light-scattering wrinkled silica nanoparticles by altering the interwrinkle distances.

Given that the $J_{sc}$ and $\eta$ is higher in DSCs with SSTNs or STNs compared to the reference DSCs, it is clear that these spherical particles did scatter light to some extent and contributed in the enhanced light harvesting. However, DSCs employing SSTNs or STNs showed lower $J_{sc}$ values lower than the case of wrinkled particles, mainly due to the fewer amounts of loaded dye molecules. Meanwhile, there is one more interesting thing from the *J-V* characteristics of the DSCs with and without scattering particles that the presence of silica cores irrespective to their morphology increased the fill factor (*FF*) of DSCs slightly. Since this observation was also made at the DSCs with scattering voids in the mesoporous $TiO_2$ photoanode [9,10], this can be attributed to the reduced spaces for $TiO_2$ conduction band electrons to travel through, because silica with its conduction band edge near vacuum level serves as insulator in this system. In this situation, larger portion of electron seem to diffuse and arrive at the current collector before charge recombination, and this can be indirectly confirmed by the higher open-circuit voltage ($V_{oc}$) of DSCs with SSTNs compared to those of DSCs with STNS or without any scattering particles,

because $V_{oc}$ is negatively correlated with the overall charge recombination rate [36]. However, $V_{oc}$ values of DSCs employing wrinkled silica/titania nanoparticles were the lowest, and this is probably due to the recombination at the $TiO_2$ shell wherein largest population of grain boundaries with defect sites are located. This can also be confirmed by lower *FF*s in DSCs with wrinkled scatters than in that with SSTNs, though the difference is very slight.

## 4.4. Conclusions

In summary, wrinkled silica nanoparticles of controllable interwrinkle distances were prepared by adding various amounts of hydrophobic co-solvent, namely 1-pentanol in this research, to the Winsor III system containing TEOS (reactant), CTAB (surfactant), cyclohexane (nonpolar solvent), and water (polar solvent). These wrinkled silica particles were coated with $TiO_2$ shell and then were used as scatterers in the photoanodes of DSCs. Compared to the conventional sphere-shaped scattering nanoparticles, wrinkled silica/titania displayed superior performance in DSCs due to their large surface area for dye loading. Moreover, observations on the relationship between interwrinkle distances of wrinkled nanoparticles and spectral reflectivity was made, and this trend was clearer in the wrinkled silica particles without $TiO_2$ shell. Considering the simplicity and reliability of the method for interwrinkle distance control, the spectral engineering of the scattering particles based on wrinkled silica is anticipated to be very useful in various applications requiring efficient utilization of photons.

## 4.5. References


[1] O'Regan, B; Grätzel, M., *Nature* **1991**, *353*, 737.

[2] Grätzel, M., *Nature* **2001**, *414*, 338.

[3] Grätzel, M., *Inorg. Chem.* **2005**, *44*, 6841.

[4] Hagfeldt, A.; Boschloo, G.; Sun, L.; Kloo, L.; Pettersson, H., *Chem. Rev.* **2010,** *110*, 6595.

[5] Wang, Z.-S.; Kawauchi, H.; Kashima, T.; Arakawa, H., *Coord. Chem. Rev.* **2004**, *248*, 1381.

[6] Zhang, Q.; Cao, G., *Nano Today*, **2011**, *6*, 91.

[7] Zhang, Q.; Myers, D.; Lan, J.; Jenekhe, S. A.; Cao, G., *Phys. Chem. Chem. Phys.* **2012**, *14*, 14982.

[8] Deepak, T. G.; Anjusree, G. S.; Thomas, S.; Arun, T. A.; Shantikumar, V. N.; Nair, A. S., *RSC Adv.* **2014**, *4*, 17615.

[9] Hore, S.; Nitz, P.; Vetter, C.; Prahl, C.; Niggemann, M.; Kern, R., *Chem. Commun.* **2005**, 2011.

[10] Pham, T. T. T.; Bessho, T.; Mathews, N.; Zakeeruddin, S. M.; Lam, Y. M.; Mhaisalkar, S.; Grätzel, M., *J. Mater. Chem.* **2012**, *22*, 16201.

[11] Nishimura, S.; Abrams, N.; Lewis, B. A.; Halaoui, L. I.; Mallouk, T. E.; Benkstein, K. D.; van de Lagemaat, J.; Frank, A. J., *J. Am. Chem. Soc.* **2003**, *125*, 6306.

[12] Halaoui, L. I.; Abrams, N. M.; Mallouk, T. E., *J. Phys. Chem. B* **2005**, *109*, 6334.

[13] Guldin, S.; Hüttner, S.; Kolle, M.; Welland, M. E.; Müller-Buschbaum, P.; Friend, R. H.; Steiner, U.; Tétreault, N., *Nano Lett.* **2010**, *10*, 2303.

[14] Mihi, A.; Zhang, C.; Braun, P. V., *Angew. Chem. Int. Ed.* **2011**, *50*, 5712.

[15] Yella, A.; Lee, H.-W.; Taso, H. N.; Yi, C.; Chandiran, A. K.; Nazeeruddin, M. K.; Diau, E. W.-G.; Yeh, C.-Y.; Zakeeruddin, S. M.; Grätzel, M., *Science* **2011**, *334*, 629.

[16] Matthew, S.; Yella, A.; Gao, P.; Humphry-Baker, R.; Curchod, B. F. E.; Ashari-Astani, N.; Tavernelli, I.; Rothlisberger, U.; Nazeeruddin, M. K.; Grätzel, M., *Nat. Chem.* **2014**, *6*, 242.

[17] Barbé, C. J.; Arendse, F.; Comte, P.; Jirousek, M.; Lenzmann, F.; Shklover, V.; Grätzel, M., *J. Am. Ceram. Soc.* **1997**, *80*, 3157.

[18] Yang, L.; Lin, Y.; Jia, J.; Xiao, X.; Li, X.; Zhou, X., *J. Power Sources* **2008**, *182*, 370.

[19] Gao, X.-D.; Li, X.-M.; Gan, X.-Y.; Wu, Y.-Q.; Zheng, R.-K.; Wang, C.-L.; Gu, Z,-Y.; He, P., *J. Mater. Chem.* **2012**, *22*, 18930.

[20] Son, S., Hwang, S. H.; Kim, C.; Yun, J. Y.; Jang, J., *ACS Appl. Mater. Interfaces* **2013**, *5*, 4815.

[21] Usami, A., *Chem. Phys. Lett.* **1997**, *277*, 105.

[22] Yu, I. G.; Kim, Y. J.; Kim, H. J.; Lee, C.; Lee, W. I., *J. Mater. Chem* **2011**, *21*, 532.

[23] Koo, H.-J.; Kim, Y. J.; Lee, Y. H.; Lee, W. I.; Kim, K.; Park, N.-G., *Adv. Mater.* **2008**, *20*, 195.

[24] Wu, W.-Q.; Xu, Y.-F.; Rao, H.-S.; Su, C.-Y.; Kuang, D.-B., *Nanoscale* **2013**, *5*, 4362.

[25] Lv, F.; Xiao, S.; Zhu, J.; Li, H., *RSC Adv.* **2014**, *4*, 36206.

[26] Hsu, W. P.; Yu, R.; Matijević, E. J., *J. Colloid Interface Sci.* **1993**, *156*, 56.

[27] Small, A.; Hong, S.; Pine, D., *J. Polym. Sci., Part B: Polym. Phys.* **2005**, *43*, 3534.

[28] Pan, W.; Ye, J.; Ning, G.; Lin, Y.; Wang, J., *Mater. Res. Bull.* **2009**, *44*, 280.

[29] Zhang, H.; Li, Z.; Xu, P.; Wu, R.; Jiao, Z., *Chem. Commun.* **2010**, *46*, 6783.

[30] Polshettiwar, V.; Cha, D.; Zhang, X.; Basset, J.-M., *Angew. Chem. Int. Ed.* **2010**, *49*, 9652.

[31] Fihri, A.; Bouhrara, M.; Patil, U.; Cha, D.; Saih, Y.; Polshettiwar, V., *ACS Catal.* **2012**, *2*, 1425.

[32] Polshettiwar, V.; Thivolle-Cazat, J.; Taoufik, M.; Stoffelbach, F.; Norsic, S.; Basset, J.-M., *Angew. Chem. Int. Ed.* **2011**, *50*, 2747.

[33] Bouhrara, M.; Ranga, C.; Fihri, A.; Shaikh, R. R.; Sarawade, P.; Emwas, A.-H.; Hedhili, M. N.; Polshettiwar, V., *ACS Sustainable Chem. Eng.* **2013**, *1*, 1192.

[34] Moon, D.-S.; Lee, J.-K., *Langmuir*, **2012**, *28*, 12341.

[35] Winsor, P. A., *Trans. Faraday Soc.* **1948**, *44*, 376.

[36] Koops, S. E.; O'Regan, B. C.; Barnes, P. R. F.; Durrant, R. R., *J. Am. Chem. Soc.* **2009**, *131*, 4808.

# Chapter 5. Anodized metal foam with multidimensional and hierarchical structure as photoelectrode

## 5.1. Introduction

Among various kinds of semiconductors, nanostructured metal oxides have shown great performances in photoelectrochemical cells, especially in dye-sensitized solar cells (DSCs) and photoelectrochemical water splitting cells (PWSCs). DSCs are highly efficient organic/inorganic hybrid photovoltaic systems with excellent reliability, and they are considered as a promising solar energy conversion devices to replace conventional silicon or thin film cells due to their environmentally and economically favorable characteristics [1-5]. Significant advances in electrolyte and light harvesters have been achieved in the last few years. For example, cobalt bipyridyl redox couples with compatible organic sensitizers enabled remarkable energy conversion efficiency by increasing photovoltage [6-9], and perovskite materials opened a new era of solid-state cells due to their outstanding light harvesting and charge transporting properties [10-12]. However, there has been no report on the mesoscopic photoanode of an excitonic solar cell that surpasses the performance of $TiO_2$ nanoparticles (NPs), which have thus been the best-performing photoanode since the inception of DSCs in 1991 [1].

Though $TiO_2$ NPs have exceptional features such as their large available surface area for light harvesting, they suffer from significant degrees of charge recombination which lead to a considerable performance drop [5,13]. To minimize recombination rates, one-dimensional structures such as nanotubes (NTs) [14-17],

nanowires [18,19], and nanorods [20] were investigated so as to confine the pathways of conduction band electrons effectively. Although these types of structural designs reduced charge recombination rates to some extent [21,22], the overall cell performance was inferior to that of NP-based cells. The reason was mainly because these structures have generated lower photocurrents due to a smaller surface area for light harvesting as compared to NPs.

In the field of PWSCs, since the pioneering work utilizing $TiO_2$ [23], various metal oxides such as $WO_3$ [24], $BiVO_4$ [25,26], $\alpha$-$Fe_2O_3$ [27-34] have been frequently used as photoelectrodes. Among these, $\alpha$-$Fe_2O_3$ is considered one of the most attractive oxides for water photoelectrolysis, because it is chemically stable, environmentally friendly, inexpensive and earth-abundant. A number of nanostructures including cauliflower [27-29], mesoporous [30], and nanotubes [31] were proposed to enhance the performance, but there are still plenty of opportunities for further advances [35].

Herein, we propose anodized Ti foams (ATFs) and anodized Fe foams (AFFs) as new types of photoelectrodes, which effectively generate a high photocurrent in DSCs and PWSCs, respectivly. In the case of ATF, we produced $TiO_2$ nanotube arrays (NTAs) on the surface of a Ti foam via electrochemical anodization [17,36,37], a robust and simple process. The resulting ATF was directly used as a transparent conducting oxide (TCO)-free photoanode after dye-sensitization. For the AFF, we anodized Fe foam with the assitance of ultrasonication, and vertically aligned iron oxide nanoflakes, similar to those formed in ATF, were synthesized on the Fe foam surfaces. We designed these photoanodes to have the following ideal characteristics: (i) large surface area for light harvesting, (ii) low-dimensionally confined semiconductor structure for enhanced charge transport, and (iii) three-dimensionally extended current collector with very low resistance. Both ATFs in DSCs and AFFs in PWSCs generated unprecedentedly large photocurrents, verifying the general advantages of this design concept.

## 5.2. Experimental section

### 5.2.1. Preparation of anodized Ti foam photoelectrodes

Unalloyed Ti powder (Aremco) composed of particles less than 45 μm in size was used. As reported elsewhere [38], a series of steps were carried out to prepare samples using the freeze-casting process. A dry mass of 4.9 g of Ti powders was added to 3.5 ml deionized, de-aired water contained within a cylindrical glass vessel with 13 mm inner diameter and 38 mm height, to which 0.2 wt% agar (as binder) and 1 μl of neutral detergent (as surfactant) were also added. After stirring the powders to form slurry, the vessel was placed on a copper chiller block held at -17 ˚C in a freezer. The side of the vessel was insulated with polystyrene foam to minimize radial heat losses. The frozen ice/Ti composite green-body was lyophilized to remove the ice via sublimation using a freeze-dryer at -40 ˚C, under a 7.5 Pa vacuum for around 24 h. The lyophilized green-body was then sintered in a vacuum furnace through a two-step heat-treatment process: first at 300 ˚C for 3 h and subsequently at 877 ˚C for 5 h. More details for the experimental procedure were reported in the previous literature [38]. The specimens for anodization were obtained from the bottom region (near the chill) of a freeze-cast Ti foam with equiaxed pore shape and 40 ± 4% porosity determined by image analysis on an SEM micrograph of a polished cross-section. Metallographic examination was carried out by both optical microscopy and scanning electron microscopy (SEM) on ground and polished, or fractured samples. After machining the fabricated foam into a uniform thickness of 500 μm, the foam was potentiostatically anodized in an ethylene glycol electrolyte containing 0.25 wt% $NH_4F$ and 2 vol% $H_2O$, as previously reported by Paulose *et al*. [39]. The anodized foam was thermally annealed at 450 ˚C for 4 h for enhancement of crystallinity and was $TiCl_4$-treated to increase the roughness and injection efficiency [40]. ATF was then subsequently immersed in an ethanol solution of 0.5 mM *cis*-bis (isothiocyanato) bis (2,2’-

bipyridyl-4,4-dicarboxylic acid) ruthenium (II) (N719 dye, Ohyoung industry) for 48 h in order to place the sensitizers on the $TiO_2$ surface.

### 5.2.2. Fabrication of dye-sensitized solar cells

The platinum counter electrode was fabricated by a thermal decomposition method as previously reported elsewhere [41]. Commercial gel-type electrolyte containing $I^-/I_3^-$ redox couples (EL-SGE, Dyesol) was pre-immersed into the DSC prior to the cell assembly by spring clamps. Fourteen layers of 50 μm thick thermoplastic gasket (Surlyn, Dupont) were used as the spacer without thermal annealing because of its chemical stability against corrosive $I_3^-/I^-$ electrolyte. A transparent glass slide was placed on the outermost part of the photoanode to prevent leakage of electrolyte through the pores of the photoanode. The conventional mesoporous $TiO_2$ photoanode was prepared by application of commercial $TiO_2$ nanoparticle paste (DSL 18NR-T, Dyesol) onto FTO glass (TEC-8, Pilkington) using a doctor blade method followed by a thermal sintering at 500 ˚C for 30 min., $TiCl_4$ treatment, and N719-sensitization. Cell assembly was done by exactly the same method used for ATF-DSCs, except for the thickness of the spacer, which was 50 μm for the NP-DSCs.

### 5.2.3. Preparation of anodized Fe foam photoelectrodes and photoelectrochemical water splitting cells

Slurry was prepared by mixing deionized water with 14.1 vol% iron oxide powder (mean particle size < 5 μm, purity ≥ 99%, Sigma-Aldrich) and 4 wt% binder (polyvinyl alcohol, $M_m$ = 89,000–98,000, purity 99+%, Sigma-Aldrich). In particular, slurry dispersion was assisted by a stirring and sonication process. The slurry was then poured into a Teflon mold (28 mm inner diameter, 70 mm height) placed onto a Cu rod cooled using liquid nitrogen. The temperature of top surface of the Cu rod was fixed at -15 ˚C and was controlled by a heater. After freezing, the

frozen slurry was dried at -90 ˚C and 5 mTorr for 48 h. The green body was reduced and sintered in a tube furnace in a 5% $H_2$–95% Ar gas mixture with a heating rate of 5 ˚C $min^{-1}$. The reduction was carried out by using a double step process at 300 ˚C for 2 h and then at 500 ˚C for 2 h, whereas sintering was carried out by using a single step process at 950 ˚C for 14 h. The Fe foam was cut and polished into a uniform thickness of 500 μm, and was potentiostatically anodized in the same electrolyte used for the anodization of Ti foam. The anodizing was carried out at 25 ˚C and 80 V for 5 min under the assistance of ultrasonication. Anodized samples were carefully washed with deionized water and ethanol, and were used as photoanode after thermal annealing at 500 ˚C for 4 h to increase crystallinity. For the *J-V* measurements, platinum mesh was used as the counter electrode where the hydrogen evolutions take place, and the Ag/AgCl reference electrode was used to create a three-electrode system. Standard 1 M NaOH solution was used as an electrolyte for the photoelectrochemical performance characterization.

### 5.2.4. Physical characterizations and measurements

SEM images, both before and after FIB milling, were taken with Carl Zeiss SUPRA 55VP and Carl Zeiss AURIGA. XRD data was measured using a Rigaku D-MAX2500-PC. TEM analysis was carried out using JEOL JEM-2100F after sampling by FIB (SMI3050SE, SII Nanotechnology). Absorbance was measured using a UV-Vis-NIR spectrophotometer (V-670, Jasco). Cell performances were characterized using a 500 W xenon isotope lamp (XIL; model 05A50KS source units) at 1 sun condition (100 mW $cm^{-2}$, AM 1.5G), which was adjusted by the Si reference cell manufactured by National Institute of Advanced Industrial Science and Technology (AIST, Japan). Potentiostats were used for *J-V* measurements of DSCs (1480 Multistat, Solartron) and PWSCs (PGSTAT128N, Autolab). EIS analysis was done by using a Zahner IM6 electrochemical workstation under 1 sun

illumination with the forward bias of open-circuit potential for each cell. Sheet resistance was measured by a four-point probe (CMT-SP 2000N, AIT).

## 5.3. Results and discussion

### 5.3.1. Anodized Ti foam for dye-sensitized solar cells

Figure 5.1a shows the schematic fabrication process of the anodized Ti foam photoelectrode for DSCs. Ti foam was prepared by using the freeze-casting process as reported elsewhere [38], cut into slices, and polished into thin foils with a uniform thickness of ~500 μm. Electrochemical anodization was carried out at 80 V for 30 min at 25 ˚C using an ethylene glycol electrolyte containing 0.25 wt% $NH_4F$ and 2 vol% $H_2O$. The anodized foam was first characterized by X-ray diffractometry (XRD) and scanning electron microscopy (SEM). From the XRD patterns in Figure 5.2, the formation of anatase $TiO_2$ is observable. Figure 3a-d shows SEM images of a Ti foam before (Figure 5.3a) and after anodization (Figsure 5.3b and 5.3c). These figures clearly show that NTAs are formed on the surface of the foam. In addition, a cross-section of the Ti foam substrate beneath the $TiO_2$ NTAs was also imaged by SEM (Figure 5.3d), after focused ion beam (FIB) milling. Energy dispersive spectroscopy (EDS) mapping (insets of Figure 5.3d) and XRD data (Figure 5.2) confirm that the fabricated NTAs are $TiO_2$, and they also show the existence of metallic Ti under the $TiO_2$ NTAs.

Nanotubes were approximately 100 nm in outside diameter and 30 nm in wall thickness (Figure 5.3c), and their lengths at the ATF surface were approximately 8.5 μm (Figure 5.3d). SEM examination of the fracture surface of the ATF confirms that the $TiO_2$ NTAs were also formed on the inner surfaces (near the center) of the ATF (Figure 5.4). These $TiO_2$ NTAs were, however, much thinner than the NTAs on the outer surfaces of the ATF. This was due to a different reaction rate between the inner and outer surfaces during the anodization process. The outer

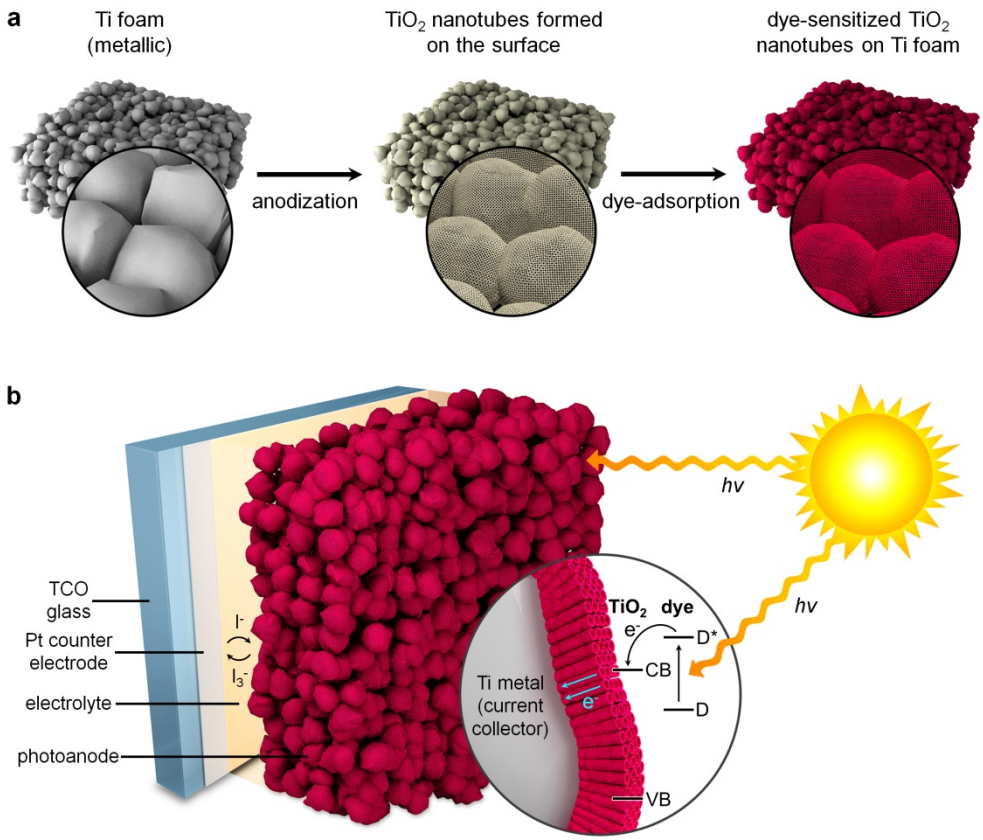


**Figure 5.1.** (a) Schematic of fabrication of anodized titanium foam (ATF) photoanode, and (b) schematic of a new dye-sensitized solar cell with ATF as photoanode.

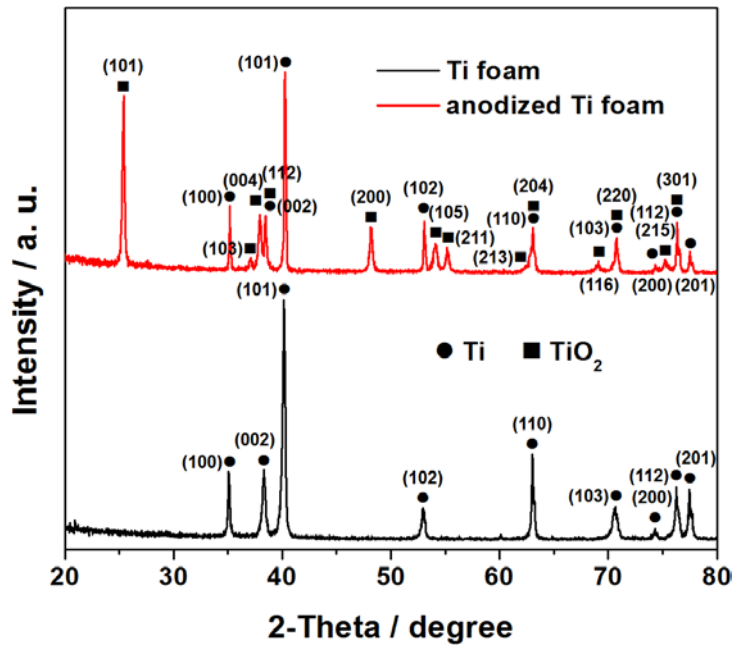


**Figure 5.2.** XRD patterns of Ti foam before and after anodization followed by heat treatment at 450 °C for 4h.

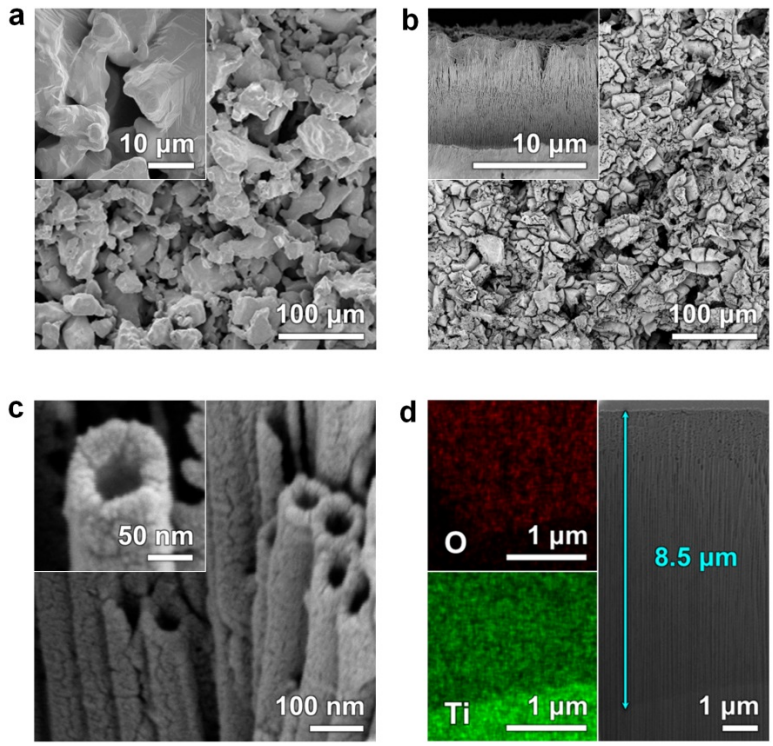


**Figure 5.3.** SEM images of (a) Ti foam and (b,c) anodized Ti foam. (d) Cross-sentional SEM image taken after FIB milling and corresponding elemental EDS maps (O and Ti).

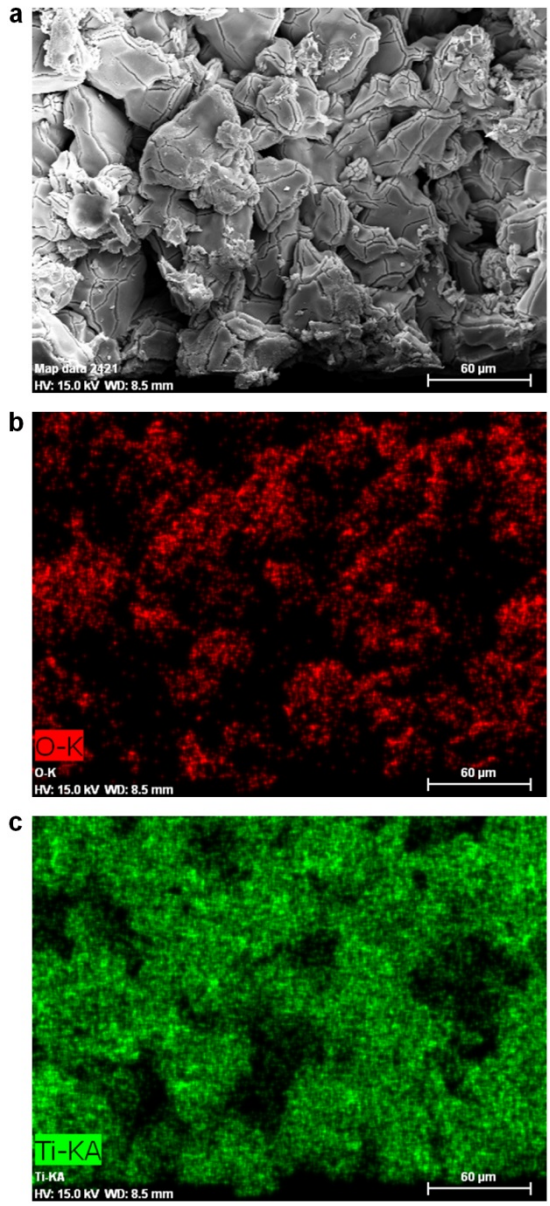


**Figure 5.4.** (a) SEM image and elemental EDS maps for (b) oxygen and (c) titanium at innermost region (near the center) of ATF.

part of the Ti foam is in the reactant ($F^-$)-richer environment compared to the inner part, because the $F^-$ concentration is generally limited by mass transfer.

Further characterization was carried out by transmission electron microscopy (TEM) on samples prepared by FIB (Figure 5.5). Three main observations were made. First, the shapes of the $TiO_2$ nanotubes in Figure 5.5a coincide with the morphologies observed in the SEM image in Figure 5.3c. Second, high-resolution (HR) images and selected area electron diffraction (SAED) patterns of internal metallic (Figure 5.5b and 5.5d) and external oxide parts (Figure 5.5c and 5.5e) indicate that monocrystalline (i.e. coarse-grained) Ti is located beneath the polycrystalline $TiO_2$. Third, the lattice plane spacing was measured to be 0.352 nm (Figure 5.5c), which matches that of the anatase $TiO_2$ (101) plane.

For the cell assembly, we used a commercial quasi-solid electrolyte (EL-SGE, Dyesol), which is a gel containing $I_3^-/I^-$ redox couples because there was no practical way to completely seal the lab-scale DSCs using the ATF photoanode (ATF-DSCs): since it needed to be in direct contact with the wire clamp, leakage of the liquid electrolyte was inevitable. Cell fabrication with the gel electrolyte consisted of the following steps. First, a Π shaped 700 μm spacer made of a chemically stable thermoplastic sealant (Surlyn, Dupont) was placed on the platinized fluorine-doped tin oxide (FTO) glass. A photoanode was then placed on top after pre-injection of quasi-solid electrolyte. One side of the dye-sensitized ATF was attached by silver paste to a 1.1 mm thick slide glass before the cell assembly, because a direct placement of ATF would lead to partial blocking of the active sites from the electrolyte. In addition, spring clamps were used instead of heating the sealant. The schematic image of the DSCs employing the ATF photoanode is presented in Figure 5.1b and Figure 5.6. On the other hand, conventional DSCs with $TiO_2$ NPs (NP-DSCs) were fabricated with 50 μm thick Surlyn film. An 8.5 μm thick $TiO_2$ NP film on FTO glass (Figure 5.7) and Pt-FTO were used as the photoanode and counter electrode for the NP-DSCs, respectively. All the

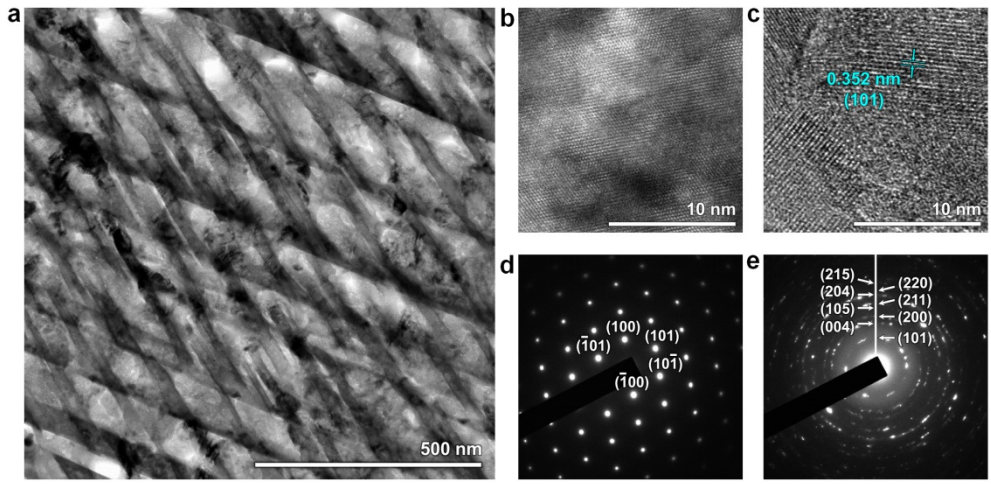


**Figure 5.5.** Bright-field TEM image of anodized titanium foam, HE-TEM images of (b) Ti foam substrate and (c) $TiO_2$ nanotubes on the surface of ATF, and the corresponding SAED patterns of (d) Ti foam and (e) $TiO_2$ nanotubes.

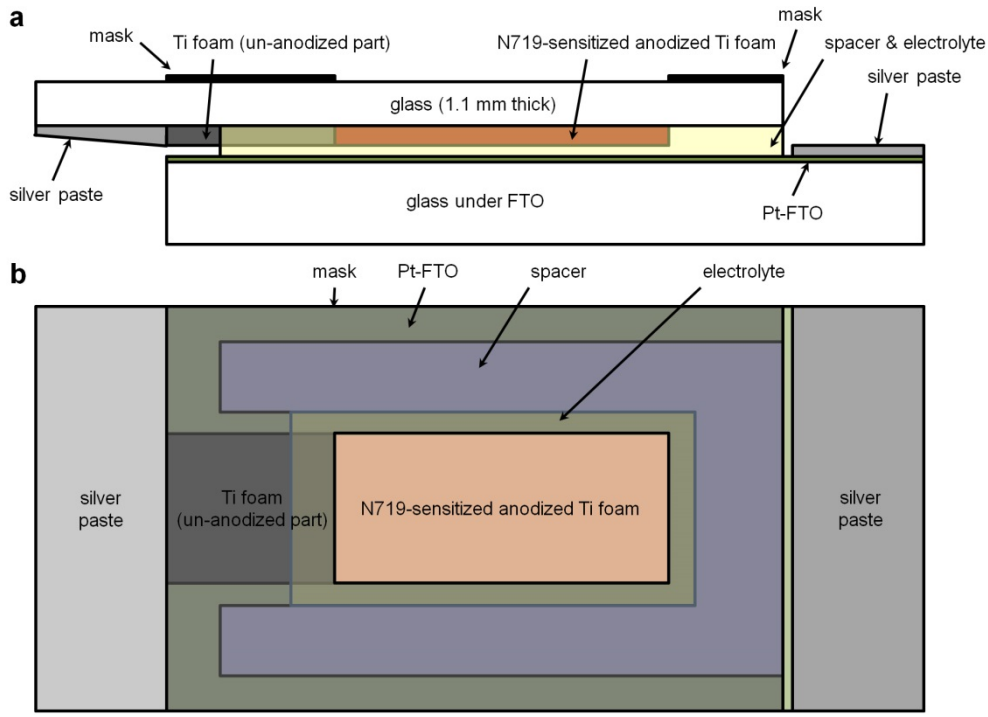


**Figure 5.6.** Schematic image showing the design of DSC (configuration of electrodes) employing ATF as phtoanode.

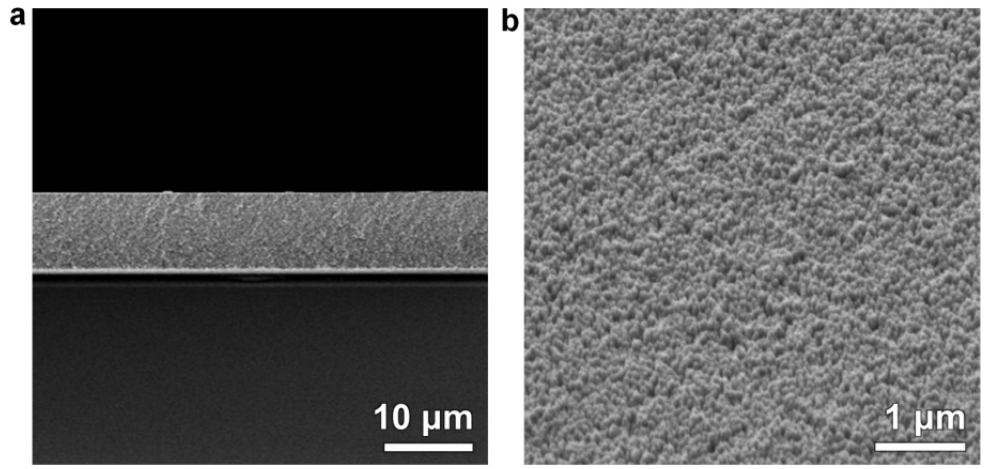


**Figure 5.7.** (a) Side- and (b) top-view SEM images of $TiO_2$ nanoparticles on FTO glass.

photoanodes were sensitized in an ethanol solution containing 0.5 mM N719 for 48 h prior to the cell assembly.

Photovoltaic performances of the DSCs were measured under 100 mW $cm^{-2}$ illumination at AM 1.5G (standard 1 sun) condition. From the *J-V* characteristics in Figure 5.8a, significant differences in both short-circuit current density ($J_{sc}$) and open-circuit potential ($V_{oc}$) were observed. Replacing $TiO_2$ NPs with ATF decreased $V_{oc}$ by 26.4% from 0.853 V to 0.628 V. However, energy conversion efficiency was increased by 12.5%, from 4.23% for the NP-DSC to 4.76% for the ATF-DSC. Most importantly, $J_{sc}$ was increased considerably from 7.4 mA $cm^{-2}$ to 22.0 mA $cm^{-2}$. Details of the photovoltaic performance and reproducibility are summarized in Table 5.1. This result is very promising, given that the photocurrent and efficiency of quasi-solid DSCs are generally inferior to liquid-electrolyte DSCs, as clearly seen from Table 5.2 and Figure 5.9. There are a few noteworthy characteristics observed for the ATF-DSCs. First, increase in photocurrent density is very substantial. A measured value of 22.0 mA $cm^{-2}$ for $J_{sc}$ is comparable to the highest value reported for DSCs with N719 dye as sensitizer [42]. Also, according to the standard AM 1.5G solar spectrum, the maximum theoretical $J_{sc}$ of the N719-sensitized solar cells is less than 26 mA $cm^{-2}$ (this value is for sensitizers with onset at 800 nm) [4,5], because the onset wavelength of N719 dye is around 775 nm. A value of 22.0 mA $cm^{-2}$ is more than 80% of the ideal value. Second, it is obvious that the fill factor of ATF-DSC was still low compared to NP-DSC, which is discussed more in depth later.

The high photocurrent density of ATF-DSCs is mainly attributed to enhanced light harvesting and current collection. We compared the relative roughness factors of ATF and $TiO_2$ NP photoanode, by measuring the comparative loading amounts of dye. Absorbance at 535 nm was measured after desorption of the dye in 1 M NaOH aqueous solution, and the number of dye molecules was calculated on the basis of extinction coefficient, $\varepsilon$ = 3748 $cm^{-1}$ $M^{-1}$. Remarkably, the amount of

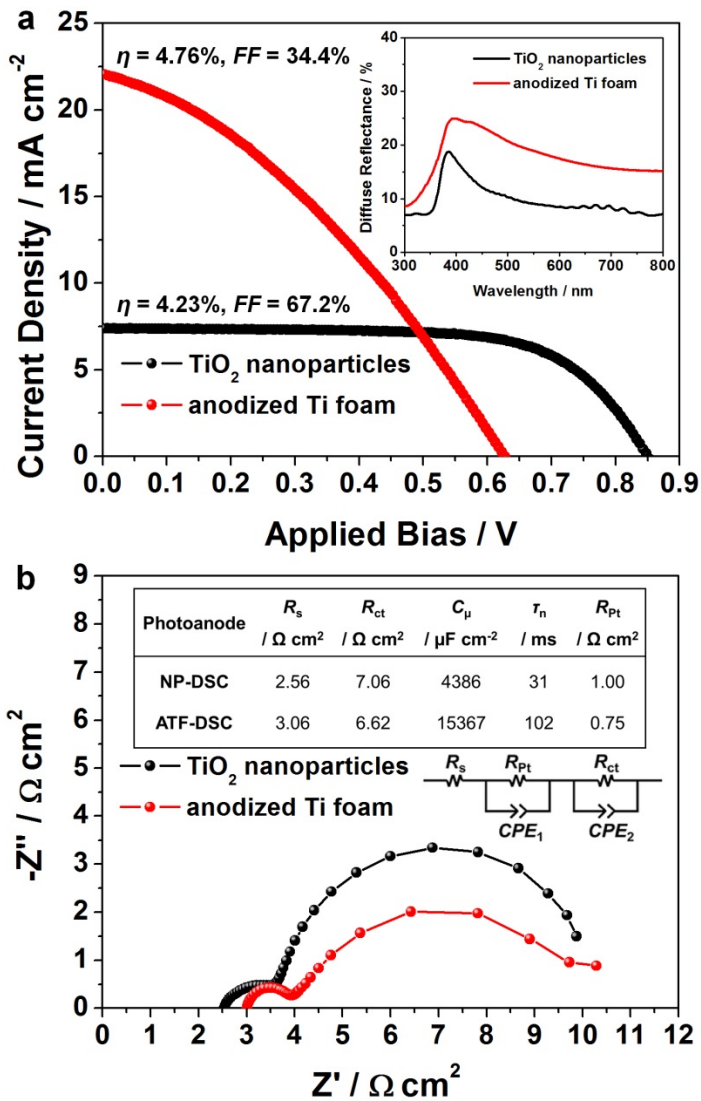


**Figure 5.8.** (a) *J-V* characteristics and (b) Nyquist plot of the best performing ATF-DSC and NP-DSC. The inset of (a) shows the diffuse reflectance of NP-FTO and ATF and the values in the inset table of (b) are the fitted parameters from electrochemical impedance spectroscopy measurements according to the presented equivalent circuit.

| | $V_{oc}$ / V | $J_{sc}$ / mA cm$^{-2}$ | $FF$ / % | $\eta$ / % |
|---|---|---|---|---|
| NP-DSC | 0.853 | 7.4 | 67.2 | 4.23 |
| ATF-DSC | 0.628 | 22.0 | 34.4 | 4.76 |

**Table 5.1.** *J-V* characteristics of NP- and ATF-DSCs.

| | $V_{oc}$ / V | $J_{sc}$ / mA $cm^{-2}$ | $FF$ / % | $\eta$ / % |
|---|---|---|---|---|
| Gel electrolyte | 0.853 | 7.4 | 67.2 | 4.23 |
| Liquid electrolyte | 0.748 | 14.4 | 67.5 | 7.26 |

**Table 5.2.** *J-V* characteristics of NP-DSCs with different types of electrolytes containing $I_3^-/I^-$ redox couples.

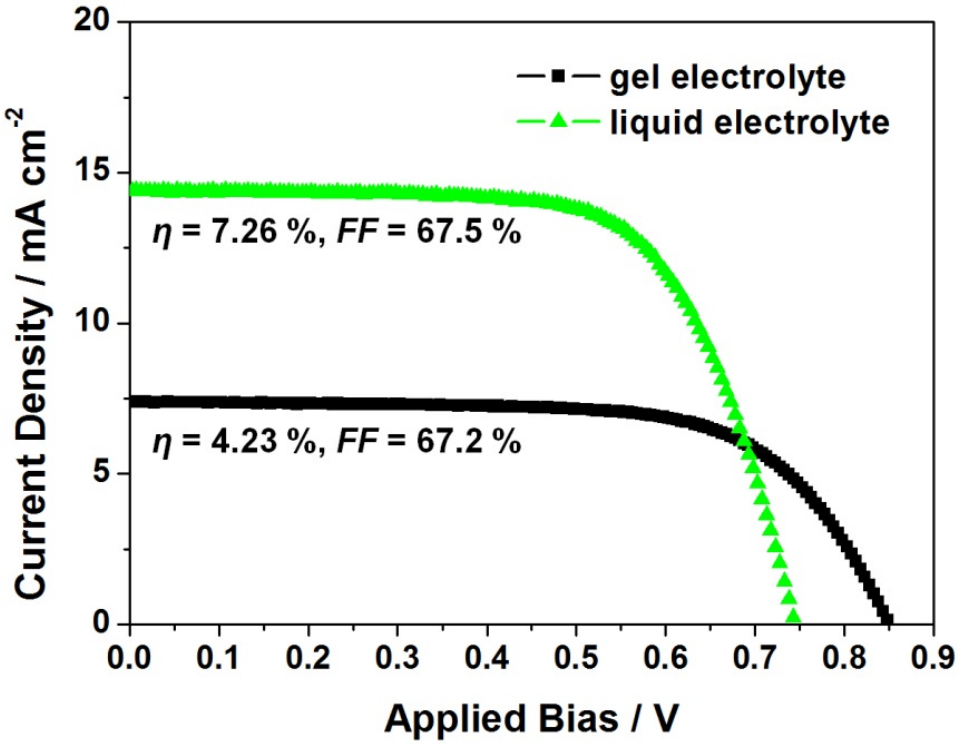


**Figure 5.9.** *J-V* data for NP-DSCs employing gel or liquid electrolyte.

adsorbed dye molecules on ATF was more than 25 times larger than that on $TiO_2$ NPs: $5.50 \times 10^{-6}$ mol $cm^{-2}$ and $1.98 \times 10^{-7}$ mol $cm^{-2}$ for ATF and NPs, respectively. This indicates that there are more photoactive surfaces for light absorption and charge separation in ATFs than $TiO_2$ NPs. Also, as shown from the diffused reflectance in the inset of Figure 5.8a, ATFs are superior to NPs in light scattering, enabling more efficient harvesting of photons.

In NP-DSCs, FTO serves as the current collector with its sheet resistance being 7.9 Ω $square^{-1}$, whereas in ATF-DSCs, the internal 3-dimensional Ti foam beneath the $TiO_2$ NTAs serves as the current collector with its sheet resistance being 12.4 mΩ $square^{-1}$. In addition, 1-dimensional $TiO_2$ structure is experimentally proven to be superior in charge transport to $TiO_2$ NP structure [21,22]. As a consequence, current collection is much more effective in ATF-DSCs due to the unique structural characteristics and properties of the ATF photoanode design. Moreover, replacing the FTO glass with a glass slide at the front minimized the loss of light (Figure 5.10) and gave additional benefit of reducing the fabrication cost.

Fill factor (*FF*), which is another primary parameter for characterization of photovoltaic performance, is significantly lower in ATF-DSCs than in NP-DSCs. The slopes of the *J-V* curve around the short-circuit region indicate that the smaller shunt resistance is the main factor for the decrease in the *FF* value of ATF-DSCs. From the SEM image in Figure 5.3b, it is noted that the $TiO_2$ NTAs are aligned vertically on the Ti foam surface, and thus, Ti metal is easily exposed to the electrolyte at the narrow inter-space between the NTAs. This direct contact between the Ti and iodide redox electrolyte might have contributed to the increase in charge recombination and may have reduced the shunt resistance.

Additional investigations, especially on the open-circuit potential drop and interfacial charge transfer kinetics of NP-DSCs and ATF-DSCs, were carried out using electrochemical impedance spectroscopy (EIS). Figure 5.8b shows the

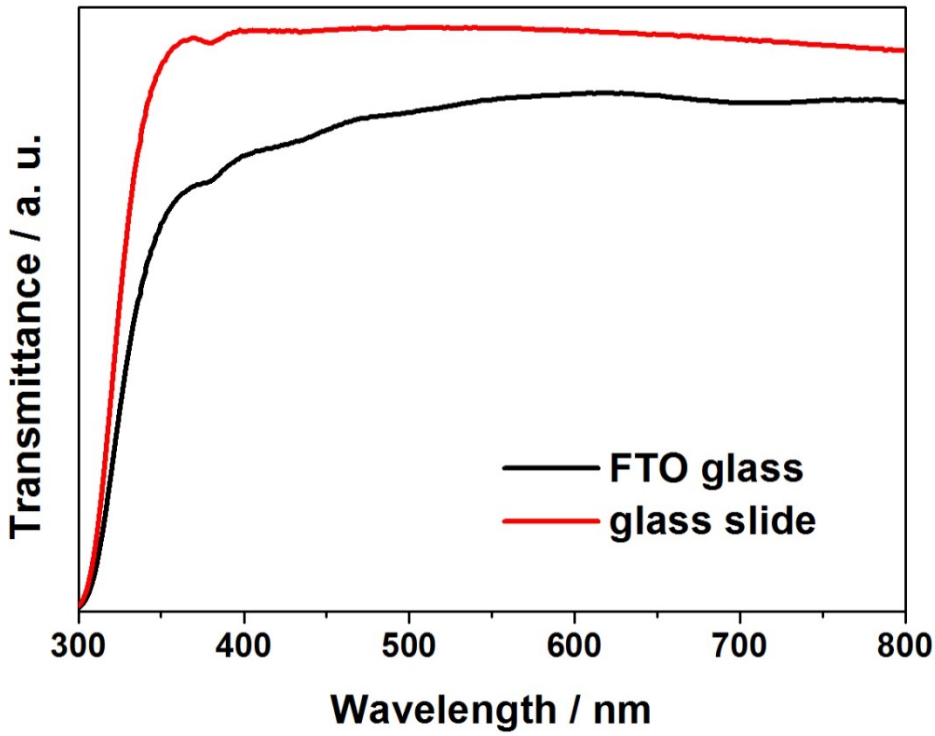


**Figure 5.10.** Transmittance spectra of the FTO galss and glass slide used at the front of NP-DSCs and ATF-DSCs, respectively.

Nyquist plot measured under standard 1 sun illumination and forward bias of open-circuit potential for each cell, showing high- and mid-frequency regions with the semicircles corresponding to Pt-FTO/electrolyte and $TiO_2$/electrolyte interfaces, respectively. The low-frequency range was not measured because of the significantly different mass transfer conditions for the two cells. The distances between the photoanode and counter electrode in the NP-DSCs and ATF-DSCs were very different in the optimized condition. However, ATF-DSCs are expected to be superior in electrolyte diffusion owing to the hierarchical dual pore structure of the ATF, with both micro- and nano-scale pores. The former pores, on the order of tens of microns, enable redox couples to penetrate easily, whereas the nanotube arrays, with the pore size on the order of tens of nanometers provide better electrolyte mass transfer than nanoparticles [43].

The table in Figure 5.8b shows the fitted values of EIS data by ZView software based on the equivalent circuit shown in the inset of Figure 5.8b. The term "constant phase element" (CPE) in general represents the interfacial capacitance of a rough electrode surface [44]. In the high frequency range, the charge transfer at the Pt-FTO/electrolyte interface was measured. The resistance at this interface ($R_{Pt}$) was different by a factor of 1/4 between the NP-DSCs and ATF-DSCs, because the evaluated parameters are affected by the applied bias potential. However, difference in $R_{Pt}$ value was considered insignificant because all counter electrodes were fabricated using exactly the same method. Series resistance ($R_s$) was larger in ATF-DSCs than in NP-DSCs, because of the longer distance between the photoanode and counter electrode, which resulted in a much larger ohmic resistance of electrolyte in ATF-DSCs (Figure 5.11).

In the quasi-solid DSCs, a larger charge transfer resistance ($R_{ct}$) value generally indicates a poorer interfacial contact between the photoelectrode and electrolyte [45]. Similar $R_{ct}$ values of NP-DSC and ATF-DSC show that there was no significant difference in the contact. The largest difference was in the chemical

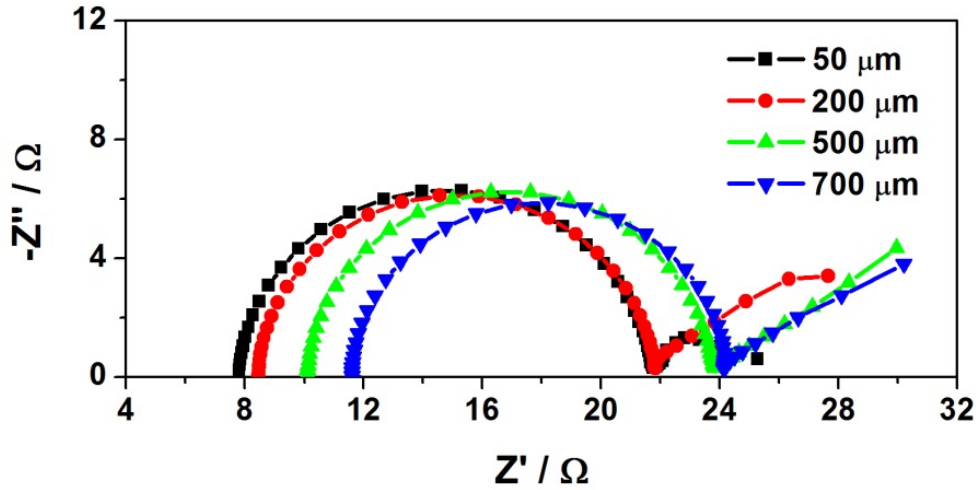


**Figure 5.11.** Nyquist plot of the symmetric cells based on Pt-FTO electrodes and $I_3^-/I^-$ redox electrolyte with different spacer thicknesses.

capacitance ($C_\mu$) at the $TiO_2$/electrolyte interface. $C_\mu$ represents the degree of photo-injected electron accumulation in the $TiO_2$ conduction band. A three-fold increase in $C_\mu$ for the ATF-DSCs suggests that a larger amount of excited electrons are produced in ATF-DSCs as compared to the NP-DSCs. A large conduction band electron density contributes to a higher photocurrent generation, and the large increase shows good match with the trends in the $J_{sc}$ values. However, the charge recombination rate increases strongly with increasing electron density in $TiO_2$ conduction band [46], resulting in a drop in open-circuit potential because of the accelerated back reaction.

The calculated values of the mean electron lifetime ($\tau_n$), which is the product of $R_{ct}$ and $C_\mu$ [47], are displayed in the inset of Figure 5.8b. $\tau_n$ is much larger in ATF-DSCs than NP-DSCs, which is ascribed to a difference in crystallite sizes and inherent charge recombination properties resulting from characteristic structures. As the crystallite size decreases, electrons encounter a larger number of grain boundaries, and this leads to an increase in the electron transport resistance. We calculated the mean crystallite size for each photoanode using Scherrer's equation and the largest (101) peaks of anatase $TiO_2$ from the XRD data in Figure 5.12. The mean crystallite sizes are 18 nm and 34 nm for NP and ATF, respectively, implying a near-doubling of the mean crystallite size in ATF. Additionally, one dimensional $TiO_2$ structure provides directionally confined pathways for electrons [21,22].

### 5.3.2. Anodized Fe foam for photoelectrochemical water splitting

For the verification of general advantages of the anodized metal foam photoelectrode, we also fabricated AFF by anodizing freeze-cast Fe foam (Figure 5.13a). Anodization was conducted under 80 V for 5 min by using the same electrolyte, but with the assistance of ultrasonication in this case. The XRD patterns in Figure 5.14 show that iron oxide is formed in mixed phase of both hematite and magnetite. The microstructure of the AFF was characterized by FE-

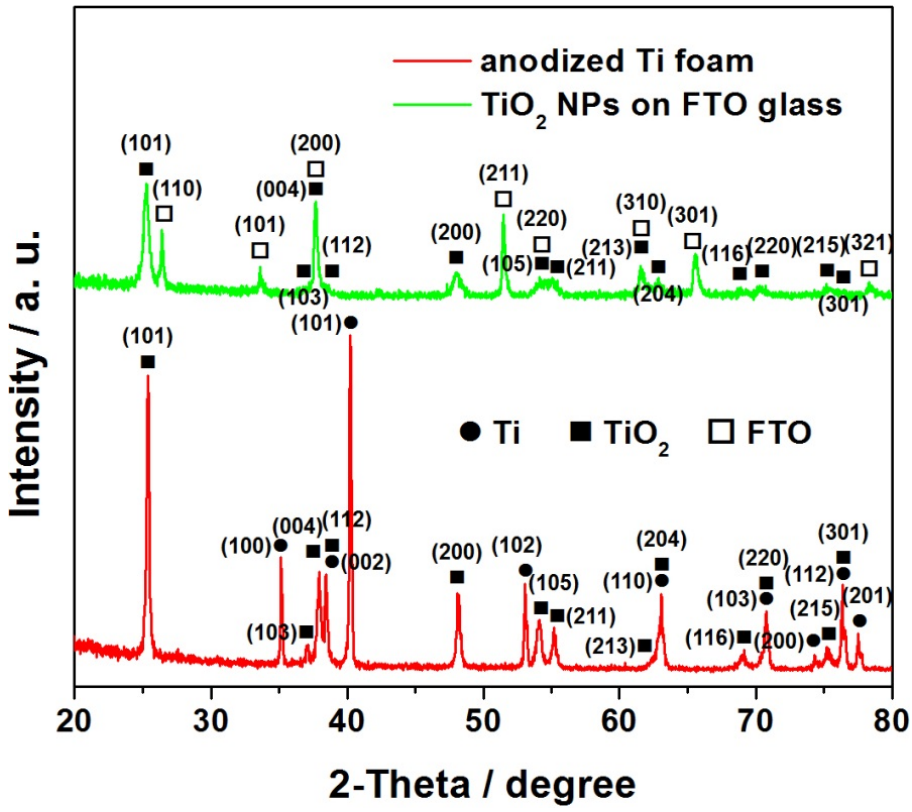


**Figure 5.12.** XRD patterns of ATF and NP-FTO photoelectrodes. FTO peaks were assigned according to JCPDS 41-1445 (cassiterite $SnO_2$).

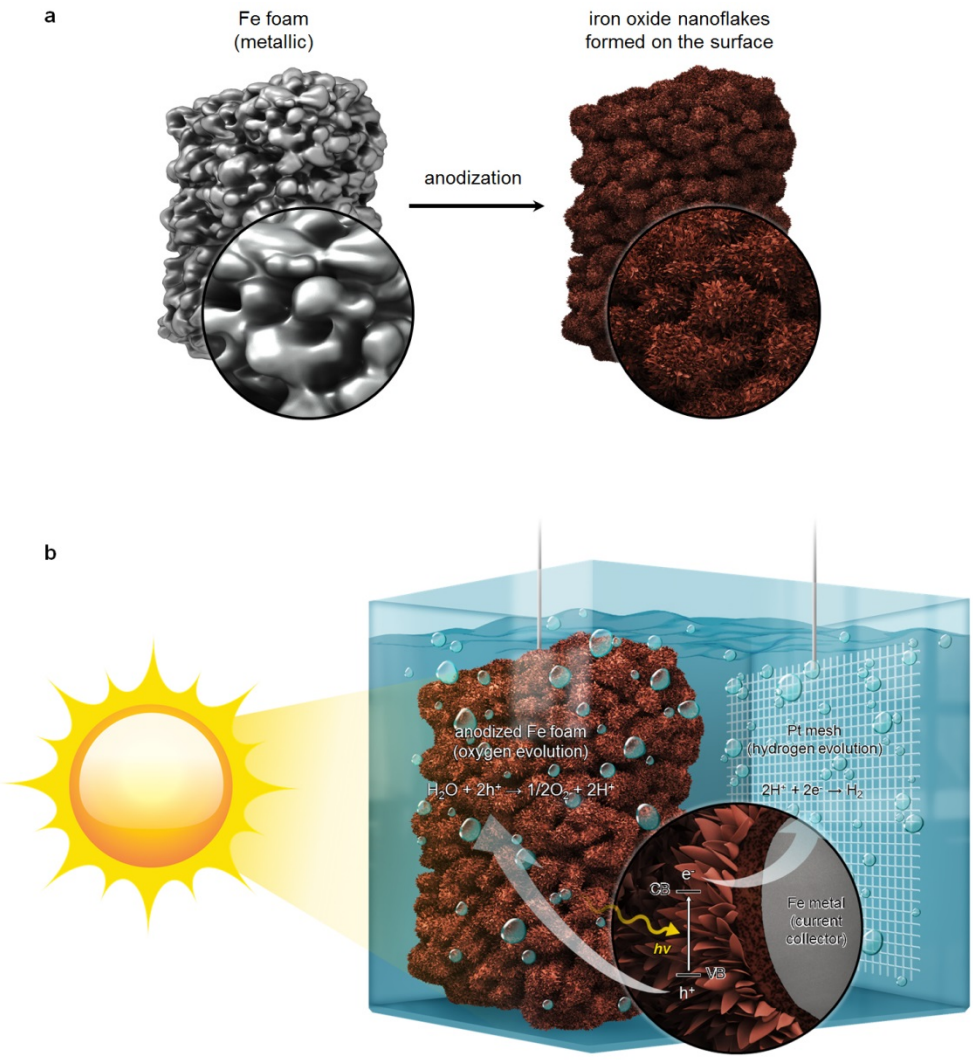


**Figure 5.13.** Schematics of (a) Fe foam before and after anodization and (b) photoelechemical water splitting reaction based on anodized Fe foam photoanode.

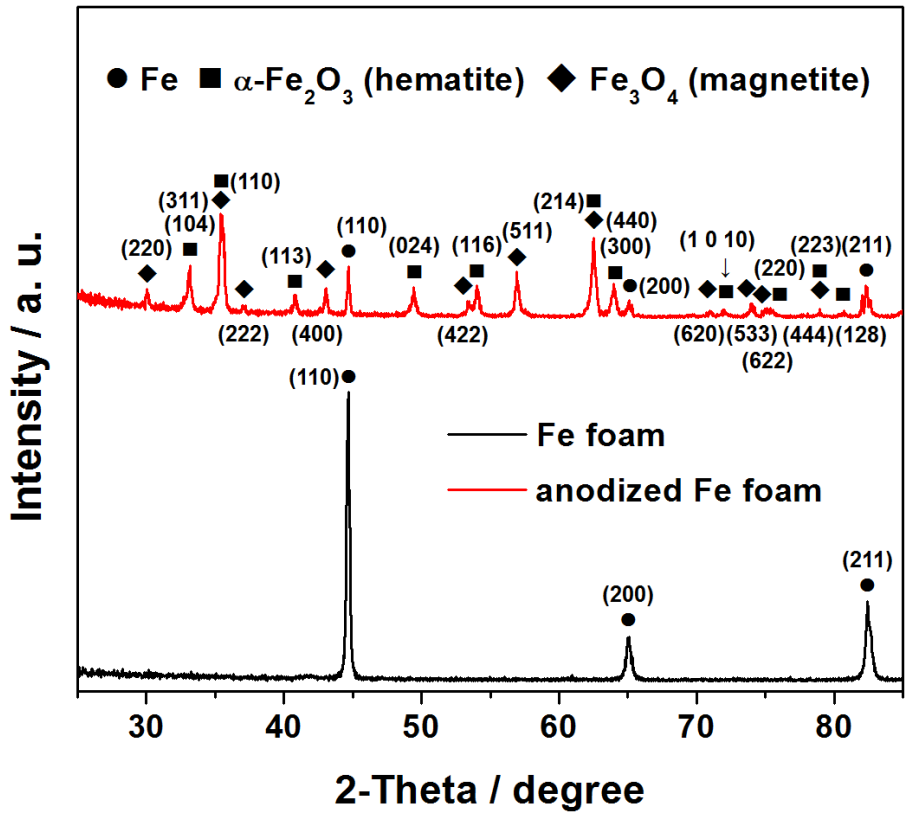


**Figure 5.14.** XRD patterns of Fe foam before and after anodization followed by heat treatment at 500 °C for 4 h. XRD peaks were assigned according to JCPDS 06-0696 (Fe), 33-0664 ($\alpha$-$Fe_2O_3$), and 19-0629 ($Fe_3O_4$).

SEM (Figsure 5.15a and 5.15b), which revealed that vertically aligned iron oxide nanoflakes were formed on the surface of the Fe foam. The SEM image of a fracture surface shown in Figure 5.15c suggests that the oxide layer, including the nanoflakes and a compact oxide below the flakes, is ~2 μm in thickness. Additionally, the existence of Fe metal beneath the iron oxide is observable from the SEM image and the corresponding EDS mapping results in the insets of Figure 5.15c, and also from the XRD patterns in Figure 5.14. This implies that Fe metal underneath the Fe oxide could serve as the current collector as in the case of Ti metal in the ATF. The internal part (near the center) of the AFF was observed by SEM, and there was no specific difference in morphology with the external region (Figure 5.16). TEM image (Figure 5.15d), SAED pattern (inset of Figure 5.15d) and XRD pattern (Figure 5.14) show that the Fe oxide formed is mainly hematite with the presence of a secondary magnetite phase. The average crystallite size is 25 nm, as calculated from the Scherrer's equation and the (104) peak of $\alpha$-$Fe_2O_3$.

Since this type of morphology is different from those in previous reports [31,48], we performed additional experiment in order to figure out the origin of the nanoflakes morphology. In general, during the electrochemical anodization process, nanostructured metal oxide gets formed on the surface of the metal substrate by the equilibrium of the rate of metal oxide formation by electric bias and chemical dissolution of metal oxides by chemical species in the electrolyte. During the metal oxide dissolution, $H^+$ from water dissociation resulted from the high electric field on the electrode surface forms HF, which is well known for metal oxide dissolving property. Therefore, two factors often affect the morphologies of anodic oxide films; magnitude of applied potential and water content of the electrolyte [49,50]. Considering the previous reports on electrochemical synthesis of anodic iron oxide nanotube arrays and that iron foams have much larger surface area than iron foil (e. g. much lower current density per unit area during the anodization process), we

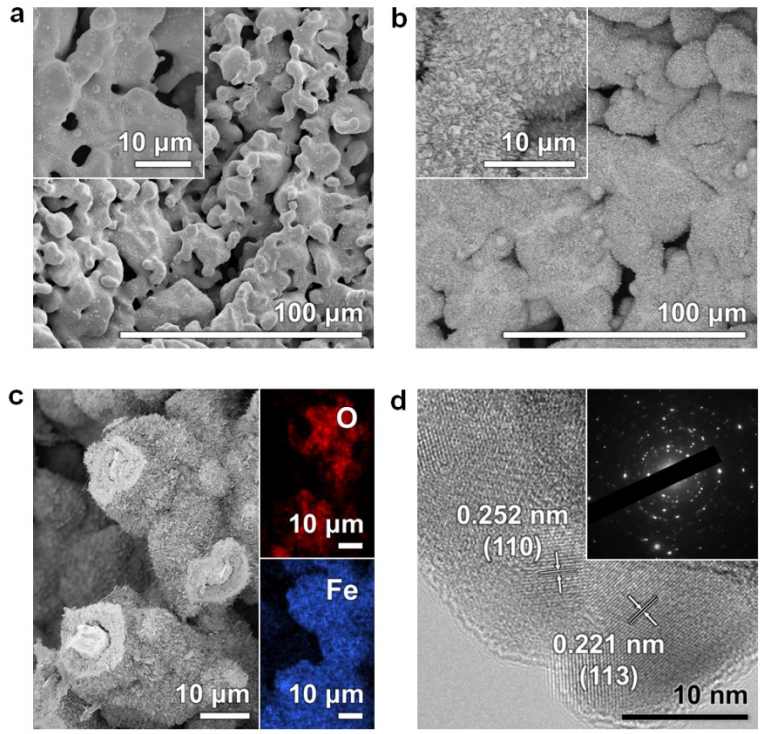


**Figure 5.15.** SEM images of (a) Fe foam and (b,c) anodized Fe foam. (d) Bright-field HR-TEM image of anodized Fe foam and SAED pattern in the inset.

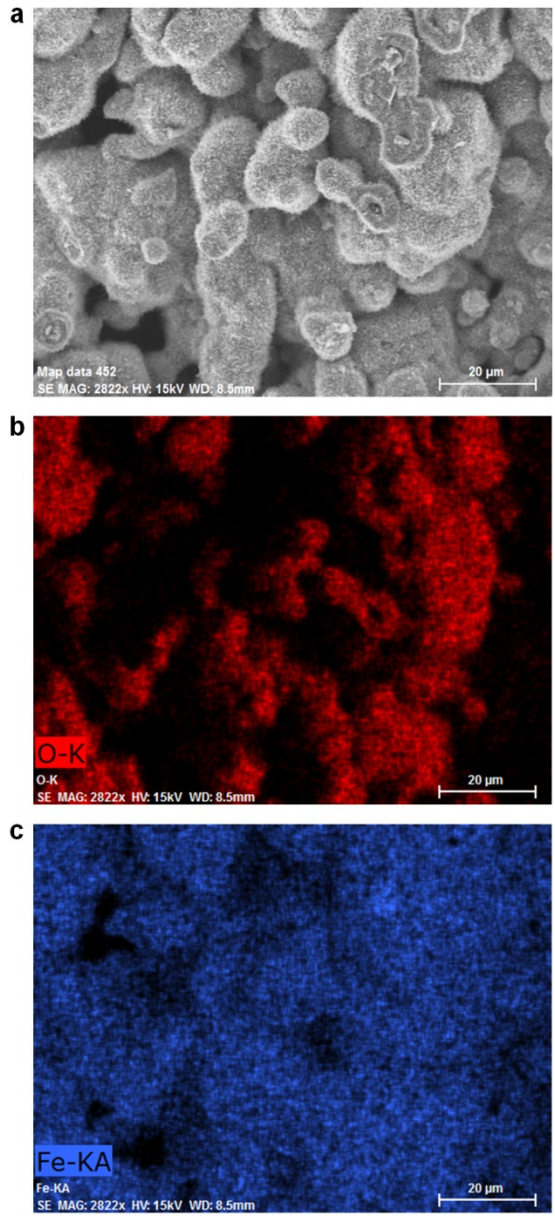


**Figure 5.16.** (a) SEM image and elemental EDS maps for (b) oxygen and (c) iron at the innermost region (near the center) of AFF.

have conducted anodization of Fe foil according to 4 different conditions described in Table 5.3. From the resulting iron oxide morphologies displayed in Figure 5.17, we concluded that the nanoflake morphology comes from the low current density per unit area and relatively large portion of $H_2O$ in the electrolyte compared to $NH_4F$.

Photoelectrochemical performance of the AFF was characterized under standard 1 sun illumination, using standard 1 M NaOH solution with the Ag/AgCl reference electrode. Potential values were calculated against the reversible hydrogen electrode (RHE) according to the Nernst equation using the value of pH = 13.6 and $E^{\circ}_{Ag/AgCl}$ = 0.1976 at 25 ˚C. For the evaluation of the AFF performance, current densities were measured by linear scans (scan rate: 50 mV $s^{-1}$) in both illumination and dark conditions. As shown in Fig. 5.18a, the photocurrent began to flow at 0.75 V vs. RHE just as in the case of the previous studies where anodized Fe sheet was used as photoanode [31]. The most noteworthy characteristic of the AFF photoanode was again a large photocurrent density. The onset of electrochemical water oxidation (dark current onset) is known to be around 1.55 V vs. RHE [30]. We observed a photocurrent density exceeding 5 mA $cm^{-2}$ before reaching 1.5 V, which is the highest value in iron oxide based water splitting reported to date, to the best of our knowledge. As in the case of ATF-DSCs, this excellent performance obtained from the AFF photoanode in the PWSC can be attributed to the large surface area for light harvesting, two-dimensionally confined semiconductor structure for enhanced charge transport, and three-dimensionally extended current collector with a very low sheet resistance, which was measured to be only 2.4 mΩ $square^{-1}$.

Pure hematite electrodes are known for its faradaic efficiency close to unity in adequate basic electrolytes [51]. However, the AFF photoanode contains magnetite phase which is inactive in photoelectrochemical water splitting reaction, and this phase might also contribute to the photocurrent by photocorrosion reaction.

| | Electrolyte 1 | Electrolyte 2 | Electrolyte 3 | Electrolyte 4 |
|---|---|---|---|---|
| $NH_4F$ (wt%) | 0.125 | 0.250 | 0.500 | 1.000 |
| $H_2O$ (vol%) | 1 | 2 | 3 | 4 |

**Table 5.3.** Electrolyte compositions used for the fabrication of anodic iron oxide nanostructured displayed in Figure 20a (Electolyte 1), 20b (Electrolyte 2), 20c (Electrolyte 3), and 20d (Electrolyte 4).

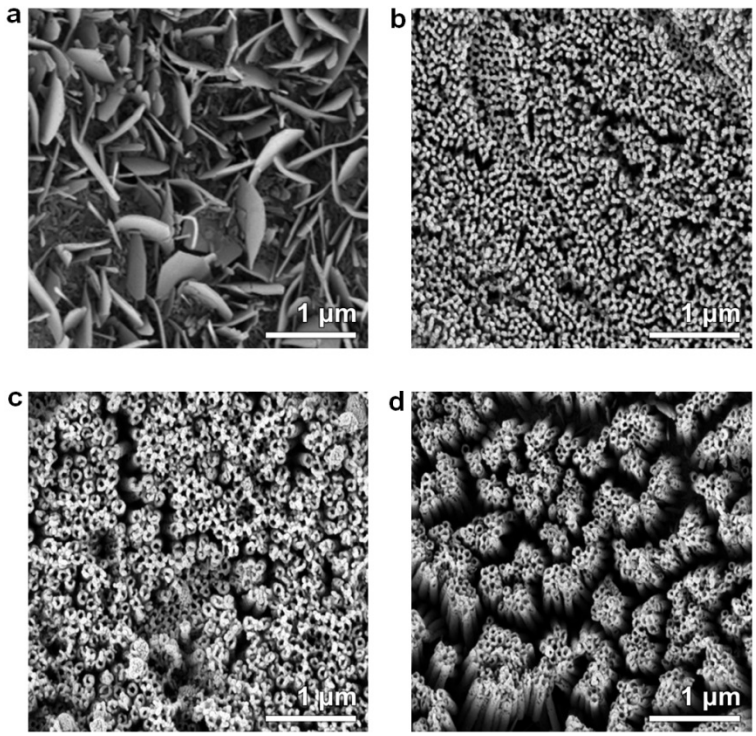


**Figure 5.17.** SEM images of iron oxide nanostructures synthesized by electrochemical anodization at 50 V for 1 h using electrolytes of various compositions displayed in Table 5.3.

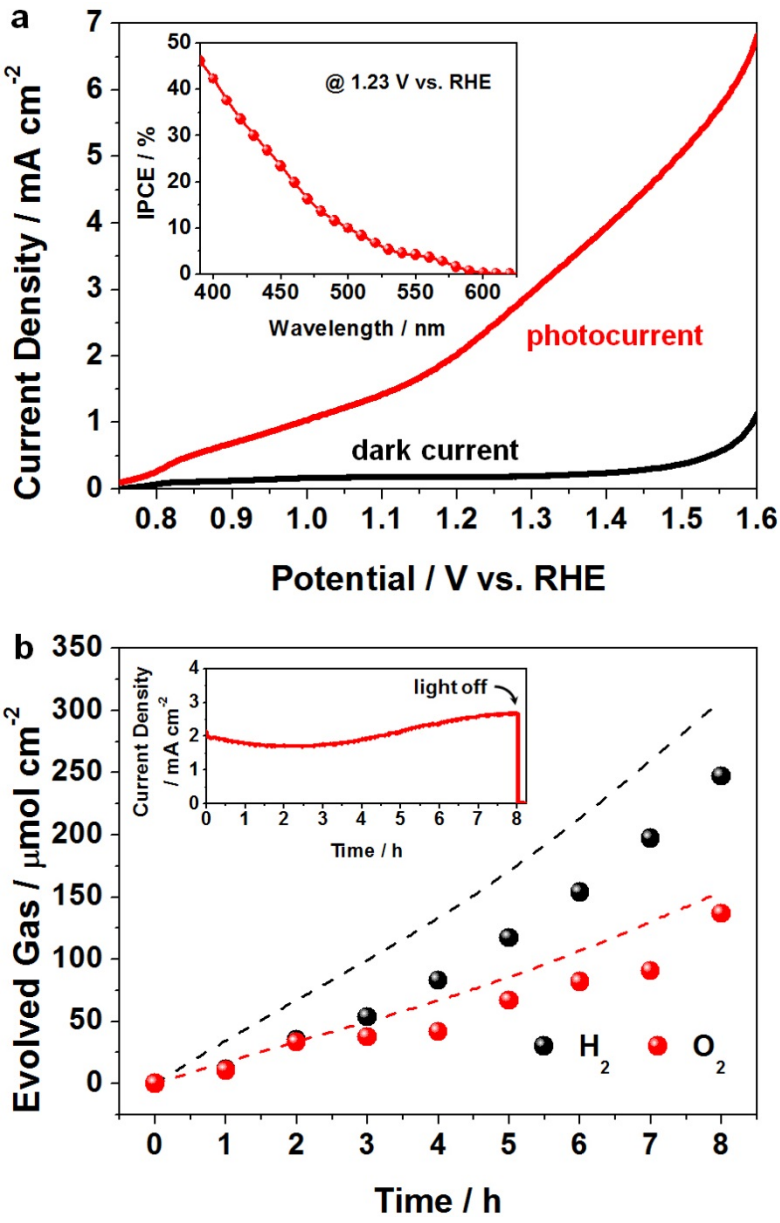


**Figure 5.18.** (a) *J-V* characteristic of the photoelectrochemical water splitting cell based on AFF photoanode and the IPCE data in the inset. (b) Quantification of gas evolution by using a gas chromatography under 1 sun illumination at 1.23 V vs. RHE. The inset shows the photocurrent density during the water splitting reaction.

Therefore, we observed the amounts of stoichiometric $H_2$ and $O_2$ evolution and the Faradaic efficiencies at 1.23 V vs. RHE under 1 sun illumination by gas chromatography (GC) analysis. Figure 5.18b shows the amount of evolved $H_2$ and $O_2$ gases, and the corresponding current densities are displayed in the inset. As can be seen from the GC results, $H_2$ and $O_2$ production is clearly observed, but the amount of evolved gas slightly falls short of 100% Faradaic efficiency, which is presented as dashed lines in Figure 5.18b. However, there is one very interesting phenomena that the photocurrent density increases as the reaction time exceeds 3 h until when the current have been under slow decay. Also, the evolution rate of the $H_2$ and $O_2$ gases increase with reaction time, indicating that the rise of photocurrents are not significantly attributed to the side reactions. The photocurrent surpasses the initial value after 6 h, and the Faradaic efficiency reached close to unity. In order to address this phenomenon, analyses on the iron oxide phase transition and surface state were performed by using Rietveld refinement method based on the XRD patterns and XPS spectra, and the results are shown in Figure 5.19 and Table 5.4. During the water splitting reaction for 8 h, inactive magnetite slowly transformed to active hematite phase, and this was quantitatively addressed by the Rietveld refinements. The molar ratio between these two phases was initially 66.23:33.57, but it changed to 68.63:31.37 after 8 h of photoelectrochemical water splitting. In Fe 2p XPS spectrum of as-prepared AFFs (black line in Figure 5.19b), the $2p_{3/2}$ peak is located around 710.8 eV, and the distance between the $2p_{3/2}$ and $2p_{1/2}$ peaks is about 13.6 eV, with clearly apparent shoulder peaks. This indicates that the surface of AFFs is mainly hematite [52]. However, the 2p peaks slighlt shift to the lower binding energy, which seems to be attributed to the formation of FeOOH on the surface. Recently, Kim *et al.* reported that the FeOOH is an excellent oxygen evolution catalyst which greatly enhances the performance of photoelectrode when applied on the surface of a photoelectrode [53]. The FeOOH layer seems to have contributed to the increament of the reaction rate (photocurrent

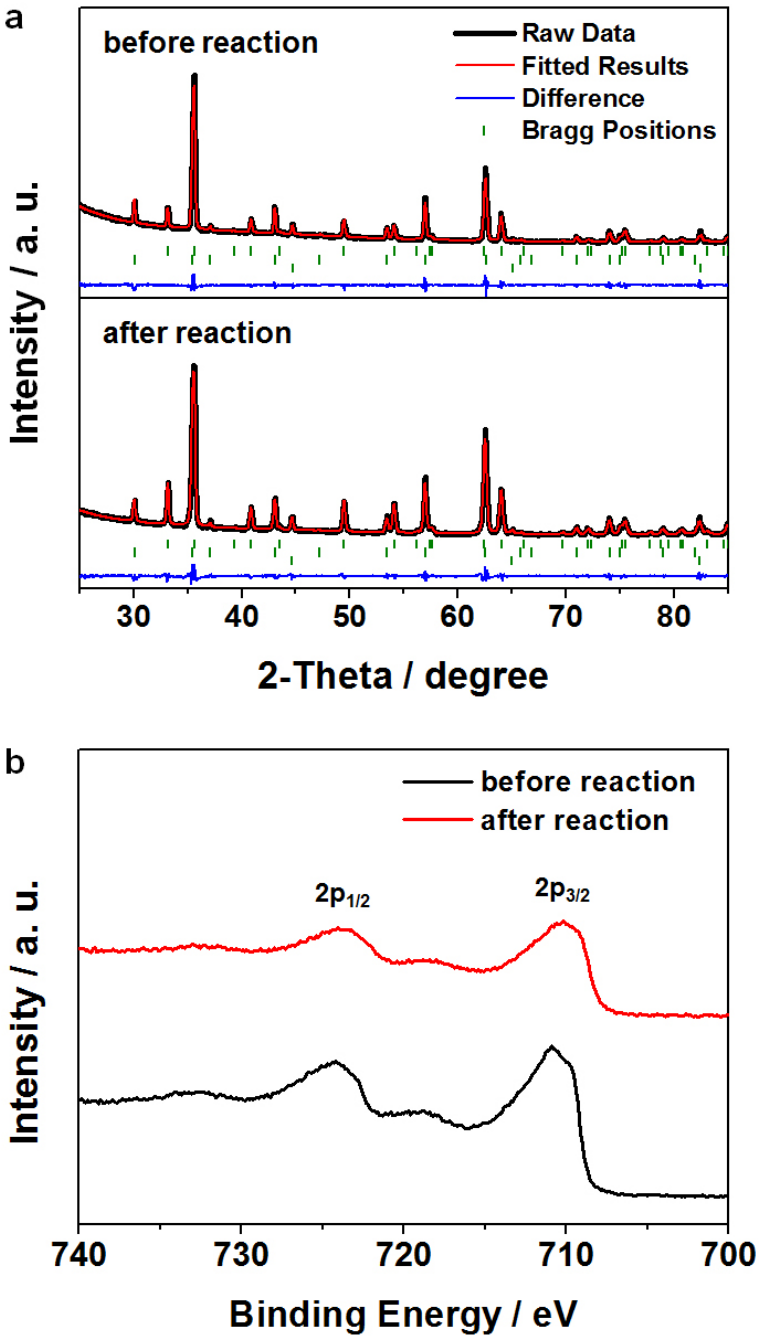


**Figure 5.19.** (a) Rietveld refinement results of the AFF phoaoanode's XRD patterns measured before and after 8 h of photoelectrochemical water splitting reaction. (b) Fe 2p XPS spectra of AFF before and after water splitting reaction.

| | Before reaction | | After reaction | |
|---|---|---|---|---|
| Phase | hematite | magnetite | hematite | magnetite |
| Weight fraction (%) | 57.71 | 42.49 | 60.14 | 39.86 |
| Molar fraction (%) | 66.43 | 33.57 | 68.63 | 31.37 |
| Lattice parameters (Å) | a: 5.03<br>c: 13.73 | a: 8.40 | a: 5.03<br>c: 13.73 | a: 8.39 |
| Reliability factors | $R_p$:8.42<br>$R_{wp}$:11.4<br>$R_{exp}$:6.87 | | $R_p$:8.13<br>$R_{wp}$:10.9<br>$R_{exp}$:6.83 | |

**Table 5.4.** Parameters obtained by Rietveld refinements of XRD patterns of AFF before and after water splitting reactionunder 1 sun illumination for 8 h at 1.23 V vs. RHE.

density). In contrast to the phase transformation of the iron oxide and change in the surface state, there was no significant change in the morphology of the AFF, as can be seen from the SEM images taken before (Figsure 5.20a and 5.20b) and after (Figure 5.20c and 5.20d) the 8 h of water splitting.

Since water photooxidation kinetics on the iron oxide surface is known to be slow, we decorated the surface of AFF with Co cocatalysts by electrodeposition as reported elsewhere [54], in order to further increase the photoelectrochemical water splitting performance of AFFs. As shown in the schematic image and electron microscope images in Figure 5.21, Co cocatalysts were deposited on the iron oxide nanoflakes' surface in the form of nanoparticles. This was confirmed by the SEM images taken before (Figure 5.21b and 5.21c) and after (Figure 5.21d and 5.21e) the Co decoration, and also by the HR-TEM analyses (Figure 5.21f) where lattice spacing of Co (101) is clearly visible. Elemental EDS maps (Figure 5.21g-5.21i) of the region shown in Figure 5.21f also shows that the Co deposition has been successful. Figure 5.22 shows the photoelectrochemical performance of Co decorated AFF photoanode. Compared to the case of bare AFF, the onset of PEC water splitting has shifted in negative direction by around 0.1 V, and the photocurrent density have increased in large amount. The photocurrent density at 1.23 V vs. RHE exceeded 3 mA $cm^{-2}$ with the IPCE value at 400 nm over 50%. Also the photocurrent density reached 7 mA $cm^{-2}$ before the dark current onset, which is the highest value ever reported.

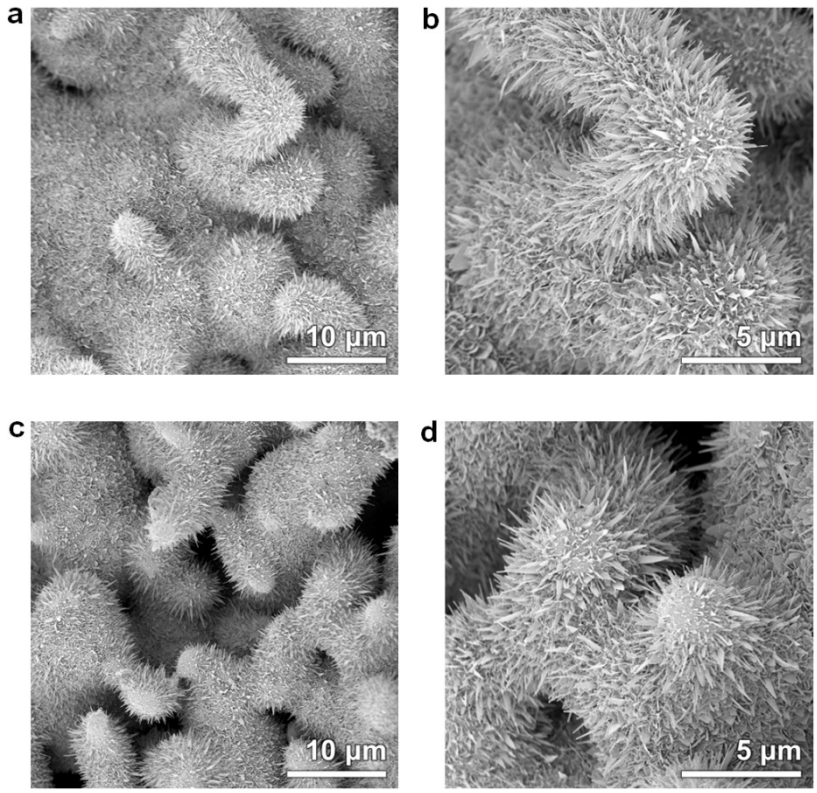


**Figure 5.20.** SEM images of AFF photoanode (a,b) before and (c,d) after 8 h of photoelectrochemical water splitting reaction.

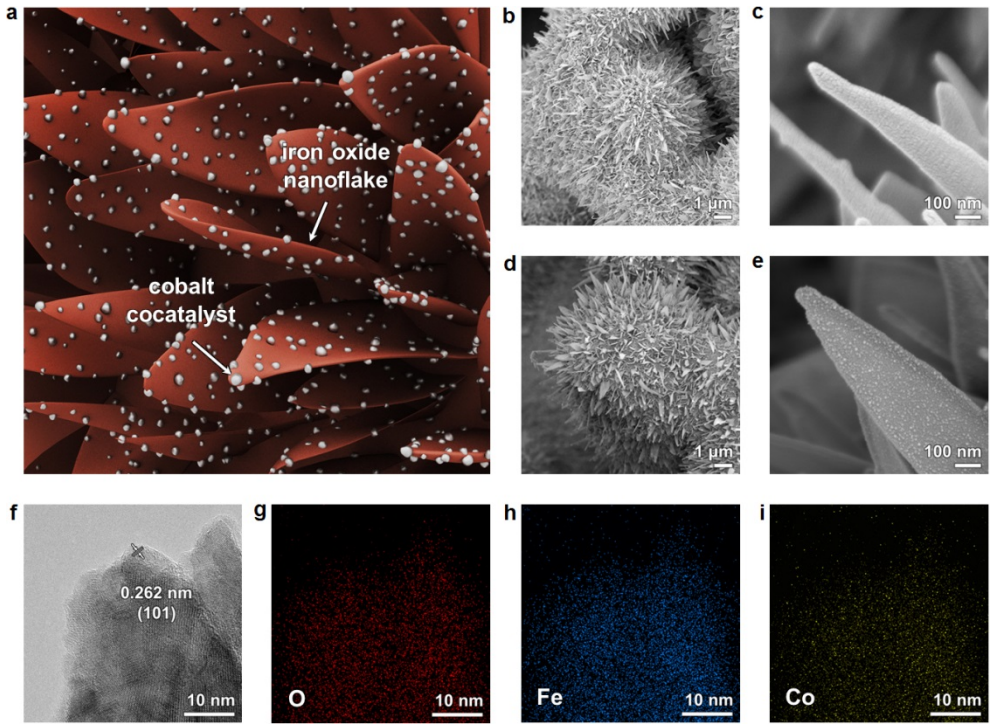


**Figure 5.21.** (a) Schematic of AFF photoanode with Co cocatalysts decorated on the surface. (b) SEM images of AFF (b,c) before and (d,e) after the deposition of Co cocatalysts. (f) HR-TEM image and (g-i) elemental EDS (g) O, (h) Fe, and (i) Co maps of Co decorated AFF.

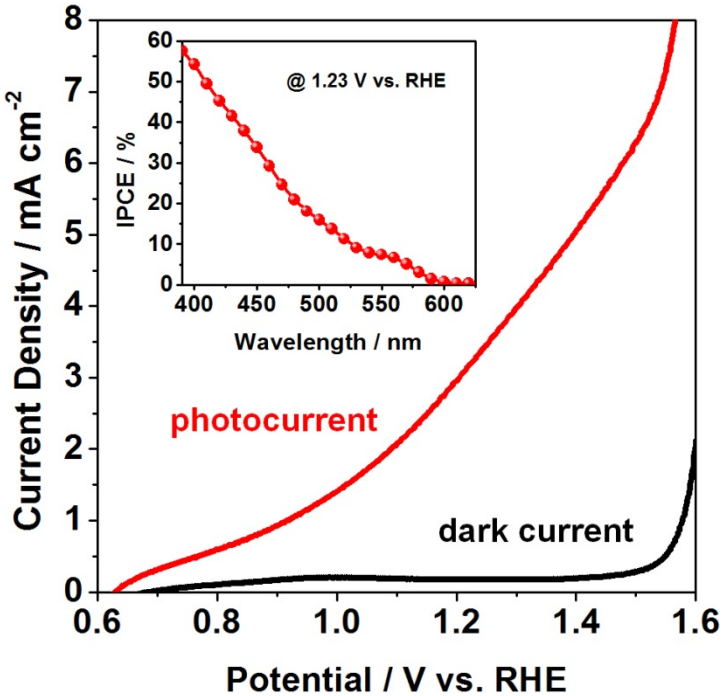


**Figure 5.22.** *J-V* characteristic of the photoelectrochemical water splitting cell based on AFF photoanode with Co cocatalysts decorated on the surface and the IPCE data in the inset.

## 5.4. Conclusions

In summary, we have demonstrated the general benefits of anodized metal foam photoelectrodes by investigating anodized Ti and Fe foams in DSCs and PWSCs, respectively. ATFs with hierarchical pore structure for use as photoanodes in DSCs resulted in a three-fold improvement in the photocurrent generation. Furthermore, we observed a photocurrent density exceeding 5 mA $cm^{-2}$ prior to the onset of water electrolysis by using AFFs in PWSCs. Although the ATF-DSCs developed in this study show a lower photovoltage and fill factor as compared to those of conventional DSCs, there is room for further optimization in terms of additional surface treatment and device architecture. The anodized metal foams are promising, because they have ideal characteristics such as a large surface area, low-dimensionally confined semiconductor nanostructure, and three-dimensional metal foam current collector with a very low electrical resistance. These combinations of advantages present in the ATF-DSCs and AFF-PWSCs are anticipated to advance the current technology of photoelectrochemical cells.

## 5.5. References


[1] O'Regan, B.; Grätzel, M., *Nature* **1991**, *353*, 737.

[2] Grätzel, M., *Nature* **2001**, *414*, 338.

[3] Hagfeldt, A.; Grätzel, M., *Chem. Rev.* **1995**, *95*, 49.

[4] Grätzel, M., *Accounts Chem. Res.* **2009**, *42*, 1788.

[5] Hagfeldt, A.; Boschloo, G.; Sun, L.; Kloo, L.; Pettersson, L., *Chem. Rev.* **2010**, *110*, 6595.

[6] Feldt, S. M.; Gibson, E. A.; Gabrielsson, E.; Sun, L.; Boschloo, G.; Hagfeldt, A., *J. Am. Chem. Soc.* **2010**, *132*, 16714.

[7] Yella, A.; Lee, H.-W.; Tsao, H. N.; Yi, C.; Chandiran, A. K.; Nazeeruddin, M. K.; Diau, E. W.-G.; Yeh, C.-Y.; Zakeeruddin, S. M.; Grätzel, M., *Science* **2011**, *334*, 629.

[8] Yum, J.-H.; Baranoff, E.; Kessler, F.; Moehl, T.; Ahmad, S.; Bessho, T.; Marchioro, A.; Ghadiri, E.; Moser J.-E.; Yi, C.; Nazeeruddin, M. K.; Grätzel, M., *Nat. Commun.* **2012**, *3*, 631.

[9] Matthew, S.; Yella, A.; Gao, P.; Humphry-Baker, R.; Curchod, B. F. E.; Ashari-Astani, N.; Tavernelli, I.; Rothlisberger, U.; Nazeeruddin, M. K.; Grätzel, M., *Nat. Chem.* **2014**, *6*, 242.

[10] Kim, H.-S.; Lee, C.-R.; Im, J.-H.; Lee, K.-B.; Moehl, T.; Marchioro, A.; Moon, S.-J.; Humphry-Baker, R.; Yum, J.-H.; Moser, J. E.; Grätzel, M.; Park, N.-G., *Sci. Rep.* **2012**, *2*, 591.

[11] Lee, M. M.; Teuscher, J.; Miyasaka, T.; Murakami, T. N.; Snaith, H. J., *Science* **2012**, *338*, 643.

[12] Burschka, J.; Pellet, N.; Moon, S.-J.; Humphry-Baker, R.; Gao, P.; Nazeerudding, M. K.; Grätzel, M., *Nature* **2013**, *499*, 316.

[13] Jose, R.; Thavasi, V.; Ramakrishna, S., *J. Am. Ceram. Soc.* **2009**, *92*, 289.

[14] Macák, J. M.; Tsuchiya, H.; Ghicov, A.; Schmuki, P., *Electrochem. Commun.* **2005**, *7*, 1133.

[15] Mor, G. K.; Shankar, K.; Paulose, M.; Varghese, O. K.; Grimes, C. A., *Nano Lett.* **2006**, *6*, 215.

[16] Varghese, O. K.; Paulose, M.; Grimes, C. A., *Nat. Nanotechnol.* **2009**, *4*, 592.

[17] Roy, P.; Berger, S.; Schmuki, P., *Angew. Chem. Int. Ed.* **2011**, *50*, 2904.

[18] Law, M.; Greene, L. E.; Johnson, J. C.; Saykally, R.; Yang, P., *Nat. Mater.* **2005**, *4*, 455.

[19] Feng, X.; Shankar, K.; Varghese, O. K.; Paulose, M.; Latempa, T. J.; Grimes, C. A., *Nano Lett.* **2008**, *8*, 3781.

[20] Liu, B.; Aydil, E. S., *J. Am. Chem. Soc.* **2009**, *131*, 3985.

[21] Zhu, K.; Neale, N. R.; Miedaner, A.; Frank, A. J., *Nano Lett.* **2007**, ***7***, 69.

[22] Zhu, K.; Vinzant, B.; Neale, N. R.; Frank, A. J., *Nano Lett.* **2007**, *7*, 3739.

[23] Fujishima, A.; Honda, K., *Nature* **1972**, *238*, 37.

[24] Santato, C.; Odziemkowski, M.; Ulmann, M.; Augustynski, J., *J. Am. Chem. Soc.* **2001**, *123*, 10639.

[25] Iwase, A.; Kudo, A., *J. Mater. Chem.* **2010**, *20*, 7536.

[26] Berglund, S. P.; Flaherty, D. W.; Hahn, N. T.; Bard, A. J.; Mullins, C. B., *J. Phys. Chem. C* **2011**, *115*, 3794.

[27] Kay, A.; Cesar, I.; Grätzel, M., *J. Am. Chem. Soc.* **2006**, *128*, 15714.

[28] Tilley, S. D.; Cornuz, M.; Sivula, K.; Grätzel, M., *Angew. Chem. Int. Ed.* **2010**, *49*, 6405.

[29] Warren, S. C.; Voïtchovsky, K.; Dotan, H.; Leroy, C. M.; Cornuz, M.; Stellacci, F.; Hébert, C.; Rothschild, A.; Grätzel, M., *Nat. Mater.* **2013**, *12*, 842.

[30] Sivula, K.; Zboril, R.; Le Formal, F.; Robert, R.; Weidenkaff, A.; Tucek, J.; Frydrych, J.; Grätzel, M., *J. Am. Chem. Soc.* **2010**, *132*, 7436–7444.

[31] Mohapatra, S. K.; John, S. E.; Banerjee, S.; Misra, M., *Chem. Mater.* **2009**, *21*, 3048.

[32] Sivula, K.; Le Formal, F; Grätzel, M., *ChemSusChem* **2011**, 4, 432.

[33] Klahr, B.; Gimenez, S.; Fabregat-Santiago, F.; Hamann, T.; Bisquert, J., *J. Am. Chem. Soc.* **2012**, *134*, 4294.

[34] Barroso, M.; Mesa, C. A.; Pendlebury, S. R.; Cowan, A. J.; Jisatomi, T.; Sivula, K.; Grätzel, M.; Klug, D. R.; Durrant, J. R., *Proc. Natl. Acad. Sci. USA* **2012**, *109*, 15640.

[35] Murphy, A. B.; Barnes, P. R. F.; Randeniya, L. K.; Plumb, I. C.; Grey, I. E.; Horne, M. D.; Glasscock, J. A., *Int. J. Hydrogen Energy* **2006**, *31*, 1999.

[36] Macák, J. M.; Tsuchiya, H.; Schmuki, P., *Angew. Chem. Int. Ed.* **2005**, *44*, 2100.

[37] Prakasam, H. E.; Shankar, K.; Paulose, M.; Varghese, O. K.; Grimes, C. A., *J. Phys. Chem. C* **2007**, *111*, 7235.

[38] Chino, Y.; Dunand, D. C., *Acta Mater.* **2008**, *56*, 105.

[39] Paulose, M.; Shankar, K.; Yoriya, S.; Prakasam, H. E.; Varghese, O. K.; Mor, G. K.; Latempa, T. A.; Fitzgerald, A.; Grimes, C. A., *J. Phys. Chem. B* **2006**, *110*, 16179.

[40] Sommeling, P. M.; O'Regan, B.; Haswell, R. R.; Smit, H. J. P.; Bakker, N. J.; Smits, J. J. T.; Kroon, J. M.; van Roosmalen, J. A. M., *J. Phys. Chem. B* **2006**, ***110***, 19191.

[41] Papageorgiou, N.; Maier, W. F.; Grätzel, M., *J. Electrochem. Soc.* **1997**, *144*, 876.

[42] Liu, Y.; Che, R.; Chen, G.; Fan, J.; Sun, Z.; Wu, Z.; Wang, M.; Li, B.; Wei, J.; Wei, Y.; Wang, G.; Guan, G.; Elzatahry, A. A.; Bagabas, A. A.; Al-Enizi, A. M.; Deng, Y.; Peng, H.; Zhao, D., *Sci. Adv.* **2015**, *1*, e1500166.

[43] Kim, J.-Y.; Lee, K. J.; Kang, S. H.; Shin, J.; Sung, Y.-E., *J. Phys. Chem. C* **2011**, *115*, 19979.

[44] Longo, C.; Nogueira, A. F.; De Paoli, M.-A., *J. Phys. Chem. B* **2002**, *106*, 5925.

[45] Chen, Z.; Tang, Y.; Yang, H.; Xia, Y.; Li, F.; Yi, T.; Huang, C., *J. Power Sources* **2007**, *171*, 990.

[46] Koops, S. E;, O'Regan, B. C.; Barnes, P. R. F.; Durrant, J. R., *J. Am. Chem. Soc.* **2009**, *131*, 4808.

[47] Fabregat-Santiago, F.; Bisquert, J.; Palomares, E.; Otero, L.; Kuang, D.; Zakeeruddin, S. M.; Grätzel, M., *J. Phys. Chem. C* **2007**, *111*, 6550.

[48] Prakasam, H. E.; Varhese, O. K.; Paulose, M.; Mor, G. P.; Grimes, C. A., *Nanotechnology* **2006**, *17*, 4285.

[49] Lim, J. H.; Choi, J., *Small* **2007**, *3*, 1504.

[50] Wu, J.; Liu, L.; Liu, S.; Yu, P.; Zheng, Z.; Shafa, M.; Zhou, Z.; Li, H.; Ji, H.; Wang, Z. M., *Nano Lett.* **2014**, *14*, 6002.

[51] Hisatomi, T.; Brillet, J.; Cornuz, M.; Le Formal, F.; Tétreault, N., Sivula, K.; Grätzel, M., *Faraday Discuss.* **2012**, *155*, 223.

[52] Wagner, C. D.; Riggs, W. M.; Davi, L. E.; Moulder, J. F.; Muilenberg, G. E., *Handbook of X-ray Photoelectron Spectroscopy*, Perkin-Elmer (Physical Electronics Division), Eden-Priarie: MN, **1979**.

[53] Kim, T. W.; Choi, K.-S., *Science* **2014**, *343*, 990.

[54] Liu, Q.; He, J.; Yao, T.; Sun, Z.; Cheng, W.; He, S.; Xie, Y.; Peng, Y.; Cheng, H.; Sun, Y.; Jiang, Y.; Hu, F.; Xie, Z.; Yan, W.; Pan, Z.; Wu, Z.; Wei, S., *Nat. Commun.* **2014**, *5*, 5122.

# Chapter 6. Electrochemically synthesized tungsten carbide as electrocatalytic counter electrode

## 6.1. Introduction

Dye-sensitized solar cells (DSCs) are attractive photoelectrochemical energy conversion devices that are economic and easy to manufacture, aesthetically feasible, and reliable in performance [1-6]. DSCs are generally composed of a photoelectrode based on dye-sensitized metal oxide semiconductor, electrocatalytic counter electrode, and an electrolyte containing redox couples. Nanostructured $TiO_2$ with adsorbed light-absorbing sensitizers on the surface and platinzed FTO glass have been the best performing photoelectrode and counter electrode, respectively, and $I_3^-/I^-$ or $[Co(bpy)_3]^{3+/2+}$ redox electrolytes are generally employed [7-12]. Among these components, Pt-based counter electrode occupies significant portion of fabrication cost, and therefore numerous attempts to replace Pt were made [13-23].

In various field of electrochemical energy conversion, tungsten based materials have been frequently used due to their favorable band positions, chemical stability, high conductivity, and electrocatalytic activity [24-33]. Among them, WC has been under the most intensive research because of its Pt-like behavior due to the electronic structure [34,35] In 2010, Jang et al. first applied mesoporous tungsten carbide materials in a counter electrode of DSCs, and achieved the energy conversion efficiency comparable to the conventional DSCs with Pt counter was obtained [36]. Also, in 2011, Wu et al. reported DSCs based on WC and MoC counter electrodes. With the assistance of ordered mesoporous carbon supports, they achieved energy conversion efficiencies higher than that of DSCs employing

Pt counter electrode [37]. This work gave rise to the numerous research works dealing with carbide electrocatalysts for DSCs [21,22].

Among processes for the preparation of nanostructured electrodes, electrochemical anodization is a fascinating method because of its highly facile and reproducible characteristics [38-41]. Also, top-down fabrication of ordered nanostructure on conductive metal substrate is superior to the bottom-up formation which often requires heat treatment at high temperature or support materials. For a successful anodization of a certain metal foil, rate of oxide formation and dissolution should be comparable [40]. Therefore, solution that moderately dissolves oxide is appropriate as an electrolyte for the anodization. For the synthesis of nanoporous anodic $WO_3$ layers by anodic oxidation of W metal, acidic solutions have been frequently employed [42-46]. The fabricated $WO_3$ has been used for various purposed including electrochromic device [45] and gas sensor [46].

In this research, nanoporous WC electrode was prepared by anodization of W foil followd by heat treatment in CO atmosphere, which is a well-known method used for the C-doping of metal oxides [47]. By physicochemical characterizations, we verified that the fabricated materials were WC with nanostructures favorable for electrochemical energy applications. Due to the instability of W metal substrate in the presence of highly corrosive iodide redox couple, the WC electrode was employed as a counter electrode for a DSC based on Y123 organic sensitizer [48] and $[Co(bpy)_3]^{3+/2+}$ redox electrolyte. WC outperformed Pt in various electrochemical and photoelectrochemical evaluations, and investigations for further understandings of kinetics were performed by electrochemical impedance spectroscopy.

## 6.2. Experimental section

### 6.2.1. Preparation of nanostructured $WO_3$ and WC electrodes

All the reagents used in this study were research grade products of Sigma-Adrich (otherwise stated) and were used without further purification. Tungsten foil (99.95%, 0.1 mm thick, Alfa Aesar) was cut into 1.5 cm × 2.0 cm size, and these foils were washed with the assistance of ultrasonication in acetone, ethanol, and deionized (DI) water for 10 min each. Then the W metal foils were anodized in 1 M $H_2SO_4$ aqueous solution containing 0.5 wt% NaF at 40 V for 2 h. Pt mesh was employed as a counter electrode for the anodic oxidation reaction, and the distance between the two electrodes was 3 cm. After the anodization, the foils were washed with ethanol and placed in a dry desicator. For the fabrication of crystalline $WO_3$ films, the anodized foils were thermally annealed at 450 °C for 4 h in air, and for the preparation of WC films, the foils were heat treated at 800 °C for 4 h in CO atmosphere.

### 6.2.2. Fabrication of reference Pt counter electrodes and dye-sensitized solar cell assembly

Conventional Pt counter electrodes were prepared by the thermal decomposition method [49]. Isopropanol containing 50 mM $H_2PtCl_6$ was cast on FTO glass by spin-coating method, and the coated FTO glass was thermally treated at 400 °C for 20 min in air. For the fabrication of mesoporous $TiO_2$ photoanodes, commercial $TiO_2$ paste (DSL 18NR-T, Dyesol) was doctor-bladed onto the FTO glass which was pretreated with 0.64 mM $TiCl_4$ aqueous solution for the formation of $TiO_2$ blocking layer. Then the electrodes were sintered at 500 °C for 30 min in air for the removal of the solvent and organic binders and also for the enhanced connectivity between the $TiO_2$ nanoparticles. In addition, $TiCl_4$ post-treatments were performed by using 0.25 mM $TiCl_4$ aqueous solution in order to increase the dye-loading

amounts and facilitate the electron injection from the dye molecules to the $TiO_2$ conduction band [50,51]. The electrodes were placed in 0.1 mM Y123 dye (DN-F05Y, Dyenamo) solution of which solvent was mixture of acetonitrile and *tert*-butanol for 48 h at 30 °C for the anchoring of dye molecules on the $TiO_2$ surface. For the assembly of DSCs, 25 μm thick thermoplastic sealants (Surlyun, Dupont) were used as spacer and the $[Co(bpy)_3]^{3+/2+}$ electrolyte with compositions as former reports [10] was injected through the pre-drilled holes located at the photoanode side.

### 6.2.3. Physical, electrochemical, and photoelectrochemical characterization of materials and devices

The morphologies of the fabricated materials were characterized with a scanning electron microscope (SEM; Carl Zeiss AURIGA) and a transmission electron microscope (TEM; JEM-2100F) equipped with an energy dispersive spectroscopy (EDS) facility. The X-ray diffraction (XRD) patterns were obtained with Rigaku D-MAX2500-PC, and the X-ray photoelectron spectroscopy (XPS) spectra were recorded by Thermo SIGMA PROBE. Cyclic voltammetry (CV) analyses were performed by using a potentiostat (Metrohm Autolab PGSTAT128N). During the CV measurements, a Pt mesh and an Ag/AgCl (saturated KCl) electrode were used as a counter electrode and a reference electrode, respectively, and the scan rate was fixed as 50 mV $s^{-1}$. For the evaluations of DSCs' performances, simulated AM 1.5G light with 100 mW $cm^{-2}$ intensity was irradiated by using a solar simulator (XIL model 05A50KS source measure units), and the responses from the solar cells were measured with Solartron 1480 multistat. Incident photon-to-current efficiency was measured with McScience K3100 composed of a xenon arc lamp and a monochromator. Electrochemical impedance spectroscopy (EIS) measurements were conducted by using Zahner Zennium electrochemical workstation with the sinusoidal perturbation of 10 mV.

## 6.3. Results and discussion

### 6.3.1. Physical characterizations of materials

Figure 6.1a-6.1d show the SEM images of anodic tungsten oxide before (Figure 6.1a and 6.1b) and after (Figure 6.1c and 6.1d) the thermal annealing at 450 °C for 4 h in air. The morphologies of the anodic oxides are interconnected structure with nanoscale pores. Meanwhile, as the heat treatment at 800 °C in CO atmosphere was performed after the anodization process, the nanostructures of the anodic oxide shrinked without damaging the overall porous macrostructure, as shown in the SEM images displayed in Figure 6.1e and 6.1f. This shrinking behavior is attributed to the replacement of 3 oxygen atoms with 1 carbon atom, which results in the decrease in the total volume of anodic tungsten compounds. Moreover, the depths of the anodic tungsten oxide and tungsten carbide were characterized by SEM analyses on the samples prepared by focused ion beam (FIB) milling. Figure 6.2a and 6.2b shows the cross-sectional view SEM images and the corresponding elemental EDS maps of the anodic tungsten oxide and carbide films, respectively. The thicknesses of the fabricated nanostructured tungsten compound layer were about 200 nm in both films, indicating that the transformation from oxide to carbide has been done without damaging the original nanostructure.

Additional characterizations on the morphologies were performed by TEM analyses. Figure 6.3a shows the porous structure of anodic tungsten oxide, and the lattice spacing of 0.31 nm displayed in the high resolution (HR)-TEM image in Figure 6.3b matches with the (112) plane of $WO_3$. Figure 6.3c and 6.3d show the TEM images of tungsten carbide, which also has porous nanostructure and crystallinity. The lattice spacing of 0.28 nm displayed in the HR-TEM image Figure 6.3d correspond to the (001) plane of WC. By keen observations at the edges of the tungsten carbide sample, the presence of carbon shells with thickness below 3 nm were observed, and they are shown in Figure 6.3f. By measuring the

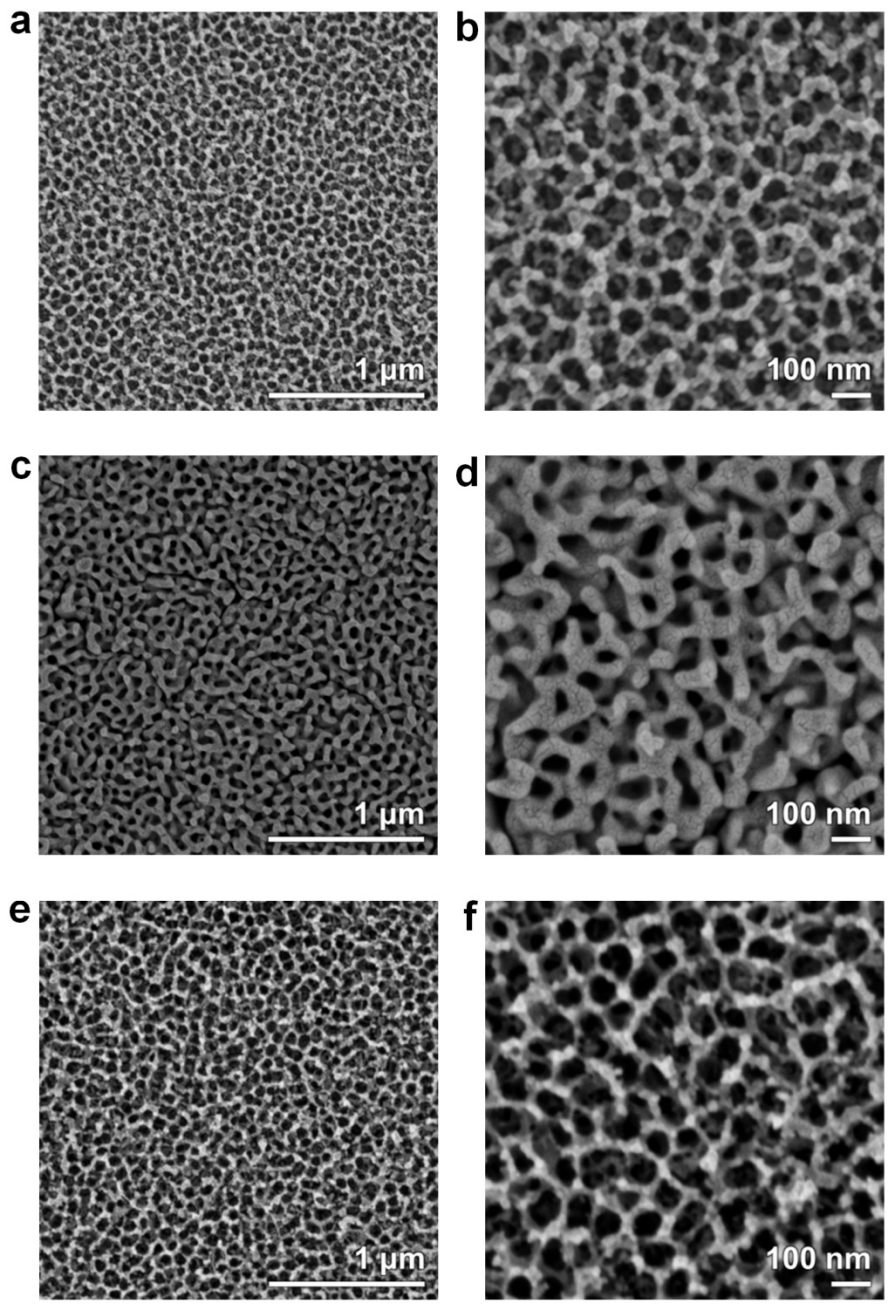


**Figure 6.1.** SEM images of anodized tungsten (a,b) before and after heat treatment in (c,d) air or (e,f) CO atmosphere.

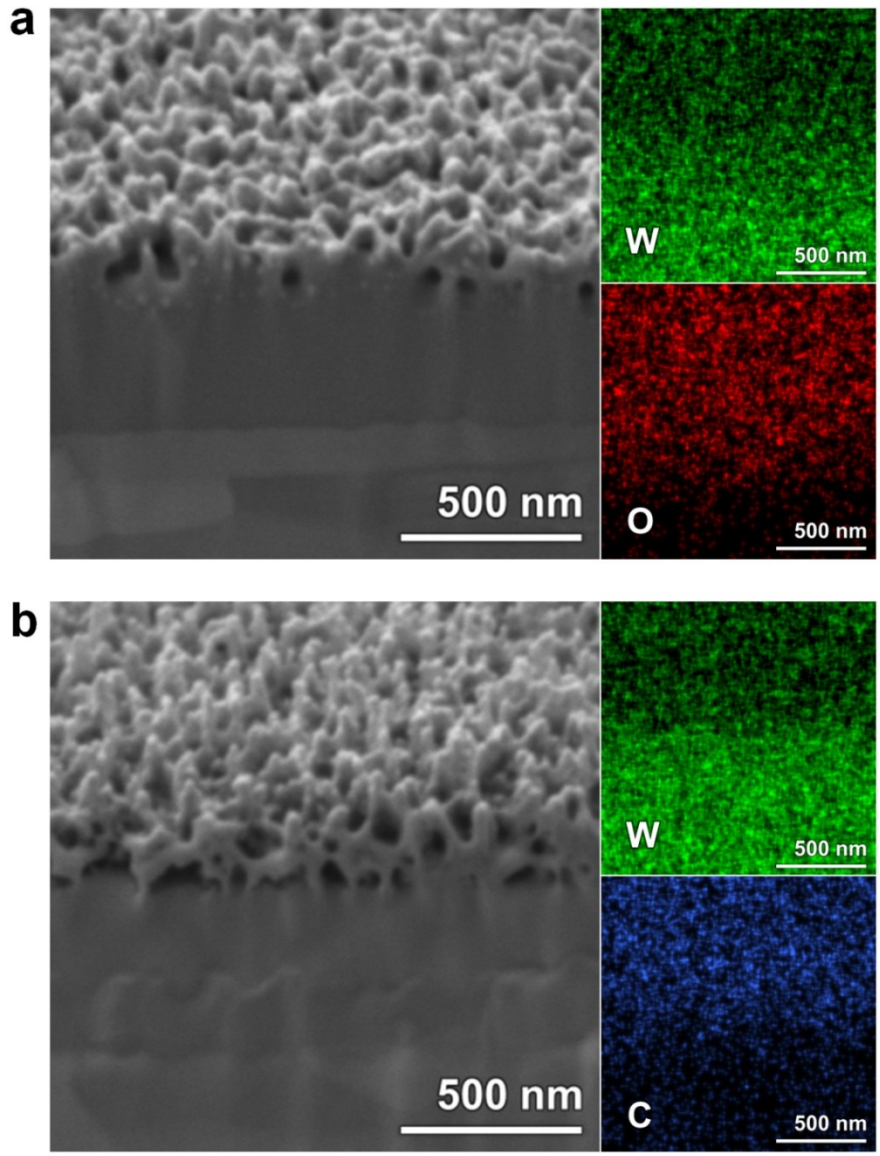


**Figure 6.2.** Cross-sectional view SEM images and corresponding elemental EDS maps of (a) tungsten oxide and (b) tungsten carbide. Samples were prepared by FIB milling before the imaging.

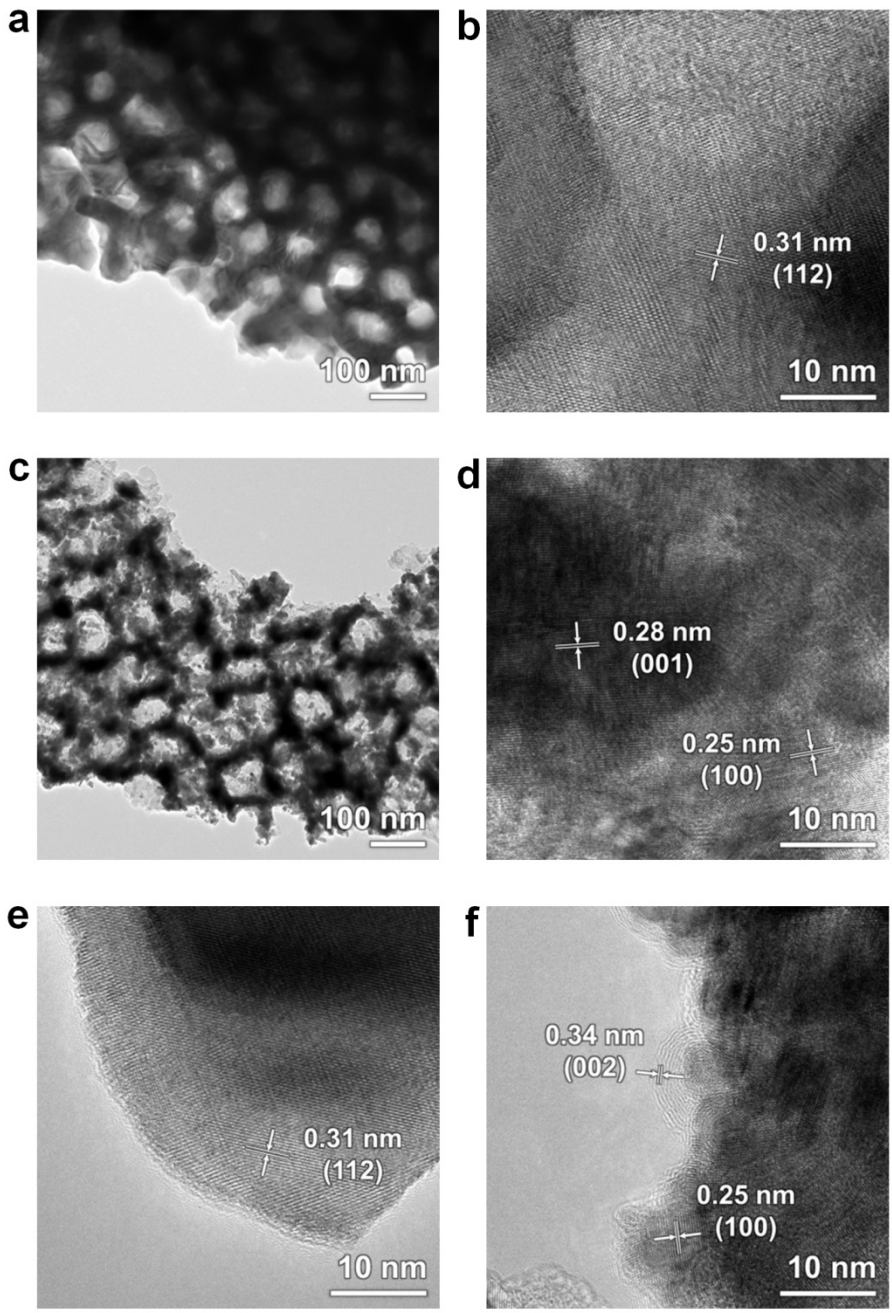


**Figure 6.3.** TEM images of (a,b) tungsten oxide and (e) its edge, and those of (c,d) tungsten carbide and (f) its edge with graphitic carbon shell.

lattice spacing, the carbon shells were addressed to be a graphitic carbon (0.33 nm lattice spacing at (002) plane), and confirmed the presence of WC below the shells (0.25 nm at (100) plane). On the contrary, there was no carbon shell observable at the $WO_3$ surface (Figure 6.3e). Moreover, elemental analyses were performed by scanning transmission electron microscopy (STEM) and EDS (Figure 6.4), and it was clearly verified that the nanostructure shown in the STEM images in Figure 6.4a is composed of W and O, and that shown in Figure 6.4b is constituted by W and C atoms.

Characterizations of the crystal structures of synthesized materials were performed with XRD analyses. Figure 6.5 shows the XRD patterns of bare tungsten, anodic tungsten oxide before and after the heat treatment in air or CO atmosphere. In all of the cases, presence of tungsten metal is clearly observed by the (110), (200), and (211) peaks located at 40.3°, 58.3°, and 73.2° 2-theta positions, respectively (assigned according to JCPDS 04-0806). As-anodized tungsten foil showed no characteristic peaks except for the metal substrate peaks, indicating that the materials formed on the surface are amorphous. In contrast, after annealing at 450 °C for 4 h in air, the $WO_3$ peaks (JCPDS 43-1035) became apparent. However, anodic tungsten oxide which went through the heat treatment at 800 °C for 8 h in CO atmosphere clearly showed WC (001), (100), and (101) peaks at 2-theta positions of 31.5°, 35.7°, and 48.3° (assigned by JCPDS 65-8828). This shows that the formation of crystalline WC has been successfully done. Moreover, the average crystallite size of the tungsten carbide was calculated by using Scherrer's equation and (100) peak, and the result was 13.78 nm. The average grain size of the tungsten oxide electrodes was hardly able to calculate due to the significant overlaps between the peaks.

Figure 6.6 shows the XPS spectra of the tungsten foil and synthesized samples. Survey spectra in Figure 6.6a show that there is negligible amount of elements other than W, O, and C in the tungsten, as-anodized tungsten, annealed

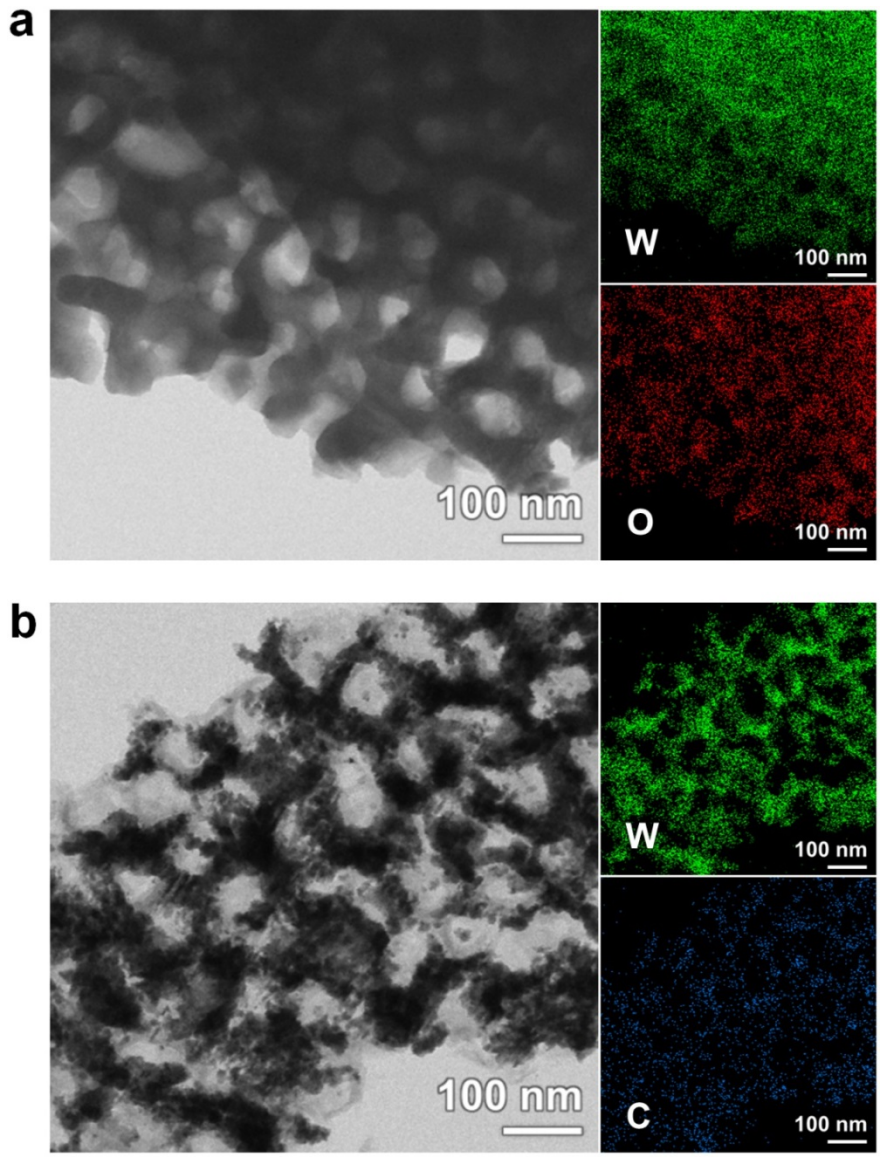


**Figure 6.4.** STEM images and corresponding elemental EDS maps of (a) tungsten oxide and (b) tungsten carbide.

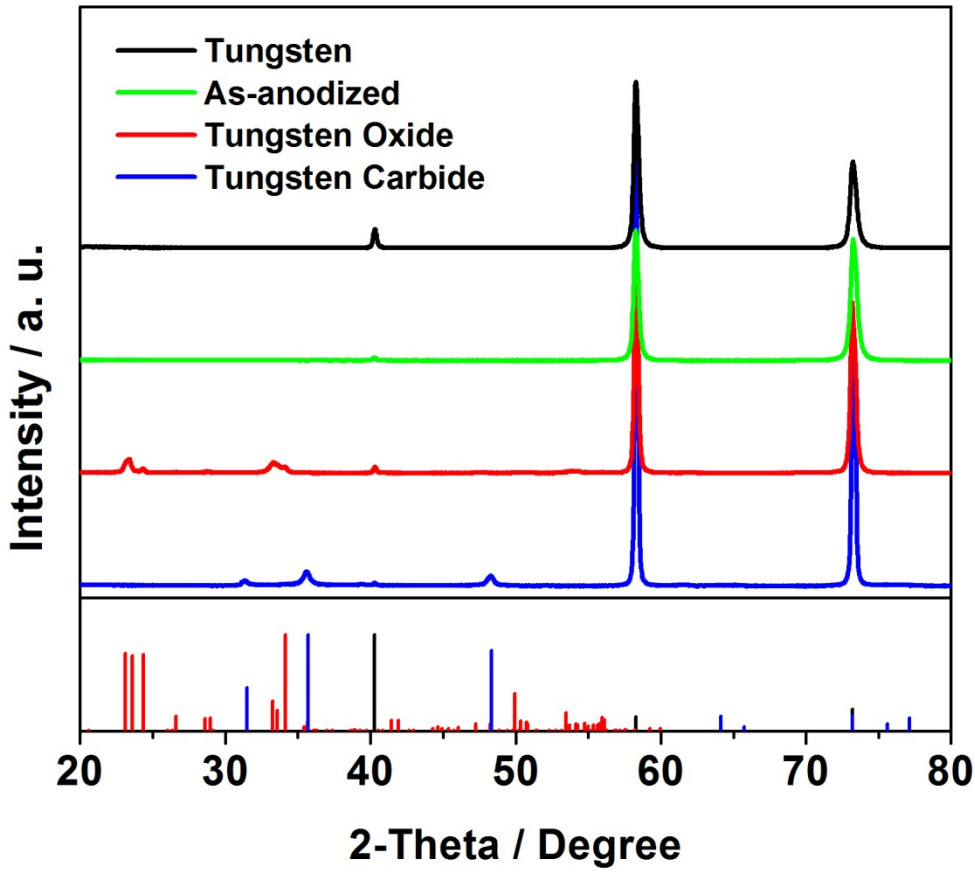


**Figure 6.5.** XRD patterns of tungsten foil and anodized tungsten before and after heat treatments in air or CO atmosphere.

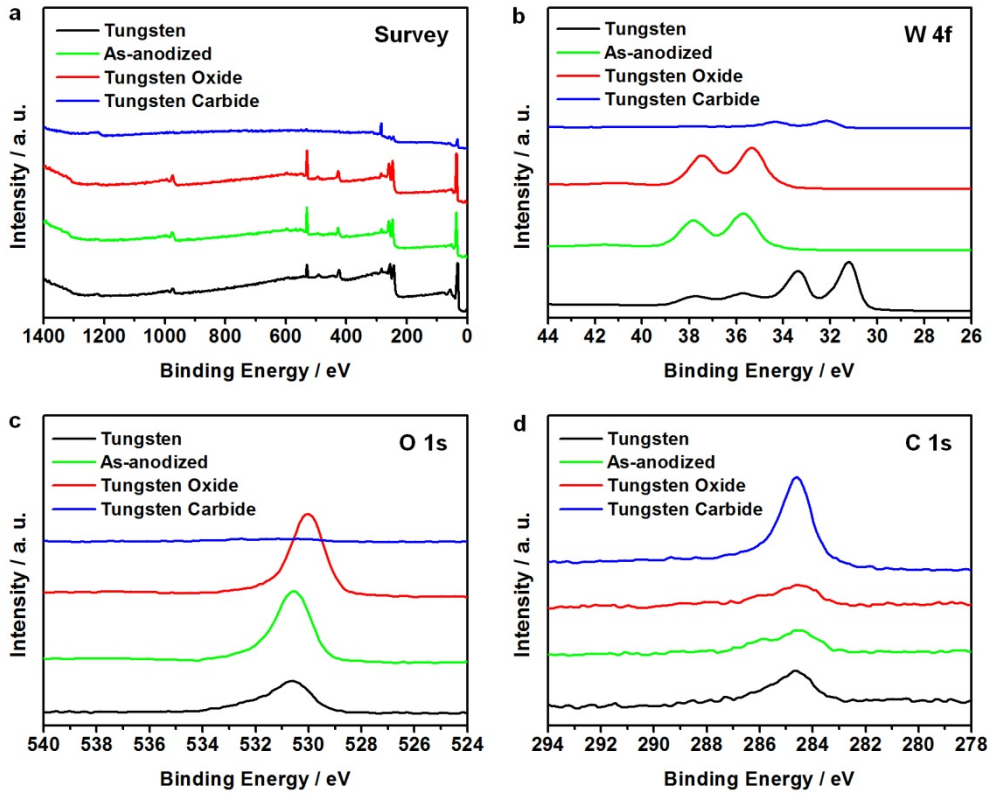


**Figure 6.6.** XPS (a) survey, (b) W 4f, (c) O 1s, and (d) C 1s spectra of tungsten foil and anodized tungsten before and after heat treatments in air or CO atmosphere.

tungsten oxide, and tungsten carbide samples. Also, by the comparison between the tungsten carbide and rest of the samples, it was clear that the transition from tungsten oxide to tungsten carbide has been distinctly done, because there was no oxygen related signals apparent at the tungsten carbide's survey data [52]. Figure 6.6b shows the W 4f XPS spectra of bare tungsten foil and synthesized electrodes before and after the post heat treatment at various atmospheres. In case of bare tungsten foil, peaks at 31.2 eV and 33.3 eV corresponding to the metallic W and minor peaks at 35.7 eV and 37.8 eV assigned to $WO_3$ species show that the foil is based on pure tungsten with very thin oxide layered formed on the surface [33]. In contrast, as-anodized tungsten foil shows only tungsten oxide peaks, indicating that the surface is totally covered with $WO_3$. Interestingly, the W 4f peaks were shifted to high binding energy in thermally annealed tungsten oxide samples, and this seems to be attributed to the proton intercalation from the moisture in air during the heat treatment. Since $WO_3$ is a well-known material with electrochromic property to proton and lithium cations [53,54], and as the thermally annealed tungsten oxide electrode shows blue color (see digital photograph image shown in Figure 6.7), the effect of proton intercalation is clear, because there is no possible route of $Li^+$ intercalation during the synthesis of tungsten oxide. This phenomenon is also apparent at the O 1s peak of the annealed tungsten oxide displayed in Figure 6.6c, which is shifted to a higher binding energy. One thing that should be stated at this point is that the as-anodized tungsten oxides were not affected by the proton intercalation because they were stored in a dry desicator, as mentioned in the experimental section. In case of the tungsten carbide electrode, the W 4f peaks were observed at 32.2 eV and 34.4 eV. Together with O 1s peak of negligible intensity, the presence of WC was clear. In all of the C 1s spectra shown in Figure 6d, there is only one peak at binding energy of 284.6 eV for all of the samples. Characteristic C 1s peak in WC is known to appear at around 283 eV [33]. However, in our result, there was no apparent signal at that binding energy. This

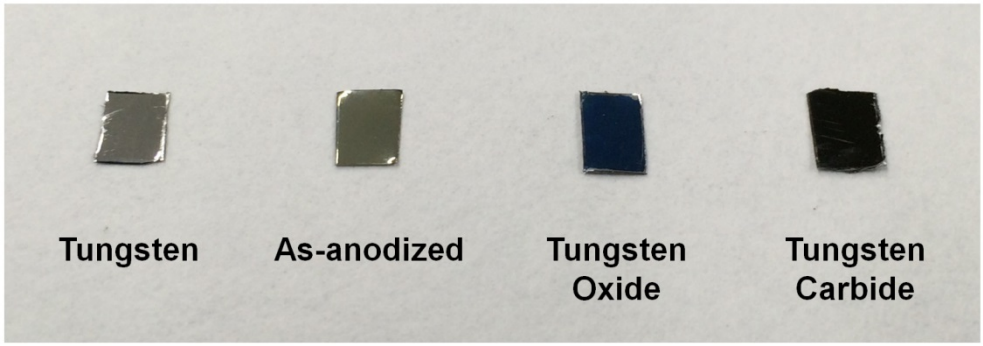


**Figure 6.7.** Digital photograph images of tungsten, as-anodized tungsten, tungsten oxide, and tungsten carbide.

seems to be the effect of graphitic carbon shells formed on the tungsten carbide surface, which blocks the X-rays to and signals from the WC.

### 6.3.2. Electrochemical and photoelectrochemical evaluations

The electrocatalytic activities of the prepared tungsten oxide, tungsten carbide, and platinized FTO electrodes were first investigated by CV analyses, and the CV diagram is shown in Figure 6.8. For the CV analyses, acetonitrile containing 10 mM $Co(bpy)_3(PF_6)_2$, 1 mM $Co(bpy)_3(PF_6)_3$, and 0.1 M $LiClO_4$ was used as the electrolyte. Among the three electrodes, tungsten oxide showed significantly low current density and late onset potentials. In contrast, tungsten carbide and Pt-FTO gave comparable results on the current densities. Therefore the comparison between these two electrodes was performed in detail. During the CV measurement, anodic current (positive current in Figure 6.8) is recorded as the potential is swept in positive direction, and cathodic current (negative current in Figure 6.8) is measured while the backward sweeping is being done. The onset and peak current density potentials appear earlier in Pt-FTO than in tungsten carbide in the anodic scan, indicating that Pt has a superior electrocatalytic activity compared to the WC. However, the peak current density was larger in tungsten carbide, possibly due to the large surface area based on its nanostructure. On the other hand, during the cathodic sweep, the onset, peak potential, and peak current density value were all higher in WC than Pt-FTO. Since the role of the counter electrode is an electrocatalyst for the reduction of the oxidized redox species in the electrolyte, it could be concluded that the tungsten carbide electrode is superior to the platinized FTO in performance. Though the electrolyte used for the CV measurement are much more dilute than the optimized electrolyte for real device applications, this result implies that the WC is a promising counter electrode for DSCs.

Figure 6.9 show the photocurrent density (*J*)-voltage (*V*) characteristics and IPCE spectra of DSCs employing tungsten oxide, tungsten carbide, and a platinized

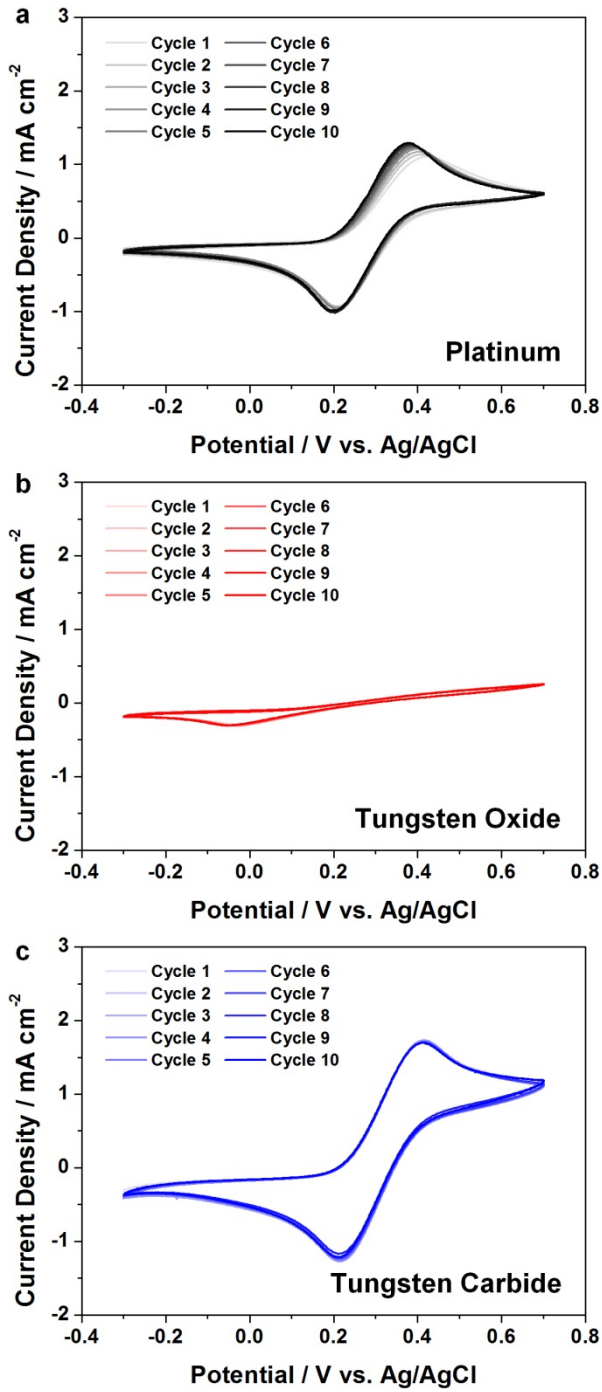


**Figure 6.8.** CV diagrams of platinum, tungsten oxide, and tungsten carbide in $[Co(bpy)_3]^{3+/2+}$ redox electrolyte.

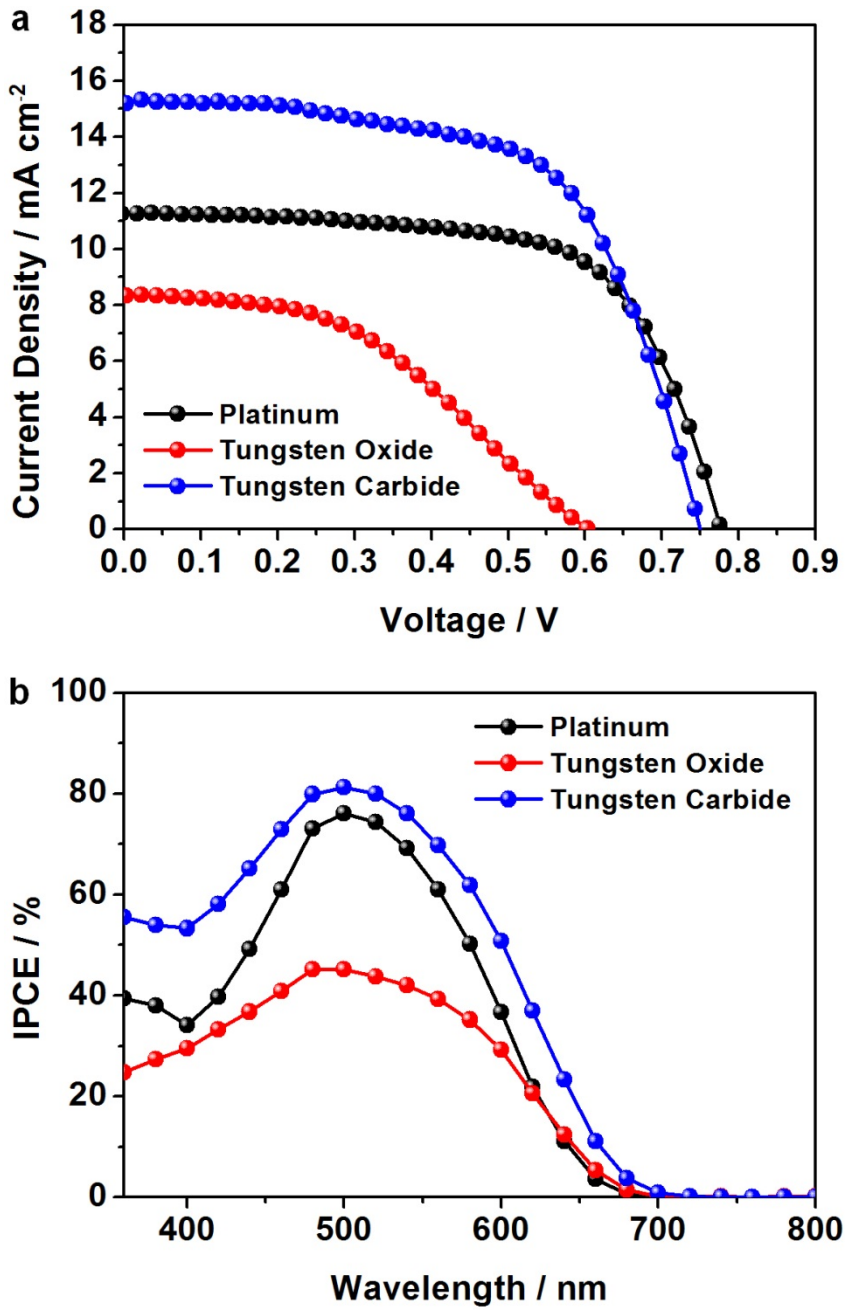


**Figure 6.9.** (a) *J-V* characteristics and (b) IPCE spectra of DSCs employing platinum, tungsten oxide, or tungsten carbide counter electrodes.

FTO glass as counter electrodes, and the open-circuit voltage ($V_{oc}$), short-circuit current density ($J_{sc}$), fill factor (*FF*), and the energy conversion efficiency ($\eta$) obtained from the *J-V* curves are displayed in Table 6.1. As could have been expected from the CV results, $WO_3$ showed the lowest values of all parameters, resulting in an efficiency of 2.18%. For the conventional DSC with Pt-FTO counter electrode, the $\eta$ increased to 5.68% with $V_{oc}$ of 0.776 V and $J_{sc}$ of 11.3 mA $cm^{-2}$. Moreover, as the tungsten carbide electrode is used as a counter, $\eta$ went up to 7.08% due to a dramatic rise in $J_{sc}$ to 15.2 mA $cm^{-2}$.

For the verification of relative charge transfer kinetics at the counter electrode/electrolyte interface, EIS analyses were performed. Figure 6.10a shows the Nyquist diagram of DSCs with Pt-FTO, tungsten oxide, and tungsten carbide counter electrode measured in dark condition with forward bias of 0.7 V. In contrast to the tungsten oxide case where one large semicircle is apparent, platinum and tungsten carbide employed DSCs showed clear three semicircles which correspond to the kinetics at counter electrode/electrolyte (high frequency region), electrolyte/photoanode (intermediate frequency region), and diffusion within the electrolyte (low frequency region). The first x-axis intercept shows the value of the series resistance ($R_s$), which indicates the general ohmic resistance of the cells. The $R_s$ was smaller in DSCs with tungsten carbide than those with platinum counter electrode. In Pt counter, FTO serves as the current collector, while the metallic tungsten foil beneath the nanoporous carbide layer does the same role in tungsten carbide electrode. Since the metal has significantly larger electric conductivity than the transparent conducting oxide, different current collectors is expected to be the most probable reason for the gap in $R_s$, and this seem to have contributed to the higher photovoltaic performance in DSCs employing tungsten carbide counter. Meanwhile, there was no significant difference in the size of semicircles at the intermediate frequency regions, because the photoanode used in this study were identical. Also, the semicircles at the low frequency region are also similar, and

| | $V_{oc}$ (V) | $J_{sc}$ (mA/cm$^2$) | *FF* (%) | $\eta$ (%) |
|---|---|---|---|---|
| Platinum | 0.776 | 11.3 | 64.8 | 5.68 |
| Tungsten Oxide | 0.605 | 8.3 | 43.2 | 2.18 |
| Tungsten Carbide | 0.753 | 15.2 | 61.9 | 7.08 |

**Table 6.1.** *J-V* characteristics of DSCs employing platinum, tungsten oxide, and tungsten carbide counter electrodes.

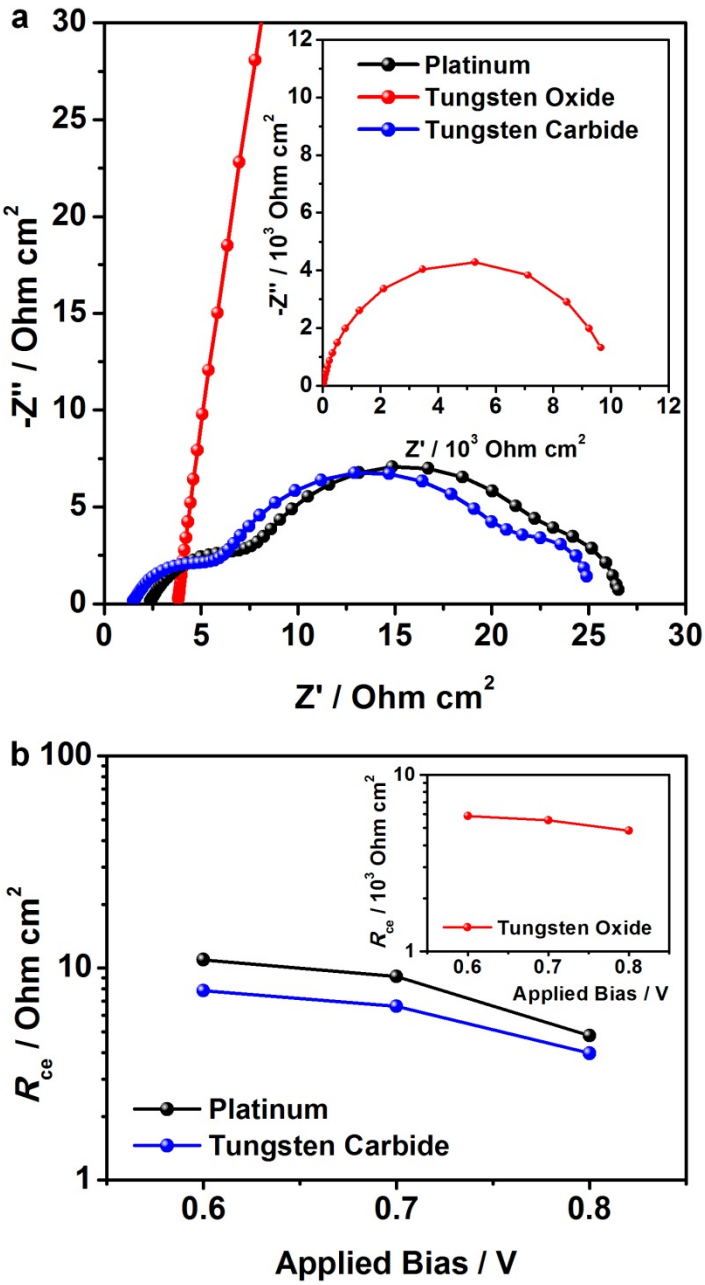


**Figure 6.10.** (a) Nyquist plotes of DSCs employing platinum, tungsten oxide, or tungsten carbide counter electrode obtained in dark condition with forward bias of 0.7 V. (b) Charge transfer resistance at counter electrode/electrolyte interface in DSCs under forward bias of 0.6, 0.7, and 0.8 V.

| Forward Bias / V | $R_{ce}$ / Ω cm$^2$ @ Platinum | $R_{ce}$ / Ω cm$^2$ @ Tungsten Oxide | $R_{ce}$ / Ω cm$^2$ @ Tungsten Carbide |
|---|---|---|---|
| 0.6 | 10.97 | 5859 | 7.82 |
| 0.7 | 9.11 | 5548 | 6.60 |
| 0.8 | 4.80 | 4834 | 3.97 |

**Table 6.2.** Charge transfer resistance at counter electrode/electrolyte interface under forward bias of 0.6, 0.7, and 0.8 V.

this indicates that the tungsten carbide electrode's nanoporous structure, of which pores are generally larger than 50 nm (Figure 6.1c and 6.1d), did not hinder the mass transport of the cobalt bipyridyl redox species.

In contrast, there was a notable difference at the semicircle shown in the high frequency region, the semicircle of tungsten carbide based DSC being smaller than the conventional Pt based one. The size of the semicircle is positively correlated to the charge transfer resistance at the counter electrode/electrolyte interface ($R_{ce}$), and smaller $R_{ce}$ means higher electrocatalytic activity. Therefore, it was clear from the EIS result that the activity of tungsten carbide was better than platinum. For a more accurate and quantitative comparison on $R_{ce}$ of the electrodes, the $R_{ce}$ values were obtained by fitting the high frequency EIS results measured with the forward bias of 0.6 V, 0.7 V, and 0.8 V using ZView software. The fitted parameters are displayed in Table 6.2 and Figure 6.10b. In all of the potentials, tungsten carbide gave lowest $R_{ce}$ values, and thus we could conclude that the high performance of DSCs with tungsten carbide counter is mainly attributed to the superior electrocatalytic activity.

## 6.4. Conclusions

In this research, nanoporous tungsten carbide was synthesized by electrochemical anodization and heat treatment at CO atmosphere. Compared to former studies on tungsten carbide electrocatalysts, this method is noteworthy, because the nanostructured electrode could be directly prepared by a top-down method based on the facile and reliable fabrication processes. Moreover, in DSCs based on the cobalt bipyridyl redox complexes and compatible organic sensitizers, the tungsten carbide showed better performance as an electrocatalytic counter electrode compared to the conventional state-of-the-art platinum electrode. Considering that the cobalt bipyridyl redox electrolyte - organic dye system gave the highest

efficiency in DSCs, and also that the manufacturing cost of tungsten carbide electrode is much more economical than that of platinum electrode, the findings in the research seems suggestive. Moreover, there are rooms for further optimizations and improvements, namely the pore size control in the mesoporous $TiO_2$ photoanode for enhanced electrolyte transport and utilization of sensitizers with higher extinction coefficient such as porphyrin derivatives. Since there are many other highly electrocatalytic nanostructured materials that could be synthesized by modifying our approach, there are possibilities for the design and synthesis of more advanced counter electrodes based on the results and approaches used in this research.

## 6.5. References


[1] O'Regan, B; Grätzel, M., *Nature* **1991**, *353*, 737.

[2] Hagfeldt, A.; Grätzel, M., *Chem. Rev.* **1995**, *95*, 49.

[3] Grätzel, M., *Nature* **2001**, *414*, 338.

[4] Grätzel, M., *Inorg. Chem.* **2005**, *44*, 6841.

[5] Grätzel, M., *Accounts Chem. Res.* **2009**, *42*, 1788.

[6] Hagfeldt, A.; Boschloo, G.; Sun, L.; Kloo, L.; Pettersson, H., *Chem. Rev.* **2010,** *110*, 6595.

[7] Nazeeruddin, M. K.; Kay, A.; Rodicio, I.; Humphry-Baker, R.; Müller, E.; Liska, P.; Vlachopoulos, N.; Grätzel, M., *J. Am. Chem. Soc.* **1993**, *115*, 6492.

[8] Chiba, Y.; Islam, A.; Watanabe, Y.; Komiya, R.; Koide, N.; Han, L., *Jpn. J. Appl. Phys.* **2006**, *45*, L368.

[9] Kinoshita, T.; Dy, J. T.; Uchida, S.; Kubo, T.; Segawa, H., *Nat. Photonics* **2013**, *7*, 535.

[10] Feldt, S. M.; Gibson, E. A.; Gabrielsson, E.; Sun, L.; Boschloo, G.; Hagfeldt, A., *J. Am. Chem. Soc.* **2010**, *132*, 16714.

[11] Yella, A.; Lee, H.-W.; Tsao, H. N.; Yi, C.; Chandiran, A. K.; Nazeeruddin, M. K.; Diau, E. W.-G.; Yeh, C.-Y.; Zakeeruddin, S. M.; Grätzel, M., *Science* **2011**, *334*, 629.

[12] Matthew, S.; Yella, A.; Gao, P.; Humphry-Baker, R.; Curchod, B. F. E.; Ashari-Astani, N.; Tavernelli, I.; Rothlisberger, U.; Nazeeruddin, M. K.; Grätzel, M., *Nat. Chem.* **2014**, *6*, 242.

[13] Wang, M.; Anghel, A. M.; Marsan, B.; Ha, N.-L. C.; Pootrakulchote, N.; Zakeeruddin, S, M.; Grätzel, M., *J. Am. Chem. Soc.* **2009**, *131*, 15976.

[14] Li, G. R.; Song, J.; Pan, G. L.; Gao, X. P., *Energy Environ. Sci.* **2011**, *4*, 1680.

[15] Sun, H.; Qin, D.; Huang, S.; Guo, X.; Li, D.; Luo, Y.; Meng, Q., *Energy Environ. Sci.* **2011**, *4*, 2630.

[16] Wang, Y.; Wu, M.; Lin, X.; Shi, Z.; Hagfeldt, A.; Ma, T., *J. Mater. Chem.* **2012**, *22*, 4009.

[17] Wu, M.; Zhang, Q.; Xiao, J.; Ma, C.; Lin, X.; Miao, C.; He, Y.; Gao, Y.; Hagfeldt, A.; Ma, T., *J. Mater, Chem.* **2011**, *21*, 10761.

[18] Mulmudi, H. K.; Batabyal, S. K.; Rao, M.; Prabhakar, R. R.; Mathews, N.; Lam, Y. M.; Mhaisalkar, S. G., *Phys. Chem. Chem. Phys.* **2011**, *13*, 19307.

[19] Guai, G. H.; Leiw, M. Y.; Ng, C. M.; Li, C. M., *Adv. Energy Mater.* **2012**, *2*, 334.

[20] Chi, W. S.; Han, J. W.; Yang, S.; Roh, D. K.; Lee, H.; Kim, J. H., *Chem. Commun.* **2012**, *48*, 9501.

[21] Wu, M.; Lin, X.; Wang, Y.; Wang, L.; Guo, W.; Qi, D.; Peng, X.; Hagfeldt, A.; Grätzel, M.; Ma, T., *J. Am. Chem. Soc.* **2012**, *134*, 3419.

[22] Liao, Y.; Pan, K.; Wang, L.; Pan, Q.; Zhou, W.; Miao, X.; Jiang, B.; Tian, C.; Tian, G.; Wang, G.; Fu, H., *ACS Appl. Mater. Interfaces* **2013**, *5*, 3663.

[23] Hou, Y.; Wang, D.; Yang, X. H.; Fang, W. Q.; Zhang, B.; Wang, H. F.; Lu, G. Z.; Hu, P.; Zhao, H. J.; Yang, H. G., *Nat. Commun.* **2013**, *4*, 1583.

[24] Costa, P. D.; Lemberton, J.-L.; Potvin, C.; Manoli, J.-M.; Perot, G.; Breysse, M.; Djega-Mariadassou, G., *Catal. Today* **2001**, *65*, 195.

[25] Oxley, J. D.; Mdleleni, M. M.; Suslick, K. S., *Catal. Today* **2004**, *88*, 139.

[26] Ganesan, R.; Lee, J. S., *Angew. Chem. Int. Ed.* **2005**, *44*, 6557.

[27] Hara, Y.; Minami, N.; Matsumoto, H.; Itagaki, H., *Appl. Catal. A: Gen.* **2007**, *332*, 289.

[28] Wang, Y.; Song, S.; Maragou, V.; Shen, P. K.; Tsiakaras, P., *Appl. Catal. B: Environ.* **2009**, *89*, 223.

[29] Zheng, H.; Tachibana, Y.; Kalantar-zadeh, K., *Langmuir* **2010**, *26*, 19148.

[30] Wu, M.; Lin, X.; Hagfeldt, A.; Ma, T., *Chem. Commun.* **2011**, *47*, 4535.

[31] Shi, X.; Choi, I. Y.; Zhang, K.; Kwon, J.; Kim, D. Y.; Lee, J. K.; Oh, S. H.; Kim, J. K., Park, J. H., *Nat. Commun.* **2014**, *5*, 4775.

[32] Ma, M.; Kim, J. K.; Zhang, K.; Shi, X.; Kim, S. J.; Moon, J. H.; Park, J. H., *Chem. Mater.* **2014**, *26*, 5592.

[33] Fan, X.; Zhou, H.; Guo, X., *ACS Nano* **2015**, *9*, 5125.

[34] Levy, R. B.; Boudadrt, M., *Science* **1973**, *181*, 547.

[35] Colton, R. J.; Huang, J.-T. J.; Rabalais, J. W., *Chem. Phys. Lett.* **1975**, *34*, 337.

[36] Jang, J. S.; Ham, D. J.; Ramasamy, R.; Lee, J.; Lee, J. S., *Chem. Commun.* **2010**, *46*, 8600.

[37] Wu, M.; Lin, X.; Hagfeldt, A.; Ma, T., *Angew. Chem. Int. Ed.* **2011**, *50*, 3520.

[38] Diggle, J. W.; Downie, T. C.; Goulding, C. W., *Chem. Rev.* **1969**, *69*, 365.

[39] Su, Z.; Zhou, W., *Adv. Mater.* **2008**, *20*, 3663.

[40] Roy, P.; Berger, S.; Schmuki, P., *Angew. Chem. Int. Ed.* **2011**, *50*, 2904.

[41] Lee, K.; Mazare, A.; Schmuki, P., *Chem. Rev.* **2014**, *114*, 9385.

[42] Mukherjee, N.; Paulose, M.; Varghese, O. K.; Mor, G. K.; Grimes, C. A., *J. Mater. Res.* **2003**, *18*, 2296.

[43] Tsuchiya, H.; Macak, J. M.; Sieber, I.; Taveira, L.; Ghicov, A.; Sirotna, K.; Schmuki, P., *Electrochem. Commun.* **2005**, *7*, 295.

[44] Hahn, R.; Macak, J. M.; Schmiki, P., *Electrochem. Commun.* **2007**, *9*, 947.

[45] Nah, Y.-C.; Ghicov, A.; Kim, D.; Schmuki, P., *Electrochem. Commun.* **2008**, *10*, 1777.

[46] Zeng, J.; Hu, M.; Wang, W.; Chen, H.; Qin, Y., *Sens. Actuators B: Chem.* **2012**, *161*, 447.

[47] Park, J. H.; Kim, S.; Bard, A. J., *Nano Lett.* **2006**, *6*, 24.

[48] Tsao, H. N.; Yi, C.; Moehl, T.; Yum, J.-H.; Zakeeruddin, S. M.; Nazeeruddin, M. K.; Grätzel, M., *ChemSusChem* **2011**, *4*, 591.

[49] N, Papageorgiou, N.; Maier, W. F.; Grätzel, M., *J. Electrochem. Soc.* **1997**, *144*, 876.

[50] Sommeling, P. M.; O'Regan, B. C.; Haswell, R. R.; Smit, H. J. P.; Bakker, N. J.; Smits, J. J. T.; Kroon, J. M.; Roosmalen, J. A. M., *J. Phys. Chem. B* **2006**, *110*, 19191.

[51] O'Regan, B. C.; Durrant, J. R.; Sommeling, P. M.; Bakker, N. J., *J. Phys. Chem. C* **2007**, *111*, 14001.

[52] Wagner, C. D.; Riggs, W. M.; Davi, L. E.; Moulder, J. F.; Muilenberg, G. E., *Handbook of X-ray Photoelectron Spectroscopy*, Perkin-Elmer (Physical Electronics Division), Eden-Priarie: MN, **1979**.

[53] Rosseinsky, D. R.; Mortimer, R. J., *Adv. Mater.* **2001**, *13*, 783.

[54] Deb, S. K., *Sol. Energy Mater. Sol. Cells* **2008**, *92*, 245.

# Chapter 7. Reactively sputtered nanostructured nickel nitride as electrocatalytic counter electrode

## 7.1. Introduction

On account of the limited fossil fuel quantities in the earth's surface, investigations into clean and renewable energy sources have been intensively performed for decades, with solar energy currently being considered as one of the most promising candidates to replace conventional energy sources. With the goal of efficiently using solar energy, various kinds of photovoltaics such as Si and thin film solar cells were proposed. Since 1991, after the pioneering report by Brian O'Regan and Michael Grätzel, mesoscopic dye-sensitized solar cells (DSCs) have attracted great attention due to their favorable characteristics: high performance and reliability, applicability of varied materials and designs, low manufacturing cost, and environmental compatibility [1-4]. In addition, quantum dot-sensitized solar cells (QDSCs), in which semiconducting quantum dots (QDs) are utilized as the light-harvesting units, also have been intensively studied due to QDs' attractive properties, such as the ability for band energy tuning, high absorption coefficients, and the multiple exciton generation effect [5-8].

Ruthenium complexes [9,10] and chalcogenide nanoparticles (such as CdS, CdSe, and PbS) [5,6,11,12] have been employed as typical sensitizers for DSCs and QDSCs, respectively. For the construction of highly efficient mesoscopic sensitized solar cells, the redox couple in the electrolyte should efficiently quench photogenerated holes in these dyes or QDs, and also be efficiently reduced at the counter electrodes (CEs) in the device [13,14]. Until now, the iodide ($I^-/I_3^-$) and polysulfide ($S^{2-}/S_n^{2-}$) redox couples have been utilized as conventional redox

electrolytes for DSCs and QDSCs, respectively. Since the CEs play a key role in the reduction of these electrolytes, their electrocatalytic activity and chemical stability significantly affect the final photovoltaic performance [13-20]. Although platinum is known as one of the best electrocatalysts for the iodide redox couple, its high cost and rarity stand in the way of its practical use. Due to these problems, various low cost materials based on carbon materials and conducting polymers were proposed for alternative CEs in DSCs [16-20]. In addition, Pt displays a poor electrocatalytic activity for the polysulfide redox couple in QDSCs due to the chemisorption of the $S^{2-}$ ions on its surface [14,21,22]. The adsorbed $S^{2-}$ ions reduce the rate of charge transfer at the Pt CE, resulting in a steep decrease in the photocurrent and fill factor of QDSCs. Therefore, copper sulfide ($Cu_2S$) CEs were proposed for efficient QDSCs; however, these suffer from sulfurization of the photoanode [15,23].

As alternative materials for DSC CEs, metal nitride materials have been studied, with some showing excellent electrocatalytic properties and stabilities, even comparable to Pt [16,20,24,25]. However, an extremely high temperature is often required for the fabrication of metal nitride CEs, leading to significant increases in the manufacturing cost. Herein, we prepared nickel nitride electrocatalysts by reactive sputtering of nickel under a $N_2$ atmosphere at room temperature. This facile and reliable method led to the formation of a $Ni_2N$ film with a cauliflower-like nanostructure. The crystal structure and chemical stability of this CE for the iodide and polysulfide redox electrolytes were investigated in detail. In addition, the electrocatalytic activities of the prepared nickel nitride CE were compared to a conventional Pt CE for both the iodide and polysulfide redox electrolytes. Furthermore, the photovoltaic performances of the DSCs and QDSCs employing either the nickel nitride or conventional Pt CEs were examined and compared.

## 7.2. Experimental section

### 7.2.1. Fabrication of the platinum and nickel nitride counter electrodes

Pt CEs were prepared by thermal decomposition of a commercial Pt precursor-containing paste (PT1, Dyesol Ltd.) applied using the doctor blading method. The paste was coated onto FTO glass (TEC-8, Pilkington) and then thermally treated in air at 450 ˚C for 30 min. Nickel nitride CEs were fabricated by a RF sputtering of nickel (Ni) onto the FTO glass for 3 h. During this deposition, the chamber was filled with 80 mTorr $N_2$ gas, and the reactive power of 150 W was maintained with a 13.56 MHz frequency. FTO glasses with only Ni deposited on the surface were also prepared for material characterization, using an identical method to the nickel nitride electrodes, except that the sputtering was conducted under an 80 mTorr Ar tmosphere.

### 7.2.2. Preparation of the iodide and polysulfide redox electrolytes

All of the chemicals mentioned below were purchased from Sigma-Aldrich and were used without further purification. Two types of iodide ($I^-/I_3^-$) and polysulfide ($S^{2-}/S_n^{2-}$) redox electrolytes were prepared, some for the measurement of electrocatalytic activity by cyclic voltammetry (CV), and the others for the optimized photovoltaic device operation. For the CV measurements, the iodide electrolytes were prepared by mixing 10 mM LiI, 1 mM $I_2$, and 0.1 M $LiClO_4$ in acetonitrile, and the polysulfide electrolytes were prepared by mixing 0.1 M $Na_2S$ and 0.1 M S in deionized (DI) water. For the symmetric cell analyses and device operation, the iodide electrolytes were prepared by mixing 0.6 M 1-butyl-3-methylimidazolium iodide, 30 mM $I_2$, 0.1 M guanidinium thiocyanate, and 0.5 M 4-*tert*-butylpyridine in a mixture of acetonitrile and valeronitrile (volumetric ratio = 85:15), and the polysulfide electrolytes were prepared by mixing 0.5 M $Na_2S$, 2 M S, and 0.2 M KCl in a mixture of DI water and methanol (volumetric ratio = 3:7).

### 7.2.3. Preparation of the working electrodes and cell assembly

For the preparation of the $TiO_2$ working electrodes, first a dense $TiO_2$ blocking layer was coated onto the FTO glasses by dipping them in a 40 mM $TiCl_4$ aqueous solution at 70 ˚C for 30 min. Then, a colloidal $TiO_2$ paste (DSL 18NR-T, Dyesol Ltd.) was deposited on these pretreated FTO glasses by the doctor blading method, followed by annealing at 500 ˚C for 30 min. The annealed electrodes were treated again with a 16 mM $TiCl_4$ aqueous solution at 70 ˚C for 30 min. For the dye-sensitization, the prepared $TiO_2$ electrodes were immersed in an ethanol solution of 0.5 mM *cis*-bis(isothiocyanato)bis(2,2'-bipyridyl-4,4-dicarboxylic acid) ruthenium (II) (N719 dye, Ohyoung Industrial Co.) for 48 h. Meanwhile, the CdSe quantum dot-sensitization was carried out by a conventional successive ionic layer adsorption and reaction (SILAR) method in a glove box filled with argon gas [26]. The prepared $TiO_2$ electrodes were dipped into a 30 mM $Cd(NO_3)_2$ solution in ethanol for 1 min, followed by rinsing with ethanol. The electrodes were then dipped into a $Na_2Se$ in ethanol solution for 1 min, followed by rinsing with ethanol. The $Na_2Se$ solution was prepared using a 30 mM $SeO_2$ and 60 mM $NaBH_4$ solution in ethanol, following a previous paper [26]. Finally, the ZnS was coated on the surface of QD-sensitized $TiO_2$ photoanode by immersion of electrode into 0.5 M $Zn(CH_3COO)_2$ and then in 0.5 M $Na_2S$ solution for 5 min each. The dye- or quantum dot-sensitized working electrodes were assembled with the CEs using a thermoplastic sealant (Surlyn, Dupont) with a 60 μm thickness. The electrolytes were injected into the assembled cell through a pre-drilled hole. Symmetric cells for the evaluation of electrocatalytic activity were fabricated with exactly the same method used for DSC and QDSC assembly except for that the two identical Pt or nickel nitride electrodes were used.

### 7.2.4. Characterization of materials, electrochemical analyses, and photovoltaic performance evaluation

Scanning electron microscopy (SEM) analyses were conducted using a Carl Zeiss SUPRA 55VP and a Carl Zeiss AURIGA. A transmission electron microscopy (TEM) analysis was performed with a JEOL JEM-2100F after sampling by a focused ion beam (FIB) milling using a SMI3050SE, SII Nanotechnology. X-ray diffraction (XRD) patterns were obtained using a Rigaku D-MAX2500-PC. An X-ray photoelectron spectroscopy (XPS) analysis was conducted using a Thermo Fisher Scientific SIGMA PROBE. X-ray absorption near edge structure (XANES) and extended X-ray absorption fine structure (EXAFS) spectra were obtained by synchrotron measurement at the 8C beamline of the Pohang Accelerator Laboratory (PAL, Republic of Korea). CV analysis was conducted using a potentiostat (PGSTAT128N, Metrohm Autolab) with a Pt mesh counter electrode and Ag/AgCl reference electrode. The scan rate for the CV analysis was 50 mV $s^{-1}$. Tafel polarization and electrochemical impedance spectroscopy measurement were done by using Metrohm Autolab PGSTAT128N and Zahner IM6 workstation, respectively, after the preparation of symmetric cells. Photovoltaic properties were characterized by solar simulators (XIL model 05A50KS source measure units, SERIC Ltd. for DSCs and PEC-L11, Peccell Technologies Inc. for QDSCs) under a 1 sun condition (AM 1.5G with an incident light intensity of 100 mW $cm^{-2}$), which was verified by a National Institute of Advanced Industrial Science and Technology (AIST, Japan) calibrated Si reference solar cell. The active area of the dye- or QD-sensitized $TiO_2$ film was 0.16 $cm^2$. Prior to the photovoltaic measurement, a black aperture mask covered the devices in order to avoid overestimation of the conversion efficiency [27]. The incident photon-to-current efficiencies (IPCE) of the DSCs and QDSCs were measured using a QEX7 (PV Measurements Inc.) or PEC-S20 (Peccell Technologies Inc.), respectively.

## 7.3. Results and discussion

### 7.3.1. Material characterization

Figure 7.1a and 7.1b show the XRD spectra of the FTO glass substrate, the Pt film, the nickel film, and the prepared nickel nitride film deposited on the FTO glasses (Figure 7.1b is a close up of a region in Figure 7.1a). The peak position of the nickel nitride film was nearly identical to the tetrahedral crystal structure of $Ni_2N$ [28]. The TEM images were obtained after the preparation of the nickel nitride film using a focused ion beam (FIB) as shown in Figure 7.2a-7.2c. The crystal structure of the prepared nickel nitride film was crosschecked by measuring the lattice spacing (Figure 7.2b) and assigning the selected area electron diffraction (SAED) pattern (Figure 7.2c) [28]. For comparison, the XRD spectrum of a Ni metal film was also obtained, as shown in Figure 7.1a and 7.1b, with its peak positions assigned to that of metallic Ni (JCPDS 04-0850). As shown in Figure 7.1a and 7.1b, the XRD spectrum of the prepared nickel nitride did not display the peaks corresponding to metallic Ni, indicating that the deposited Ni was effectively nitrided by the reactive sputtering process. The Pt film was also prepared as a conventional CE. Its XRD spectrum is in accordance with that of metallic Pt as shown in Figure 7.1a and 7.1b (JCPDS 04-0802). As shown in the SEM images (Figure 7.2d and 7.2e), both Pt and nickel nitride films were uniformly deposited on the FTO glasses. In particular, the nickel nitride films exhibited a porous and cauliflower-like nanostructure. The thickness of the deposited nickel nitride was about 130 nm, which was estimated from its TEM image showing the film prepared by FIB milling.

The chemical states of the prepared nickel nitride films were examined by XPS measurement. Figure 7.3a shows the spectra of the nickel and nickel nitride films over a wide scan range. The composition of both films was Ni, O, and C. In addition, N was observed on the nickel nitride film. As shown in Figure 7.3b, the

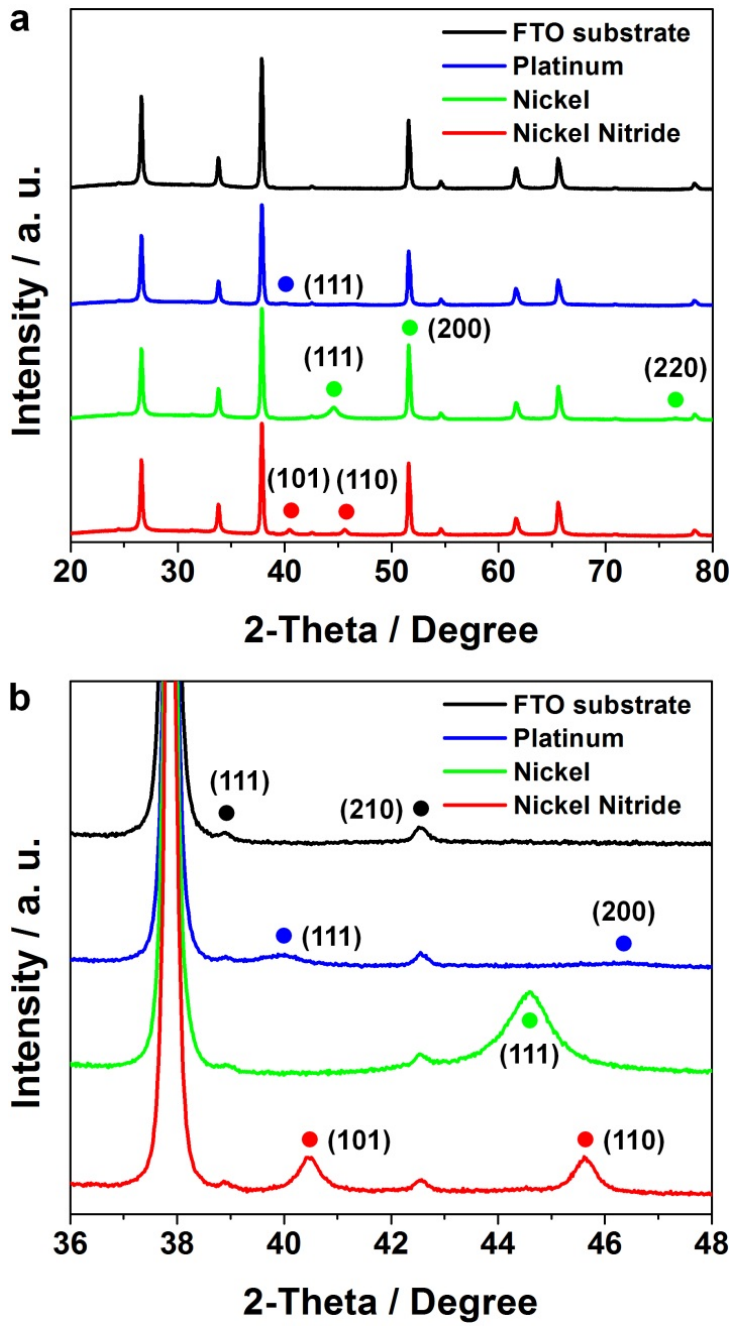


**Figure 7.1.** (a,b) The XRD spectra of Pt (blue lines), Ni (green lines), and nickel nitride films (red lines) on FTO glasses (black lines), with (b) showing a close-up region within (a).

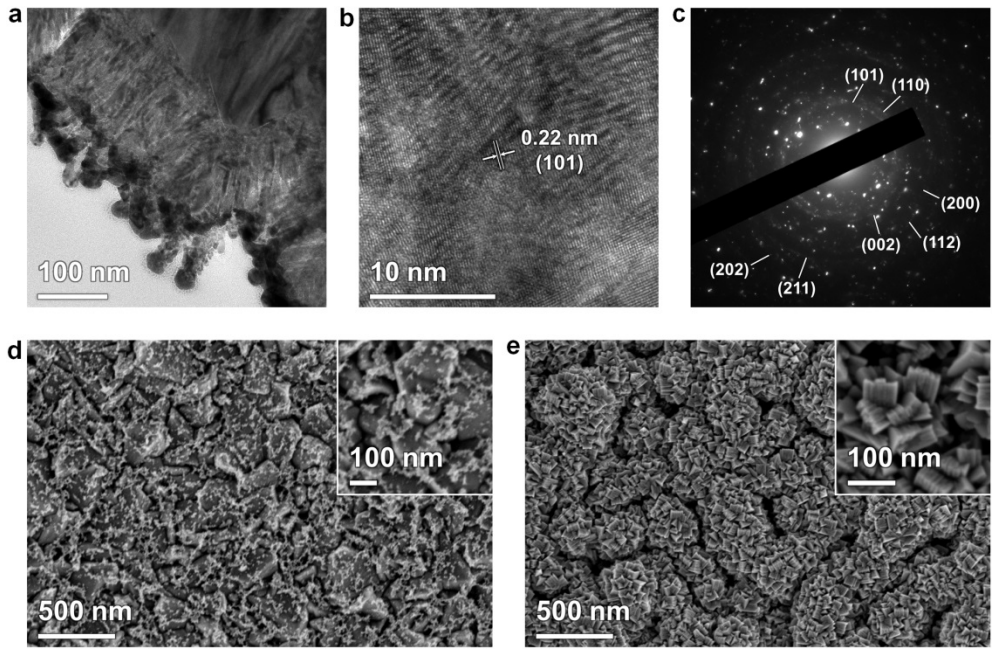


**Figure 7.2.** (a,b) TEM images at different magnifications and the (c) SAED pattern of a nickel nitride film. (d, e) SEM image of the (d) Pt and (e) nickel nitride film on the FTO glasses. The insets of (d) and (e) are high-magnification images.

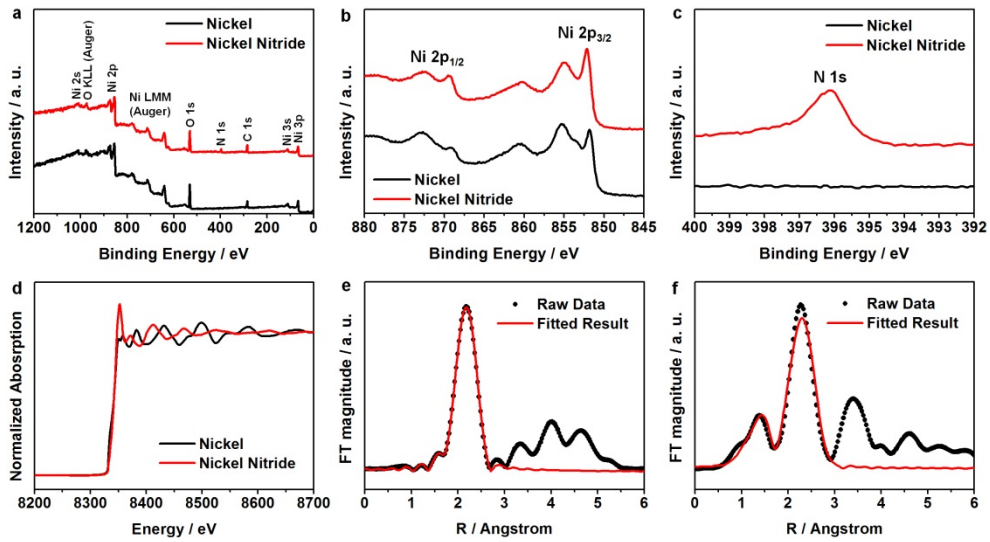


**Figure 7.3.** (a) XPS spectra of the nickel (black lines) and nickel nitride (red lines) films across a wide scan range for (b) the Ni 2p core level peak, and (c) the N 1s core level peak. (d) The Ni K-edge XANES spectra of nickel and nickel nitride. (e,f) The $k^3$-weighted Fourier transforms of the EXAFS spectra at the Ni K-edge for (e) nickel and (f) nickel nitride.

metal Ni film exhibited three peaks corresponding to the Ni $2p_{3/2}$ in the lower binding energy region (850–862 eV), and two peaks corresponding to the Ni $2p_{1/2}$ in the higher binding energy region (867–875 eV) [29]. The Ni $2p_{3/2}$ peak at 851.5 eV can be assigned to the Ni-Ni bond [30,31], and the peaks at 855.0 and 860.0 eV can be assigned to the Ni-O bond [29,31], indicating that the film's surface may be partially oxidized. The nickel nitride film presented nearly the same spectrum as that of the metal Ni film. However, the peak of the Ni-Ni bond shifted to a higher binding energy (851.8 eV) compared to that of the metal Ni film due to the formation of N-Ni bonds [20]. The evidence of the nickel nitridation by the reactive sputtering process was clearly revealed by the N 1s peak shown in Figure 7.3c. The nickel nitride film exhibited a clear N 1s peak at 395.8 eV [32], while the metal Ni film demonstrated no peaks in the same binding energy region.

For further characterization of the prepared nickel nitride's crystal structure, an X-ray absorption fine structure (XAFS) analysis at the Ni K-edge was performed. From the XANES data (Figure 7.3d), it was confirmed that the oxidation state of the nickel nitride film was considerably larger than that of the metal Ni film based on its high-energy shifted edge position and increased white line intensity. This implies a successful nitridation by the reactive sputtering process. The EXAFS was also observed in order to characterize the lattice structure of the nickel nitride film. Figure 7.3e and 7.3f show the Fourier transformed $k^3$-weighted EXAFS spectra of the metal Ni and nickel nitride, with the fitted results based on the Kaiser-Bessel window function with d$k$ = 1.0 and d$R$ = 0.5. The R-factor for the EXAFS fitting of the metal Ni and nickel nitride films was 0.0017 and 0.0196, respectively. The lattice structure of the Ni metal is known to be face centered cubic, while the nickel nitride is comprised of Ni atoms in a body centered tetragonal structure with N atoms located at the two opposite faces of the tetragonal unit cell. In the metal Ni film, the Ni-Ni distance was 2.483 Å from the fitted results. However, the Ni-Ni interatomic distances were much larger in the nickel

nitride, which were 2.699 and 2.800 Å, and the Ni-N distance was 1.972 Å. The lattice constants of the nickel nitride, based on the EXAFS results, were a = b = 2.800 and c = 3.686.

### 7.3.2. Electrocatalytic activity and stability of the nickel nitride electrodes

The electrocatalytic activity and stability of the nickel nitride electrodes were compared with those of conventional Pt electrodes by CV analyses, as shown in Figure 7.4. Figure 7.4a shows two clear pairs of redox potentials for the Pt electrodes with the iodide redox couple. The more positive and negative pairs correspond to the redox reaction of $I_2/I_3^-$and $I^-/I_3^-$, respectively [33]. On the other hand, the nickel nitride electrodes did not exhibit clear pairs of redox potentials for the iodide redox couple, and the redox current density was considerably lower compared to the Pt electrodes, as shown in Figure 7.4b. However, these electrocatalytic behaviors were reversed for the polysulfide redox couple. While the Pt electrodes did not display remarkable performance for the polysulfide redox couple, the nickel nitride electrodes showed clear redox potentials with a significantly higher current density [34], as shown in Figure 7.4c and 7.4d. These results imply that the nickel nitride electrodes have an inferior electrocatalytic activity for the iodide redox couple compared to the conventional Pt electrodes; however, they have a superior electrocatalytic activity for the polysulfide redox couple. The nickel nitride electrodes maintained the intensity and shape of their CV curves over 10 cycles for both redox couples, indicating that they are electrochemically stable for both redox couples.

From Figure 7.4d, relatively large drop in electrocatalytic activity after the first CV cycle is observed. Since this might be attributed to the interaction between the nickel nitride and the polysulfide electrolyte, the electrochemical stability of the nickel nitride electrode was further examined by comparing its crystal structure and chemical states before and after the 10 CV cycles. Figure 7.5a and 7.5b compare

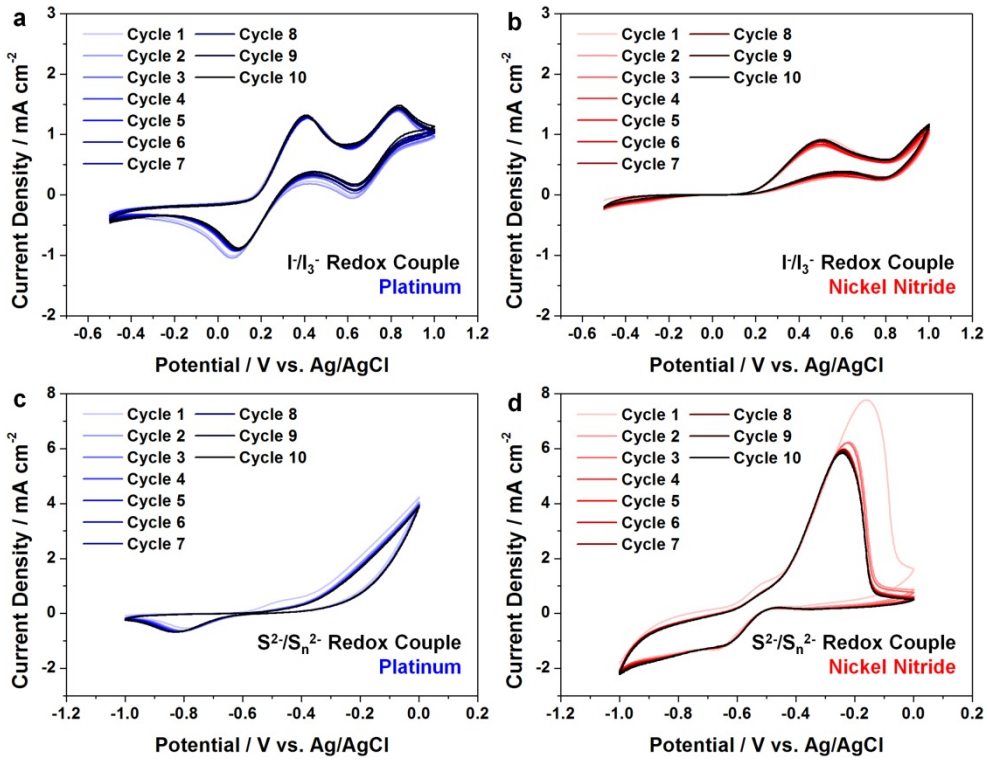


**Figure 7.4.** Cyclic voltammograms (CVs) of (a) Pt and (b) nickel nitride electrodes for the iodide redox couple. CVs of (c) Pt and (d) nickel nitride electrodes for the polysulfide redox couple.

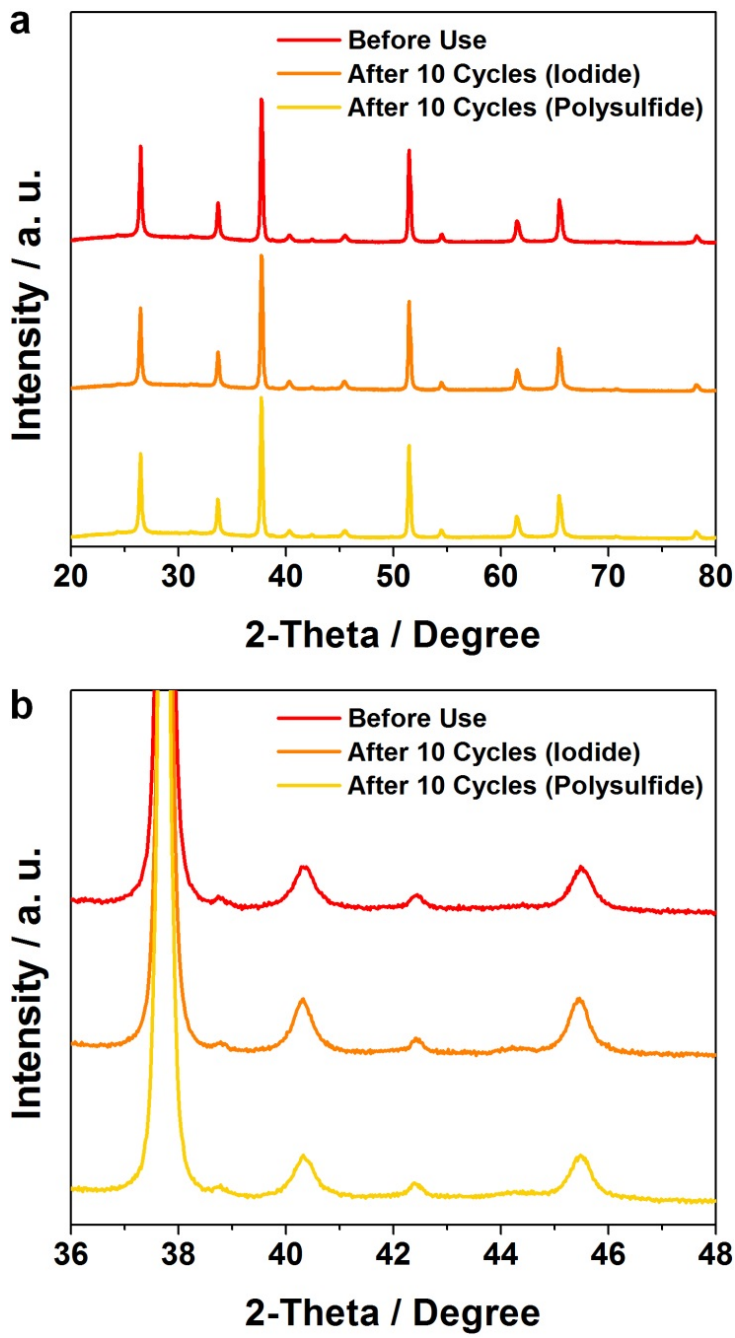


**Figure 7.5.** XRD spectra of nickel nitride electrodes before (red lines) and after 10 CV cycles in the iodide (orange lines) and polysulfide electrolytes (yellow lines), with (b) being a close-up of a region in (a).

the XRD spectra of the nickel nitride electrode before and after 10 CV cycles. It was confirmed that the crystal structure was maintained after multiple CV cycles for both electrolytes (the iodide and polysulfide redox electrolytes), indicating that the nickel nitride was not chemically dissolved in either electrolyte. The chemical states were examined by elemental energy filtered (EF)-TEM maps after the sampling by using FIB (Figure 7.6a-7.6c). For this analysis, the electrodes were washed with acetonitrile or DI water after the CV cycles in the iodide or polysulfide electrolyte, respectively, in order to remove remaining redox species on the surface. As shown in Figure 7.6, the distributions of Ni and N were preserved after multiple CV cycles in both electrolytes. In addition, iodine (I) was not detected after 10 CV cycles in the iodide electrolyte, indicating that the iodide ions did not adsorb on or chemically react with the nickel nitride. However, sulfur (S) was detected in the electrode after 10 CV cycles in the polysulfide electrolyte. This indicates that the sulfide ions in the electrolytes adsorbed on or chemically reacted with the nickel nitride. The chemical interaction between the nickel nitride and sulfide ions was also confirmed by comparing the XPS spectra of the nickel nitride electrode before and after 10 CV cycles in the polysulfide electrolyte (Figure 7.7). Compared to the Ni $2p_{3/2}$ peak of the Ni-Ni bond for the as-prepared electrode (at a binding energy of 851.8 eV), that of the electrode after 10 CV cycles shifted considerably to a higher binding energy (853.3 eV), inferring that the sulfide ions chemically reacted with the nickel nitride [35]. Furthermore, the Ni $2p_{3/2}$ peaks of the Ni-O bond for the as-prepared electrode (at binding energies of 854.7 and 859.8 eV) became indistinct after 10 CV cycles. This may be due to the sulfide ions substituting for the oxygen atoms at the electrode's surface. The chemical bond of the Ni-S was clearly detected by the S 2p peak (at a binding energy of 161.5 eV) for the electrodes after 10 CV cycles [35]. Given that XPS is a technique chiefly for surface analysis, and that the bulk distributions of the Ni and N species were maintained after numerous CV cycles (as confirmed by the elemental EF-TEM

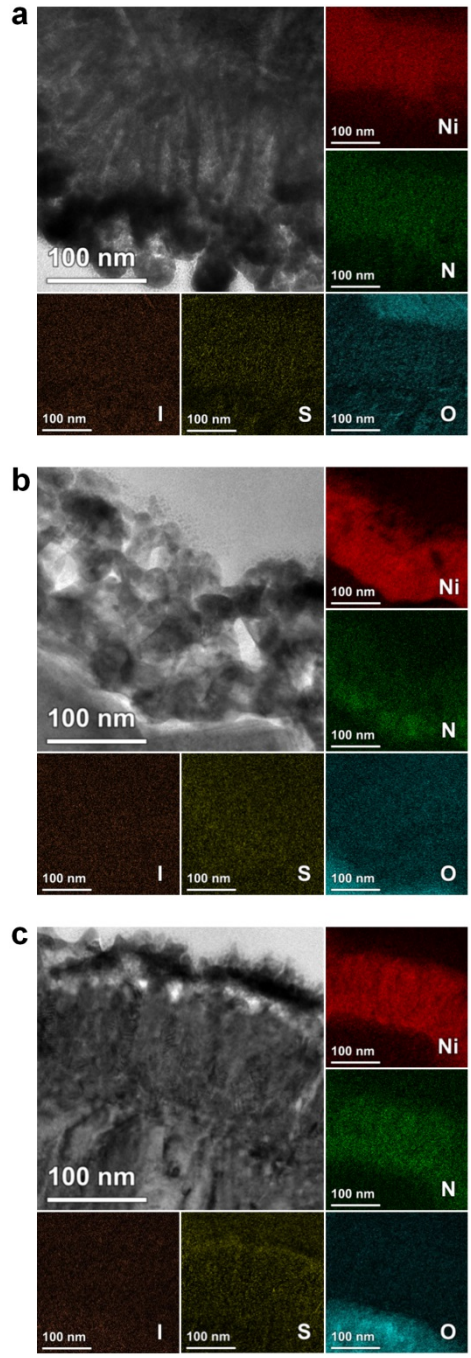


**Figure 7.6.** TEM images and elemental EF-TEM maps of the nickel nitride electrodes (a) before and (b,c) after 10 CV cycles in the iodide and polysulfide redox electrolytes.

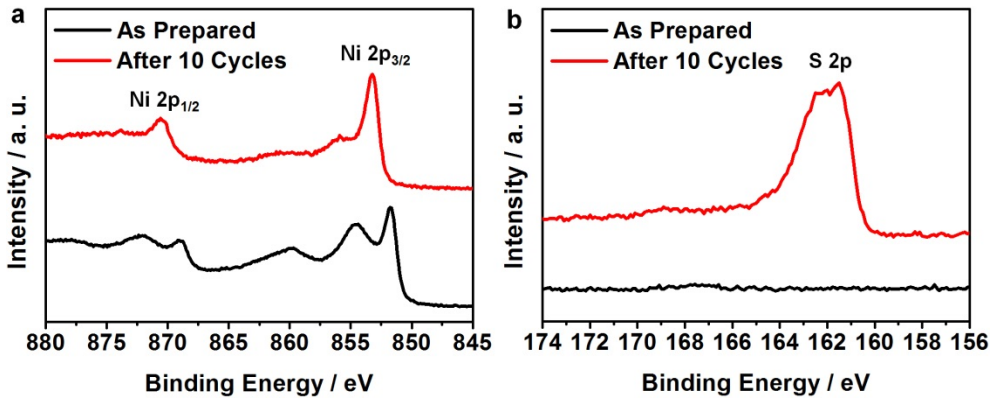


**Figure 7.7.** (a) Ni 2p and (b) S 2p core level XPS spectra of nickel nitride electrodes before and after 10 CV cycles in the polysulfide electrolytes.

maps), it can be concluded that the bulk structure of the nickel nitride electrodes is chemically stable toward the polysulfide electrolyte; however, a chemical reaction is possible between the electrode surface and the sulfide ions. Recently, Kim et al. reported that the nickel sulfide (NiS) films displayed a high electrocatalytic activity toward the polysulfide redox couple [36]. Considering these results, the chemical reaction with sulfide ions at the electrode surface may not deteriorate the electrocatalytic activity of the nickel nitride toward the polysulfide electrolyte. In addition, as already shown in Figure 7.3, the chemical bond between Ni and O was detected by XPS; however, these oxygen species were not detected by the elemental EF-TEM maps (Figure 7.6a-7.6c) except in the region of the FTO glass, implying that the prepared nickel nitride electrode was oxidized only at the surface.

The electrocatalytic activities of the Pt and nickel nitride electrodes were reconfirmed by Tafel polarization measurements [16], as shown in Figure 7.8a and 5.8b. For these measurements, we prepared symmetric dummy cells with the Pt or nickel nitride electrodes. The Tafel polarization curves reveal a logarithmic current density ($J$) as a function of voltage ($V$). A larger slope of the Tafel curve means a higher exchange current density ($J_0$), and this indicates superior electrocatalytic activity. As shown in Figgure 7.8a, the Pt electrode showed a significantly higher $J_0$ for the iodide electrolyte compared to that of the nickel nitride electrode. However, this situation was reversed for the polysulfide electrode, shown in Figure 7.8b, with the nickel nitride electrode showing a considerably higher $J_0$ than the Pt electrode. These results suggest that the electrocatalytic activity of the nickel nitride electrode is inferior for the iodide redox couple, but superior for the polysulfide electrolyte compared to the Pt electrode, which is coincident with the CV data. In order to quantitatively compare the electrocatalytic activities of the Pt and nickel nitride electrodes, we obtained impedance spectra from the same symmetric dummy cells, shown in Figure 7.8c and 7.8d. We used the equivalent circuit model, comprising a series resistance ($R_s$), an impedance at the

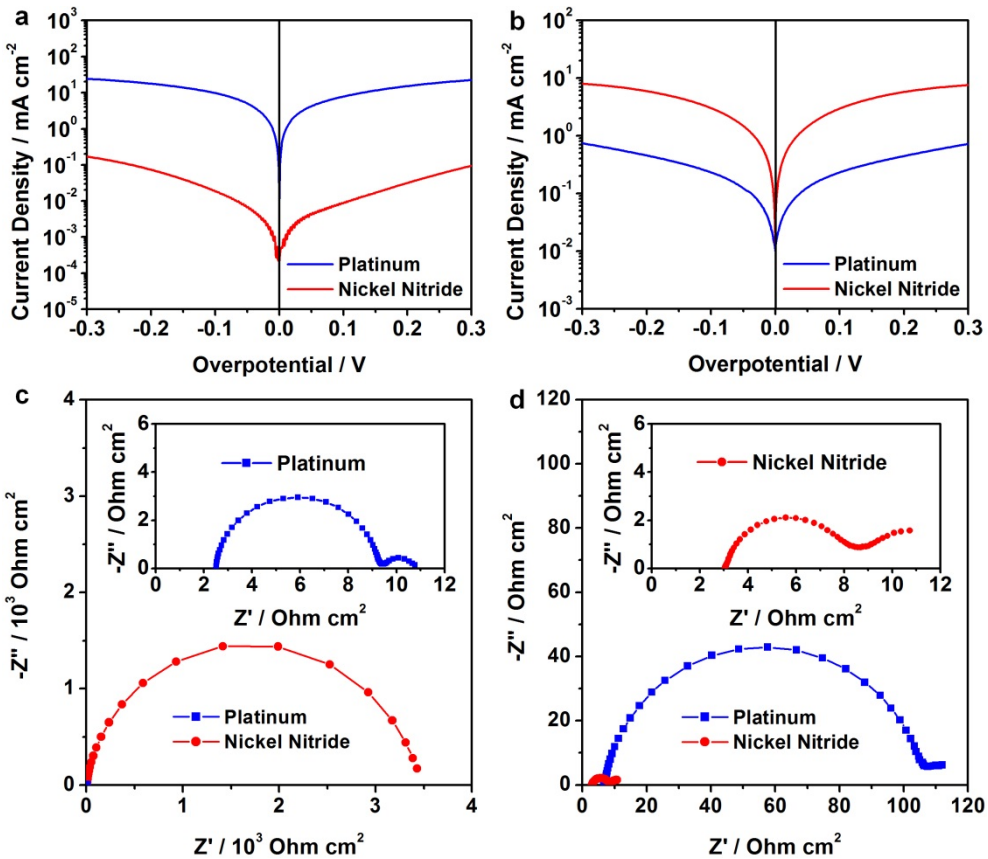


**Figure** 7.**8.** Tafel polarization curves of symmetric dummy cells with Pt (blue lines/squares) or nickel nitride (red lines/circles) electrodes for (a) iodide and (b) polysulfide electrolytes. Impedance spectra of the symmetric dummy cells for (c) iodide and (d) polysulfide electrolytes, with the insets showing the enlarged spectra.

electrolyte/electrode interface ($R_{ct}$ and CPE), and a finite Warburg impedance ($W_s$) related to the electrolyte diffusion (Figure 7.9) [17,37]. $R_{ct}$ is related to the charge transfer at the interface between the electrode and the electrolyte. CPE stands for "constant phase element", which usually replaces a capacitor in the equivalent circuit, is attributed to the electrodes' roughness [38]. From the CPE, a double-layer capacitance ($C_{dl}$) can be evaluated. These two values ($R_{ct}$ and $C_{dl}$), which are related to the electrocatalytic activity, were obtained after fitting the impedance spectra by the ZView software, as listed in Table 7.1. For the iodide redox couple, the nickel nitride electrode had a considerably larger $R_{ct}$ compared to the Pt electrode, indicating its inferior electrocatalytic activity, because the $R_{ct}$ is related to the $J_0$ by $J_0$=(RT)/(n$FR_{ct}$) [17,37]. In contrast, for the polysulfide redox couple, the nickel nitride electrode exhibited significantly increased $C_{dl}$ as well as the reduced $R_{ct}$, implying numerous electrochemical reaction sites. Significantly enhanced electrocatalytic activity of the Ni nitride can be attributed to fast charge transfer and numerous electrochemical reaction sites. From these results, it can be expected that the nickel nitride CEs may be suitable for the QDSCs rather than for the DSCs.

### 7.3.3. Application of the nickel nitride electrodes to the mesoscopic dye- or quantum dot-sensitized solar cells

Finally, the prepared nickel nitride electrodes were introduced as CEs to the mesoscopic DSCs and QDSCs. Figure 7.10 shows the photocurrent density-voltage (*J-V*) characteristics and the IPCE spectra of the DSCs and QDSCs with either the Pt or nickel nitride CEs. The photovoltaic performance parameters are listed in Table 7.2. As listed in Table 7.2, the DSC with the nickel nitride CE exhibited a lower conversion efficiency ($\eta$, $\eta$ = 3.75%) than that with the conventional Pt CE ($\eta$ = 7.62%). This lower efficiency was mainly due to a poor fill factor, which is closely related to the inferior electrocatalytic activity of the nickel nitride electrode

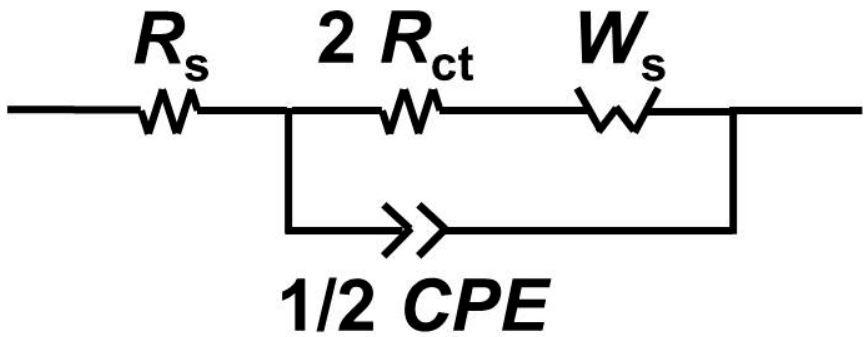


**Figure 7.9.** The equivalent circuit model for the impedance spectra of symmetric dummy cells shown in Figure 7.8c and 7.8d.

| Electrode | Electrolyte | $R_{ct}$ / Ω cm$^2$ | $C_{dl}$ / μF cm$^{-2}$ |
|---|---|---|---|
| Pt | Iodide | 3.37 | 64.2 |
| Nickel nitride | Iodide | 1719.50 | 73.6 |
| Pt | Polysulfide | 51.80 | 266.8 |
| Nickel nitride | Polysulfide | 2.49 | 3192.0 |

**Table 7.1.** Parameters determined by fitting the impedance spectra of symmetric dummy cells with Pt and nickel nitride electrodes.

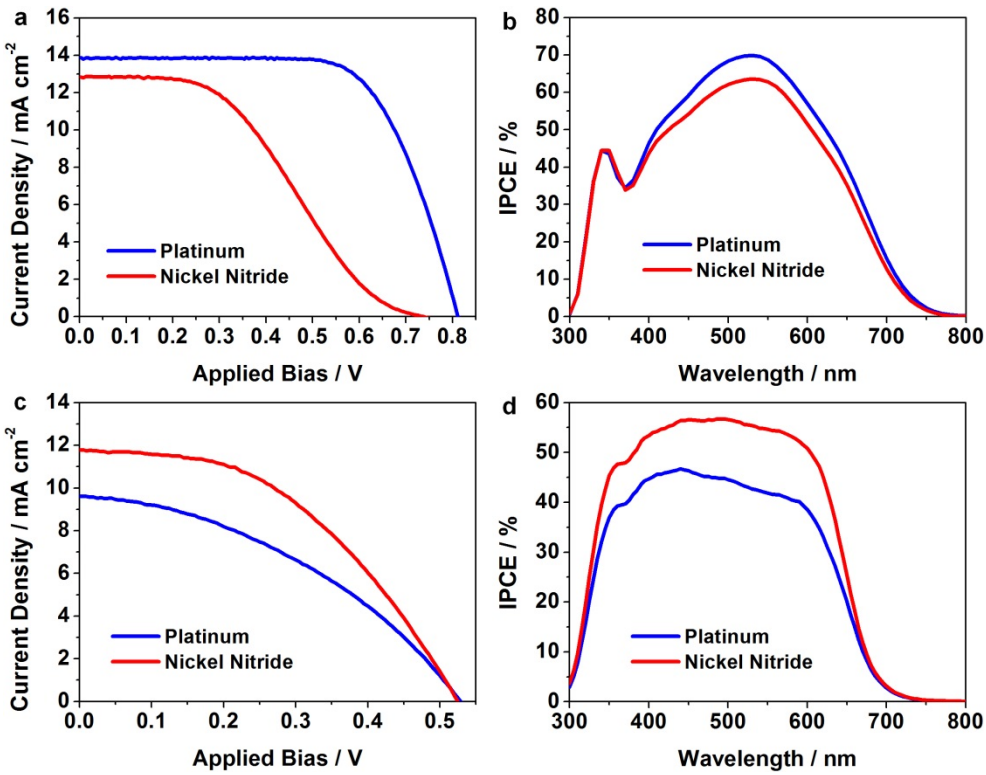


**Figure 7.10.** (a) Photocurrent density-voltage (*J*-*V*) characteristics under illumination (light intensity: 100 mW/cm$^2$, AM 1.5G filter) and (b) IPCE spectra of the DSCs with Pt (blue lines) or nickel nitride (red lines) CEs. (c) Photocurrent density-voltage (*J*-*V*) characteristics under illumination (light intensity: 100 mW/cm$^2$, AM 1.5G filter) and (d) IPCE spectra of the QDSCs with each type of CE. The DSCs and QDSCs utilized the iodide and polysulfide redox electrolyte, respectively.

| Electrode | $V_{oc}$ / V | $J_{sc}$ / mA cm$^{-2}$ | *FF* / % | $\eta$ / % |
|---|---|---|---|---|
| DSCs with Pt CEs | 0.812 | 13.8 | 68.0 | 7.62 |
| DSCs with nickel nitride CEs | 0.738 | 12.8 | 39.7 | 3.75 |
| QDSCs with Pt CEs | 0.529 | 9.6 | 39.4 | 2.01 |
| QDSCs with nickel nitride CEs | 0.525 | 11.8 | 45.2 | 2.80 |

**Table 7.2.** Summary of *J-V* characteristics for DSCs and QDSCs employing Pt and nickel nitride CEs.

for the iodide redox electrolyte [16]. The lower short-circuit current density ($J_{sc}$) of the nickel nitride CE was also confirmed by the IPCE spectra (Figure 7.10b). However, when applied in the QDSCs, the nickel nitride CE exhibited significantly enhanced cell performances over the Pt CE. The $J_{sc}$ and fill factor were all enhanced for the QDSC with the nickel nitride CE, resulting in a significantly increased conversion efficiency (by 39%) compared to that with the Pt CE. The far higher $J_{sc}$ was also confirmed by the IPCE spectra (Figure 7.10d). This enhanced photovoltaic performance was attributed to the excellent electrocatalytic activity of the nickel nitride CE for the polysulfide redox electrolyte. This trend of photovoltaic performances accorded well with the CV, Tafel polarization, and impedance data. These results suggest that the nickel nitride CE can be utilized promisingly for the QDSCs employing the polysulfide electrolyte. In this work, we investigated the electrocatalytic activity of the nickel nitride CE only for the iodide and polysulfide redox couples; meanwhile, there are several alternative redox couples for the mesoscopic dye- and QD-sensitized solar cells, including the cobalt-based [2,39] or disulfide/thiolate [40] redox couples. Further studies on examining the electrocatalytic activity of the nickel nitride CE for these redox couples may be worthwhile as future work.

## 7.4. Conclusions

We developed nickel nitride CEs for application in mesoscopic dye- and QD-sensitized solar cells through a new process, that of reactive sputtering at room temperature. In-depth studies revealed that this facile and reliable method led to the formation of a $Ni_2N$ film with a cauliflower-like nanostructure and tetrahedral crystal lattice. In addition, the prepared nickel nitride electrodes showed excellent chemical stability toward both iodide and polysulfide redox electrolytes. Compared to conventional Pt electrodes, the nickel nitride electrodes displayed an inferior

electrocatalytic activity for the iodide redox electrolyte; however, they revealed a significantly enhanced electrocatalytic activity for the polysulfide redox electrolyte. In DSCs employing the iodide redox electrolyte, the nickel nitride CEs showed lower conversion efficiency than the conventional Pt CEs. However, when applied in QDSCs employing the polysulfide redox electrolyte, the nickel nitride CEs demonstrated significantly enhanced conversion efficiency over the conventional Pt CEs. These results infer that reactive sputtering is a reliable method for the preparation of efficient nickel nitride CEs at room temperature, and these prepared nickel nitride CEs should be promising electrocatalysts in the mesoscopic QD-sensitized solar cells.

## 7.5. References


[1] O'Regan, B.; Grätzel, M., *Nature* **1991**, *353*, 737.

[2] Yella, A.; Lee, H.-W.; Tsao, H. N.; Yi, C.; Chandiran, A. K.; Nazeeruddin, M. K.; Diau, E. W.-G.; Yeh, C.-Y.; Zakeeruddin, S. M.; Grätzel, M., *Science* **2011**, *334*, 629.

[3] Ito, S.; Zakeeruddin, S. M.; Comte, P.; Liska, P.; Kuang, D.; Grätzel, M., *Nat. Photonics* **2008**, *2*, 693.

[4] Lee, K.; Park, S. W.; Ko, M. J.; Kim, K.; Park, N.-G., *Nat. Mater.* **2009**, *8*, 665.

[5] Robel, I.; Subramanian, V.; Kuno, M.; Kamat, P. V., *J. Am. Chem. Soc.* **2006**, *128*, 2385.

[6] Santra, P. K.; Kamat, P. V., *J. Am. Chem. Soc.* **2012**, *134*, 2508.

[7] Yang, J.; Kim, J.-Y.; Yu, J. H.; Ahn, T.-Y.; Lee, H.; Choi, T.-S.; Kim, Y.-W.; Joo, J.; Ko, M. J.; Hyeon, T., *Phys. Chem. Chem. Phys.* **2013**, *15*, 20517.

[8] Pan, Z.; Mora-Seró, I.; Shen, Q.; Zhang, H.; Li, Y.; Zhao, K.; Wang, J.; Zhong, X.; Bisquert, J., *J. Am. Chem. Soc.* **2014**, *136*, 9203.

[9] Nazeeruddin, M. K.; De Angelis, F.; Fantacci, S.; Selloni, A.; Viscardi, G.; Liska, P.; Ito, S.; Takeru, B.; Grätzel, M., *J. Am. Chem. Soc.* **2005**, *127*, 16835.

[10] Hagfeldt, A.; Grätzel, M., *Accounts Chem. Res.* **2000**, *33*, 269.

[11] Lee, J.-W.; Son, D.-Y.; Ahn, T. K.; Shin, H.-W.; Kim, I. Y.; Hwang, S.-J.; Ko, M. J.; Sul, S.; Han, H; Park, N.-G., *Sci. Rep.* **2013**, *3*, 1050.

[12] Sung, S. D.; Lim, I.; Kang, P.; Lee, C.; Lee, W. I., *Chem. Commun.* **2013**, *49*, 6054.

[13] Hagfeldt, A.; Boschloo, G.; Sun, L.; Kloo, L.; Pettersson, H., *Chem. Rev.* **2010**, *110*, 6595.

[14] Radich, J. G.; Dwyer, R.; Kamat, P. V., *J. Phys. Chem. Lett.* **2011**, *2*, 2453.

[15] Tachan, Z.; Shalom, M.; Hod, I.; Rühle, S.; Tirosh, S.; Zaban, A., *J. Phys. Chem. C* **2011**, *115*, 6162.

[16] Wu, M.; Lin, X.; Wang, Y.; Wang, L.; Guo, W.; Qi, D.; Peng, X.; Hagfeldt, A.; Grätzel, M.; Ma, T., *J. Am. Chem. Soc.* **2012**, *134*, 3419.

[17] Kavan, L.; Yum, J. H.; Grätzel, M., *ACS Nano* **2011**, *5*, 165.

[18] Tai, Q.; Chen, B.; Guo, F.; Xu, S.; Hu, H.; Sebo, B.; Zhao, X.-Z., *ACS Nano* **2011**, *5*, 3795.

[19] Ramasamy, E.; Chun, J.; Lee, J., *Carbon* **2010**, *48*, 4556.

[20] Jiang, Q. W.; Li, G. R.; Liu, S.; Gao, X. P., *J. Phys. Chem. C* **2010**, *114*, 13397.

[21] Loučka, T., *J. Electroanal. Chem. Interfacial Electrochem.* **1972**, *36*, 355.

[22] Lee, Y.-L.; Lo, Y.-S., *Adv. Funct. Mater.* **2009**, *19*, 604.

[23] Hodes, G.; Manassen, J.; Cahen, D., *J. Electrochem. Soc.* **1980**, *127*, 544.

[24] Li, G. R.; Song, J.; Pan, G. L.; Gao, X. P., *Energy Environ. Sci.* **2011**, *4*, 1680.

[25] Wang, Y.; Wu, M.; Lin, X.; Shi, Z.; Hagfeldt, A.; Ma, T., *J. Mater. Chem.* **2012**, *22*, 4009.

[26] Lee, H. J.; Wang, M.; Chen, P.; Gamelin, D. R.; Zakeeruddin, S. M.; Grätzel, M.; Nazeeruddin, M. K., *Nano Lett.* **2009**, *9*, 4221.

[27] Park, J.; Koo, H.-J.; Yoo, B.; Yoo, K.; Kim, K.; Choi, W.; Park, N.-G., *Sol. Energy Mater. Sol. Cells* **2007**, *91*, 1749.

[28] Dorman, G. J. W. R.; Sikkens, M., *Thin Solid Films* **1983**, *105*, 251.

[29] Zhao, B.; Ke, X.-K.; Bao, J.-H.; Wang, C.-L.; Dong, L.; Chen, Y.-W.; Chen, H.-L., *J. Phys. Chem. C* **2009**, *113*, 14440.

[30] Wagner, C. D.; Riggs, W. M.; Davis, L. E.; Moulder, J. F.; Muilenberg, G. E., *Handbook of X-ray Photoelectron Spectroscopy*; Perkin-Elmer (Physical Electronics Division), Eden-Prairie: MN, **1979**.

[31] Hotový, I.; Huran, J.; Janík, J.; Kobzev, A. P., *Vacuum* **1998**, *51*, 157.

[32] Jouan, P.-Y.; Peignon, M.-C.; Cardinaud, C.; Lempérière, G., *Appl. Surf. Sci.* **1993**, *68*, 595.

[33] Roy-Mayhew, J. D.; Bozym, D. J.; Punckt, C.; Aksay, I. A., *ACS Nano* **2010**, *4*, 6203.

[34] Dong, J.; Jia, S.; Chen, J.; Li, B.; Zheng, J.; Zhao, J.; Wang, Z.; Zhu, Z., *J. Mater. Chem.* **2012**, *22*, 9745.

[35] Galtayries, A.; Grimblot, J., *J. Elect. Spect. Rel. Phen.* **1999**, *98*, 267.

[36] Kim, H.-J.; Kim, D.-J.; Rao, S. S.; Savariraj, A. D.; Kim, S.-K.; Son, M.-K.; Gopi, C. V. V. M.; Prabakar, G. K., *Electrochim. Acta* **2014**, *127*, 427.

[37] Kim, J.-Y.; Kim, J. Y.; Lee, D.-K.; Kim, B. S.; Kim, H.; Ko, M. J., *J. Phys. Chem. C* **2012**, *116*, 22759.

[38] Longo, C.; Nogueira, A. F.; De Paoli, M.-A.; Cachet, H., *J. Phys. Chem. B* **2002**, *106*, 5925.

[39] Yum, J.-H.; Baranoff, E.; Kessler, F.; Moehl, T.; Ahmad, S.; Bessho, T.; Marchioro, A.; Ghadiri, E.; Moser, J.-E.; Yi, C.; Nazeeruddin, M. K.; Grätzel, M., *Nat. Commun.* **2012**, *3*, 631.

[40] Wang, M.; Chamberland, N.; Breau, L.; Moser, J.-E.; Humphry-Baker, R.; Marsan, B.; Zakeeruddin, S. M.; Grätzel, M., *Nat. Chem.* **2010**, *2*, 385.

# Chapter 8. Vapor deposited nanostructured cobalt nitride as electrocatalytic counter electrode

## 8.1. Introduction

Mesoscopic sensitized solar cells, or Grätzel cells, have been under intensive research due to their high performance, reliable and stable characteristics, environmental friendliness, and facile and economical fabrication methods [1-6]. In general, mesoscopic sensitized solar cells are categorized according to the type of sensitizers which are light harvesters chemisorbed on the mesoporous semiconductor oxide layer typically composed of ~20 nm sized $TiO_2$ nanoparticles. In dye-sensitized solar cells (DSCs), metal-organic complexes or pure organic dye molecules are used as sensitizers [7-11], and in quantum dot-sensitized solar cells (QDSCs), inorganic quantum dots (QDs) serves as light harvesters [12-20]. Since the mesoporous photoanode drives the whole photoelectrochemical reactions [6], electrocatalytic counter electrodes and electrolytes compatible with the sensitized semiconductor electrodes are employed for the cells in general.

In DSCs, iodide redox ($I_3^-/I^-$) electrolyte has been used in most cases, because of the large charge recombination resistance at the $TiO_2$/iodide electrolyte interface [2,4]. Moreover, recent advances in the organic dyes which minimize the recombination reaction by steric hindrance enabled the utilization of cobalt bipyridyl redox electrolyte ($[Co(bpy)_3]^{2+/3+}$) which is superior to the iodide electrolyte due to a smaller overpotential [10,11,21-26]. With the assistance of the development of porphyrin organic sensitizers with extremely high extinction coefficients [22], the conversion efficiency of DSCs exceeded 12% [10] and went up to 13% lately [11]. However, these high performances can be obtained only

under a condition with keen optimizations of pore sizes in $TiO_2$ photoelectrode [27], because otherwise the mass transport limitation is severe due to the large molecular size of cobalt bipyridyl redox species.

Platinum is generally known as the best electrocatalyst material for the reduction of electrolytes in DSCs [6,8,11]. Therefore, the research works on the DSCs' counter electrodes have been focused on the following direction; development of low-cost electrocatalysts with comparable performance to that of Pt. Various materials, such as numerous types of carbon [28-33], conducting polymers [34-41], nanoscale transition metal compounds [42-52], metal alloys [53-55] have been proposed, and they showed high performances. However, these materials suffered from deficient chemical stability or complicated fabrication processes, and thus there are many on-going researches over the world to replace Pt counter efficiently.

Meanwhile, in QDSCs, charcogenide QDs such as CdS, CdSe, and PbS have been utilized due to their high quantum yield [13,53-63], and further improvements in the performances were obtained by doping [17,18] or core/shell [19,60] approaches. Recently, $CuInSe_2$ [64] and $CuInS_2$ [20] based QDSCs were reported, and the efficiency exceeded 7%. During the solar cell operation, electron deficient QDs are regenerated by the redox electrolyte, and polysulfide ($S_n^{2-}/S^{2-}$) redox couple gives the best performance due to their excellent hole scavenging ability [65]. For the reduction of $S_n^{2-}$ to $S^{2-}$, $Cu_2S$ is the best electrocatalyts that have been reported [17-20,66,67], and many other sulfide materials have shown fine performances [68-70]. However, their stabilities under illumination are known to be very poor, and there is also a problem of sulfurization of the photoelectrode [66,68]. Among noble metals, Pt suffer from the decrease of activity due to the chemisorption of $S^{2-}$ (poisoning) on the surface, resulting in a low fill factor [67,71,72].

On the basis of the need for a highly electrocatalytic and stable counter

electrode for QDSCs, in this research, we prepared cobalt nitride electrodes by reactive sputtering of cobalt in $N_2$ atmosphere. Fluorine-doped tin oxide (FTO) glass (TEC-8, Pilkington) was used as a conducting substrate, and cauliflower-shaped nanostructures were formed on the FTO. By physical characterization of the synthesized material based on X-ray analyses, the chemical composition was verified as CoN. The electrocatalytic activity of cobalt nitride was tested in iodide, cobalt, and polysulfide electrolyte, and then the electrodes were utilized as counter electrode in DSCs based on Ru complex dye/iodide redox electrolyte and organic dye/cobalt bipyridyl redox electrolyte, and QDSCs with CISe/polysulfide redox electrolyte. In DSCs, though the electrocatalytic activity of cobalt nitride for the reduction of iodide and cobalt bipyridyl electrolyte was lower than that of Pt, CoN gave comparable energy conversion efficiency to conventional Pt based cells. Also, in QDSCs, cobalt nitride was inferior to $Cu_2S$ in activity and initial solar cell performance, but the results were reversed due to the better stability of CoN electrode.

## 8.2. Experimental section

### 8.2.1. Preparation of platinum and cobalt nitride counter electrodes

All the reagents used in this research work were obtained from Sigma-Aldrich and were used without further purification (otherwise stated in the text). Platinum counter electrodes were prepared by thermal decomposition of Pt precursor on the fluorine-doped tin oxide (FTO) glass substrates. 50 mM $H_2PtCl_6$ in isopropanol solution was used as the precursor, and Pt was cast on the FTO glasses by spin-coating followed by heat treatment at 400 °C in air for 20 min. Cobalt nitride counter electrodes were fabricated by a radio frequency sputtering of cobalt onto the FTO glass for 8 h, at reactive power of 300 W and 13.56 MHz frequency, in a chamber filled with 80 mTorr $N_2$ gas. For the characterization of cobalt nitride film,

cobalt film was prepared by using the same method except for that the Ar gas was used instead of the $N_2$ gas.

### 8.2.2. Preparation of iodide, cobalt, and polysulfide redox electrolytes

Electrolytes for cyclic voltammetry (CV) analyses and solar cell device applications were prepared with different compositions. Iodide redox electrolyte for CV was fabricated by mixing 10 mM LiI, 1 mM $I_2$, 0.1 mM $LiClO_4$ in acetonitrile, and that for the DSCs was composed of 0.6 M 1-butyl-3-methylimidazolium iodide, 30 mM $I_2$, 0.1 M guanidinium thiocyanate, and 0.5 M 4-*tert*-butylpyridine in a mixture of acetonitrile and valeronitrile (volumetric ratio = 85:15). In case of cobalt bipyridyl redox electrolyte, 10 mM $Co(bpy)_3(PF_6)_2$ (DN-C01, Dyenamo), 1 mM $Co(bpy)_3(PF_6)_3$ (DN-C02, Dyenamo), and 0.1 M $LiClO_4$ containing acetronitrile solution was used for the CV measurements, and 0.22 M $Co(bpy)_3(PF_6)_2$, 0.05 M $Co(bpy)_3(PF_6)_3$, 0.1 M $LiClO_4$, and 0.2 M 4-*tert*-butylpyridine in acetonitrile was used for the device. Polysulfide redox electrolyte for CV analyses was a mixture of 0.1 M $Na_2S$ and 0.1 M S in deionized (DI) water, and that for QDSCs was 1.0 M $Na_2S$ and 1.0 M S containing (DI) water solution.

### 8.2.3. Preparation of photoanodes and cell assembly

The $TiO_2$ photoanode was fabricated by a conventional method. $TiO_2$ paste containing ~20 nm sized nanoparticles was prepared via the method in a previous report [73], and was cast on a FTO glass with $TiO_2$ blocking layer by doctor blading method. Then the electrode was sintered at 500 °C in air for 30 min, and $TiCl_4$ post-treatment was performed in order to increase the roughness factor and enhance the electron injection from dye molecules to the $TiO_2$ conduction band. Dye molecules were adsorbed on the $TiO_2$ surface by immersing the electrolyte in ethanolic solution of 0.5 mM N719 (Ru 535-bisTBA) or 0.1 mM Y123 (DN-F05Y, Dyenamo) in mixture solution of acetonitrile and *tert*-butanol (1:1 in vol. ratio) for

48 h at 30 °C. For the positioning of CISe QDs, which was synthesized as reported previously, $TiO_2$ electrodes were placed in the QD dispersion in dichloromethane at 25 °C. The CISe-sensitized electrodes were then passivated by a protecting ZnS overlayer, which was conducted by the alternative dipping of the electrode in 0.1 M $Zn(CH_3COO)_2$ and 0.1 M $Na_2S$ solution [64]. For the preparation of a mesoscopic sensitized solar cell, a photoanode and a counter electrode were assembled by using a thermoplastic sealant (Surlyn, Dupont), of which thickness was 60 μm for N719-sensitized or CISe-sensitized solar cells and 25 μm for Y123-sensitized solar cells. The electolytes were injected into the cell through a pre-drilled hole at the photoanode.

### 8.2.4. Physical and electrochemical characterzations

The crystal structures and surface states of the prepared electrodes were characterized by obtaining X-ray diffraction (XRD) patterns using Rigaku D-MAX2500-PC and X-ray photoelectron spectroscopy (XPS) spectra using Thermo SIGMA PROBE. The morphologies and structures of the electrodes were observed with a scanning electron microscope (SEM; Carl Zeiss AURIGA) and a transmission electron microscope (TEM; FEI Technai F20) with electron energy loss spectroscopy (EELS) equipment. X-ray absorption fine structure (XAFS) analyses were performed by synchrotron measurement at 8C beamline (Nanoprobe XAFS) of Pohang Accelerator Laboratory (PAL) in fluorescence mode. For the CV analyses, a potentiostat (Metrohm Autolab PGSTAT128N) was used. A Pt mesh was used as a counter electrode, and an Ag/AgCl (saturated KCl) reference electrode was dipped into the solution during the CV measurements of wherein the scan rate was fixed as 50 mV $s^{-1}$. For the DSCs' performance characterzations, AM 1.5G light with 100 mW $cm^{-2}$ intensity was irradiated on the solar cells by using a solar simulator equipped with a 1600 W xenon lamp (Yamashita Denso YSS-200A). Photocurrent density (*J*)-voltage (*V*) curves were obtained with Solartron

1287 potentiostat. Incident photon-to-current efficiency was measured at short-circuit conditions by using a 75 W xenon lamp and a monochromator. Electrochemical impedance spectroscopy (EIS) analyses were performed by Zahner Zennium electrochemical workstation with the sinusoidal perturbation of 10 mV.

## 8.3. Results and discussion

### 8.3.1. Physical characterization of materials by X-ray analyses

Figure 8.1 shows the XRD patterns of the cobalt nitride and platinum counter electrodes, with those of cobalt and bare FTO glass substrate for the comparison. The locations of the XRD peaks of cobalt nitride electrode were significantly different from the cobalt peaks, indicating that the nitridation has been done thoroughly. The peaks were assigned with JCPDS 41-1445 (cassiterite $SnO_2$), 04-0802 (Pt), 05-0727 (Co), and 16-0116 (CoN), and completely assigned results show that the chemical composition of the cobalt nitride electrode is CoN, and also the other electrodes are fabricated properly. The grain size of the CoN was calculated by Scherrer's equation and (111) peak, and the result was 16.3 nm. Since Pt was cast on the FTO glass by thermal decomposition method, there were only small and broad signals, and the crystallite size calculated based on the (111) peak was 9.64 nm.

Figure 8.2a-8.2c shows the XPS survey spectra of the cobalt and cobalt nitride electrodes. The presence of Co metal is clear in both samples, and the O peaks show that the surfaces of the electrodes are oxidized, expected to be mainly attributed to the contact with oxygen molecules in air. As we take a close look at the Co 2p spectra (Figure 8.2b), it is clear from the binding energies at the Co $2p_{3/2}$ (780.8 eV) and Co $2p_{1/2}$ (796.2 eV) peaks which can be assigned to the Co-O bond that the significant portion of the cobalt sample's surface exist in $Co_3O_4$ form

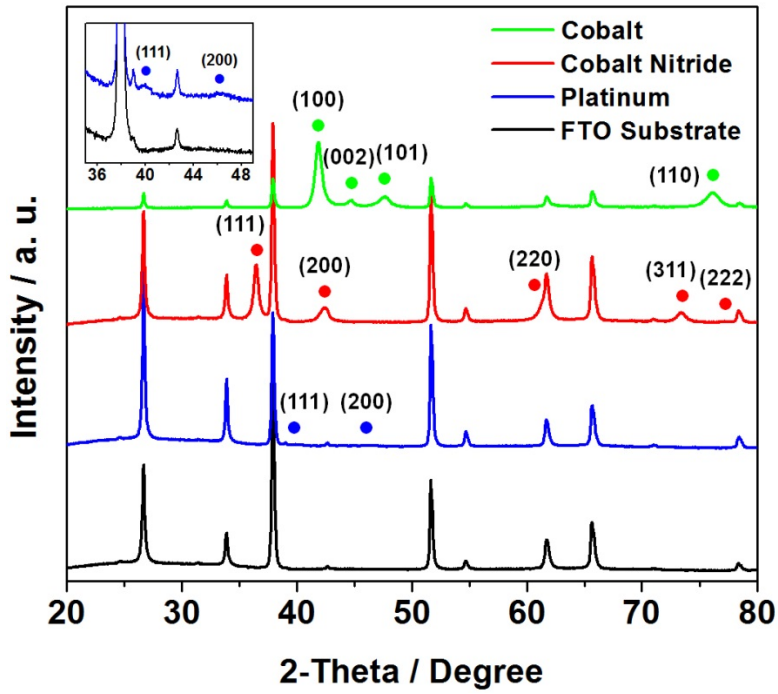


**Figure 8.1.** (a,b) The XRD spectra of Pt (blue lines), Co (green lines), and cobalt nitride films (red lines) on FTO glasses (black lines).

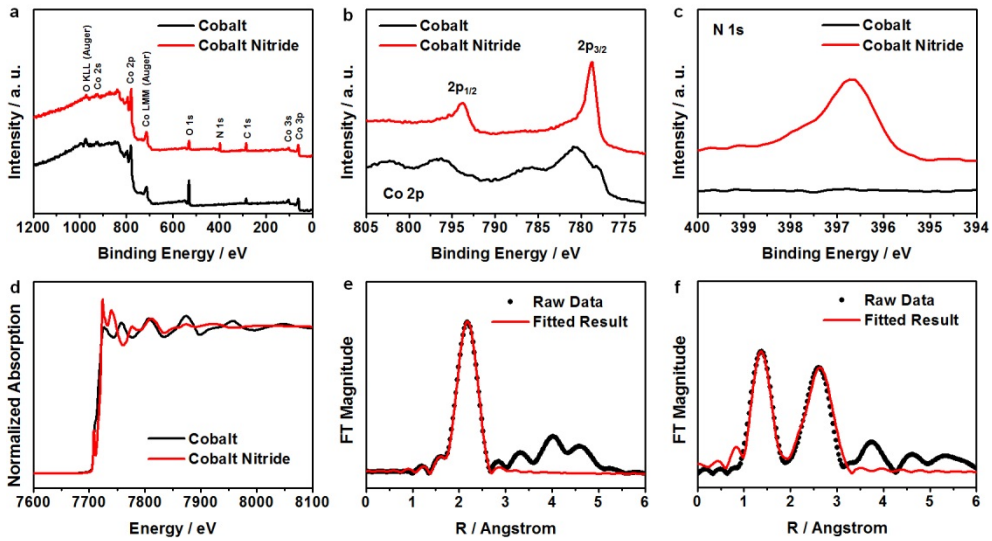


**Figure 8.2.** (a) XPS spectra of the cobalt (black lines) and cobalt nitride (red lines) films across a wide scan range for (b) the Co 2p core level peaks, and (c) the N 1s core level peak. (d) The Co K-edge XANES spectra of cobalt and cobalt nitride. (e,f) The $k^3$-weighted Fourier transforms of the EXAFS spectra at the Co K-edge for (e) nickel and (f) cobalt nitride.

[74,75]. However, there were Co 2p peaks at 778.2 eV ($2p_{3/2}$) and 793.0 eV ($2p_{1/2}$) that correspond to the Co-Co bond, indicating that there are metallic phase remaining at the surface, enabling the direct comparison between the Co 2p peaks of cobalt and cobalt nitride electrodes [76]. In cobalt nitride sample, the Co 2p peaks appear at the binding energies of 778.7 eV ($2p_{3/2}$) and 793.7 eV ($2p_{1/2}$), of which values are significantly shifted to higher binding energy compared to the metallic Co peaks. Together with the shift in Co 2p peaks, the presence of N 1s peak at 396.7 eV verifies that the formation of Co-N bond has been properly done.

In order to further characterize the oxidation state and the crystal structure of the cobalt nitride electrode, XAFS analyses were performed. Figure 8.2d shows the X-ray absorption near edge structure (XANES) cobalt and cobalt electrodes at the Co K-edge. From the significantly increased white line intensity and high-energy shifted edge position of the cobalt nitride, it was clear that the bulk oxidation state of the cobalt nitride is significantly larger than that of cobalt sample, indicating that the nitridation has been successful in whole region through the reactive sputtering process. The clear pre-edge line in the cobalt nitride sample indicates that the Co atom in cobalt nitride has tetrahedral symmetry [77]. Moreover, since the crystal structure and compositions of the films prepared by reactive sputtering is very sensitive to the vapor pressure and the sputtering power, the coordination number and bond lengths of the cobalt nitride film was confirmed by the extended X-ray absorption fine structure (EXAFS) analysis. Figure 8.2e and 8.2f show the Fourier transformed $k^3$-weighted EXAFS spectra of the cobalt and cobalt nitride sample, with the fitted results which were calculated using Kaiser-Bessel function with d$k$ = 0.5 and d$R$ = 0.5 (R-factor being 0.0020 and 0.0032 for cobalt and cobalt nitride, respectively). The crystal structures of cobalt and cobalt nitride are hexagonal and cubic structure according to the XRD results, and this information was used for the fitting process. In cobalt electrode, the Co-Co bond length was 2.490 Å, based on the assumption that the film was bulk Co with coordination number 12*. However,

the Co-Co interatomic distance in cobalt nitride sample was 3.066 Å, which is a significantly larger value compared to the case of cobalt film, and the coordination number was 11.5. On the other hand, Co-N bond length was 1.847 Å, with coordination number of 2.21.

### 8.3.2. Characterization on the morphologies of the film by electron microscopy

Figure 8.3a and 8.3b show the top-view SEM images of the platinized FTO glass, which is the most conventional and frequently used counter electrode in mesoscopic sensitized solar cells. As discussed from the XRD results, Pt existed in the form of thin nanoparticle layer on the substrate, leaving the rough surface structure of FTO. In contrast, cobalt nitride film showed specific morphologies different from the substrate. Top-view SEM images in Figure 8.3c and 8.3d show the cobalt nitride formed nanostructure with rough surfaces. For further understanding of this structure, we observed the cross-sectional morphology by milling the samples using focused ion beam (FIB) before the SEM analyses, and the image is shown in Figure 8.3e. The cobalt nitride showed cauliflower like structure with height of around 800 nm.

Further observations were made by TEM analyses on the sample prepared by FIB milling. TEM image in Figure 8.4a clearly verifies that the cobalt nitride has been formed on the FTO surface with cauliflower-like nanostructure, and the high resolution (HR)-TEM image in Figure 8.4b shows the lattice spacing of 0.25 nm, which matches with the d-spacing of (111) plane of CoN. The selected area diffraction pattern (SAED) displayed in Figure 8.4c indicates that the reactively sputtered cobalt nitride is polycrystalline CoN, and this precisely matches with the results from the XRD analyses. Moreover, to confirm the uniform and complete nitridation in cobalt nitride films, elemental energy filtered (EF)-TEM maps were obtained on Co and N. Figure 8.4d shows the overlapped EF-TEM images in which red colored and green colored region correspond to the location of Co and N,

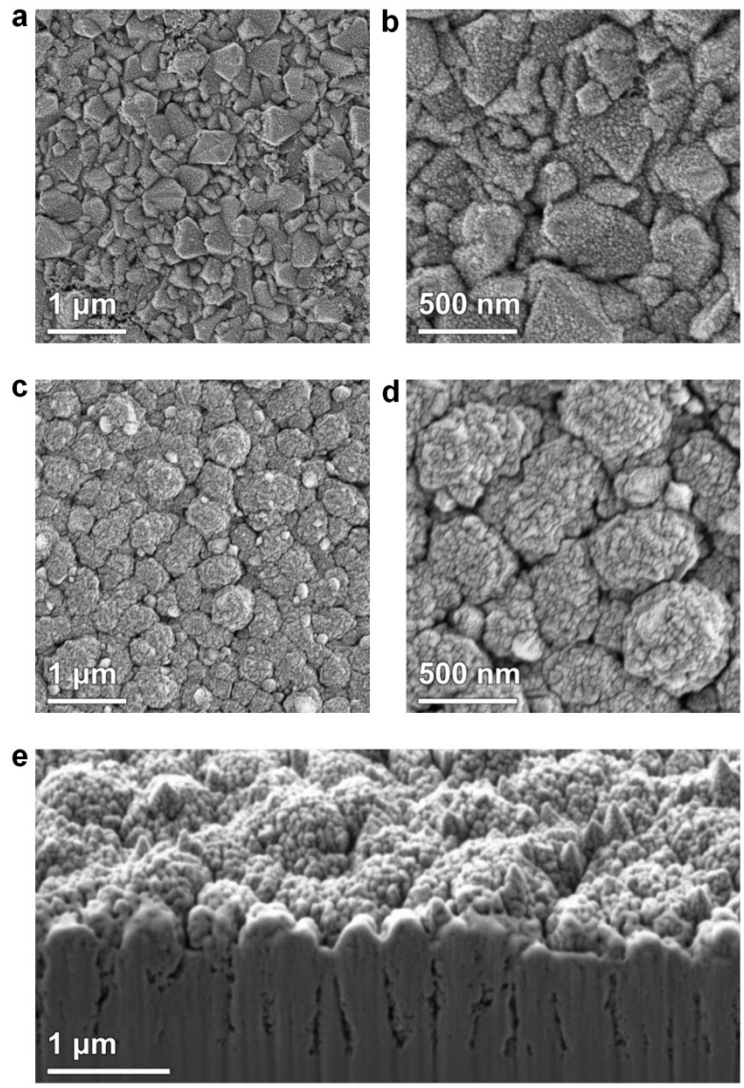


**Figure 8.3.** Top-view SEM images of (a,b) Pt and (c,d) cobalt nitride films on FTO glasses. (e) Cross-sectional SEM image of cobalt nitride taken after FIB milling.

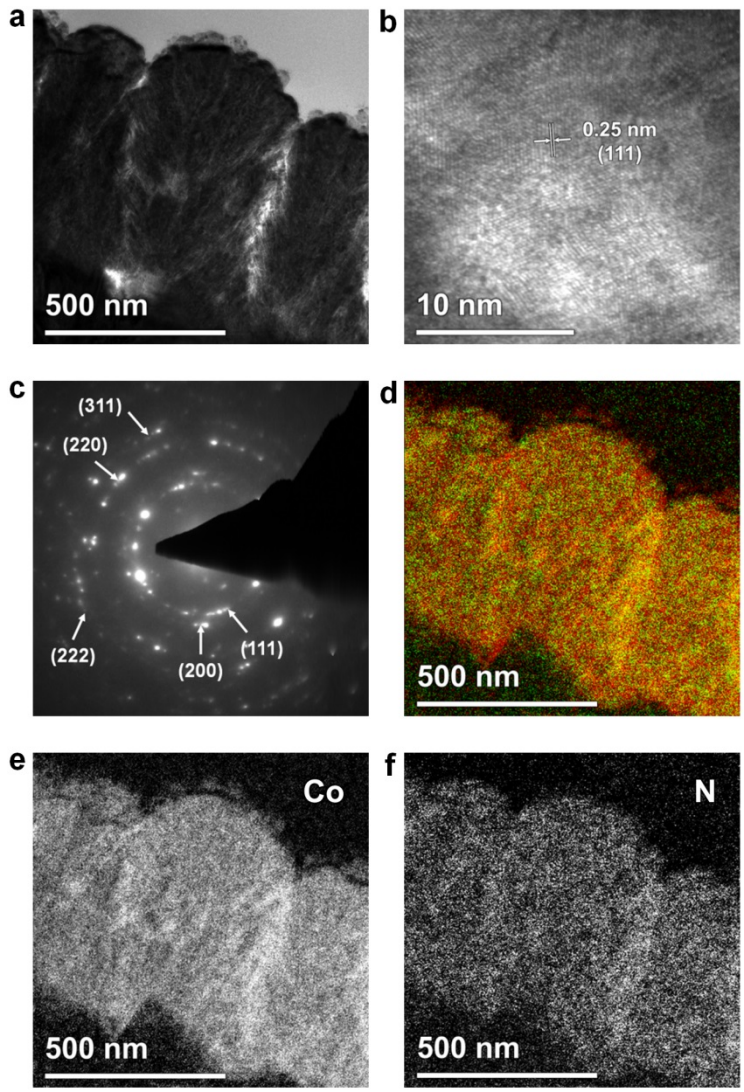


**Figure 8.4.** (a) TEM and (b) HR-TEM images of cobalt nitride film on FTO glass. (c) SAED patterns of cobalt nitride and elemental EF-TEM maps of (d) Co (red) & N (green), (e) Co, and (f) N for the image in (a).

respectively. Also, separated elemental Co and N EF-TEM maps in Figure 8.4e and 8.4f, respectively, imply that the cobalt nitride has been formed uniformly at all locations.

### 8.3.3. Electrochemical characterization of electrocatalytic activities

In order to compare the electrocatalytic activities of cobalt nitride with platinum, CV, Tafel polarization, and EIS analyses were performed. Figure 8.5 show the CV results of platinum and cobalt nitride electrode in various redox electrolytes. Generally, in a CV diagram, earlier onset and peak current potential indicate higher electrocatalytic activity. In iodide electrolyte (Figure 8.3a and 8.3b), there were two clearly apparent two redox peaks in both direction of potential sweep, which correspond to the two step reactions of $I_3^-/I^-$ redox couple [78], while the cobalt bipyridyl redox electrolyte with one step $[Co(bpy)_3]^{3+/2+}$ reaction resulted in a only one redox peak (Figure 8.3c and 8.3d). By comparing the CV diagrams of Pt and CoN in iodide and cobalt bipyridyl electrolytes, it was clarified that the Pt shows higher electrocatalytic performance in DSCs compared to the CoN. In contrast, in polysulfide electrolyte for QDSCs, CoN was significantly better than Pt in activity, as can be clearly seen from the earlier onset and peak current potentials. There is one noteworthy behavior of CoN electrode in the region below -0.7 V vs. Ag/AgCl that some other reactions are taking place other than the reduction of $S^{2-}$ to $S_n^{2-}$. However, since QDSCs are not operated in that potential region, and also there is no significant indication for the stability problem by the side reactions as the cycle number increases, the reactions at that potential range was considered unimportant.

Figure 8.6a-8.6c show the Tafel polarization curves of the platinum and cobalt nitride electrodes in iodide, cobalt, and polysulfide redox electrolytes, respectively. In $I_3^-/I^-$ and $[Co(bpy)_3]^{3+/2+}$ electrolytes, exchange current densities were significantly larger at Pt compared to CoN, by more than a degree of order. In contrast, cobalt nitride was around ten times better than Pt for the redox reaction of

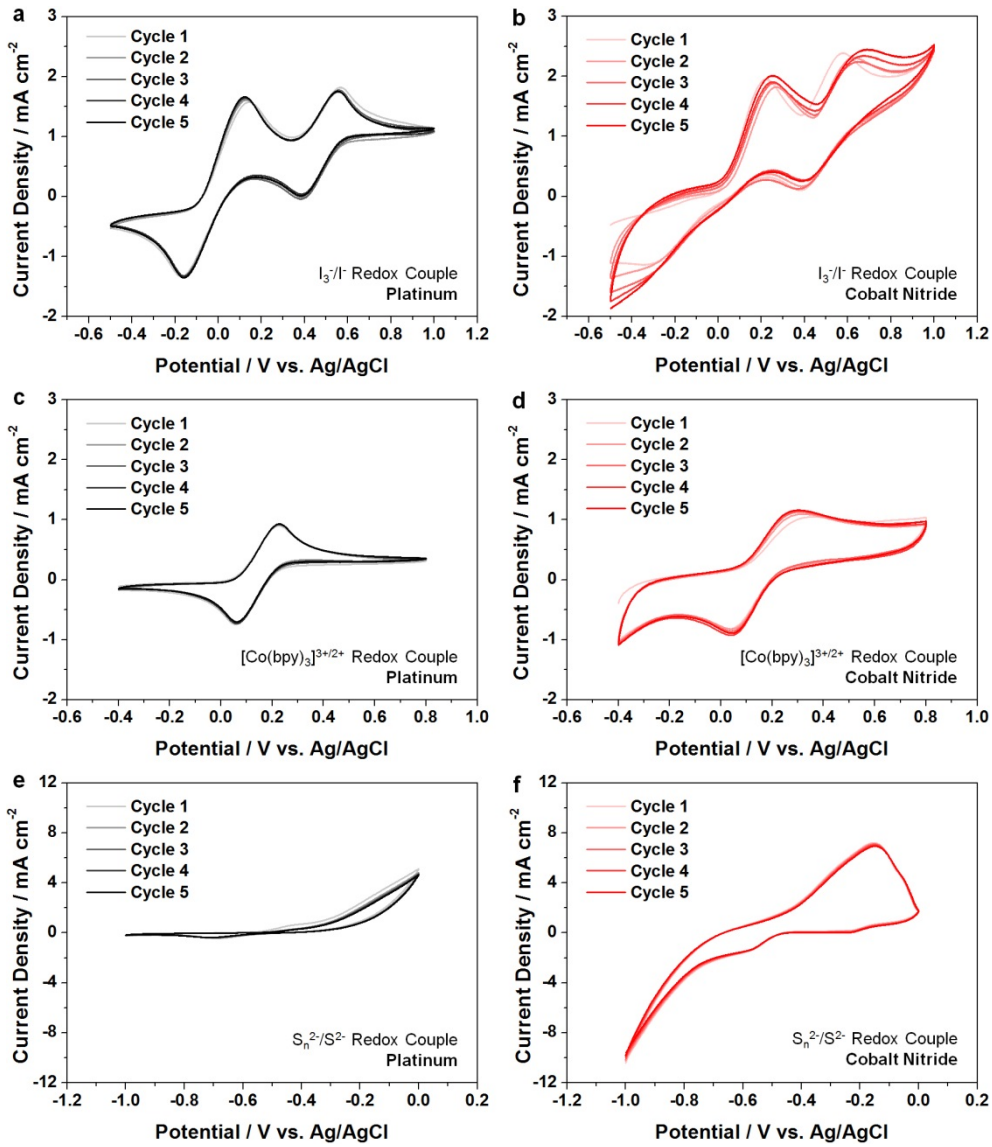


**Figure 8.5.** CV diagrams of Pt (black lines) and cobalt nitride (red lines) electrodes for (a,b) iodide redox couple, (c,d) cobalt bipyridyl redox couple, and (e,f) polysulfide redox couple.

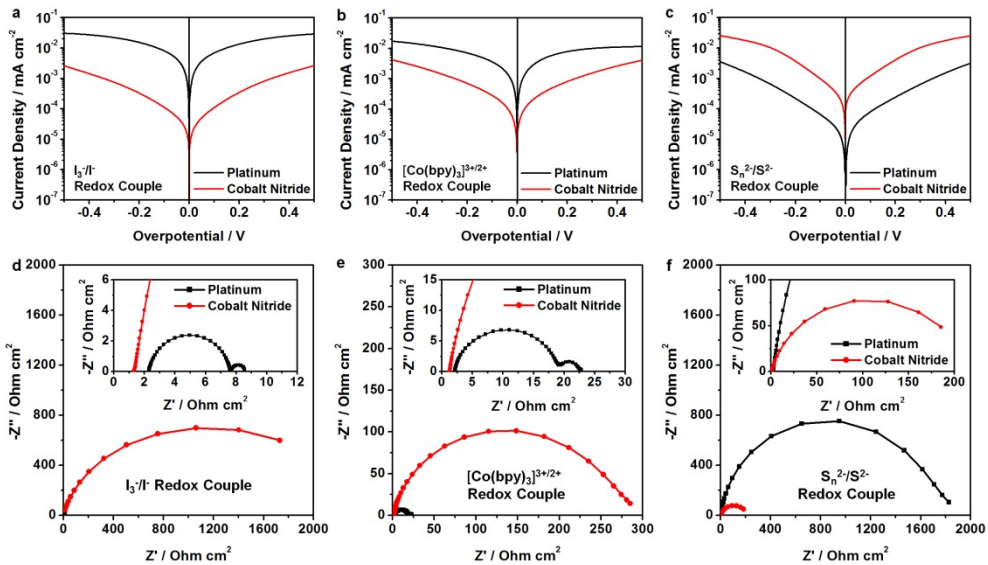


**Figure 8.6.** Tafel polarization curves for symmetric dummy cells with Pt (black lines) or cobalt nitride (red) electrodes for (a) iodide, (b) cobalt bipyridyl, and (c) polysulfide redox electrolytes. Electrochemical impedance spectra of the symmetric dummy cells composed of Pt (black lines/squares) or cobalt nitride (red lines/circles) for (d) iodide, (e) cobalt bipyridyl, and (f) polysulfide redox electrolytes.

polysulfide redox couples. These behaviors were confirmed once more by measuring the charge transfer resistance ($R_{ct}$) at the electrolyte/electrode interface based on the EIS analyses. Figure 8.6d-8.6f shows the Nyquist diagrams obtained by using the symmetric cells composed of the identical electrodes, and the curves were fitted based on the symmetric circles shown in Figure 8.7a. The constant phase element (*CPE*) term often stands for the roughness of a nanostructured electrodes [79], and double-layer capacitance ($C_{dl}$) can be obtained from the *CPE*. Other terms in the equivalent circuit contains ohmic resistance (series resistnace; $R_s$) and electrolyte diffusion kinetics (Warburg impedance; $W_s$). The $R_{ct}$ and $C_{dl}$ values, which are directly related with the interfacial kinetics at the electrode/electrolyte interface are displayed in Table 8.1. The $R_{ct}$ values were coincident with the CV and Tefel polarization results. For the iodide and cobalt bipyridyl electrolytes, Pt had considerably lower $R_{ct}$ compared to the CoN. However, this trend was reversed in polysulfide electrolyte. The CoN was around ten times less resistive for the $S_n^{2-}/S^{2-}$ redox reactions than the Pt. The overall results from various electrochemical analyses verified that the CoN is inferior to Pt for use as a counter electrode of DSCs, but this trend is opposite in the case of QDSCs wherein the CoN has superior electrocatalytic activity. However, it should be stated in this spot that the solar cell performance does not directly depend on the performance of counter electrodes, because electron transport within the semiconductor has the slowest timescale in general [6]. Meanwhile, in all cases, CoN showed larger $C_{dl}$ than Pt, indicating that the CoN has larger roughness factor due to its cauliflower-like nanostructure. Also, among various redox electrolytes, Pt electrodes showed significantly larger $C_{dl}$ in polysulfide electrolyte, compared to the other two. This is mainly attributed to the adsorption of $S^{2-}$ on the Pt surface, which is a well-known phenomenon causing a decrease in the electrocatalytic activity of Pt, as mentioned above.

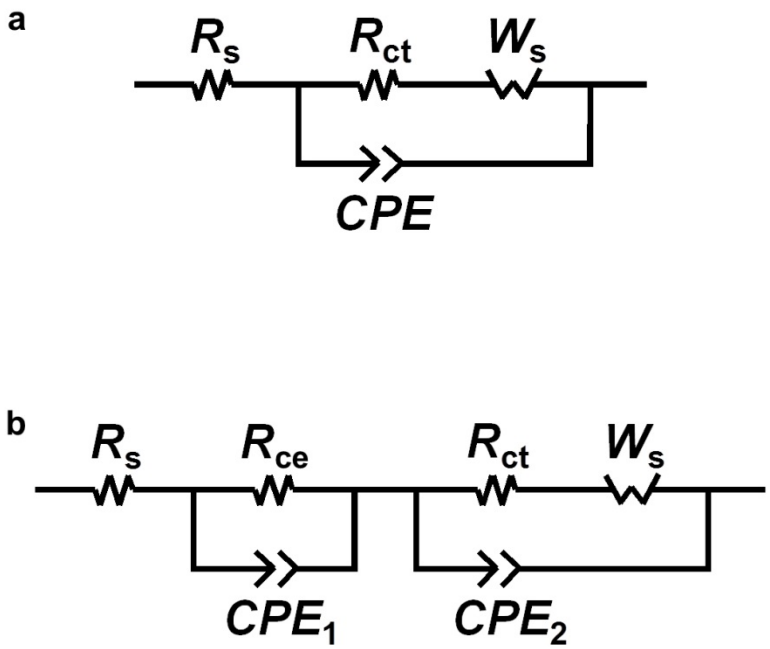


**Figure 8.7.** Equivalent circuits of a (a) symmetric dummy cell and a (b) mesoscopic sensitized solar cell for EIS analyses.

| Electrode | Electrolyte | $R_{ct}$ / Ω cm$^2$ | $C_{dl}$ / μF cm$^{-2}$ |
|---|---|---|---|
| Platinum | Iodide | 2.626 | 54.20 |
| Cobalt Nitride | Iodide | 892.5 | 855.8 |
| Platinum | Cobalt | 8.165 | 65.96 |
| Cobalt Nitride | Cobalt | 138.5 | 522.2 |
| Platinum | Polysulfide | 859.5 | 164.6 |
| Cobalt Nitride | Polysulfide | 94.15 | 676.3 |

**Table 8.1.** Parameters determined by fitting the impedance spectra of symmetric dummy cells composed of Pt or cobalt nitride electrodes.

### 8.3.4. Applications of the electrodes in mesoscopic sensitized solar cells

For the device applications, cobalt nitride electrodes were directly used as counter electrodes in DSCs and QDSCs (CISe with $S_n^{2-}/S^{2-}$). DSCs were prepared by using N719 or Y123 dye molecules with $I_3^-/I^-$ or $[Co(bpy)_3]^{3+/2+}$ electrolytes, respectively. In QDSCs, 4 nm sized CISe QDs reported elsewhere [64] and $S_n^{2-}/S^{2-}$ redox electrolyte. Figure 8.8 shows the *J-V* curves measured under incident light of AM 1.5G condition (light intensity: 100 mW $cm^{-2}$) and the IPCE spectra of DSCs and QDSCs employing Pt and CoN counter electrodes. In case of QDSCs, $Cu_2S$ electrode fabricated according to the previous reports [18-20] was also employed for the precise comparison of the performance of the CoN electrodes with the state-of-the-art technologies. The parameters obtained from the *J-V* curves showing the solar cell performances, namely open-circuit voltage ($V_{oc}$), short-circuit current density ($J_{sc}$), fill factor (*FF*), and energy conversion efficiency ($\eta$), are displayed in Table 8.2. In N719 sensitized DSCs with iodide redox electrolyte, CoN's performance was as high as that of the Pt's, resulting in a conversion efficiency of 7.31% while the conventional Pt based DSC showed 7.55% efficiency. From the IPCE spectra in Figure 8.8b, it was verified that there is no significant difference in spectral quantum efficiencies. This result indicates that the CoN electrode is a promising candidate to replace Pt without significant loss of solar cell performances.

In the cases of DSCs with Y123 dyes as sensitizers, overall performances were generally lower than the N719-DSCs, because the $TiO_2$ pastes used for the fabrication of photoanodes were optimized for the iodide redox electrolyte. The size of cobalt bipyridyl molecules are significantly larger than the iodide redox couples, and thus suffer from the limitations from the mass transport. Therefore, numerous research groups focusing on the optimization of the DSCs with cobalt bipyridyl electrolyte use $TiO_2$ photoanode with increases porosity of which average pore sizes are over 30 nm. However, though our best paste was not optimized for

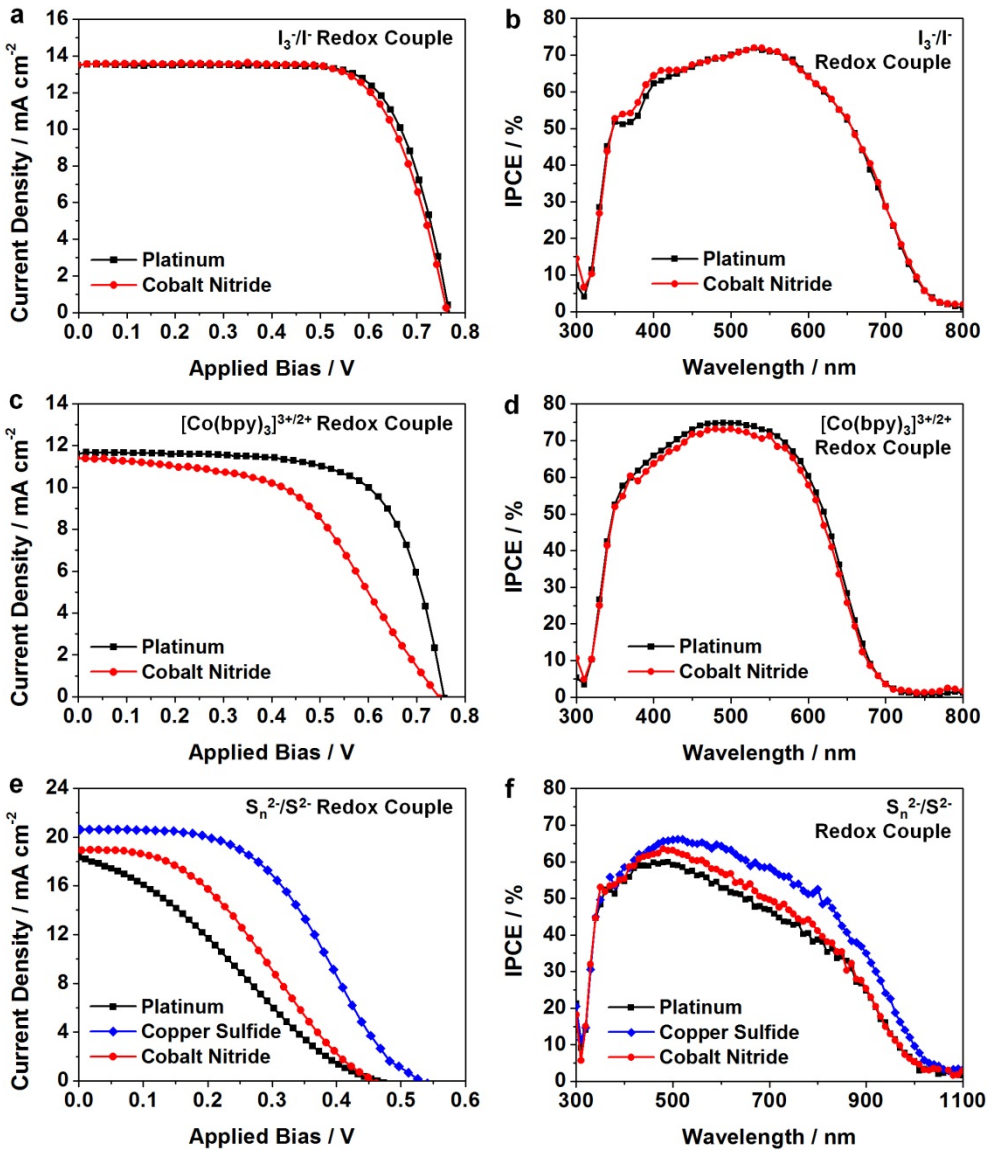


**Figure 8.8.** *J-V* characteristics and IPCE spectra of (a,b) N719-DSCs with iodide redox couple, (c,d) Y123-DSCs with cobalt bipyridyl redox ecouple, and CISe-QDSCs with polysulfide redox couple employing platinum (black lines/squares), copper sulfide (blue lines/diamonds), and cobalt nitride (red lines/circles) counter electrodes.

| Solar Cell Type | Electrolyte | $V_{oc}$ / V | $J_{sc}$ / mA cm$^{-2}$ | $FF$ / % | $\eta$ / % |
|---|---|---|---|---|---|
| N719-DSCs with Platinum CEs | Iodide | 0.766 | 13.50 | 73 | 7.55 |
| N719-DSCs with Cobalt Nitride CEs | Iodide | 0.762 | 13.52 | 71 | 7.31 |
| Y123-DSCs with Platinum CEs | Cobalt | 0.756 | 11.61 | 68 | 5.97 |
| Y123-DSCs with Cobalt Nitride CEs | Cobalt | 0.745 | 11.39 | 51 | 4.33 |
| CISe-QDSCs with Platinum CEs | Polysulfide | 0.462 | 18.37 | 28 | 2.35 |
| CISe-QDSCs with Copper Sulfide CEs | Polysulfide | 0.532 | 20.62 | 46 | 5.06 |
| CISe-QDSCs with Cobalt Nitride CEs | Polysulfide | 0.457 | 18.90 | 38 | 3.28 |

**Table 8.2.** Summary of *J-V* characteristics of DSCs and QDSCs employing various kinds of counter electrodes.

the cobalt bipyridyl redox electrolyte, the comparison between the Pt and CoN counter electrodes could be done properly, because there was no valid difference in experimental setups and conditions. CoN exhibited considerably lower efficiency compared to Pt. Among the parameters for the solar cell performance evaluation, *FF* was significaltly lower in DSC with CoN counter electrodes, being 51% compared to the 68% of conventional DSC with Pt counter. Since there were slight differences in $V_{oc}$ and $J_{sc}$, the difference seems to have been resulted from an increased resistance which is attributed to the nanostructure of the CoN electrode. As have been characterized with electron microscope images, the cauliflower-like structure of CoN has mesopores at the boundaries and surface of the cauliflowers. These porous structures might have impeded the rapid mass transport of the cobalt bipyridyl redox couples, resulting in a significantly increased diffusion resistance. The spectral responses of the DSCs employing Pt and CoN counter electrodes were almost identical, as displayed in the IPCE spectra at Figure 8.4d.

In QDSCs, the trend in performances of the cells with Pt and CoN counter was reversed. Though the differences in $V_{oc}$ and $J_{sc}$ were not noteworthy, *FF* was significantly larger in QDSC with CoN counter electrode. As a result, the $\eta$ increased from 2.35% to 3.28% as the counter electrode was replaced from Pt to CoN. Also, as stated above, QDSC with $Cu_2S$ electrode was prepared for the comparison, because $Cu_2S$ is the best performing electrocatalyst for the reduction of polysulfide redox couples. The $Cu_2S$ employed QDSC showed significantly larger voltage and photocurrent, with an enhanced *FF* resulting in a 5.06% of efficiency. Since the $Cu_2S$ electrode was prepared by using a brass foil, the symmetric cell analyses could not be done on the $Cu_2S$ due to the lack of capability for the electrolyte injection through a pre-drilled hole. Therefore, the EIS analyses on the QDSC full cell were performed. Figure 8.9 shows the Nyquist plot of the QDSCs employing various counter electrodes in high-frequency region. The kinetics of the electron transfer at the electrode/electrolyte interface can be

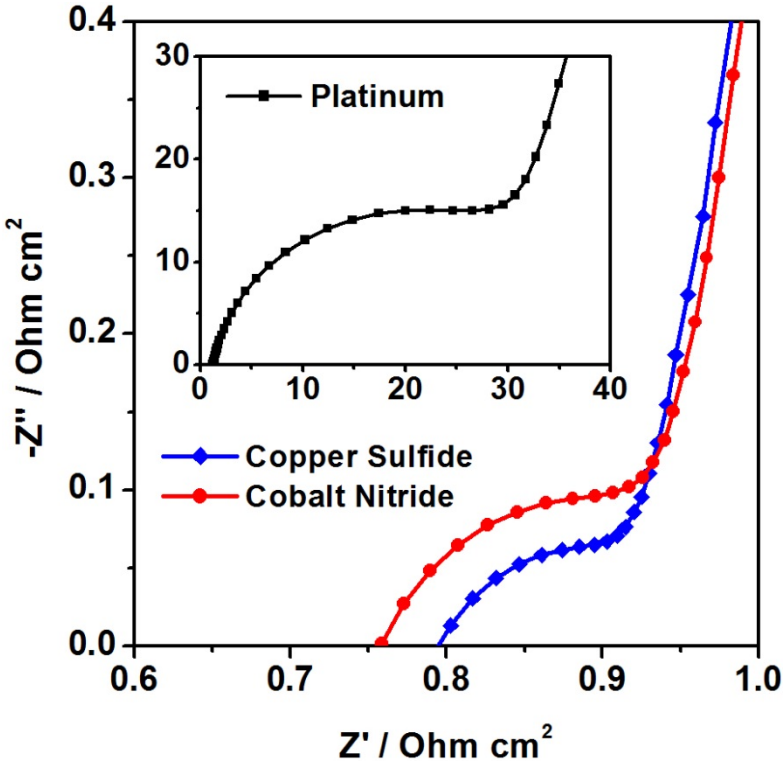


**Figure 8.9.** Nyquist plots at high-frequency region of QDSCs with platinum, copper sulfide, or cobalt nitride counter electrodes measured under forward bias of 0.45 V in dark condition.

determined by the observation and interpretation of the first semicircle [80], and thus the charge transfer resistance at and capacitance of the counter electrodes ($R_{ce}$ and $C_{\mu}$, respectively) were obtained by fitting based on the equivalent circuit shown in Figure 8.7b. The $R_{ce}$ and $C_{\mu}$ values are displayed in Table 8.3, and the $C_{\mu}$ was obtained by the $CPE_{ce}$ term in Figure 8.7b. The $R_{ce}$ was smallest in $Cu_2S$ (0.11 $\Omega$ $cm^{-2}$), and it was slightly larger in CoN (0.14 $\Omega$ $cm^{-2}$). However, Pt showed more than 20 times larger resistance value, namely 36.18 $\Omega$ $cm^{-2}$. This shows that the electrocatalytic activity of CoN is significantly larger than Pt, and slight smaller than the state-of-the-art $Cu_2S$ electrode.

Since the main issue of $Cu_2S$ counter electrode in QDSC is its photostability, $J_{sc}$ measurements of QDSCs employing Pt, $Cu_2S$, and CoN counter were performed under AM 1.5G illumination (light intensity: 100 mW $cm^{-2}$), and the results are shown in Figure 8.10. In general decrease of $J_{sc}$ occurred in all of the cells to some extent, because our QDSC device was sealed with a laboratory keptone tape which does not provide complete nor permanent sealing. Therefore, small amount of electrolytes evaporated during the measurement, causing decrease in the photocurrent, so we compared the relative photostabilities of the cells. As can be clearly seen from the $J_{sc}$ values and $J_{sc}$ retention in Figure 8.10, until 10 min, the decreasing rate was similar in all of the QDSCs. However, $Cu_2S$ showed steep decrease in photocurrent density after 10 min, and the $J_{sc}$ after 60 min was less than the 40% of the initial value. However, CoN showed about 70% photocurrent retention, indicating that the stability of CoN is close to that of Pt, of which $J_{sc}$ retention after 60 min was around 80%. At last, $J_{sc}$ value of CoN was 12.23 mA $cm^{-2}$ which is slightly larger than the case of Pt (12.89 mA $cm^{-2}$) but considerably larger than 7.28 mA $cm^{-2}$ of $Cu_2S$. Given that the Pt in QDSCs shows intrinsically low FF due to the chemisorption of $S^{2-}$ on the surface, CoN seems to be the best counter electrode for QDSCs among three due to its high electrocatalytic activity and decent photostability.

| Electrode | $R_{ce}$ / Ω cm$^2$ | $C_{\mu}$ / μF cm$^{-2}$ |
|---|---|---|
| Platinum | 36.18 | 506 |
| Copper Sulfide | 0.11 | 303 |
| Cobalt Nitride | 0.14 | 98.1 |

**Table 8.3.** Parameters determined by fitting the impedance spectra of QDSCs employing platinum, copper sulfide, or cobalt nitride counter electrodes.

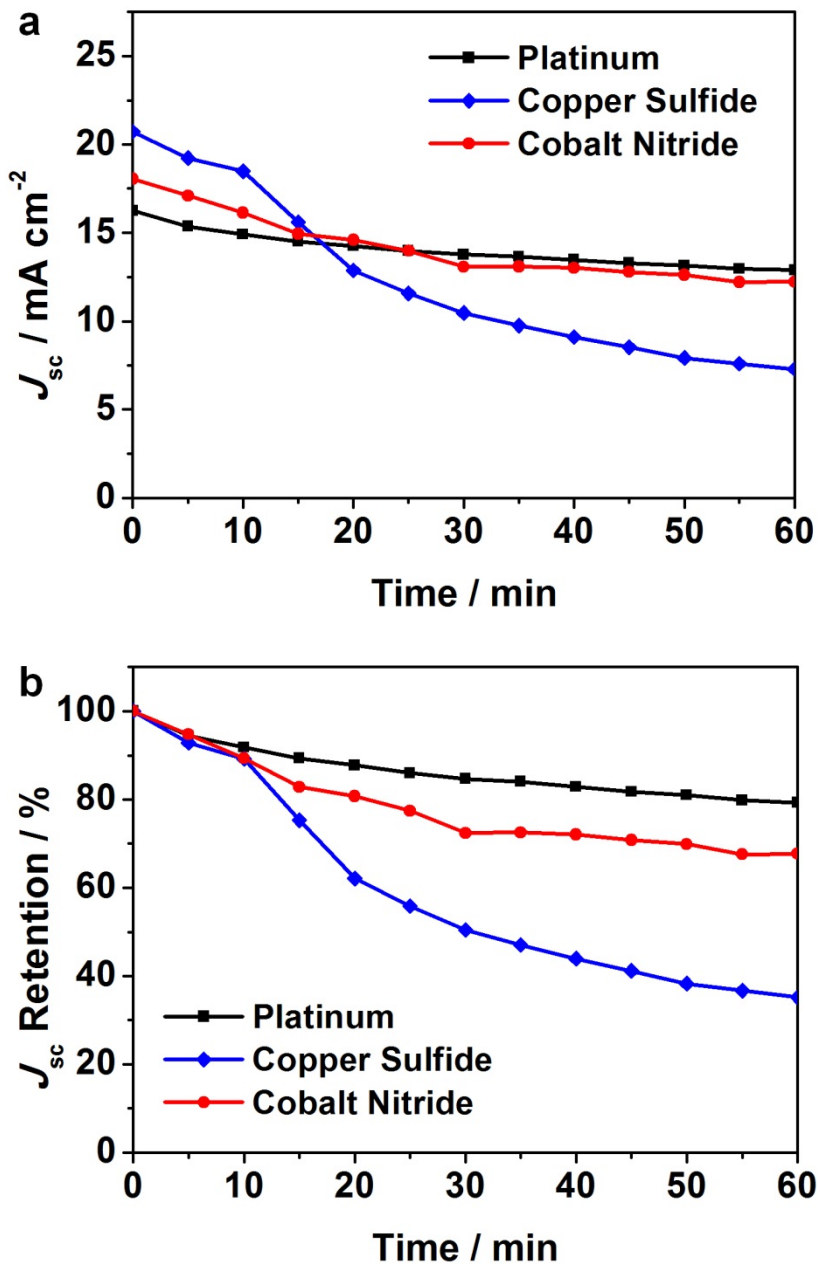


**Figure 8.10.** (a) $J_{sc}$ of QDSCs measured under 1 sun illumination for 1 h and (b) corresponding $J_{sc}$ retention compared to the initial value.

## 8.4. Conclusions

In this research, cauliflower-shaped nanostructured cobalt nitride film was fabricated by reactive sputtering of cobalt in $N_2$ atmosphere. The cobalt nitride exhibited fine electrocatalytic activities for the reduction and oxidation of iodide, cobalt bipyridyl, and polysulfide redox couples that are often employed in mesoscopic sensitized solar cells. When the cobalt nitride was applied as counter electrodes for the solar cells, the DSCs based on iodide electrolyte showed comparable performances to the conventional DSCs with Pt counter electrode. Moreover, CoN showed higher performance in QDSC than Pt. In addition, the CoN was verified as a superior counter electrode to a state-of-the-art $Cu_2S$, which suffers from the significant instability under incident light. In mesoscopic sensitized solar cells, high cost of Pt used for the electrocatalysis have been the largest obstacle for the practical utilization and large-scale commercialization. CoN is composed of low cost and earth abundant elements, and the fabrication method is industrially favorable. Together with the high performances, these advantages of CoN are anticipated to expedite the everyday use of sensitized solar cells.

## 8.5. References


[1] O'Regan, B; Grätzel, M., *Nature* **1991**, *353*, 737.

[2] Hagfeldt, A.; Grätzel, M., *Chem. Rev.* **1995**, *95*, 49.

[3] Grätzel, M., *Nature* **2001**, *414*, 338.

[4] Grätzel, M., *Inorg. Chem.* **2005**, *44*, 6841.

[5] Grätzel, M., *Accounts Chem. Res.* **2009**, *42*, 1788.

[6] Hagfeldt, A.; Boschloo, G.; Sun, L.; Kloo, L.; Pettersson, H., *Chem. Rev.* **2010,** *110*, 6595.

[7] Nazeeruddin, M. K.; Kay, A.; Rodicio, I.; Humphry-Baker, R.; Müller, E.; Liska, P.; Vlachopoulos, N.; Grätzel, M., *J. Am. Chem. Soc.* **1993**, *115*, 6492.

[8] Chiba, Y.; Islam, A.; Watanabe, Y.; Komiya, R.; Koide, N.; Han, L., *Jpn. J. Appl. Phys.* **2006**, *45*, L368.

[9] Kinoshita, T.; Dy, J. T.; Uchida, S.; Kubo, T.; Segawa, H., *Nat. Photonics* **2013**, *7*, 535.

[10] Yella, A.; Lee, H.-W.; Tsao, H. N.; Yi, C.; Chandiran, A. K.; Nazeeruddin, M. K.; Diau, E. W.-G.; Yeh, C.-Y.; Zakeeruddin, S. M.; Grätzel, M., *Science* **2011**, *334*, 629.

[11] Matthew, S.; Yella, A.; Gao, P.; Humphry-Baker, R.; Curchod, B. F. E.; Ashari-Astani, N.; Tavernelli, I.; Rothlisberger, U.; Nazeeruddin, M. K.; Grätzel, M., *Nat. Chem.* **2014**, *6*, 242.

[12] Nozik, A. J., *Physica E* **2002**, *14*, 115.

[13] Robel, I.; Subramanian, V.; Kuno, M.; Kamat, P. V., *J. Am. Chem. Soc.* **2006**, *128*, 2385.

[14] Hodes, G., *J. Phys. Chem. C* **2008**, *112*, 17778.

[15] Kamat, P. V., *J. Phys. Chem. C* **2008**, *112*, 18737.

[16] Rühle, S.; Shalom, M.; Zaban, A., *ChemPhysChem* **2010**, *22*, 2290.

[17] Santra, P. K.; Kamat, P. V., *J. Am. Chem. Soc.* **2012**, *134*, 2508.

[18] Lee, J.-W.; Son, D.-Y.; Ahn, T. K.; Shin, H.-W.; Kim, I.-Y.; Hwang, S.-J.; Ko, M. J.; Sul, S.; Han, H.; Park, N.-G., *Sci. Rep*. **2013**, *3*, 1050.

[19] Wang, J.; Mora-Seró, I.; Pan, Z.; Zhao, K.; Zhang, H.; Feng, Y.; Yang, G.; Zhong, X.; Bisquert, J., *J. Am. Chem. Soc.* **2013**, *135*, 15913.

[20] Pan. Z.; Mora-Seró, I.; Shen, Q.; Zhang, H.; Li, Y.; Zhao, K.; Wang, J.; Zhong, X.; Bisquert, J., *J. Am. Chem. Soc.* **2014**, *136*, 9203.

[21] Feldt, S. M.; Gibson, E. A.; Gabrielsson, E.; Sun, L.; Boschloo, G.; Hagfeldt, A., *J. Am. Chem. Soc.* **2010**, *132*, 16714.

[22] Bessho, T.; Zakeeruddin, S. M.; Yeh, C.-Y.; Diau, E. W.-G.; Grätzel, M., *Angew. Chem. Int. Ed.* **2010**, *49*, 6646.

[23] Tsao, H. N.; Yi, C.; Moehl, T.; Yum, J.-H.; Zakeeruddin, S. M.; Nazeeruddin, M. K.; Grätzel, M., *ChemSusChem* **2011**, *4*, 591.

[24] Lan. C.-M.; Wu, H.-P.; Pan, T.-S.; Chang, C.-W.; Chao, W.-S.; Chen, C.-T.; Wang, C.-L. Lin, C.-Y.; Diau, E. W.-G., *Energy Environ. Sci.* **2012**, *5*, 6460.

[25] Yella, A.; Humphry-Baker, R.; Curchod, B. F. E.; Astani, N. A.; Teuscher, J.; Polander, L. E.; Mathew, S.; Moser, J.-E.; Tavernelli, I.; Rothlisberger, U.; Grätzel, M.; Nazeeruddin, M. K.; Frey, J., *Chem. Mater.* **2013**, *25*, 2733.

[26] Yella, A.; Mai, C.-L.; Zakeeruddin, S. M.; Chang, S.-N.; Hsieh, C.-H.; Yeh, C.-Y.; Grätzel, M., *Angew. Chem. Int. Ed.* **2014**, *53*, 2973.

[27] Yum, J.-H.; Baranoff, E.; Kessler, F.; Moehl, T.; Ahmad, S.; Bessho, T.; Marchioro, A.; Ghadiri, E.; Moser, J.-E.; Yi, C.; Nazeeruddin, M. K.; Grätzel, M., *Nat. Commun.* **2012**, *3*, 631.

[28] Kay, A.; Grätzel, M., *Sol. Energy Mater. Sol. Cells.* **1996**, *44*, 99.

[29] Suzuki, K.; Yamaguchi, M.; Kumagai, M; Yanagida, S., *Chem. Lett.* **2003**, *32*, 1.

[30] Murakami, T. N.; Ito, S.; Wang, Q.; Nazeeruddin, M. K.; Bessho, T.; Cesar, I.; Liska, P.; Humphry-Baker, R.; Comte, P.; Péchy, P.; Grätzel, M., *J. Electrochem. Soc.* **2006**, *153*, A2255.

[31] Ramasamy, E.; Lee, W. J.; Lee, D. Y.; Song, J. S., *Appl. Phys. Lett.* **2007**, *90*, 173103.

[32] Huang, Z.; Liu, X.; Li, K.; Li, D.; Luo, Y.; Li, H.; Song, W.; Chen, L. Q.; Meng, Q., *Electrochem. Commun.* **2007**, *9*, 596.

[33] Lee, W. J.; Ramasamy, E.; Lee, D. Y.; Song, J. S., *ACS Appl. Mater. Interfaces* **2009**, *1*, 1145.

[34] Saito, Y.; Kubo, W.; Kitamura, T.; Wada, Y.; Yanagida, S., *J. Photochem. Photobiol. A* **2004**, *164*, 153.

[35] Ahmad, S.; Yum, J.-H.; Xianxi, Z.; Grätzel, M.; Butt, H.-J.; Nazeeruddin, M. K., *J. Mater. Chem.* **2010**, *20*, 1654.

[36] Lee, K. S.; Lee, H. K.; Wang, D. H.; Park, N.-G.; Lee, J. Y.; Park, O. O.; Park, J. H., *Chem. Commun.* **2010**, *46*, 4505.

[37] Trevisan, R.; Döbbelin, M.; Boix, P. P.; Barea, E. M.; Tena-Zaera, R.; Mora-Seró, I.; Bisquert, J., *Adv. Energy Mater.* **2011**, *1*, 781.

[38] Tan, S.; Zhai, J.; Xue, B.; Wan, M.; Meng, Q.; Li, Y.; Jiang, L.; Zhu, D., *Langmuir* **2004**, *20*, 2934.

[39] Li, Q.; Wu, J.; Tang, Q.; Lan, Z.; Li, P.; Lin, J.; Fan, L., *Electrochem. Commun.* **2008**, *10*, 1299.

[40] Li, Z.; Ye, B.; Hu, X.; Ma, X.; Zhang, X.; Deng, Y., *Electrochem. Commun.* **2009**, *11*, 1768.

[41] Sun, H.; Luo, Y.; Zhang, Y.; Li, D.; Yu, Z.; Li, K.; Meng, Q., *J. Phys. Chem. C* **2010**, *114*, 11673.

[42] Wang, M.; Anghel, A. M.; Marsan, B.; Ha, N.-L. C.; Pootrakulchote, N.; Zakeeruddin, S, M.; Grätzel, M., *J. Am. Chem. Soc.* **2009**, *131*, 15976.

[43] Li, G. R.; Song, J.; Pan, G. L.; Gao, X. P., *Energy Environ. Sci.* **2011**, *4*, 1680.

[44] Sun, H.; Qin, D.; Huang, S.; Guo, X.; Li, D.; Luo, Y.; Meng, Q., *Energy Environ. Sci.* **2011**, *4*, 2630.

[45] Wu, M.; Zhang, Q.; Xiao, J.; Ma, C.; Lin, X.; Miao, C.; He, Y.; Gao, Y.; Hagfeldt, A.; Ma, T., *J. Mater, Chem.* **2011**, *21*, 10761.

[46] Wang, Y.; Wu, M.; Lin, X.; Shi, Z.; Hagfeldt, A.; Ma, T., *J. Mater. Chem.* **2012**, *22*, 4009.

[47] Mulmudi, H. K.; Batabyal, S. K.; Rao, M.; Prabhakar, R. R.; Mathews, N.; Lam, Y. M.; Mhaisalkar, S. G., *Phys. Chem. Chem. Phys.* **2011**, *13*, 19307.

[48] Guai, G. H.; Leiw, M. Y.; Ng, C. M.; Li, C. M., *Adv. Energy Mater.* **2012**, *2*, 334.

[49] Chi, W. S.; Han, J. W.; Yang, S.; Roh, D. K.; Lee, H.; Kim, J. H., *Chem. Commun.* **2012**, *48*, 9501.

[50] Wu, M.; Lin, X.; Wang, Y.; Wang, L.; Guo, W.; Qi, D.; Peng, X.; Hagfeldt, A.; Grätzel, M.; Ma, T., *J. Am. Chem. Soc.* **2012**, *134*, 3419.

[51] Liao, Y.; Pan, K.; Wang, L.; Pan, Q.; Zhou, W.; Miao, X.; Jiang, B.; Tian, C.; Tian, G.; Wang, G.; Fu, H., *ACS Appl. Mater. Interfaces* **2013**, *5*, 3663.

[52] Hou, Y.; Wang, D.; Yang, X. H.; Fang, W. Q.; Zhang, B.; Wang, H. F.; Lu, G. Z.; Hu, P.; Zhao, H. J.; Yang, H. G., *Nat. Commun.* **2013**, *4*, 1583.

[53] Chen, X.; Tang, Q.; He, B.; Lin, L.; Yu, L., *Angew. Chem. Int. Ed.* **2014**, *53*, 10799.

[54] Wan, J.; Fang, G.; Yin, H.; Liu, X.; Liu, D.; Zhao, M.; Ke, W.; Tao, H.; Tang, Z., *Adv. Mater.* **2014**, *26*, 8101.

[55] He, B.; Meng, X.; Tang, Q.; Li, P.; Yuan, S.; Yang, P., *J. Power Sources* **2014**, *260*, 180.

[56] Shalom, M.; Rühle, S.; Hod, I.; Yahav, S.; Zaban, A., *J. Am. Chem. Soc.* **2009**, *131*, 9876.

[57] Farrow, B.; Kamat, P. V., *J. Am. Chem. Soc.* **2009**, *131*, 11124.

[58] Bang, J. H.; Kamat, P. V., *ACS Nano* **2009**, *3*, 1467.

[59] Tvrdy, K.; Frantsuzov, P. A.; Kamat, P. V., *Proc. Natl. Acad. Sci. USA* **2011**, *108*, 29.

[60] Hossain, M. A.; Jennings, J. R.; Koh, Z. Y.; Wang, Q., *ACS Nano* **2011**, *5*, 3172.

[61] Kang, S. H.; Zhu, K.; Neale, N. R.; Frank, A. J., *Chem. Commun.* **2011**, *47*, 10419.

[62] Braga, A.; Giménez, S.; Corcina, I.; Vomiero, A.; Mora-Seró, I., *J. Phys. Chem. Lett.* **2011**, *2*, 454.

[63] Zhou, N.; Chen, G.; Zhang, X.; Cheng, L.; Luo, Y.; Li, D.; Meng, Q., *Electrochem. Commun.* **2012**, *20*, 97.

[64] Yang, J.; Kim, J.-Y.; Yu, J. H.; Ahn, T.-Y.; Lee, H.; Choi, T.-S.; Kim, Y.-W.; Joo, J.; Ko, M. J.; Hyeon, T., *Phys. Chem. Chem. Phys.* **2013**, *15*, 20517.

[65] Chakrapani, V.; Baker, D.; Kamat, P. V., *J. Am. Chem. Soc.* **2011**, *133*, 9607.

[66] Hodes, G.; Manassen, J.; Cahen, D., *J. Electrochem. Soc.* **1980**, *127*, 544.

[67] Radich, J. G.; Dwyer, R.; Kamat, P. V., *J. Phys. Chem. Lett.* **2011**, *2*, 2453.

[68] Tachan, Z.; Shalom, M.; Hod, I.; Rühle, S.; Tirosh, S.; Zaban, A., *J. Phys. Chem. C* **2011**, *115*, 6162.

[69] Yang, Z.; Chen, C.-Y.; Liu, C.-W.; Li, C.-L.; Chang, H.-T., *Adv. Energy Mater.* **2011**, *1*, 259.

[70] Kim, H.-J.; Kim, D.-J.; Rao, S. S.; Savariraj, A. D.; Kim, S.-K.; Son, M.-K.; Gopi, C. V. V. M.; Prabakar, K., *Electrochim. Acta* **2014**, *127*, 427.

[71] Louka, T., *J. Electroanal. Chem.* **1972**, *36*, 355.

[72] Lee, Y.-L.; Lo, Y.-S., *Adv. Funct. Mater.* **2009**, *19*, 604.

[73] Koo, H.-J.; Yoo, P. B.; Yoo, K.; Kim, K.; Park, N.-G., *Inorg. Chim. Acta* **2008**, *361*, 677.

[74] Petitto, S. C.; Langell, M. A., *J. Vac. Sci. Technol. A* **2004**, *22*, 1690.

[75] Lee, C.-Y.; Lee, K.; Schmuki, P., *Angew. Chem. Int. Ed.* **2013**, *52*, 2077.

[76] Wagner, C. D.; Riggs, W. M.; Davis, L. E.; Moulder, J. F.; Muilenberg, G. E., *Handbook of X-ray Photoelectron Spectroscopy*; Perkin-Elmer (Physical Electronics Division), Eden-Prairie: MN, **1979**.

[77] Modrow, H., Bucher, S.; Rehr, J. J.; Ankudinov, A. L., *Phys. Rev. B* **2003**, *67*, 035123.

[78] Roy-Mayhew, J. D.; Bozym, D. J.; Punckt, C.; Aksay, I. A., *ACS Nano* **2010**, *4*, 6203.

[79] Longo, C.; Nogueira, A. F.; De Paoli, M. A.; Cachet, H., *J. Phys. Chem. B* **2002**, *106*, 5925.

[80] Wang, Q.; Moser, J.-E.; Grätzel, M. *J. Phys. Chem. B* **2005**, *109*, 14945.

# Chapter 9. Conclusions

## 9.1. Summary

### 9.1.1. Semiconductor photoelectrodes

Semiconductor photoelectrodes, which is considered as the heart of photoelectrochemical cells, is the component that has largest influence on the overall performance of the cells. For this reason, main issues in photoelectrodes are enhancement of charge collection and light harvesting of the electrodes. Therefore, in this thesis, research works on semiconductor photoelectrodes were performed in order to increase charge collection and light harvesting efficiencies.

In chapter 2 and 3, anodic ZnO and $SnO_2$ nanostructure arrays with one-dimensional alignments were employed as photoelectrodes of dye-sensitized solar cells (DSCs). ZnO and $SnO_2$ are well known materials for fast electron transport, and one-dimensional structure is a typical morphology for efficient charge collection. With these theoretical and experimental bases, highly uniform and vertically aligned ZnO nanowires and $SnO_2$ nanochannels fabricated by optimized and modified anodic oxidation processes were successfully utilized in dye-sensitized solar cells (DSCs). Moreover, with very thin $TiO_2$ shells deposited by atomic layer deposition (ALD) method, significant increases in the cell performances were observed.

In chapter 4 and 5, attempts for the maximization of surface area for light harvesting were performed. In general, mesoporous $TiO_2$ layer composed of ~20 nm sized $TiO_2$ nanoparticles with scattering particles of a few hundred nanometer size are known as state-of-the-art photoelectrode for mesoscopic sensitized solar cells. For further improvements in light harvesting, $TiO_2$ coated wrinkled silica

nanoparticles were employed as scatterers instead of spherical particles, and the overall cell performance significantly increased. Moreover, for additional benefit of enhanced charge collection, $TiO_2$ nanotube arrays formed on the 3-dimensional Ti metal foam by electrochemical anodization were introduced as photoanode of DSCs. $TiO_2$ nanotubes are well known electrode materials for efficient charge collection due to the physical confinement of conduction band electron pathways. However, the surface area for dye-loading is significantly smaller than the conventional $TiO_2$ nanoparticle layer, and the overall performance has been inferior due to the lower amount of generated photocurrent caused by insufficient light harvesting. In contrast, anodized Ti foam had larger roughness factor compared to $TiO_2$ nanoparticles by more than a degree of order, and a high short-curcuit photocurrent density exceeding the 80% of the theoretical maximum were obtained, though the overall energy conversion efficiency did not increase significantly due to the low fill factor and photovoltage values resulted from the significant charge recombination taking place at the exposed Ti metal substrate. The design concept of anodized metal foam was extended to photoelectrochemical water splitting based on iron oxide photoanode, and by using anodized Fe foam electrode, unprecedented photocurrent density was observed before dark current onset. Moreover, with the assistance of Co catalysts, the best photoelectrochemical water splitting performance among iron oxide based photoelectrodes were obtained.

### 9.1.2. Electrocatalytic counter electrodes

In photoelectrochemical cells, oxidized or reduced species in the electrolyte get regenerated by accepting or donating electrons at the counter electrode, respectively. In order not to limit the overall performance of the cells, materials with high electrocatalytic activity, typically Pt, have been utilized, and this caused cost issues. Until now, the main issue in the electrocatalytic counter electrode field is the development of economical electrode with high performance and stability. In

order to achieve this goal, nanostructured carbide and nitride electrodes were proposed in this thesis.

In chapter 6, nanoporous WC electrodes were fabricated by electrochemical anodization of W foil followed by heat treatment in CO atmosphere. Due to the amorphous nature of anodic oxides, complete transition of oxide into carbide was successfully done. From 1970s, Pt-like behavior of WC was well known, and also in this study, WC showed excellent electrocatalytic activity, which was even superior to that of Pt probably due to the nanoporous structure. Since these WC electrodes had interconnected pores slightly larger than 50 nm, they were applied as counter electrodes of DSCs employing cobalt bipyridyl redox electrolyte which suffer from the significant mass transport limitations. DSCs with WC counter electrode exhibited considerably larger photocurrent density and energy conversion efficiency compared to the conventional DSCs with Pt counter.

In chapter 7 and 8, nanostructured nitride counter electrodes were prepared by room temperature reactive sputtering. For the synthesis of nitride materials, high temperature heat treatment in toxic $NH_3$ atmosphere has been the most common procedure, and this has been an obstacle for the practical utilization of nitride electrocatalysts. In contrast, Ni nitride and Co nitride with cauliflower-like nanostructure were synthesized by sputtering of Ni and Co in $N_2$ atmosphere. These nitrides showed excellent performance and stability in quantum dot-sensitized solar cells (QDSCs) employing polysulfide redox electrolyte. Moreover, in the case of Co nitride, photovoltaic parameters and energy conversion efficiency of DSCs with conventional iodide redox couple were comparable to Pt based ones, implying the possibility for the complete replacement of Pt in mesoscopic sensitized solar cells.

### 9.1.3. Facile preparation of nanostructured transition and post-transition metal compound electrodes

In the studies presented in previous chapters, nanostructured transition and post-transition metal compound electrodes were prepared by various facile methods such as electrochemical anodization, hydrolysis and condensation in bicontinous microemulsion, and room temperature reactive sputtering. In general, there are two obstacles for the preparation of high-performance electrodes with nanostructures for electrochemical energy applications: (i) harsh synthesis condition which often requires keen control and (ii) constitution of electrodes with prepared nanomaterials. In contrast, the methods employed here enabled direct fabrication of nanostructured thin film electrodes or enabled precise control during the synthesis of nanomaterials very easily. In addition, the electrodes were composed of low-cost and earth-abundant elements. Considering these, the results and findings explained in the previous chapters are anticipated to contribute to the research and industry of photoelectrochemical cells and further to the field of electrochemical applications.

## 9.2. Perspectives

### 9.2.1. Outlooks for mesoscopic sensitized solar cells

Recent advances in third generation organic solar cells, especially lead halide perovskite solar cells are eye-opening. As can be clearly seen from the certified efficiency chart in Figure 9.1, there were steep increase in the performance within last two years, exceeding 20% efficiency recently [1-16]. This makes the perovskite solar cells extremely feasible for large scale commercialization due to their low manufacturing cost and high performance that is even comparable to crystalline silicon solar cells, which constitute the largest portion of the market [17,18]. Meanwhile, since the origin of the perovskite solar cells is mesoscopic sensitized solar cells, the constitution and operation of these two types of

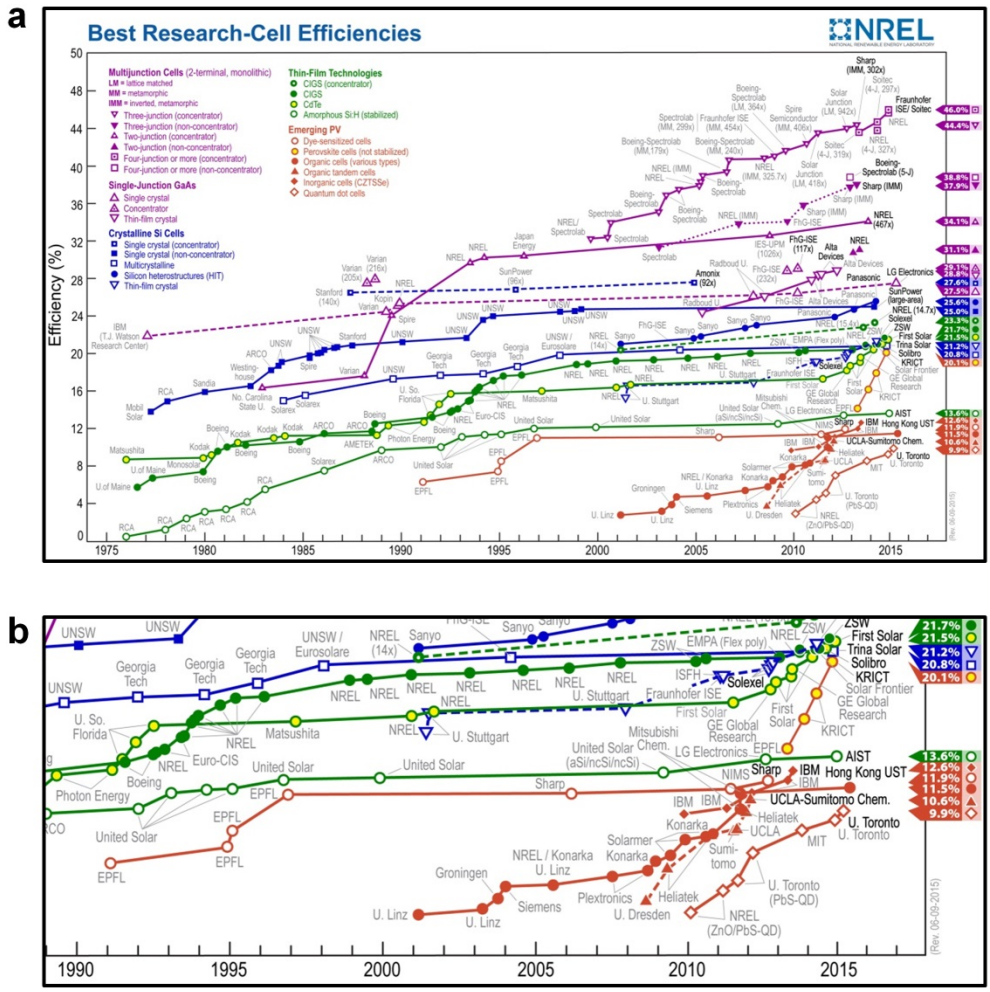


**Figure 9.1.** (a) Latest research solar cell efficiency chart and (b) its enlarged region showing the performances of third generation organic solar cells. (Adapted from http://www.nrel.gov/ncpv; National Center for Photovoltaics, National Renewable Energy Laboratory)

photovoltaics are very similar.

In the pioneering works by Kojima et al. [1] and Im et al. [2], the authors attempted to utilize $CH_3NH_3PbX_3$ as light harvesters in quantum dot-sensitized solar cells (QDSCs). Though the cell performances were of the highest level, these perovskite QDSCs severely suffered from the instability of $CH_3NH_3PbX_3$ in contact with the redox electrolyte. This problem was solved by Chung et al., who reported the possibility and application of the $CsSnI_3$ as solid hole conducting material in dye-sensitized solar cells (DSCs) [3,19]. Since the crystal structure of $CsSnI_3$ is identical with $CH_3NH_3PbX_3$, Kim et al. [4] and Lee et al. [5] deposited lead halide perovskite on the mesoscopic film, and developed solid-state solar cells with high performances. Based on this cell configuration (Figure 9.2), steep enhancements were resulted from various optimization and improvements in components [6,9,12-16].

These intrinsic similarity of mesoscopic sensitized solar cells and perovskite solar cells indicate that there are compatible materials and technologies for these two photovoltaic devices. For instance, $TiO_2$ blocking layers for the preparation of efficient on photoelectrode and solid hole conducting materials used in perovskite solar cells are introduced from the works done in the filed of mesoscopic sensitized solar cells [20-22]. Also, structural engineering which came out to be effective in DSCs are valid in perovskite solar cells [23,24]. Regarding this situation, the findings and insights discussed in this thesis are expected to contribute in the state-of-the-art organic solar cell technologies.

As introduced in chapter 6–8, transition metal compounds are displaying both high performance and stability as counter electrodes of mesoscopic sensitized solar cells. Though the origin of electrocatalytic activity is still unclear, there are numerous attempts to develop low-cost electrocatalyst with performance comparable to that of Pt [25-35]. Experimental screening [33] and computational analyses [35] verified that the adsorption energy is a critical parameter for the

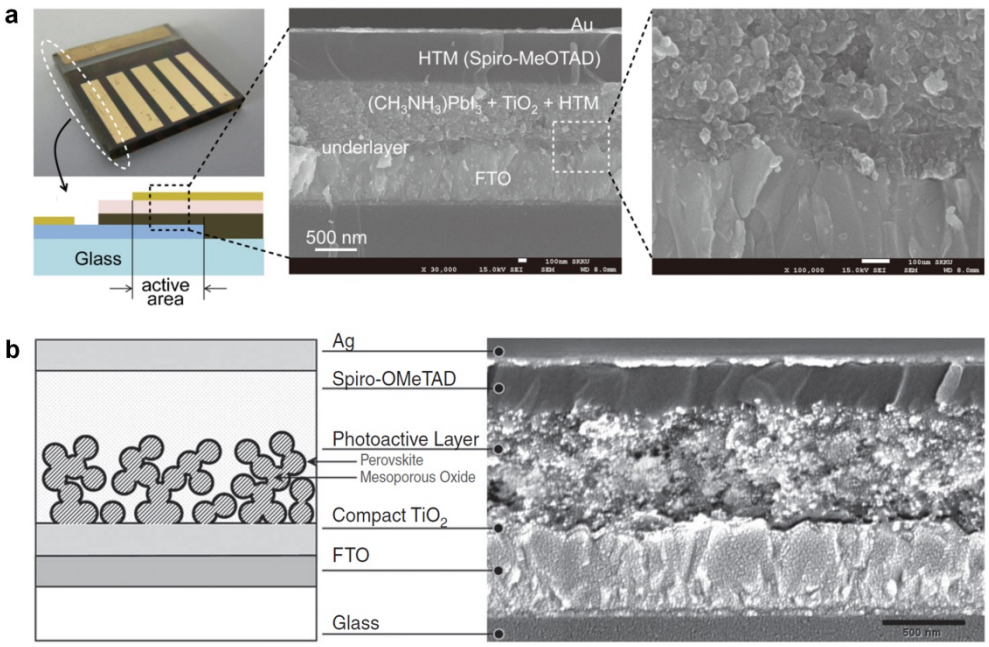


**Figure 9.2.** (a) Digital photograph images and cross-sectional SEM images of perovskite solar cells. (b) Comparison of schematic image and SEM images of perovskite solar cell's cross-section. (Adapted from Kim, H.-S. et al., *Sci. Rep.* **2012**, *2*, 591 and Lee, M. M. et al., *Science* **2012**, *338*, 643)

determination of catalytic activity, and based on those results on chemical compositions or facets, further improvements are being made by structural engineering for more efficient interfacial charge transfer and mass transport of the redox electrolyte. Moreover, since these materials are in charge of electrolyte regeneration (reduction), there are possibilities for them to replace hole quenchers in perovskite solar cells wherein sputtered Au is often employed [4,6,9,12-16]. Therefore, investigations and optimizations of transition metal compound electrodes for use in photovoltaic as counter electrodes are anticipated to be done more intensively in the days to come.

### 9.2.2. Outlooks for photoelectrochemical water splitting cells

The issues in photoelectrochemical water splitting were described in detail at the introduction chapter. Alternation of photoelectrode materials' properties by doping [36-42], structural engineering for enhanced charge transport [41-43], development of efficient heterojunction [44-47], and cocatalyst decoration at the electrode [48-51] surface have been done intensively by numerous researchers over the world. Moreover, in these days, the findings and approaches employed in mesoscopic sensitized solar cells for more efficient utilization of photons are frequently applied in photoelectrochemical water splitting cells (Figure 9.3 and 9.4) [52,53]. Dye- or quantum dot-sensitized metal oxide electrodes are utilized as photoelectrodes with excellent visible light harvesting ability, and significant advances have been achieved [54-59]. These approaches are especially noteworthy because of the easeness of tailoring the absorption properties and potentials for development by introducing various kinds of high performance materials.

Recently, photoelectrochemical water spitting cells are being challenged by the electrochemical cells comprising hydrogen evolution and oxygen evolution catalyst based electrodes operated by state-of-the-art photovoltaic devices. This combination of photovoltaics and electrocatalysts enabled 12.3% efficient

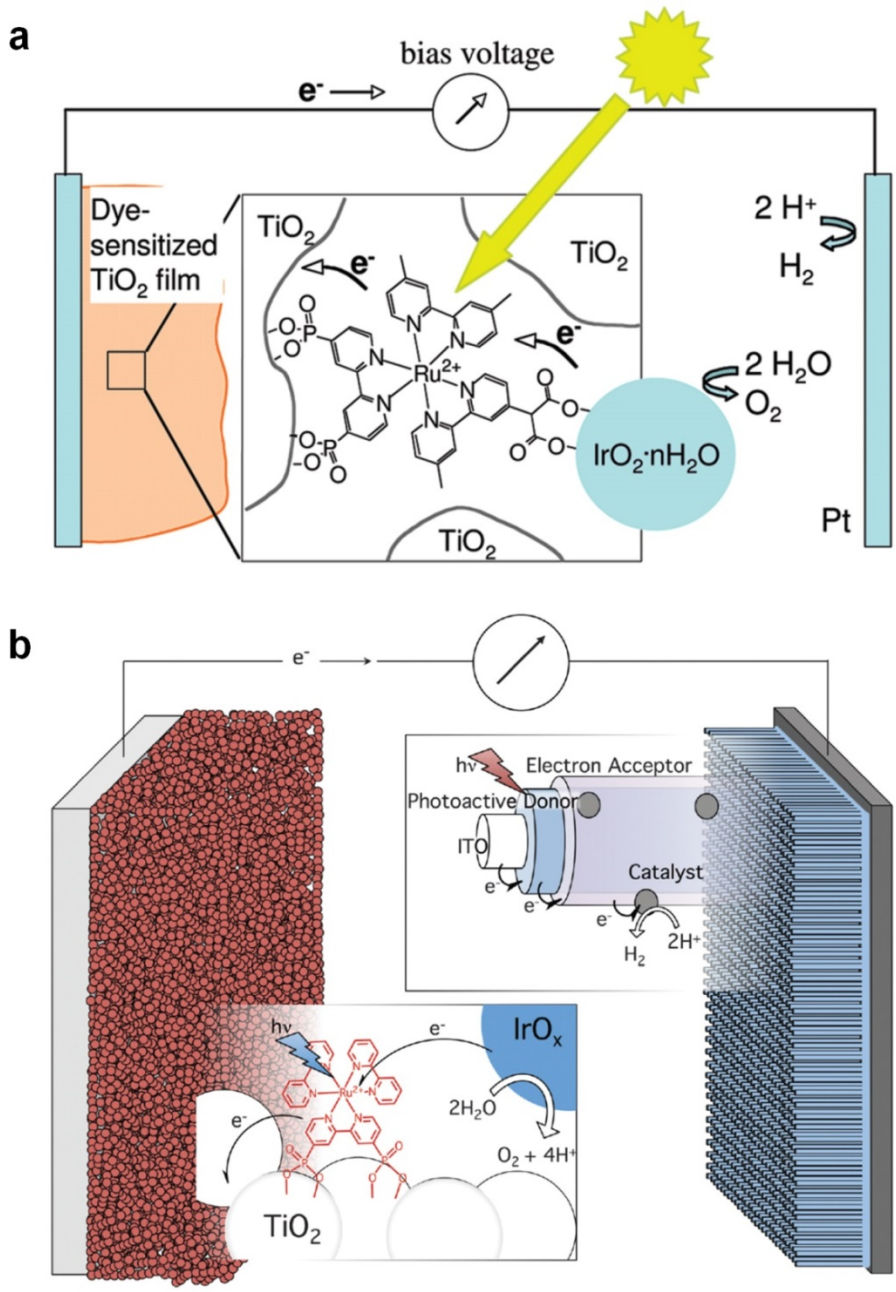


**Figure 9.3.** (a) Operation principles and (b) schematic image of dye-sensitized photoelectrochemical water splitting cells. (Adapted from Youngblood, W. J. et al., *Accouts Chem. Res.* **2009**, *42*, 1966 and Swierk, J. R. et al., *Chem. Soc. Rev.* **2013**, *42*, 2357)

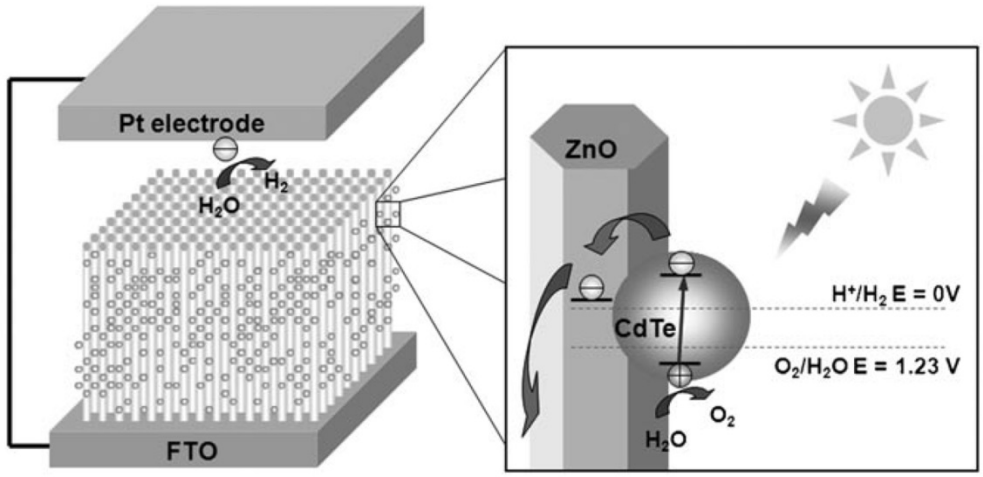


**Figure 9.4.** Schematic image and operation principles of quantum dot-sensitized photoelectrochemical water splitting cells. (Adapted from Chen, H. M. et al., *Angew. Chem. Int. Ed.* **2010**, *49*, 5966)

photolysis with low-cost perovskite solar cells and earth-abundant catalysts [60]. However, since the external bias significantly increases the water splitting ability in photoelectrochemial water splitting, assistance of photovoltaic devices is anticipated to bring great improvements to the overall performances of photoelectrochemical water splitting cells, as had been proved by the tandem approaches [61-65]. In short, combination of latest technologies for efficient utilization of photons is giving rise to the advances in this field, and this trend is expected to be same in the future.

## 9.3. References


[1] Kojima, A.; Teshima, K.; Shirai, Y.; Miyasaka, T., *J. Am. Chem. Soc.* **2009**, *131*, 6050.

[2] Im, J.-H.; Lee, C.-R.; Lee, J.-W.; Park, S.-W.; Park, N.-G., *Nanoscale* **2011**, *3*, 4088.

[3] Chung, I.; Lee, B.; He, J.; Chang, R. P. H.; Kanatzidis, M. G., *Nature* **2012**, *485*, 486.

[4] Kim, H.-S.; Lee, C.-R.; Im, J.-H.; Lee, K.-B.; Moehl, T.; Marchioro, A.; Moon, S.-J.; Humphry-Baker, R.; Yum, J.-H.; Moser, J. E.; Grätzel, M; Park, N.-G., *Sci. Rep.* **2012**, *2*, 591.

[5] Lee, M. M.; Teuscher, J.; Miyasaka, T.; Murakami, T. N.; Snaith, H. J., *Science* **2012**, *338*, 643.

[6] Burschka, J.; Pellet, N.; Moon, S.-J.; Humphry-Baker, R.; Gao, P.; Nazeeruddin, M. K.; Grätzel, M., *Nature* **2013,** *499,* 316.

[7] Liu, M.; Johnston, M. B.; Snaith, H. J., *Nature* **2013**, *501*, 395.

[8] Kim, H.-S.; Mora-Sero, I.; Gonzalez-Pedro, V.; Fabregat-Santiago, F.; Juarez-Perez, E. J.; Park, N.-G.; Bisquert, J., *Nat. Commun.* **2013**, *4*, 2242.

[9] Heo, J. H.; Im, S. H.; Noh, J. H.; Mandal, T. N.; Lim, C.-S.; Chang, J. A.; Lee, Y. H.; Kim, H.-J.; Sarkar, A.; Nazeeruddin, M. K.; Grätzel, M.; Seok, S. I., *Nat. Photonics* **2013**, *7*, 486.

[10] Stranks, S. D.; Eperon, G. E.; Grancini, G.; Menelaou, C.; Alcocer, M. J. P.; Leijtens, T.; Herz, L. M.; Petrozza, A.; Snaith, H. J., *Science* **2013**, *342*, 341.

[11] Xing, G.; Mathews, N.; Sun, S.; Lim, S. S.; Lam, Y. M.; Grätzel, M.; Mhaisalkar, S.; Sum, T. C., *Science* **2013**, *342*, 344.

[12] Jeon, N. J.; Noh, J. H.; Kim, Y. C.; Yang, W. S.; Ryu, S.; Seok, S. I., *Nat. Mater.* **2014**, *13*, 897.

[13] Im, J.-H.; Jang, I.-H.; Pellet, N.; Grätzel, M.; Park, N.-G., *Nat. Nanotechnol.* **2014**, *9*, 927.

[14] Zhou, H.; Chen, Q.; Li, G.; Luo, S.; Song, T.-B.; Duan, H.-S.; Hong, Z.; You, J.; Liu, Y.; Yang, Y., *Science* **2014**, *345*, 542.

[15] Jeon, N. J.; Noh, J. H.; Yang, W. S.; Kim, Y. C.; Ryu, S.; Seo, J.; Seok, S. I., *Nature* **2015**, *517*, 476.

[16] Yang, W. S.; Noh, J. H.; Jeon, N. J.; Kim, Y. C.; Ryu, S.; Seo, J.; Seok, S. I., *Science* **2015**, *348*, 1234.

[17] Park, N.-G., *J. Phys. Chem. Lett.* **2013**, *4*, 2423.

[18] Snaith, H. J., *J. Phys. Chem. Lett.* **2013**, *4*, 3623.

[19] Chung, I.; Song, J.-H.; Im, J.; Androulakis, J.; Malliakas, C. D.; Li, H.; Freeman, A. J.; Kenney, J. T.; Kanatzidis, M. G., *J. Am. Chem. Soc.* **2012**, *134*, 8579.

[20] Ito, S.; Liska, P.; Comte, P.; Charvet, R.L.; Pechy, P.; Bach, U.; Schmidt-Mende, L.; Zakeeruddin, S. M.; Kay, A.; Nazeeruddin, M. K.; Grätzel, M., *Chem. Commun.* **2005**, 4351.

[21] Bach, U.; Lupo, D.; Comte, P.; Moser, J. E.; Weissörtel, F.; Salbeck, J.; Spreitzer, H.; Grätzel, M., *Nature* **1998**, *395*, 583.

[22] Hagfeldt, A.; Boschloo, G.; Sun, L.; Kloo, L.; Pettersson, H., *Chem. Rev.* **2010,** *110*, 6595.

[23] Feng, X.; Shankar, K.; Varghese, O. K.; Paulose, M.; Latempa, T. J.; Grimes, C. A., *Nano Lett.* **2008**, *8*, 3781.

[24] Kim, H.-S.; Lee, J.-W.; Yantara, N.; Boix, P. P.; Kulkarni, S. A.; Mhaisalkar, S.; Grätzel, M.; Park, N.-G., *Nano Lett.* **2013**, *13*, 2412.

[25] Wang, M.; Anghel, A. M.; Marsan, B.; Ha, N.-L. C.; Pootrakulchote, N.; Zakeeruddin, S, M.; Grätzel, M., *J. Am. Chem. Soc.* **2009**, *131*, 15976.

[26] Li, G. R.; Song, J.; Pan, G. L.; Gao, X. P., *Energy Environ. Sci.* **2011**, *4*, 1680.

[27] Sun, H.; Qin, D.; Huang, S.; Guo, X.; Li, D.; Luo, Y.; Meng, Q., *Energy Environ. Sci*. **2011**, *4*, 2630.

[28] Wu, M.; Zhang, Q.; Xiao, J.; Ma, C.; Lin, X.; Miao, C.; He, Y.; Gao, Y.; Hagfeldt, A.; Ma, T., *J. Mater, Chem.* **2011**, *21*, 10761.

[29] Wang, Y.; Wu, M.; Lin, X.; Shi, Z.; Hagfeldt, A.; Ma, T., *J. Mater. Chem.* **2012**, *22*, 4009.

[30] Mulmudi, H. K.; Batabyal, S. K.; Rao, M.; Prabhakar, R. R.; Mathews, N.; Lam, Y. M.; Mhaisalkar, S. G., *Phys. Chem. Chem. Phys.* **2011**, *13*, 19307.

[31] Guai, G. H.; Leiw, M. Y.; Ng, C. M.; Li, C. M., *Adv. Energy Mater.* **2012**, *2*, 334.

[32] Chi, W. S.; Han, J. W.; Yang, S.; Roh, D. K.; Lee, H.; Kim, J. H., *Chem. Commun.* **2012**, *48*, 9501.

[33] Wu, M.; Lin, X.; Wang, Y.; Wang, L.; Guo, W.; Qi, D.; Peng, X.; Hagfeldt, A.; Grätzel, M.; Ma, T., *J. Am. Chem. Soc.* **2012**, *134*, 3419.

[34] Liao, Y.; Pan, K.; Wang, L.; Pan, Q.; Zhou, W.; Miao, X.; Jiang, B.; Tian, C.; Tian, G.; Wang, G.; Fu, H., *ACS Appl. Mater. Interfaces* **2013**, *5*, 3663.

[35] Hou, Y.; Wang, D.; Yang, X. H.; Fang, W. Q.; Zhang, B.; Wang, H. F.; Lu, G. Z.; Hu, P.; Zhao, H. J.; Yang, H. G., *Nat. Commun.* **2013**, *4*, 1583.

[36] Kay, A.; Cesar, I.; Grätzel, M., *J. Am. Chem. Soc.* **2006**, *128*, 15714.

[37] Tilley, S. D.; Cornuz, M.; Sivula, K.; Grätzel, M., *Angew. Chem. Int. Ed*. **2010**, *49*, 6405.

[38] Warren, S. C.; Voïtchovsky, K.; Dotan, H.; Leroy, C. M.; Cornuz, M.; Stellacci, F.; Hébert, C.; Rothschild, A.; Grätzel, M., *Nat. Mater.* **2013**, *12*, 842.

[39] Sivula, K.; Zboril, R.; Le Formal, F.; Robert, R.; Weidenkaff, A.; Tucek, J.; Frydrych, J.; Grätzel, M., *J. Am. Chem. Soc.* **2010**, *132*, 7436–7444.

[40] Chen, X.; Burda, C., *J. Am. Chem. Soc.* **2008**, *130*, 5018.

[41] Park, J. H.; Kim, S.; Bard, A. J., *Nano Lett.* **2006**, *6*, 24.

[42] Wang, G.; Wang, H.; Ling, Y.; Tang, Y.; Yang, X.; Fitzmorris, R. C.; Wang, C.; Zhang, J. Z.; Li, Y., *Nano Lett.* **2011**, *11*, 3026.

[43] Mor, G. K.; Shankar, K.; Paulose, M.; Varghese, O. K.; Grimes, C. A., *Nano Lett.* **2005**, *5*, 191.

[44] Moniz, S. J. A.; Shevlin, S. A.; Martin, D. J.; Guo, Z.-X.; Tang, J., *Energy Environ. Sci.* **2015**, *8*, 731.

[45] Jeong, H. W.; Jeon, T. H.; Jang, J. S.; Choi, W.; Park, H., *J. Phys. Chem. C* **2013**, *117*, 9104.

[46] Chi, X.; Choi, I. Y.; Zhang, K.; Kwon, J.; Kim, D. Y.; Lee, J. L.; Oh, S. H.; Kim, J. K.; Park, J. H., *Nat. Commun.* **2014**, *5*, 4775.

[47] Ma, M.; Kim, J. K.; Zhang, K.; Shi, X.; Kim, S. J.; Moon, J. H.; Park, J. H., *Chem. Mater.* **2014**, *26*, 5592.

[48] Steinmiller, E. M. P.; Choi, K. S., *Proc. Natl. Acad. Sci. USA* **2009**, *106*, 20633.

[49] Kiwi, J.; Grätzel, M., *Angew. Chem. Int. Ed.* **1978**, *17*, 860.

[50] Kiwi, J.; Grätzel, M., *Angew. Chem. Int. Ed.* **1979**, *18*, 624.

[51] Kim, T. W.; Choi, K.-S., *Science* **2014**, *343*, 990.

[52] Youngblood, W. J.; Lee, S.-H. A.; Maeda, K.; Mallouk, T. E., *Accouts Chem. Res.* **2009**, *42*, 1966.

[53] Swierk, J. R.; Mallouk, T. E., *Chem. Soc. Rev.* **2013**, *42*, 2357.

[54] Youngblood, W. J.; Lee, S.-H. A.; Kobayashi, Y.; Hernandez-Pagan, E. A.; Hoertz, P. G.; Moore, T. A.; Moore, A. L.; Gust, D.; Mallouk, T. E., *J. Am. Chem. Soc.* **2009**, *131*, 926.

[55] Li, L.; Duan, L.; Xu, Y.; Gorlov, M.; Hagfeldt, A.; Sun, L., *Chem. Commun.* **2010**, *46*, 7307.

[56] Zhao, Y.; Swierk, J. R.; Megiatto Jr, J. D.; Sherman, B.; Youngblood, W. J.; Qin, D.; Lentz, D. M.; Moore, A. L.; Moore, T. A.; Gust, D.; Mallouk, T. E., *Proc. Natl. Acad. Sci. USA* **2012**, *109*, 15612.

[57] Chen, H. M.; Chen, C. K.; Chang, Y.-C.; Tsai, C.-W.; Liu, R.-S.; Hu, S.-F.; Chang, W.-S.; Chen, K.-H., *Angew. Chem. Int. Ed.* **2010**, *49*, 5966.

[58] Wang, G.; Yang, X.; Qian, F.; Zhang, J. Z.; Li, Y., *Nano Lett.* **2010**, *10*, 1088.

[59] Sheng, W.; Sun, B.; Shi, T.; Tan, X.; Peng, Z.; Liao, G., *ACS Nano* **2014**, *8*, 7163.

[60] Luo, J.; Im, J.-H.; Mayer, M. T.; Schreier, M.; Nazeeruddin, M. K.; Park, N.-G.; Tilley, S. D.; Fan, H. J.; Grätzel, M., *Science* **2014**, *345*, 1593.

[61] Grätzel, M., *Nature* **2001**, *414*, 338.

[62] Arakawa, H.; Shiraishi, C.; Tatemoto, M.; Kishida, H.; Usui, D.; Suma, A.; Takamisawa, A.; Yamaguchi, T., *Proc. SPIE* **2007**, *6650*, 665003.

[63] Brillet, J.; Cornuz, M.; Le Formal, F.; Yum, J.-H.; Grätzel, M.; Sivula, K., *J. Mater. Res.* **2010**, *25*, 17.

[64] Brillet, J.; Yum, J.-H.; Cornuz, M.; Hisatomi, T.; Solarska, R.; Augustynski, J.; Grätzel, M.; Sivula, K., *Nat. Photonics* **2012**, *6*, 824.

[65] Shi, X.; Zhang, K.; Shin, K.; Ma, M.; Kwon, J.; Choi, I. T.; Kim, J. K.; Kim, H. K.; Wang, D. H.; Park, J. H., *Nano Energy* **2015**, *13*, 182.

# 국문초록

# 광전기화학전지를 위한 나노구조 전이금속 및 전이후금속 화합물 전극 연구

광전기화학전지는 반도체 기반의 광전극, 전기화학촉매활성을 지닌 상대전극, 그리고 전해질로 구성된 전기화학전지로, 전해질의 구동 방식에 따라 광전기화학 태양전지와 광합성전지로 분류된다. 이 두 가지 종류의 전지에서 각각의 경우 가장 대표적으로는 감응형 태양전지와 수전해전지를 들 수 있는데, 본 논문에서는 감응형 태양전지와 수전해전지를 위한 나노구조 전이금속 및 전이후금속 화합물 전극에 관한 연구를 진행하였다.

금속 산화물이 주로 사용되는 반도체 광전극 개발에서의 가장 주된 고려사항은 높은 광흡수 및 전하수집 능력이고, 이와는 달리 상대전극 분야에서는 가격이 높고 매장량이 적은 귀금속 전기화학촉매를 효과적으로 대체할 수 있는 재료를 만드는 노력이 중점적으로 이루어지고 있다. 이러한 상황들을 고려하여 이 논문에서는 전하전도도가 좋은 소재를 기반으로 한 나노구조 산화물 광전극을 개발하고, 기존에 사용되던 소재의 표면적을 극대화하여 광흡수율을 높이는 연구를 진행하였다. 또한 산업적으로 응용가능성이 높은 양극산화와 반응성 박막증착 방법으로 나노구조 탄화물 및 질화물을 제조하여 감응형 태양전지의 상대전극으로 적용하였다.

1장에서는 광전기화학 전지의 역사, 이론적 기반, 기존 연구에 관하여 전반적으로 설명하였고, 2장과 3장에서는 전하전도도가 좋은 아연산

화물과 주석산화물로 제조한 나노구조 광전극에 관한 연구를 진행하였다. 아연산화물은 화학적으로 매우 안정한 조건에서의 양극산화를 통해 메조포러스 나노와이어 구조로 합성되었고, 주석 산화물은 초음파의 보조를 받는 양극산화 방법으로 균일성이 높은 나노채널 형태로 만들어졌다. 이 두 전극 모두 준-고체의 염료감응 태양전지에서 우수한 성능을 나타냈고, 원자층증착을 통해 전극 표면에 티타늄 산화물을 코팅함으로써 더 높은 성능을 얻을 수 있었다.

4장과 5장에서는 광전극의 표면적을 극대화함으로써 광흡수율을 향상시키는 연구를 진행하였다. 4장에서는 주름구조의 규소산화물에 티타늄산화물을 코팅한 입자를 광전극에 도입하여 빛을 효과적으로 흡수 및 산란시키도록 하였다. 이를 감응형 태양전지에 적용했을 때 주름진 구조에 의한 표면적 증대로 인해 기존에 사용되던 구형 산란 입자를 사용한 경우보다 더 높은 성능을 보임을 확인하였고, 이에서 더 나아가 주름 간격이 파장에 따른 빛의 산란 정도에 미치는 영향에 관하여 고찰하였다. 5장에서는 동결-주조 방식으로 제조한 티타늄 폼과 철 폼을 양극산화하여 감응형 태양전지와 수전해전지의 광전극으로 사용하였다. 양극산화 과정에서 티타늄 폼 표면에는 일차원 구조의 티타늄 산화물 나노튜브가 생성되었고, 철 폼 표면에는 이차원 구조의 철 산화물 나노플레이크가 만들어졌다. 이러한 계층적 차원구조의 광전극은 세 가지 장점을 가지고 있었는데, 첫 번째는 광흡수를 극대화할 수 있는 넓은 표면적이었고, 두 번째는 낮은 차원의 산화물 구조를 통해 전하의 이동통로를 제한함으로써 전하의 수집률을 높일 수 있다는 것, 마지막은 삼차원 구조로 뻗어있는 금속 집전체를 통한 효과적인 전하 수집이 가능하다는 점이었다. 이러한 특성을 바탕으로 감응형 태양전지와 산화철 기반의 수전해전지 모두에서 큰 값의 광전류 밀도를 얻을 수 있었다.

6장에서는 양극산화에 이은 일산화탄소 열처리를 통해 나노구조 텅스텐 탄화물 전극을 제조하여 염료감응 태양전지의 상대전극으로 적용하였다. 양극산화 방식으로 제조한 산화물이 무정형이기 때문에 탄화물로의 전환이 용이하게 이루어질 수 있었고, 완성된 전극은 전해질 내의 산화환원쌍의 물질전달이 원활하게 일어날 수 있는 구조를 가지고 있었다. 뿐만 아니라 감응형 태양전지의 상대전극으로 사용했을 때, 기존에 가장 높은 성능을 보이는 것으로 알려진 백금보다 더 높은 전기화학적 촉매활성과 에너지 변환 효율을 얻을 수 있었는데, 이는 텅스텐 탄화물의 전자구조가 백금과 유사하고, 또 표면적이 넓은 나노구조로 인해 단위 면적 당 반응성이 더 좋기 때문인 것으로 추정되었다.

7장과 8장에서는 각각 나노구조 니켈 질화물과 코발트 질화물을 상온에서의 반응성 박막증착을 통해 제조하여 감응형 태양전지의 상대전극으로 사용하는 연구를 진행하였다. 특히 이 연구들에서는 다양한 전자현미경 및 엑스선 분석을 통해 만들어진 니켈 질화물과 코발트 질화물의 조성과 결정구조를 면밀하게 조사하였다. 두 전극 모두 양자점감응 태양전지에서 백금보다 더 좋은 성능을 보여주었고, 특히 코발트 질화물의 경우에는 염료감응 태양전지에서도 백금을 사용한 경우와 유사한 결과를 나타내었다. 더 나아가서 코발트 질화물은 양자점 감응태양전지의 상대전극 물질 중 가장 좋은 성능을 나타내는 것으로 알려져 있는 황화구리에 비해 매우 안정적인 활성을 보였고, 처음에는 상대적으로 낮은 성능을 보였으나 측정을 시작한 후 20분 이내에 광전류 밀도가 역전되는 것을 관찰할 수 있었다.

**주요어:** 광전기화학전지, 감응형 태양전지, 광전기화학 수전해전지, 양극 산화, 반응성 박막증착

**학번:** 2012-22577